JOURNAL OF COMPUTATIONAL AND APPLIED MECHANICS

A Publication of the University of Miskolc

VOLUME 2, NUMBER 1 (2001)

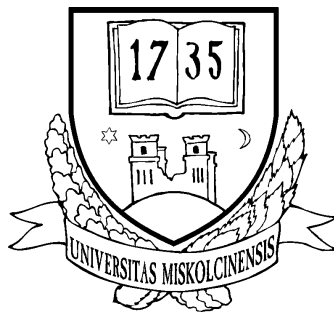**MISKOLC UNIVERSITY PRESS**

JOURNAL OF COMPUTATIONAL AND APPLIED MECHANICS

A Publication of the University of Miskolc

PREFACE

This special issue of the Journal of Computational and Applied Mechanics is dedicated to Prof. Tibor Czibere on the occasion of his 70th birthday. The range of topics covered by the various contributions reflects the scientific interests of Prof. Czibere. We are also pleased to include a paper on his newest research in this special issue.

Tibor Czibere was born in Tapolca in Western Hungary in 1930. After graduating from a high school in Keszthely in 1949 he was admitted to the Faculty of Mechanical Engineering of the Technical University for Heavy Industry in Miskolc (now the University of Miskolc). His aptitude was acknowledged early. Even as an undergraduate student he was asked to give tutorials for his fellow students in mathematics. In 1953 he obtained an M.Sc. degree in Mechanical Engineering with first class honors.

Tibor Czibere

After graduation he started to work as an assistant lecturer at the Department of Mathematics at the Technical University for Heavy Industry under the guidance of the famous Hungarian mathematician Professor Samu Borbély. He began to deal with nonlinear heat conduction problems, and it was this field which constituted his thesis for which the University of Miskolc awarded him the Ph.D. degree in 1961. In 1956 he became a research engineer at the Ganz-MÁVAG Locomotive and Railway Carriage Manufacturers. His first task was the investigation of flow in the bladed space of torque converters, and he developed a method based on the method of hydrodynamic singularities for the analysis and design of flow in turbomachines. Even after returning to the university in 1963, Prof. Czibere continued to do research there on a part-time basis until 1988.

In 1960 he delivered a well-received lecture at the Tenth International Conference in Applied Mechanics in Stresa (Italy) on his method for the design of straight and radial cascades of airfoils. His lecture attracted the attention of the world-famous scientist of Hungarian origin, Theodore von Kármán. This lecture brought him acclaim. In 1962, he was awarded the Kossuth Prize in acknowledgment of his scientific contributions. He was invited to spend three months as a guest lecturer at the Technical University of Berlin-Charlottenburg for three months in the following year.

In 1963 he defended his thesis entitled *A design method for straight cascade of highly cambered airfoils* for the Ph. D. degree conferred by the Hungarian Academy of Sciences and four years later he defended his thesis for D.Sc. (the highest academic degree, conferred also by the Hungarian Academy of Sciences) entitled *Solution of the two main problems of the hydrodynamic cascade theory by theory of potentials*. He was appointed full professor in 1968, at the early age of 38. In 1976 Prof. Czibere became a corresponding member of the Hungarian Academy of Sciences, and in 1985 an ordinary member.

Professor Czibere gave several lecture series about his research at different institu-

tions. Let us mention just a few of these: in Turboinstitut in Ljubljana in 1978 and in 1984; at the Technical University of Brno in 1990; at the Technical University of Braunschweig in 1994; and several times at the Otto von Guericke Technical University in Magdeburg. The Technical University of Brno awarded him its gold medal for the fruitful scientific cooperation between the two universities.

A more detailed account of Professor Czibere's scientific contributions can be found in this special issue, in the paper written by Professor A. Nyíri.

Throughout the greater part of his career, Prof. Czibere has been involved in administrative matters in a leadership role. Since his scientific activities and engineering proficiency had been recognized and awarded by the Kossuth Prize, he was chosen in 1963 to fill the vacancy of the chair of the Department of Machine Operation, which became the current Department of Fluid and Heat Engineering. He held the post of Head of Department for 25 years, from 1963 till 1988. As Head of Department, he modified the research and educational profiles of the department substantially to meet changing requirements, and the teaching staff was strengthened and broadened by the addition of young researchers who had been educated in the department. He encouraged staff to investigate research topics directly connected with industrial problems.

Prof. Czibere also played an important role in the administration of the Faculty of Mechanical Engineering and that of the University of Miskolc. He was appointed Vice-dean of the Faculty for the period 1966 to 1968, and in 1968 he was elected to be the Dean. He held this position till 1974. During this time the structure of education was changed substantially at the university, and Prof. Czibere contributed significantly to the introduction of the modular educational system. In recognition of his scientific contributions and his leadership qualities he was elected to be the Rector of the University in 1978. As the leader of the University he made efforts to introduce the training of lawyers and economists at the University. With his support, the Faculty of Law was established in 1981. During his eight years in this post, he worked closely with the leaders of the city of Miskolc, and this contribution was recognized by the prize 'Pro Urbe' (For the City). In 1988, Prof. Czibere was asked to contribute his expertise in educational administration as the Minister of Culture and Education of Hungary, in the difficult period of transition from the socialist system. Ultimately, his concepts and those of the national leadership differed, and the following year he returned to the University of Miskolc and resumed teaching at the Department of Fluid and Heat Engineering.

Prof. Czibere has always put a great deal of effort into educational endeavors, in the lecture hall as well as in administrative offices. He developed the curriculum of several courses such as Fluid Mechanics, Turbomachines, Continuum Mechanics of Fluids, and Heat Transfer. He wrote textbooks for most of the subjects he taught, and his *Fluid Mechanics*, among others, has been and still is used by engineering students across the nation. His teaching materials reflect his view of engineering as an applied science. He is an excellent lecturer who prepares carefully and composes his lectures in a very logical way. He has the gift of being able to present very complicated matters in an elegant and simple fashion and to make his audience understand what at first seems difficult. By using mathematical means, he derives equations or formulae describing flow phenomena in a concise manner.

Prof. Czibere played an active role in establishing the Ph.D. training at the university. He personally has supervised several researchers. He was the supervisor of three persons who defended their D.Sc. dissertations, and supervised altogether twenty Ph.D. disertations. Of course, the number of researchers directly and indirectly influenced by Prof. Czibere is much larger, and followers of the "Czibere School" have produced results of great merit.

Prof. Czibere has always been supported in his activities by his wife Gabriella. They have two children, both of whom have gone into technical fields. Prof. Czibere is also a proud grandfather of five. He continues to be an active researcher, often working even at home. His current research is on a three-dimensional stochastic turbulence model.

Recent awards recognizing Prof. Czibere's many and varied contributions are: the Albert Szentgyörgyi Prize, 1996, for his influential scientific contributions; honorary citizenship of Miskolc, 2000, awarded by the City Council; and 'Doctor Honoris causa' of the University of Miskolc in 2000.

On behalf of his friends, colleagues and his former students, the editors are pleased to dedicate this special issue to Prof. Czibere in honor of his 70th birthday.

<div align="right">

László Baranyi
the Editor of the Present Issue

</div>

THREE DIMENSIONAL STOCHASTIC MODEL OF TURBULENCE

Tibor Czibere
Department of Fluid and Heat Engineering, University of Miskolc
3515 Miskolc-Egyetemváros, Hungary
aramczt@gold.uni-miskolc.hu

Abstract. Mean velocity distributions of fully developed turbulent flows show a similarity revealed by experiments. The theoretical approach of *Kármán's* similarity hypothesis [1] concerning two-dimensional turbulent velocity fluctuations was based on experiments, but it was criticized on the basis of the generally accepted view that the turbulence phenomena was always three-dimensional. This paper intends to reveal that the mechanical similarity hypothesis is applicable to the 3-D boundary layer flow and a 3-D model of turbulence will be shown according to which the inner mechanism of the turbulence can be represented by a stochastic process including 5 independent probability variables.

Keywords: Similarity hypothesis, stochastic, turbulence model, turbulent vortex diffusion, Reynolds' stress tensor, vector potential of turbulent velocity fluctuation.

1. Governing equations of turbulent motion

In the *Eulerian* description of the turbulent motion of a fluid, continuum can be composed by the superposition of two velocity fields depending on the space coordinates and time. The first is the very rapid stochastic velocity fluctuation in time, which is the turbulence phenomenon. The second one is the time dependent mean velocity describing the motion of the continuum. All the characteristics of the motion can be composed of two components: *instantaneous value = mean value + fluctuation.* The mean value of a variable in a time interval t_0 is

$$\Phi\left(\mathbf{r}, t\right) = \frac{1}{t_0} \int\limits_t^{t+t_0} \Phi_T\left(\mathbf{r}, \tau\right) \mathrm{d}\tau \tag{1.1}$$

where Φ can be scalar, vector or tensor field, and the subscript T refers to the turbulent instantaneous value. Accordingly, the instantaneous value of the velocity field has the form:

$$\mathbf{v}_T\left(\mathbf{r}, t\right) = \mathbf{v}\left(\mathbf{r}, t\right) + \mathbf{v}'\left(\mathbf{r}, t\right),$$

where $\mathbf{v}\left(\mathbf{r}, t\right)$ is the turbulent mean value of the motion taken on a sufficiently long interval of t_0 compared to the periodicity of the fluctuation, and $\mathbf{v}'\left(\mathbf{r}, t\right)$ is the turbulent velocity fluctuation, the mean value of which is zero. Due to the velocity fluctuation in the turbulent flow, a very intensive change of momentum takes place, increasing the

resistance against the deformation of the flowing fluid. In other words, the apparent viscosity of the flowing fluid will be increased due to the change of momentum.

This study will be restricted to isothermal motion of incompressible fluids. The equation of continuity concerning the instantaneous velocity field $\mathbf{v}_T(\mathbf{r}, t)$ is as follows:

$$\nabla \cdot \mathbf{v}_T = 0. \tag{1.2}$$

The *Stokes* molecular viscosity law is valid for the instantaneous turbulent motion as is commonly accepted. Consequently, the turbulent stress tensor can be written for the instantaneous values:

$$\mathbf{F}_T = -p_T \mathbf{I} + \boldsymbol{\sigma}_T = -p_T \mathbf{I} + \eta \left(\mathbf{v}_T \circ \nabla + \nabla \circ \mathbf{v}_T \right), \tag{1.3}$$

where p_T is the instantaneous pressure, $\boldsymbol{\sigma}_T$ is the deviator of the instantaneous stress tensor $\mathbf{F}_T$, η is the dynamic viscosity and $\mathbf{I}$ is the unit tensor. If the force field is derivable from a potential U, the *Navier-Stokes* momentum equation for the viscous turbulent flow with instantaneous quantities takes the form

$$\frac{\partial \mathbf{v}_T}{\partial t} + \left(\mathbf{v}_T \cdot \nabla \right) \mathbf{v}_T = -\nabla U + \frac{1}{\rho} \operatorname{Div} \left[-p_T \mathbf{I} + \boldsymbol{\sigma}_T \right]. \tag{1.4}$$

Here and in the sequal $\operatorname{Div} [] = [] \cdot \nabla$. Introducing the vortex vector $\boldsymbol{\Omega}_T = \nabla \times \mathbf{v}_T$ and taking the curl of the previous equation, we obtain the *Helmholz-Thomson* vortex theorem for the instantaneous velocity field:

$$\frac{\partial \boldsymbol{\Omega}_T}{\partial t} + \left(\mathbf{v}_T \cdot \nabla \right) \boldsymbol{\Omega}_T - \left(\boldsymbol{\Omega}_T \cdot \nabla \right) \mathbf{v}_T = \nu \triangle \boldsymbol{\Omega}_T. \tag{1.5}$$

Let $\mathbf{a}(\mathbf{r}, t)$ be a given vector field in the velocity field $\mathbf{v}(\mathbf{r}, t)$. The necessary and sufficient condition for the vector lines to satisfy equation $\mathbf{a} \times d\mathbf{r} = \mathbf{0}$ and to be constituted by the same fluid particles during the motion, and for the intensity of the vector tubes $\mathbf{a} \cdot d\mathbf{A} = a dA_n$ to remain constant is:

$$\frac{\partial \mathbf{a}}{\partial t} + \left(\mathbf{v} \cdot \nabla \right) \mathbf{a} - \left(\mathbf{a} \cdot \nabla \right) \mathbf{v} + \mathbf{a} \left(\nabla \cdot \mathbf{v} \right) = \mathbf{0}.$$

This equation is called *Friedman* conservation law of vector tubes [2]. Consequently, according to equation (1.5) the vortex lines $(\nabla \times \mathbf{v}_T) \times d\mathbf{r} = \mathbf{0}$ in an incompressible fluid flow with potential force field are not conserved but vanish, i.e., diffuse in the surroundings. The measure of diffusion is determined by the term on the right-hand side (RHS) of equation (1.5), i.e., by $\nu \triangle \boldsymbol{\Omega}_T$. In case of inviscid fluid for which $\nu \to 0$ the vortex lines are conserved.

The equation of continuity for an incompressible fluid can be given in terms of the velocity field $\mathbf{v}(\mathbf{r}, t)$:

$$\nabla \cdot \mathbf{v} = \mathbf{0}. \tag{1.6}$$

The time-mean value of equation (1.4) is to be taken to obtain the *Reynolds* momentum equation for the turbulent motion of fluid particles

$$\frac{\partial \mathbf{v}}{\partial t} + \left(\mathbf{v} \cdot \nabla \right) \mathbf{v} = -\nabla U + \frac{1}{\rho} \operatorname{Div} \left[-p\mathbf{I} + \boldsymbol{\sigma} - \rho \left(\overline{\mathbf{v}' \circ \mathbf{v}'} \right) \right], \tag{1.7}$$

where the time-mean value is denoted by an overbar, $\boldsymbol{\sigma}$ is the time-mean value of the stress tensor given by the *Stokes* relation

$$\boldsymbol{\sigma} = \eta \ (\mathbf{v} \circ \nabla + \nabla \circ \mathbf{v}) . \tag{1.8}$$

The last expression in the bracket on the RHS of equation (1.7) is the apparent turbulent stress tensor named after *Reynolds*: $\mathbf{F}_R = -\rho \left(\overline{\mathbf{v}' \circ \mathbf{v}'} \right)$.

The vortex theorem for the vector $\boldsymbol{\Omega} = \nabla \times \mathbf{v}$ in the mean velocity field $\mathbf{v}\,(\mathbf{r},t)$ determining the phenomena of the vortex lines $(\nabla \times \mathbf{v}) \ \times \mathrm{d}\mathbf{r} = \mathbf{0}$ follows from equation (1.5) by taking its time-mean value:

$$\frac{\partial \boldsymbol{\Omega}}{\partial t} + (\mathbf{v} \cdot \nabla)\,\boldsymbol{\Omega} - (\boldsymbol{\Omega} \cdot \nabla)\,\mathbf{v} = \nu \triangle \boldsymbol{\Omega} + \nabla \times \ \left(\overline{\mathbf{v}' \times \boldsymbol{\Omega}'} \right) . \tag{1.9}$$

Here $\boldsymbol{\Omega}' = \nabla \times \mathbf{v}'$ is the vortex field of the velocity fluctuation. Consequently, vortex lines in the turbulent mean velocity field $\mathbf{v}\,(\mathbf{r},t)$ are not conserved even in the extreme case when $\nu \to 0$, but diffuse. The measure of vortex diffusion is determined by the viscosity of fluid and dominantly by the velocity fluctuation of turbulence.

2. Vector Potential of Turbulent Velocity Fluctuation

Let P be a fixed arbitrary point, $\mathbf{v}_P$ the turbulent mean velocity and $\boldsymbol{\Omega}_P = \nabla \times \mathbf{v}_P$ the vortex vector in the flow. Furthermore let Q be a *varying* point in the vicinity of P in which the turbulent instantaneous values are

$$\mathbf{v}_T = \mathbf{v}_Q + \mathbf{v}' \qquad \text{and,} \qquad \boldsymbol{\Omega}_T = \nabla \times \mathbf{v}_T = \boldsymbol{\Omega}_Q + \boldsymbol{\Omega}'$$

where $\mathbf{v}_Q$ and $\boldsymbol{\Omega}_Q$ are time-mean values, $\mathbf{v}'$ and $\boldsymbol{\Omega}' = \nabla \times \mathbf{v}'$ are the turbulent fluctuations. Because the order of the change in time of the fluctuations $\mathbf{v}'$ is much greater than that of the mean velocity, the error will not be significant supposing the mean value field together with $\mathbf{v}_P$ and $\boldsymbol{\Omega}_P$ are *constants*. The *Helmholz-Thomson* vortex theorem (1.5) is obviously valid in a relative coordinate system with its origin in P and moving with the constant turbulent mean velocity $\mathbf{v}_P$. Consequently, it can be applied to the vortex field $\boldsymbol{\Omega}_T$ in the velocity field moving with $\mathbf{v}_T - \mathbf{v}_P$, and we get:

$$\frac{\partial \boldsymbol{\Omega}_T}{\partial t} + [(\mathbf{v}_T - \mathbf{v}_P) \cdot \nabla]\,\boldsymbol{\Omega}_T - (\boldsymbol{\Omega}_T \cdot \nabla)\,(\mathbf{v}_T - \mathbf{v}_P) = \nu \triangle \boldsymbol{\Omega}_T.$$

To examine the turbulent motion let us substitute the instantaneous values of $\mathbf{v}_T$ and $\boldsymbol{\Omega}_T$ and take the limit $Q \to P$, $\mathbf{v}_T \to \mathbf{v}_P$ and $\boldsymbol{\Omega}_T \to \boldsymbol{\Omega}_P$ to obtain the differential equation:

$$\frac{\partial \boldsymbol{\Omega}'}{\partial t} + \left(\mathbf{v}' \cdot \nabla \right) \boldsymbol{\Omega}' - \left(\boldsymbol{\Omega}' \cdot \nabla \right) \mathbf{v}' = \nu \triangle \boldsymbol{\Omega}' + (\boldsymbol{\Omega} \cdot \nabla)\,\mathbf{v}'. \tag{2.1}$$

As P is arbitrary, the subscript at $\boldsymbol{\Omega}$ can be omitted without causing any misunderstanding. Equation (2.1) is a *vortex theorem for the turbulent velocity fluctuation field* $\mathbf{v}'$ meaning that the vector lines determined by the differential equation $\left(\nabla \times \mathbf{v}' \right) \times \mathrm{d}\mathbf{r} = \mathbf{0}$ are not conserved even if $\nu \to 0$ but scattered and diffused while moving.

The effect of molecular viscosity will decrease due to the change of momentum amongst the fluid particles in the turbulent flow; therefore, the term $\nu\triangle\boldsymbol{\Omega}'$ on the RHS of equation (2.1) becomes negligible. The boundary layer flows where the shear stress is dominant and $\mathbf{v}$ and $\nabla \times \mathbf{v}$ are not parallel will be examined in a suitable coordinate system. An orthogonal curvilinear coordinate system q_1', q_2', q_3' will be attached to the mean velocity field as well, for which the base vectors are determined by $\mathbf{v}$ and $\nabla \times \mathbf{v}$ – see Figure 1 – as follows:

$$\mathbf{e}_3' = \frac{\nabla \times \mathbf{v}}{|\nabla \times \mathbf{v}|}; \ \mathbf{e}_2' = \frac{\mathbf{v} \times \nabla \times \mathbf{v}}{|\mathbf{v} \times \nabla \times \mathbf{v}|}; \ \mathbf{e}_1' = \mathbf{e}_2' \times \mathbf{e}_3' = \frac{1}{\sqrt{1-\lambda^2}} \left(\frac{\mathbf{v}}{|\mathbf{v}|} - \lambda \frac{\nabla \times \mathbf{v}}{|\nabla \times \mathbf{v}|} \right),$$

where

$$\lambda = \frac{\mathbf{v}}{|\mathbf{v}|} \cdot \frac{\nabla \times \mathbf{v}}{|\nabla \times \mathbf{v}|}.$$

This is called the natural coordinate system of the boundary layer flow. The turbulent mean velocity can be expressed by its components in the q_1', q_2', q_3' system:

$$\mathbf{v} = v_{1'} \cdot \mathbf{e}_1' + v_{3'} \cdot \mathbf{e}_3' = v\sqrt{1-\lambda^2}\mathbf{e}_1' - \lambda\, v\, \mathbf{e}_3'$$

Here $v = \sqrt{v_{1'}^2 + v_{3'}^2}$ is the absolute value of the velocity. The vorticity of the mean velocity can be written as

$$\boldsymbol{\Omega} = \nabla \times \mathbf{v} = -|\nabla \times \mathbf{v}|\,\mathbf{e}_3' = -\Omega\mathbf{e}_3', \tag{2.2}$$

where Ω is the rate of change of the q_1' component of the velocity in the direction q_2'. One can see in Figure 1 that $\Omega = -\Omega_{3'}$ is the negative component of $\boldsymbol{\Omega}$ in the direction q_3':

$$\Omega = -\Omega_{3'} = \frac{1}{H_1' H_2'} \frac{\partial\left(v_{1'} H_1'\right)}{\partial q_2'}, \tag{2.3}$$

where H_i' $(i = 1, 2, 3)$ are the Lamé's metric coefficients in the natural coordinate system q_1', q_2', q_3'. One can easily see that if $\mathbf{v}$ and $\nabla \times \mathbf{v}$ are perpendicular vectors as is true for two-dimensional flows, then $\mathbf{v} \cdot \boldsymbol{\Omega} = 0$, and therefore $\mathbf{e}_1' = \frac{\mathbf{v}}{|v|}$, i.e., the streamlines coincide with the coordinate q_1'.

Making use of equation (2.1) the turbulent fluctuation can be investigated separately from the mean flow in a coordinate system moving with the mean velocity $\mathbf{v}$. The base vectors in thes coordinates sysytem are the same as those we introduced earlier. In this system the differential operator ∇ and the product $\nabla \cdot \boldsymbol{\Omega}$ can be expressed as follows:

$$\nabla = \frac{\mathbf{e}_1'}{H_1'}\frac{\partial}{\partial q_1'} + \frac{\mathbf{e}_2'}{H_2'}\frac{\partial}{\partial q_2'} + \frac{\mathbf{e}_3'}{H_3'}\frac{\partial}{\partial q_3'} \quad \text{and} \quad \boldsymbol{\Omega} \cdot \boldsymbol{\nabla} = -\Omega\left(\mathbf{e}_3' \cdot \nabla\right) = -\frac{\Omega}{H_3'}\frac{\partial}{\partial q_3'}.$$

By applying the vortex theorem (2.1) in the q_1', q_2', q_3' coordinate system moving with the flow for the velocity fluctuation $\mathbf{v}'$ we obtain the following differential equation

$$\frac{\partial\left(\nabla \times \mathbf{v}'\right)}{\partial t} + \left(\mathbf{v}' \cdot \nabla\right)\left(\nabla \times \mathbf{v}'\right) - \left(\left(\nabla \times \mathbf{v}'\right)\cdot \nabla\right)\mathbf{v}' = -\frac{\Omega}{H_3'}\frac{\partial \mathbf{v}'}{\partial q_3'}. \tag{2.4}$$
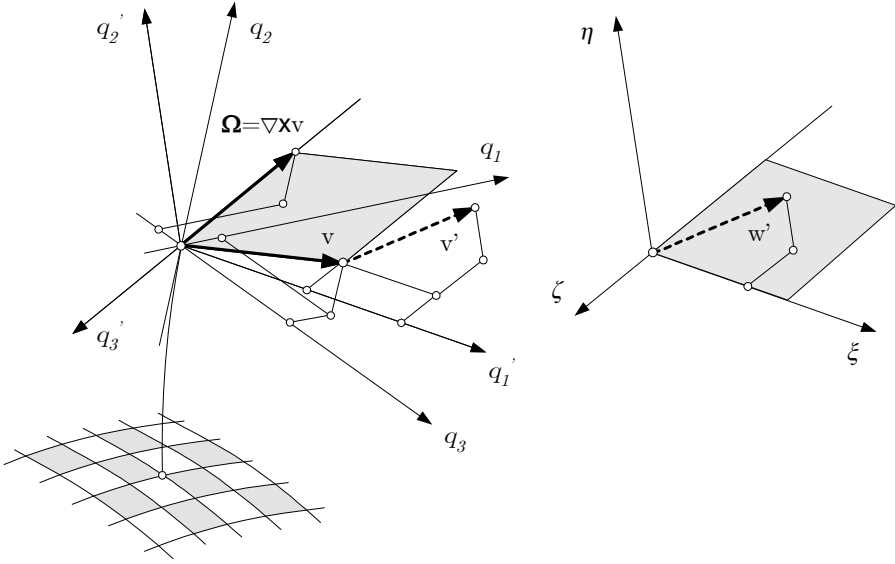
Figure 1. The boundary layer flow in the natural orthogonal curvilinear coordinate system

This equation is considered as the *momentum equation of turbulence* describing the fluctuation in the moving coordinate system. The sole dependence is obvious from equation (2.4) relating the turbulent fluctuation $\mathbf{v}'$ to the vorticity of the turbulent mean velocity $\mathbf{v}$. Consequently the dependence between $\mathbf{F}_R = -\rho \left(\overline{\mathbf{v}' \circ \mathbf{v}'} \right)$, the apparent *Reynolds'* stress tensor and the vorticity of the mean velocity is obvious and *no relation exists* between the stress and deformation velocity tensors [1].

As the turbulent fluctuation velocity $\mathbf{v}'\left(\mathbf{r}, t \right)$ is a rotational vector field there exists a vector potential function $\boldsymbol{\Psi}\left(\mathbf{r}, t \right)$ from which v' can be obtained as $\mathbf{v}' = \nabla \times \boldsymbol{\Psi}$. Supposing that the vector potential is sourceless, as is commonly supposed, we obtain $\nabla \times v' = \nabla \times \left(\nabla \times \boldsymbol{\Psi} \right) = -\triangle \boldsymbol{\Psi}$ and we arrive at the following differential equation for the vector potential $\boldsymbol{\Psi}$ by substituting it into equation (2.4):

$$\frac{\partial \triangle \boldsymbol{\Psi}}{\partial t} + \left(\left(\nabla \times \boldsymbol{\Psi} \right) \cdot \nabla \right) \triangle \boldsymbol{\Psi} - \left(\triangle \boldsymbol{\Psi} \cdot \nabla \right) \left(\nabla \times \boldsymbol{\Psi} \right) = \Omega \left(\mathbf{e}_3' \cdot \nabla \right) \left(\nabla \times \boldsymbol{\Psi} \right) . \quad (2.5)$$

The character of this equation is that of a momentum equation such as (2.4) so it is suitable to investigate the similarity phenomena of turbulent motion. Two patterns of motion are similar to each other if the momentum equations of each can be transformed by geometrical and dynamic transformations. For the moving q_1', q_2', q_3' orthogonal curvilinear coordinate system, we introduce the following geometrical transformation

$$H_1' dq_1' = \ell \ d\xi; \ \ H_2' dq_2' = \ell \ d\eta; \ H_3' dq_3' = \ell \ d\zeta \, ,$$

---

[1] The equation of continuity (1.6) and the Reynolds' momentum equation (1.7) together with Equ. (2.4) is a closed differential equation system of seven equations and there are seven unknown functions, namely the three mean velocity components, the three velocity fluctuation components and the pressure to be determined.

which transforms the physical space of the velocity fluctuation $\mathbf{v}'(\mathbf{r}, t)$ to the points of an orthogonal coordinate system where the fixed point P corresponds to the origin $O(0,0,0)$ (Figure 1) in the coordinates ξ, η, ζ. Let us introduce the transformations $dt = T d\tau$ for the time and $\boldsymbol{\Psi}\left(q_1', q_2', q_3', t\right) = C \cdot \mathbf{f}(\xi, \eta, \zeta, \tau)$ for the vector potential. Here ℓ is the length scale, T is the time scale and C is the scale of vector potential. The last three scales are independent of the q_1', q_2', q_3' and ξ, η, ζ coordinates. These transformations will be substituted to the (2.5) momentum equation. By this transformation the turbulent motion is transformed into the ξ, η, ζ orthogonal coordinate system, therefore it is called the *map of turbulence*.

The turbulent stream patterns in the points of the flow can be considered similar if the differential equation for the dimensionless vector potential $\mathbf{f}$ transformed from the differential equation (2.5) for $\boldsymbol{\Psi}$ does not depend on the specification of motion in point P. It is easy to see that the similarity conditions are as follows:

$$\frac{C}{\ell^2 T} = \frac{C^2}{\ell^4} = \frac{C\,\Omega}{\ell^2}$$

If these conditions are fulfilled, then the transformed equation of motion (2.5) for the vector potential $\mathbf{f}$ takes the form

$$\frac{\partial \Delta \mathbf{f}}{\partial \tau} + ((\nabla \times \mathbf{f}) \cdot \nabla) \Delta \mathbf{f} - (\Delta \mathbf{f} \cdot \nabla)(\nabla \times \mathbf{f}) = \frac{\partial}{\partial \zeta}(\nabla \times \mathbf{f}) \qquad (2.6)$$

The last equation does obviously not depend on the characteristics of flow in a point P. Consequently, the turbulent velocity fluctuation $\mathbf{v}'(\mathbf{r}, t)$ in the points of the boundary layer flow mapped to the space of ξ, η, ζ will have the same $\mathbf{f}(\xi, \eta, \zeta, \tau)$ vector potential, which is exactly the expression of the mechanical similarity for the three dimensional turbulence phenomena. From these three conditions of similarity for ℓ, T and C, only one can be selected freely because of the relationship amongst them. Selecting one of them, the two remaining are determined. Let us select the length scale ℓ we get for the left two scale factors:

$$T = \frac{1}{\Omega} \; ; \; C = \ell^2 \Omega.$$

As a consequence of the mechanical similarity hypothesis in the point ξ, η, ζ of the mapped space of three dimensional turbulence, the vector potential $\mathbf{f}(\xi, \eta, \zeta, \tau)$ determines the structure of turbulence up to a certain measure of dimensionless size, and converting it by the length scale ℓ, the result will be the true for the local turbulent motion corresponding to the geometrical circumstances. The length scale ℓ characterizes the size of the local turbulence.

3. Three Dimensional Stochastic Model of Turbulence

It is clear from previous considerations that the partial differential equation (2.6) for $\mathbf{f}(\xi, \eta, \zeta, \tau)$ is equivalent to the creation of the inner mechanism of turbulence models. The particular solutions of equation (2.6) lead to different models for turbulence.

Since direct physical tests theoretically cannot be carried out, only the numerical results computed on the base of the models can justfy them. It is always advisable to make simplifications when seeking particular solutions. Therefeore we shall make the following restrictions when seeking the particular solutions of equation (2.6):

$$\nabla \cdot \mathbf{f} = 0 \qquad \text{and} \qquad \Delta\,\mathbf{f} = a\,\mathbf{f} + b\,\nabla\times\mathbf{f}\,.$$

Here a and b are scalars. Since the effect of molecular viscosity can be excluded in the mapped space of turbulence, we suppose that the vector lines satisfying the equation $\mathbf{f}\times d\mathbf{r} = \mathbf{0}$ will remain in this space. By introducing the notation $\mathbf{w}' = \nabla\times\mathbf{f}$ *Friedman*'s law of conservation of vector tubes becomes:

$$\frac{\partial\mathbf{f}}{\partial\tau} + (\mathbf{w}'\cdot\nabla)\,\mathbf{f} - (\mathbf{f}\cdot\nabla)\,\mathbf{w}' = \mathbf{0}\,. \tag{3.1}$$

The equation to be solved under these conditions is as follows:

$$\frac{\partial}{\partial\tau}\,(\nabla\times\mathbf{f}) = \omega\,\frac{\partial}{\partial\zeta}\,(\nabla\times\mathbf{f})\,. \tag{3.2}$$

Here $\omega = 1/b$. One can see that only $\nabla\times\mathbf{f}$ is sought and not the vector potential $\mathbf{f}$ itself and by this the inner mechanism of turbulence can be determined.

A possible particular solution, which characterizes the mechanism by a stochastic process, for example may be following:

$$\nabla\times\mathbf{f}\ (\xi,\eta,\zeta,\tau) = \varepsilon\sum_{n=1}^{N}\left(\begin{array}{c} C_{1n}e^{n\xi}\cos\left[n\left(\zeta+\omega\tau\right)+\alpha_{1n}\right] \\ C_{2n}\cos\left[n\left(\zeta+\omega\tau\right)+\alpha_{2n}\right] \\ C_{3n}e^{-n\eta}\cos\left[n\left(\zeta+\omega\tau\right)+\alpha_{3n}\right] \end{array}\right) -$$

$$-\,\varepsilon\sum_{n=1}^{N}\left(\begin{array}{c} C_{2n}\sin\left[n\left(\zeta+\omega\tau\right)+\alpha_{2n}\right] \\ C_{3n}e^{-n\eta}\sin\left[n\left(\zeta+\omega\tau\right)+\alpha_{3n}\right] \\ C_{1n}e^{n\xi}\sin\left[n\left(\zeta+\omega\tau\right)+\alpha_{1n}\right] \end{array}\right)\,. \tag{3.3}$$

The parameters ε and ω are optional. The meaning of ω is the lowest angular frequency of the turbulent fluctuation. The $C_{in}\ (i=1,2,3)$ are the random amplitudes of the wave components, which are probability variables with uniform probability distributions in the given $[0,\delta_i]$ intervals. The probability variables $\alpha_{in}\ (i=1,2,3)$ are the random phase angles determining a certain direction in space therefore the relation $cos^2\alpha_{1n} + cos^2\alpha_{2n} + cos^2\alpha_{3n} = 1$ should be satisfied.

According to our conditions the origin of the ξ,η,ζ coordinate system in the mapped space of turbulence corresponds to an arbitrary point P in the physical space. Consequently, the fluctuation velocity $\mathbf{v}'$ in the moving q_1',q_2',q_3' coordinate system can be written as follows:

$$\mathbf{v}'\left(q_1',q_2',q_3',t\right) = \ell\left(q_1',q_2',q_3'\right)\,\Omega\left(q_1',q_2',q_3',t\right)\,\nabla\times\mathbf{f}\,(0,0,0,\tau)\,. \tag{3.4}$$

Taking equation (3.3) into consideration for the fluctuation velocity we obtain:

$$\mathbf{v}'\left(q_1',q_2',q_3',t\right) = l\Omega\varepsilon\sum_{n=1}^{N}\left(\begin{array}{c} C_{1n}\cos\left(n\omega\tau+\alpha_{1n}\right) - C_{2n}\sin\left(n\omega\tau+\alpha_{2n}\right) \\ C_{2n}\cos\left(n\omega\tau+\alpha_{2n}\right) - C_{3n}\sin\left(n\omega\tau+\alpha_{3n}\right) \\ C_{3n}\cos\left(n\omega\tau+\alpha_{3n}\right) - C_{1n}\sin\left(n\omega\tau+\alpha_{1n}\right) \end{array}\right)\,.$$

The turbulent stress tensor $\mathbf{F}_R$ can be given in the q_1', q_2', q_3' coordinate system, considering equation (2.3):

$$
\begin{aligned}
\mathbf{F}_R &= -\rho\left(\overline{\mathbf{v}' \circ \mathbf{v}'}\right) = -\rho\left(\ell\,\Omega\right)^2\left(\overline{\nabla \times \mathbf{f} \circ \nabla \times \mathbf{f}}\right) = \\
&= -\rho l^2\left(\overline{\nabla \times \mathbf{f} \circ \nabla \times \mathbf{f}}\right)\left(\frac{1}{H_1' H_2'}\frac{\partial\left(v_{1'} H_1'\right)}{\partial q_2'}\right)^2.
\end{aligned}
$$

Let us introduce the following notations:

$$
\alpha = \frac{\overline{\left(\nabla \times \mathbf{f}\right)_\xi^2}}{\overline{\left(\nabla \times \mathbf{f}\right)_\xi\left(\nabla \times \mathbf{f}\right)_\eta}} \;;\quad \beta = \frac{\overline{\left(\nabla \times \mathbf{f}\right)_\eta^2}}{\overline{\left(\nabla \times \mathbf{f}\right)_\xi\left(\nabla \times \mathbf{f}\right)_\eta}} \;;\quad \gamma = \frac{\overline{\left(\nabla \times \mathbf{f}\right)_\zeta^2}}{\overline{\left(\nabla \times \mathbf{f}\right)_\xi\left(\nabla \times \mathbf{f}\right)_\eta}}
$$

$$
\mu = \frac{\overline{\left(\nabla \times \mathbf{f}\right)_\xi\left(\nabla \times \mathbf{f}\right)_\zeta}}{\overline{\left(\nabla \times \mathbf{f}\right)_\xi\left(\nabla \times \mathbf{f}\right)_\eta}} \;;\quad \vartheta = \frac{\overline{\left(\nabla \times \mathbf{f}\right)_\eta\left(\nabla \times \mathbf{f}\right)_\zeta}}{\overline{\left(\nabla \times \mathbf{f}\right)_\xi\left(\nabla \times \mathbf{f}\right)_\eta}} \;;\quad \kappa^2 = \overline{\left(\nabla \times \mathbf{f}\right)_\xi\left(\nabla \times \mathbf{f}\right)_\eta}.
$$

With these notations the so-called similarity tensor assumes the form

$$
\mathbf{H} = \begin{pmatrix} \alpha & 1 & \mu \\ 1 & \beta & \vartheta \\ \mu & \vartheta & \gamma \end{pmatrix}. \tag{3.5}
$$

We accept the convention that the sign of the dominant shear stress on the surface with a normal vector perpendicular to the direction of the flow, is the same as that of the derivative of the velocity in the direction of the normal vector.

The turbulent stress tensor $\mathbf{F}_R$ in the q_1', q_2', q_3' natural coordinate system is of the form

$$
\mathbf{F}_R\left(q_1', q_2', q_3', t\right) = \rho\,\kappa^2\,\ell^2\,\mathbf{H}\left|\frac{1}{H_1' H_2'}\frac{\partial\left(v_{1'} H_1'\right)}{\partial q_2'}\right|\frac{1}{H_1' H_2'}\frac{\partial\left(v_{1'} H_1'\right)}{\partial q_2'}. \tag{3.6}
$$

The parameter ε in equation (3.3) is to be chosen in such a way that the *Kármán constant* has the value $\kappa = 0,40704$. The components of the similarity tensor $\mathbf{H}$ in the q_1', q_2', q_3' natural coordinate system are constants so they express a kind of proportionality, which is the reason for the name of similarity. Furthermore introducing the notation:

$$
\Theta\left(q_1', q_2', q_3', t\right) = \rho\,\kappa^2\,\ell^2\,\left|\Omega\right|\,\Omega = \rho\,\kappa^2\,\ell^2\,\left|\frac{1}{H_1' H_2'}\frac{\partial\left(v_{1'} H_1'\right)}{\partial q_2'}\right|\frac{1}{H_1' H_2'}\frac{\partial\left(v_{1'} H_1'\right)}{\partial q_2'}, \tag{3.7}
$$

the turbulent stress tensor $\mathbf{F}_R$ can be written in the natural coordinate system in the following form:

$$
\mathbf{F}_R = \Theta\left(q_1', q_2', q_3', t\right)\mathbf{H}, \tag{3.8}
$$

where Θ is the element in the first row and second column of the stress tensor, $\Theta \equiv \tau_{12}' = \tau_{21}'$ is the dominant turbulent stress in the flow.

The first step in determining the components of the similarity tensor $\mathbf{H}$ in our example (3.3), the coefficients C_{in} $(i = 1, 2, 3)$ and the phase angles α_{in} $(i = 1, 2, 3)$ must be properly chosen. These quantities are probability variables with uniform

distribution functions in the intervals fixed in advance. The next step is to obtain the elements of the turbulent stress tensor $\mathbf{F}_R$, i.e., the time mean values of the components $(\nabla \times \mathbf{f})_j$ $(j = \xi, \eta, \zeta)$ must be determined. These will have the form:

$$\overline{(\nabla \times \mathbf{f})_k (\nabla \times \mathbf{f})_l} = \varepsilon^2 \, U_{k,l} \; ; \quad (k, l = \xi, \eta, \zeta) \; ,$$

in which $U_{k,l}$ are the sums of the products as follows:

$$
\begin{aligned}
U_{\xi,\eta} \;=\; U_{\eta,\xi} &= \frac{1}{2} \sum_{n=1}^{N} \left\{ C_{1n} C_{2n} \cos\left(\alpha_{1n} - \alpha_{2n}\right) \right\} + \\
&+ \frac{1}{2} \sum_{n=1}^{N} \left\{ C_{1n} C_{3n} \sin\left(\alpha_{1n} - \alpha_{3n}\right) + C_{2n} C_{3n} \cos\left(\alpha_{2n} - \alpha_{3n}\right) \right\} ,
\end{aligned}
$$

$$
\begin{aligned}
U_{\eta,\zeta} \;=\; U_{\zeta,\eta} &= \frac{1}{2} \sum_{n=1}^{N} \left\{ C_{2n} C_{3n} \cos\left(\alpha_{2n} - \alpha_{3n}\right) \right\} + \\
&+ \frac{1}{2} \sum_{n=1}^{N} \left\{ C_{2n} C_{1n} \sin\left(\alpha_{2n} - \alpha_{1n}\right) + C_{3n} C_{1n} \cos\left(\alpha_{3n} - \alpha_{1n}\right) \right\} ,
\end{aligned}
$$

$$
\begin{aligned}
U_{\zeta,\xi} \;=\; U_{\xi,\zeta} &= \frac{1}{2} \sum_{n=1}^{N} \left\{ C_{3n} C_{1n} \cos\left(\alpha_{3n} - \alpha_{1n}\right) \right\} + \\
&+ \frac{1}{2} \sum_{n=1}^{N} \left\{ C_{3n} C_{2n} \sin\left(\alpha_{3n} - \alpha_{2n}\right) + C_{1n} C_{2n} \cos\left(\alpha_{1n} - \alpha_{2n}\right) \right\} ,
\end{aligned}
$$

$$U_{\xi,\xi} = \frac{1}{2} \sum_{n=1}^{N} \left\{ C_{1n}^2 + C_{2n}^2 + 2 C_{1n} C_{2n} \sin\left(\alpha_{1n} - \alpha_{2n}\right) \right\} ,$$

$$U_{\eta,\eta} = \frac{1}{2} \sum_{n=1}^{N} \left\{ C_{2n}^2 + C_{3n}^2 + 2 C_{2n} C_{3n} \sin\left(\alpha_{2n} - \alpha_{3n}\right) \right\}$$

$$U_{\zeta,\zeta} = \frac{1}{2} \sum_{n=1}^{N} \left\{ C_{3n}^2 + C_{1n}^2 + 2 C_{3n} C_{3n} \sin\left(\alpha_{3n} - \alpha_{1n}\right) \right\} .$$

The quantities $U_{k,l}$ $(k, l = \xi, \eta, \zeta)$ strictly determine the components of the similarity tensor $\mathbf{H}$ defined by equation (3.5). It is to be mentioned that numerous turbulence models can be created by the selection of the coefficients C_{in}. One of them could be:

$$C_{in} = k_{in} \, exp\left[- \left((n-1)/K \right)^2 \right] .$$

The mean random numbers k_{in} $(i = 1, 2, 3)$ are probability variables having uniform distribution functions in the intervals $[0, \delta_i]$, K is an integer fixed in advance.
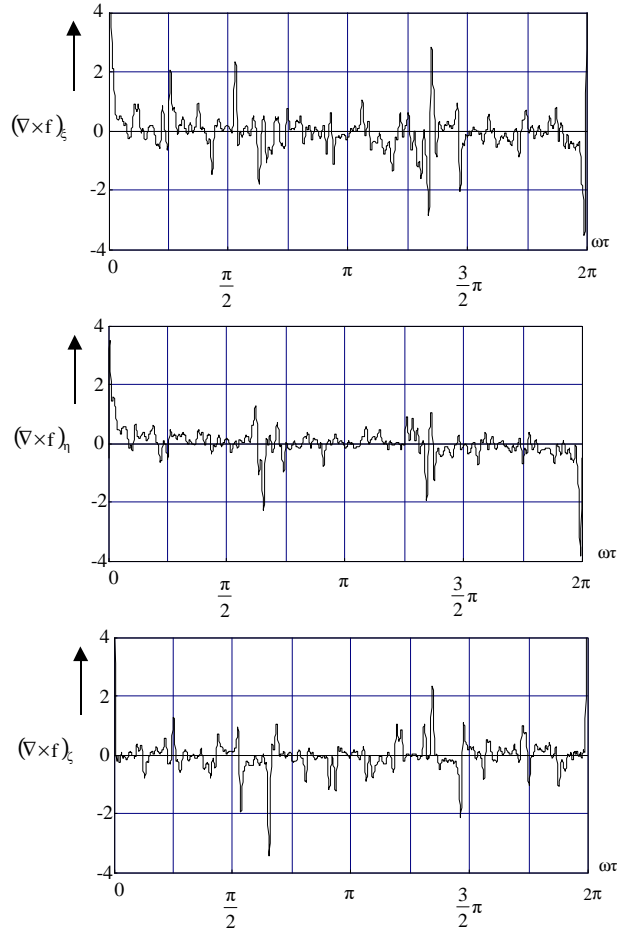
Figure 2. Components of the curl of the vector potential **f** within one period

The variation of the three components of the curl of the dimensionless vector potential can be seen in Figure 2. In this example the data are: $K = 100$; $\delta_1 = 1,0$; $\delta_2 = 0,75$; $\delta_3 = -0,093$, and the components of tensor **H** are:

$$\alpha = 3,9714; \;\; \beta = 1,5734; \;\; \gamma = 2,8203; \;\; \mu = 0,9871; \;\; \vartheta = 0,0002.$$

The *Kármán-constant* $\kappa = 0,40704$ can be obtained by the selection of $\varepsilon = 0,20844$. The α, β, γ values are based on the experimental results of *Laufer* [3] obtained from tests of fully developed turbulent flow in circular pipes. Our aim was simply to show that by the selection of a particular solution of the differential equation (2.6) for the dimensionless vector potential an appropriate stochastic model could be created. Since many particular solutions of the differential equation (2.6) exist, there are various possibilities to create stochastic models fitting different tasks.

The sum of the results is as follows. A natural coordinate system can be attached to the velocity field of the turbulent fluctuation based on the similarity hypothesis. The mean velocity $\mathbf{v}$ and the $\nabla \times \mathbf{v}$ vector determine the basic directions of this system. Moreover, a dimensionless vector potential changing periodically can be associated with this system. The components of the vector potential are composed by a series of waves of random amplitudes and phase angles. The turbulent velocity fluctuation v' can be derived from the vector potential. A 3-D turbulence model is obtained in the way in which the inner mechanism of the turbulence is represented by a stochastic process including 5 independent variables.

4. Turbulence Model in the 3-D Boundary Layer Flow

Along a solid wall in the boundary layer flow below a certain *Reynolds'* number the flow is laminar and it is turbulent above it. The viscosity effect prevails throughout the full layer in case of laminar flow but in the turbulent case only in a thin layer called laminar sublayer. Beyond this sublayer, i.e., in the turbulent boundary layer, the mean characteristic of flow is the turbulent fluctuation causing apparent stress phenomena or in other words apparent friction. The frictionless potential flow is outside of the turbulent layer.

The equations describing the potential flow of an incompressible fluid follow from the equation of continuity and the irrotational velocity field

$$\nabla \cdot \mathbf{v} = 0 \; ; \qquad \nabla \times \mathbf{v} = \mathbf{0}.$$

The velocity field can be calculated as the gradient of a velocity potential Φ. Substituting it into the continuity equation, we obtain a differential equation for the velocity potential:

$$\Delta \Phi = 0. \tag{4.1}$$

The boundary conditions for this *Laplace* equation on the solid walls and on the inflow and outflow surfaces respectively of the domain are:

$$(\mathbf{n}\cdot\nabla)\,\Phi = 0 \qquad \text{and} \qquad (\mathbf{n}\cdot\nabla)\,\Phi = v_{B,K}.$$

The unit vector $\mathbf{n}$ is directed outward and normal to the surfaces. The velocity v_B is the distribution normal to the inflow surfaces and v_K is that to the outflow surfaces. There are potential theoretical methods to solve equation (4.1).

The equation of continuity and the momentum equation are decisive in determining the flow of a real fluid. The momentum equation can be replaced by the vortex theorem obtained by taking the curl of the momentum equation. Doing so will increase the order of equations, but the number of unknowns will be less by one. Therefore, it will become easier to set up the closed system of equations for the numerical solution.

We are going to investigate the turbulent flow of incompressible fluid ($\rho = const$) in a force field having potential function ($\mathbf{g} = -\nabla U$). The mean velocity in the q_1, q_2, q_3 orthogonal curvilinear coordinate system is $\mathbf{v} = v_1\mathbf{e}_1 + v_2\mathbf{e}_2 + v_3\mathbf{e}_3$ and the velocity

fluctuation is $\mathbf{v}' = v_1' \mathbf{e}_1 + v_2' \mathbf{e}_1 + v_3' \mathbf{e}_3$. The law of mass conservation is expressed by

$$\nabla \cdot \mathbf{v} = 0. \tag{4.2}$$

The *Reynolds'* momentum equation of the turbulent motion of a fluid described by equation (1.7) will be reformulated. The gauge pressure p_R caused by the turbulent velocity fluctuation will be defined by the first scalar invariant of the turbulent stress tensor $\mathbf{F}_R$:

$$p_R = \tfrac{1}{3} \left(\overline{v_1' v_1'} + \overline{v_2' v_2'} + \overline{v_3' v_3'} \right).$$

The deviator $\boldsymbol{\sigma}_R$ of turbulent stress tensor $\mathbf{F}_R$ is created as usual:

$$\sigma_R = -\rho \begin{pmatrix} \sigma_{11} & \sigma_{12} & \sigma_{13} \\ \sigma_{21} & \sigma_{22} & \sigma_{23} \\ \sigma_{31} & \sigma_{32} & \sigma_{33} \end{pmatrix},$$

where

$$\begin{aligned}
\sigma_{11} &= \tfrac{1}{3} \left(2\overline{v_1' v_1'} - \overline{v_2' v_2'} - \overline{v_3' v_3'} \right), \\
\sigma_{22} &= \tfrac{1}{3} \left(2\overline{v_2' v_2'} - \overline{v_3' v_3'} - \overline{v_1' v_1'} \right), \\
\sigma_{33} &= \tfrac{1}{3} \left(2\overline{v_3' v_3'} - \overline{v_1' v_1'} - \overline{v_2' v_2'} \right), \\
\sigma_{12} &= \sigma_{21} = \overline{v_1' v_2'} = \overline{v_2' v_1'}, \\
\sigma_{13} &= \sigma_{31} = \overline{v_1' v_3'} = \overline{v_3' v_1'}, \\
\sigma_{23} &= \sigma_{32} = \overline{v_2' v_3'} = \overline{v_3' v_2'}.
\end{aligned}$$

The *Reynolds'* momentum equation of the turbulent flow of viscid fluid in a conservative force field has the form:

$$\rho \frac{\partial \mathbf{v}}{\partial t} + \rho \left(\mathbf{v} \cdot \nabla \right) \mathbf{v} = \rho \, \nabla \mathit{\Pi} + \eta \, \triangle \mathbf{v} + \mathrm{Div} \, \boldsymbol{\sigma}_R. \tag{4.3}$$

Here $\mathit{\Pi} = U + p/\rho + p_R/\rho$, the total potential of the incompressible fluid is the sum of the force field potential and the pressure potential. Let $\boldsymbol{\sigma}_R$ be the deviator of the turbulent stress tensor $\mathbf{F}_R$. It follows from equation (3.8) that in the natural coordinate system q_1', q_2', q_3'

$$\boldsymbol{\sigma}_R = \Theta \left(q_1', q_2', q_3', t \right) \mathbf{H}^*.$$

Here $\mathbf{H}^*$ is the deviator of the similarity tensor $\mathbf{H}$:

$$\mathbf{H}^* = \begin{pmatrix} \alpha_* & 1 & \mu \\ 1 & \beta_* & \vartheta \\ \mu & \vartheta & \gamma_* \end{pmatrix} = \begin{pmatrix} \tfrac{1}{3}(2\alpha - \beta - \gamma) & 1 & \mu \\ 1 & \tfrac{1}{3}(2\beta - \gamma - \alpha) & \vartheta \\ \mu & \vartheta & \tfrac{1}{3}(2\gamma - \alpha - \beta) \end{pmatrix}.$$

Working in an arbitrary q_1, q_2, q_3 orthogonal curvilinear system the deviator tensor $\boldsymbol{\sigma}_R$ should be written in its transformed form:

$$\boldsymbol{\sigma}_R = \Theta \left(q_1', q_2', q_3', t \right) \mathbf{G}^*. \tag{4.4}$$

The tensor $\mathbf{G}^*$ is the transformed form of the deviator $\mathbf{H}^*$ in the q_1, q_2, q_3 system:

$$\mathbf{G}^* = \mathbf{E} \cdot \mathbf{H}^* \cdot \mathbf{E}^T.$$

The elements of the transformation tensor $\mathbf{E}$ (and its transposed $\mathbf{E}^T$) are the scalar products of the base vectors $E_{ij} = \mathbf{e}_i \cdot \mathbf{e}'_j$ $(i, j = 1, 2, 3)$. As the base vectors of the system q'_1, q'_2, q'_3 have previously been given, the elements of $\mathbf{E}$ are as follows:

$$E_{11} = \frac{1}{\sqrt{1-\lambda^2}}\left(\frac{v_1}{v} - \lambda\frac{\Omega_1}{\Omega}\right) \;;\; E_{12} = \frac{1}{\sqrt{1-\lambda^2}}\frac{v_2\Omega_3 - v_3\Omega_2}{v\,\Omega} \;;\; E_{13} = -\frac{\Omega_1}{\Omega};$$

$$E_{21} = \frac{1}{\sqrt{1-\lambda^2}}\left(\frac{v_2}{v} - \lambda\frac{\Omega_2}{\Omega}\right) \;;\; E_{22} = \frac{1}{\sqrt{1-\lambda^2}}\frac{v_3\Omega_1 - v_1\Omega_3}{v\,\Omega} \;;\; E_{23} = -\frac{\Omega_2}{\Omega};$$

$$E_{31} = \frac{1}{\sqrt{1-\lambda^2}}\left(\frac{v_3}{v} - \lambda\frac{\Omega_3}{\Omega}\right) \;;\; E_{32} = \frac{1}{\sqrt{1-\lambda^2}}\frac{v_1\Omega_2 - v_2\Omega_1}{v\,\Omega} \;;\; E_{33} = -\frac{\Omega_3}{\Omega}.$$

Here Ω_i are the scalar components of $\boldsymbol{\Omega} = \nabla \times \mathbf{v}$ and λ is determined by the scalar product of the unit vectors in the direction velocity and the vortex vector:

$$\Omega_1 = \frac{1}{H_3 H_2}\left(\frac{\partial(v_3 H_3)}{\partial q_2} - \frac{\partial(v_2 H_2)}{\partial q_3}\right);$$

$$\Omega_2 = \frac{1}{H_3 H_1}\left(\frac{\partial(v_1 H_1)}{\partial q_3} - \frac{\partial(v_3 H_3)}{\partial q_1}\right);$$

$$\Omega_3 = \frac{1}{H_1 H_2}\left(\frac{\partial(v_2 H_2)}{\partial q_1} - \frac{\partial(v_1 H_1)}{\partial q_2}\right);$$

$$\lambda = \frac{v_1\Omega_1 + v_2\Omega_2 + v_3\Omega_3}{\sqrt{v_1^2 + v_2^2 + v_3^2}\,\sqrt{\Omega_1^2 + \Omega_2^2 + \Omega_3^2}}.$$

The elements of $\mathbf{G}^*$ can be calculated easily utilizing the previous relationships, and therefore they may be omitted here.

The *Reynolds'* momentum equation (4.3) with the expression (4.4) for the deviator $\boldsymbol{\sigma}_R$ of the turbulent stress tensor takes the form:

$$\rho\frac{\partial \mathbf{v}}{\partial t} + \rho\left(\mathbf{v}{\cdot}\boldsymbol{\nabla}\right)\mathbf{v} = \rho\,\nabla II + \eta\,\Delta\mathbf{v} + \text{Div}\,\left(\Theta\mathbf{G}^*\right). \tag{4.5}$$

The motion of real fluid is described by two differential equations namely the *Reynolds'* momentum equation (4.5) and the continuity equation (4.2). Five unknown functions can be found in these four scalar equations $[v_1(q_1, q_2, q_3, t)$, $v_2(q_1, q_2, q_3, t)$, $v_3(q_1, q_2, q_3, t)$, $\Pi(q_1, q_2, q_3, t)$ and $\Theta(q_1, q_2, q_3, t)]$. Since this system of equations is not closed, one more equation is needed to accomplish numerical calculations. The divergence of equation (4.5) is a possible scalar differential equation for the following reasons. As the fluid is incompressible $\nabla{\cdot}\mathbf{v} = 0$, while the following vector relationship is valid:

$$\nabla \cdot [(\mathbf{v} \cdot \boldsymbol{\nabla})\,\mathbf{v}] = \nabla \cdot [(\mathbf{v} \circ \mathbf{v}){\cdot}\nabla] = (\mathbf{v}\circ\nabla) : (\nabla\circ\mathbf{v}).$$

Applying these relationships to equation (4.5) for the total potential Π we obtain the following scalar differential equation:

$$\rho \, \Delta\Pi = -\rho \left(\mathbf{v} \circ \nabla\right) : \left(\nabla \circ \mathbf{v}\right) + \nabla \cdot \text{Div} \ \left(\Theta \mathbf{G}^*\right). \tag{4.6}$$

Here the colon means double scalar products of tensors or dyads. Since in the equation (4.6) a further unknown function does not occur, it will make the differential equation system (4.2) and (4.5) closed.

There is another way to determine the flow of a real fluid numerically apart from the previously mentioned system composed of equations (4.2), (4.5) and (4.6). The vortex theorem (1.9) can be reshaped utilizing the stochastic turbulence model. The time mean value of $\mathbf{v}' \times \mathbf{\Omega}'$ can be determined taking into consideration the fact that $\nabla \cdot \mathbf{v}' = 0$ and the following relationship:

$$\mathbf{v}' \times \left(\nabla \times \mathbf{v}'\right) = \tfrac{1}{2}\nabla \left(\mathbf{v}' \cdot \mathbf{v}'\right) - \left(\mathbf{v}' \cdot \nabla\right)\mathbf{v}' = \tfrac{1}{2}\nabla\left(\mathbf{v}' \cdot \mathbf{v}'\right) - \text{Div} \ \left(\mathbf{v}' \circ \mathbf{v}'\right).$$

Thus the time average will be:

$$\overline{\mathbf{v}' \times \mathbf{\Omega}'} = \nabla \frac{\overline{\mathbf{v}'^2}}{2} - \text{Div} \ \left(\overline{\mathbf{v}' \circ \mathbf{v}'}\right) = \nabla \frac{\overline{\mathbf{v}'^2}}{2} + \frac{1}{\rho}\text{Div} \ \mathbf{F}_R.$$

Since *Reynolds'* stress tensor is $\mathbf{F}_R = -p_R \mathbf{I} + \Theta \mathbf{G}^*$ and $\nabla \times \left(\overline{\mathbf{v}' \times \mathbf{\Omega}'}\right) = \nabla \times \text{Div}$ $\left(\Theta \mathbf{G}^*\right)$, the vortex theorem (1.9) with the stochastic model of turbulence has the form:

$$\frac{\partial \mathbf{\Omega}}{\partial t} + \left(\mathbf{v} \cdot \nabla\right)\mathbf{\Omega} - \left(\mathbf{\Omega} \cdot \nabla\right)\mathbf{v} = \nu\Delta\mathbf{\Omega} + \frac{1}{\rho}\nabla \times \text{Div} \ \left(\Theta\mathbf{G}^*\right). \tag{4.7}$$

This equation consists of three scalar equations, which together with the continuity equation (4.2) compose a closed differential equation system. Namely, there are four unknown functions $[v_1\left(q_1, q_2, q_3, t\right), v_2\left(q_1, q_2, q_3, t\right), v_3\left(q_1, q_2, q_3, t\right)$ and $\Theta\left(q_1, q_2, q_3, t\right)]$ and because the components of vortex vector $\mathbf{\Omega}$ can be expressed by the velocity components, the last quantity is not considered as an unknown function.

The sum of this study is as follows. On the basis of the stochastic model of turbulence for the *Reynolds'* stress tensor (and its deviator) a tensor equation can be established in which in addition to the three velocity components there is only one unknown scalar function, namely, the dominant turbulent stress component. With the help of this tensor equation a closed differential equation system can be set up for numerical determination of the turbulent boundary flow of viscid fluid.

REFERENCES

1. KÁRMÁN, TH. V.: *Mechanische Ähnlichkeit und Turbulenz* Proc. 3rd Congress of Applied Mechanics 1930, 86-93.

2. KOTSCHIN, N.J. KIEBEL, L.A. ROSE, N.W: *Theoretische Hydromechanik,* Akademie Verlag Berlin 1954 I, 138-142.

3. LAUFER, J: *The Structure of Turbulence in Fully Developed Pipe Flow,* NACA Report 1147, 1954.

LARGE EDDY SIMULATION OF DISPERSION OF PARTICLES IN TURBULENT JETS

ZHILEI WU AND LASZLO FUCHS
Division of Fluid Mechanics, Lund Institute of Technology
S-221 00 Lund, Sweden
Laszlo.Fuchs@vok.lth.se

Abstract. The objective of this study is to closely investigate the interaction between turbulence and particles in a free jet. The round jet is loaded with heavy but small particles. The continuous phase is simulated using LES while particles are tracked using a Lagrangian (LPT) approach. The particle volume fraction is supposed to be small enough to exclude direct particle-particle interactions. We have also considered the case of one-way interaction in which the particles have no effect on the continuous phase turbulence. The effect of the large vortex ring structures on particle dispersion has been studied. Particles with Stokes numbers in the range 0.03 to 10 have been considered. The computed results have been compared to our simultaneous double PIV measurements. The computed and the experimental results show very good agreement for the spatially developing jet both in terms of mean quantities as well as in terms of the correlation between the fluctuating velocities of the two phases. For forced jets the phase averaged particle concentration field shows that particles of different sizes tend to form particle-size dependent regions with high particle concentrations.

Keywords: Multi-phase flows, turbulent dispersion, LES, jet flows

1. Introduction

Particle dispersion by turbulent shear flows is superficially a simple problem, yet it is very common, and, therefore, an interesting test-bed for experimental and numerical tools. In many industrial processes the instantaneous particle concentration contains more important information than the mean concentration. One such example is the mixing process of fuel particles/droplets injected into a combustion device. Due to non-linear effects, the average of the interactions does not equal the averages of the interactions. This difference has to be accounted for in the form of a model. Otherwise, a more straightforward approach could be handling the non-linearities by computing the time-dependent problem (using Large Eddy Simulations, LES) and from such data compute the averaged values that are of interest.

The relative importance of the presence of the particles in the flow can be estimated by considering the different time-scales of the problem. For small particles one may assume that their shape is spherical and the "slip-velocity" is small. With these assumptions the particle Reynolds number is so small that the flow is (almost) Stoksian from the particle point of view. Under such assumptions, the aerodynamic response time of a particle is given by $\tau_A = \rho_p d_p^2 / 18\mu$, where ρ_p is the particle density, d_p is the particle diameter and μ is the fluid viscosity. This quantity represents

the time-scale required for a particle to adjust its velocity to the (continuous phase) flow velocity. The characteristic time-scale of a flow is given by $\tau_F = \delta/U$, where δ is the characteristic length-scale and U is the characteristic velocity of the flow. For jets the flow time-scale (of the large scales) can be estimated by $\tau_F = D/U_0$, with D being the inlet diameter and U_0 the inlet center-line velocity of the jet. The extent of dispersion of particles in such a flow situation is then determined by the Stokes number, which is defined as the ratio of the two time-scales: $\gamma_\tau = \tau_A/\tau_F$. This non-dimensional number characterizes the ability of the particle to follow the fluid elements. For particles with Stokes numbers much greater than unity, i.e.. $\gamma_\tau >> 1$, the particles will not respond to the large scale structures of the flow while particles with Stokes numbers much less than unity, i.e. $\gamma_\tau << 1$, will adjust to flow field very rapidly and will follow the flow field. Particles with Stokes numbers around unity will only partially respond to the local flow conditions. Such particles also affect largely the flow itself.

Particle dispersion in turbulent flows has been studied experimentally by several researchers. Longmire and Eaton [1] studied the interaction of solid particles with a turbulent flow by examining particle dispersion in jets. In their work, the jet was forced acoustically to form large vortex-ring structures. They confirmed that local particle dispersion and concentration are governed by convection due to large-scale structures. Some particles become clustered in the saddle regions downstream of the vortex-rings while others are ejected away from the main stream of the flow. The phase-averaged (during the forcing cycles) results revealed the mechanisms for the formation of particle clusters and the dispersion of particles. The large-scale structures and convection mechanisms have been shown to persist for particle-to-air mass loading ratios up to 0.65. Longmire and Eaton [1] did not examine the effect of different Stokes numbers on the results. Kiger and Lasheras [2] have also done experiments to investigate particles dispersion by vortex parings. In their experiment, the shear layer was forced with a fundamental frequency and sub-harmonic perturbations. Their results show that the vortex-ring structures play a role in homogenizing the particle concentration field. However, the amount of homogenization is strongly dependent on the particle relaxation time, the eddy turn over time as well as the time that the particles interact with each scale prior to a paring event (i.e. "residence time"). Small particles will be dispersed homogeneously, but larger ones are dispersed in an inhomogeneous fashion. The above mentioned papers give a global understanding of how the particles interact with large vortex-ring structures. These papers lack, however, information about the effects of the initial conditions on the particles and on their dispersion. This aspect is addressed here.

Several numerical simulations have been done to investigate particle behavior in turbulent flow fields. Squires and Eaton [3] have investigated the preferential concentration of particles by turbulence. They use Direct Numerical Simulation (DNS) to simulate an isotropic turbulence and investigated the effect of turbulence on the concentration field of heavy particles. Their results show that heavy particles gather in low vorticity and high strain rate regions. This accumulation effect is most pronounced for particles with a Stokes number of around 0.15. Recent development has shown that particles are greatly dispersed by large-scale structures rather than

three-dimensional turbulence. Chung and Troutt [4] have simulated particle dispersion in an axi-symmetric air jet. They use the discrete vortex method to simulate the vortex-rings of the jet. In their simulations, particles with different particle Stokes numbers are released at the jet inlet with the speed of the fluid. The results show that particles with Stokes numbers around unity might be dispersed beyond the corresponding dispersion of a passive scalar. Numerical simulations have been carried out by different researchers using both DNS and LES applied to the continuous phase in different geometries. Uijttewaal and Oliemans [5] have simulated particle dispersion in a vertical pipe flow based on DNS solver for the continuous phase. They point out that the interaction between particles and turbulence, neglecting wall effects, can result in particle segregation. Marcu and Meiburg [6] simulated particle dispersion by the braid vortices in a plane mixing-layer. An analytical expression for the critical particle diameter below which accumulation is possible has been derived. Tang et al. [7] have investigated particle dispersion in a plane wake as well as the effect of particle dispersion patterns at different particle Stokes numbers. Tang et al. [7] have also pointed out that particles at Stokes numbers around unity will be mostly dispersed.

This paper is aimed at studying effects of particle initial conditions for the dispersion in unforced and forced jets. Further, we consider the effect of Stokes number on the dispersion. By using LES also the non-linear drag effects can be assessed.

2. Mathematical models

2.1. The flow field of the continuous phase. In our simulations, the turbulence of the continuous phase is modeled by Large Eddy Simulation (LES). In LES, the large turbulence scales are resolved directly, while the effect of scales smaller than the finest grid size are modeled. The dominant force acting on heavy particles is primarily the drag. Since the drag varies non-linearly with the "slip-velocity", it is reasonable to assume that these non-linear effects are neglected if the flow field is computed in the framework of the Reynolds Averaged Navier Stokes (RANS) equations. One may compensate for the non-linear drag effects by adding an additional model term to the mean equations. Currently, there exist no such models in the literature. Therefore, it is natural to work within the LES framework. By this approach one avoids the need for temporal averaging. On the other hand, one has to make a series of assumptions. First, we assume that the particles are spherical and that the mean distance between the particles is much larger than the particle diameters. We also assume that the mean distance among particles is larger than the small resolved scales and hence the dispersed phase cannot be considered as a continuum. The relatively large distance among the particles implies that one may neglect interaction among particles. Thus, with the assumptions made here we take into account only one- and two-way interactions. Thus, the individual particles are tracked independently of each other, assuming that the particles displace a negligible amount of fluid. As stated above, the main force that acts on the heavy spherical particles is the aerodynamic drag. A disturbing effect arises with the combination of LES with the Lagrangian approach for Stokes numbers of $O(1)$ (or larger). This is so since LES requires adequate spatial resolution. That resolution should be such that eddies of the size of the Taylor

micro-scale are resolved, i.e., the spatial resolution if then of $O(Re_T^{-1/2})$. For heavy particles ($\rho_p/\rho_f = O(10^3)$) and if the Stokes number is $O(1)$ or larger, then the particle diameter is not much smaller than the grid size in our calculations. In spite of this potential inconsistency we do assume in the following that the spherical particles do not displace fluid.

In LES, the space filtering of a function $f(x_i, t)$ is defined as:

$$\overline{f(x_i, t)} = \int_{-\infty}^{\infty} G(x_i - x_i^{'}) f(x_i^{'}, t) \mathrm{d}x_i^{'} \tag{2.1}$$

where G is a filter function.

Filtering the Navier-Stokes equations leads to the equations for the resolved variables $\bar{u}_i$ and $\bar{p}$. The filtered incompressible equations are as follows:

$$\frac{\partial \bar{u}_i}{\partial x_i} = 0 \tag{2.2}$$

$$\frac{\partial \bar{u}_i}{\partial t} + \bar{u}_j \frac{\partial \bar{u}_i}{\partial x_j} = -\frac{1}{\rho} \frac{\partial \bar{p}}{\partial x_i} + \nu \frac{\partial}{\partial x_j} \frac{\partial \bar{u}_i}{\partial x_j} - \frac{\partial \tau_{ij}}{\partial x_j} + \bar{F}_i \tag{2.3}$$

$$\tau_{ij} = \overline{u_i u_j} - \bar{u}_i \bar{u}_j \tag{2.4}$$

where $\bar{F}_i$ is a source term and τ_{ij} is the Sub-Grid-Scale (SGS) stress tensor which reflects the effect of unresolved scales on the resolved ones. The role of the SGS term includes dissipation of turbulent kinetic energy. Such dissipation is needed to prevent a build-up of turbulent kinetic energy on the small scales. Since the (mean) rate of transfer of energy from the large to the small scales is independent of viscosity in the inertial sub-range (Kolmogorovs theory), any form of viscosity will be adequate. The dissipative effects should, however, maintain the inertial sub-range intact (i.e. not too much dissipation). Hence, any dissipative numerical scheme which provides adequate *amount* of dissipation can play the role of the SGS, independent of its functional form. Of course, explicit SGS models can account for another role of the SGS term, namely backscatter. The energy cascade is uni-directional only in the average sense. Instantaneously, there may be localized energy transfer from the smaller eddies to the larger (resolved) one. Different SGS models can give rise to backscatter. Gullbrand and Fuchs [8] have studied the effects of several SGS models, including the "Divergence Dynamic Model", the "Scale Similarity Model" and the "Exact Differential Model". The effect of different SGS on mean quantities is important only for low resolution situations. The gain by a SGS model is equivalent to a computation on a refined grid (by a factor two in each direction) without any explicit SGS term. Therefore, in this paper, no explicit SGS model is applied.

2.2. Particle motion equation. Particles are tracked by a Lagrangian method assuming that the particles have the properties as stated above. The momentum equation for the particles satisfies:

$$m \frac{d\mathbf{u}}{dt} = \mathbf{F} \tag{2.5}$$

Where $\mathbf{F}$ is the force on the particle and m is its mass. The forces acting on a single particle are detailed in the expression by Maxey and Riley [9]. They identified

different components of the force: drag, added-mass, buoyancy and history term. For heavy particles in gas the primary component of this force is the drag. This has the form:

$$\mathbf{F} = \frac{1}{8}\pi d^2 \rho C_D \left| V_R \right| V_R \qquad (2.6)$$

where the drag coefficient is given by:

$$C_D = 24(1 + 0.15Re^{0.687})/Re \qquad (2.7)$$

The particle Reynolds number is defined:

$$Re = \rho V_R d/\mu \qquad (2.8)$$

where, d is the particle diameter, ρ and μ are the density and viscosity of the continuous phase, V_R is the relative velocity of the particle relative to the surrounding fluid.

3. Numerical methods

The spatial discretization of the governing equations for the continuous flow field is performed on a uniform Cartesian staggered grid. Locally refined grids can be introduced where required for adequate resolution. The convective terms are discretized using hybrid scheme and higher (third- and fifth-) order can be achieved by deferred correction. A proof of this process is given in Gullbrand et al. [10]. The lower order scheme is used only during the relaxation procedure which maintains the global high order. The time derivatives are discretized using a three level second order implicit scheme. The discretized conservation equations are solved iteratively using a multi-grid method. The particles are tracked by integrating the equation of motion for the particles, based upon the instantaneous velocity field, using a second order Runge-Kutta scheme.

4. Problem description

We simulate a particle-laden turbulent jet. Large Eddy Simulation is used to simulate the continuous phase, while the individual particles are tracked. In the case of the forced jet it is excited with a frequency of 364 Hz. The round jet has an inlet diameter of 2 cm. The fluid (air) has a mean inlet velocity of 14.4 m/s, corresponding to a Reynolds number of 19000. The particles are released at inlet at each time step during the simulations. The rigid spherical particles have a density of 2400 kg/m^3. To assess the effects of different particle sizes we consider three classes of particle-Stokes numbers (γ_τ): $0.03, 1$ and 10, respectively. We also want to study the effects of particle velocity on the particle dispersion. Therefore, we consider three different inlet particle velocities (relative to the fluid). For each of these particle velocities, we consider the three particle groups. The computed cases are summarized in the following table:

Case 1	Case 2	Case 3
forced jet	forced jet	forced jet
$U_p = U_f$	$U_p = 0.75U_f$	$_p = 0.5U_f$
$\gamma_\tau = 0.03, 1, 10$	$\gamma_\tau = 0.03, 1, 10$	$\gamma_\tau = 0.03, 1, 10$

Here, U_p, U_f and γ_τ are the averaged particle inlet centerline velocity, averaged fluid inlet centerline velocity and particle Stokes number, respectively. The forced jet inlet velocity profile (of the fluid phase) as a function of time is as follows:

$$u_f(t) = 14.4 * (1 + 0.15 * \sin(2\pi \; 364 \; t)) \tag{4.1}$$

At each time step, a group of particles is released at the jet inlet. The particles are randomly distributed at the inlet, which results in a statistically uniform distribution. Particles are specified with different inlet velocities to examine the influence of initial slip velocity on particle dispersion. No radial velocity is imposed on the particles, which may be quite different from the real experimental set-up. This ideal situation may be advantageous in understanding the interaction between the particles and the flow structures. Since we are interested in the particle dispersion by the continuous phase, we use a dilute system, which means that no particle-particle interaction will be taken into account. Due the low volume fraction, the particles are supposed to have no effect on the continuous phase. Thus, the results for the forced jet have been computed using mostly a one-way coupling. Two-way coupling has been used in some of the cases, such as those displayed in Figures 1-3.

5. Results and discussion

5.1. Model validation. First, we consider the flow of a turbulent jet at a Reynolds number of 5100. For this low Re we do not use any Sub-Grid-Scale term, since the fine grid computations are close to DNS. This case has also been studied by us
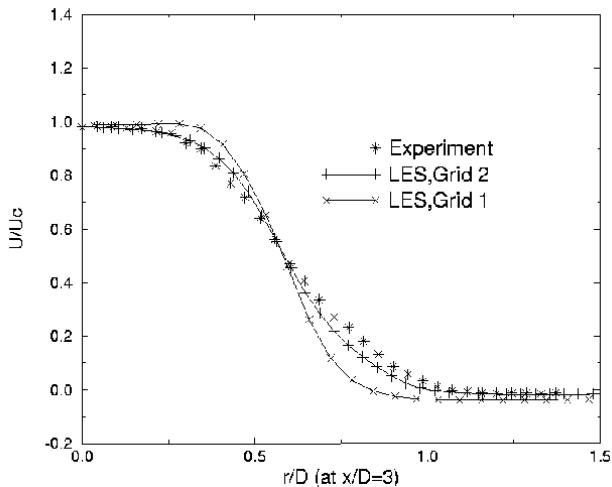

Figure 1. Fluid mean axial velocity at $x/D = 3$

experimentally by using an enhanced PIV system. The system allows one to measure simultaneously the velocity fields of both phases. This is done by using fluorescing tracer particles, while the Ni particles (sized around 165 μm) are measured directly. Figures 1 and 2 depict the mean velocity profiles of the two phases, respectively, at a distance of three jet diameters downstream of the nozzle. The figures compare the experimental results with those obtained by LES/LPT on two different grids (about 0.5 and 1.5 Million grid points, respectively). As seen, these quantities are captured quite well even on the coarser grid.
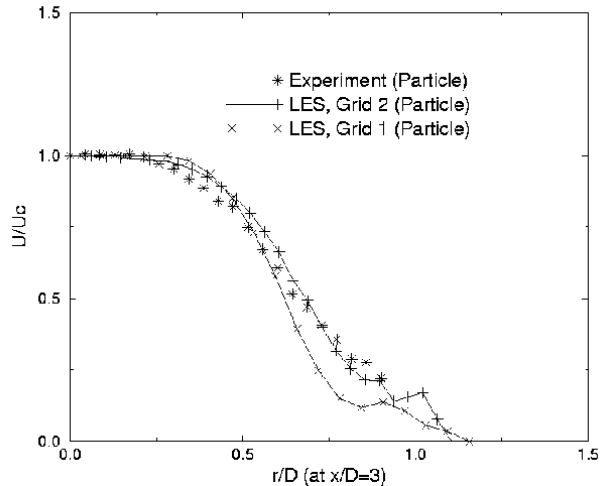
Figure 2. Mean axial velocity at $x/D = 3$ – particle phase
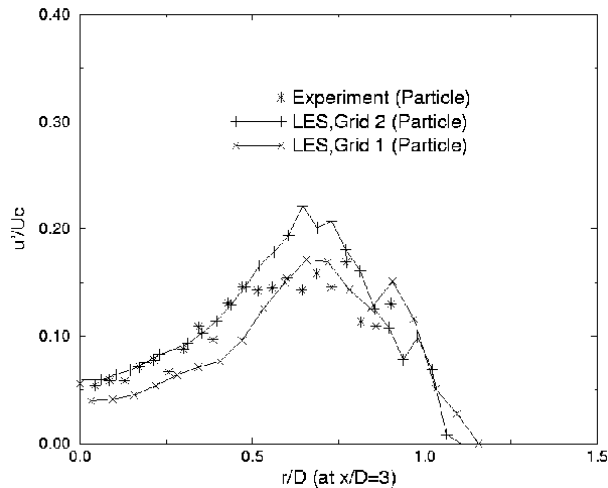
Figure 3. Mean axial velocity fluctuations, $x/D = 3$ – particle phase

The quality of the numerical results can be assessed better if one considers the fluctuating components. Figure 3. depicts the radial distribution of the axial velocity

fluctuations of the dispersed phase at a distance of three diameters form the nozzle exit. The non-smoothness of the results depends on the too low number of samples in the numerical and in particular in the experimental results.

For further validation, a case with the similar situation to that in [1] has been chosen. Simulation results are compared with those experiments.
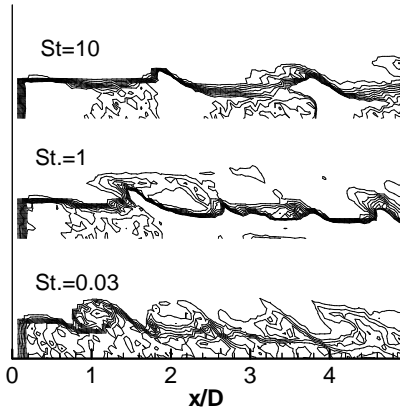

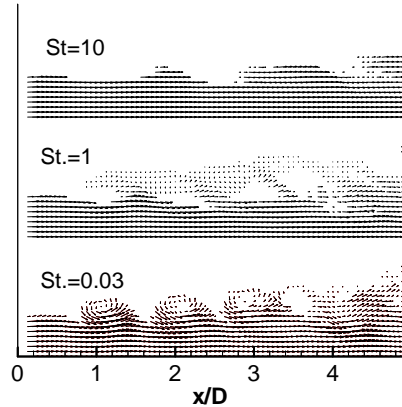Figure 4. Phase average particle density map (Case 1)

Figure 5. Phase averaged particle velocity field (Case 1)

First, we examine phase averaged particle and fluid properties qualitatively in the forced cases. The averages are obtained from a bin of phase angles of 1° centered at phase angle $\Phi = 0°$. For other phase angles, the pictures may be quite different, but to understand particle vortex-ring interaction, the results from any phase angle may be helpful and quite representative. Since large vortex-ring structures are only dominant in the proximal region of the jet, we present the result from jet inlet up to around 5 inlet diameters distance downstream.

Figures 4 and 5 correspond to Case 1. The figures show only a half plane due to the axi-symmetry of the phase averaged data. In this case, particles are released at each time step with the same velocity as that of the local fluid. Figure 4 is the phase averaged particle concentration field and Figure 5 is the corresponding phase averaged particle velocity vector field. Particles with Stokes number of 0.03 adjust to the fluid very quickly and follow the fluid motion quite well. Thus, the phase averaged concentration field clearly outlines the large vortex-ring structures. But even particles with such small Stokes numbers can not follow the fluid motion exactly. As these particles move downstream, they are thrown outwards slightly by the vortex-ring structures, which results in a "source" region in the vector field at about 3.6 inlet diameters downstream (Figure 5). When particle Stokes number is about unity, the particle responds to the fluid flow so that at the vortex-rings the particles follow a curved path. However, due to the particles' own inertia, they cannot follow the vortex-ring exactly and are thrown away from the center region of the vortex by the centrifugal force. Particles which are originally located at the outer region of the large vortex-ring structures may be just ejected away form the main stream, while

other particles may be dragged back to the main stream again. In the vortex core region, there are no particles left. Since some particles are ejected away from the main stream, they will show up in a region outside of the jet resulting in a wider particle dispersion than the corresponding single phase jet. This can be seen both from the concentration field and from the velocity vector field. Particles with a Stokes number of 10 are only displaced slightly compared to those with Stokes numbers of 0.03 and 1. The phase averaged concentration map of these particles is distorted a little and the distortion of the particle concentration field does not follow the fluid vortex paring events. From the above we note that when the particles at the inlet have the same velocity as the fluid, the particles with Stokes number of 1 exhibit the strongest dispersion pattern. Particles with
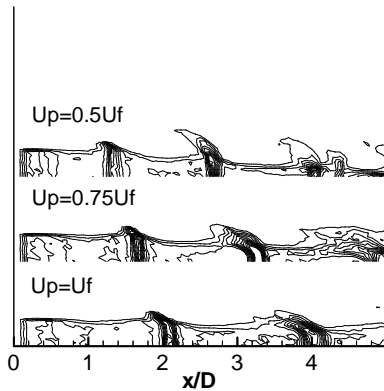
Figure 6. Phase averaged particle density map for different particle inlet velocities ($\gamma_\tau = 10$)
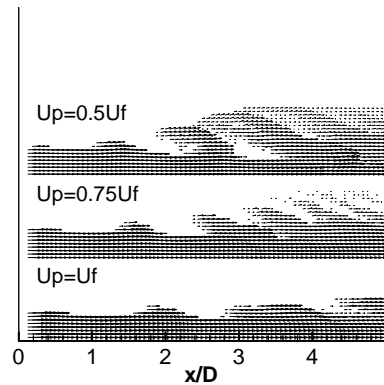

Figure 7. Phase averaged particle velocity field ($\gamma_\tau = 10$)
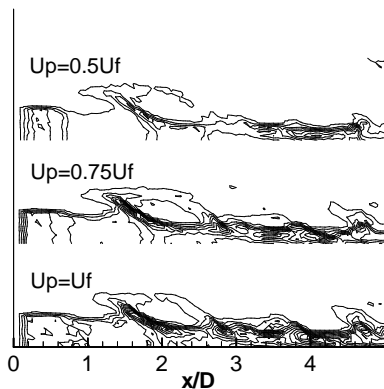

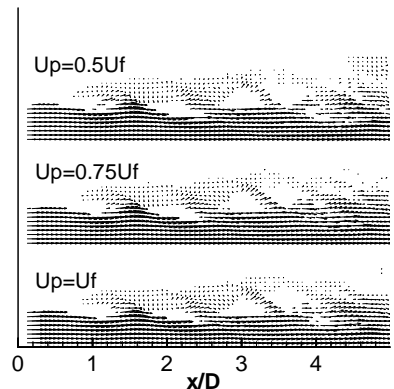Figure 8. Phase averaged particle density map ($\gamma_\tau = 1$)

Figure 9. Phase averaged particle velocity field ($\gamma_\tau = 1$)

Stokes number of 10 will respond only slightly to the fluid and be hardly dispersed. Particles with Stokes number of 0.03 will follow the fluid motion quite well and will

not be dispersed much beyond that of the single phase turbulent jet.

Next, we consider the effects of particle slip velocity at the inlet. Particles of the same size are released at the inlet with different inlet velocity i.e., particles take 100%, 75%, and 50% of the local fluid velocity. Figures 6, 7 and 8, 9 correspond to particles of Stokes numbers of 10 and 1, respectively. For particles with Stokes number of 10, it is quite clear that different initial velocity changes the particle dispersion pattern and the particle velocity field dramatically. When particles initially take the same velocity as the fluid, they are only slightly dispersed by the vortex-ring structures. In this case the particles are clustered in "pockets" traveling downstream. The interval among the clusters is quite large compared to that of the vortex-rings. As the particle initial velocities are reduced, particles are dispersed further and further and the interval between particle clusters becomes smaller and smaller. As the particles initial velocity is decreased, the "tail" of the particle clusters become more and more clear. This behavior can be explained rather easily. When the particles have small velocities they have longer time to interact with the vortex-ring structures, leading to a stronger dispersion than those particles which have a smaller slip velocity. For particles with Stokes number of 1, different initial velocities do not have that much effect on the particle dispersion pattern and hence the extent of particle dispersion. Even though particles are released at the inlet with different velocities, they exhibit clusters at the same axial positions, with the same spacing (around $1\ D$) among the clusters. This is clearly seen in Figures 8 and 9. For particles with Stokes number of 0.03, different initial velocities have even smaller effect on the particle dispersion pattern. This behavior is rather obvious since the smaller the Stokes number is, the quicker the particle will adjust to the surrounding flow conditions. From these results we can draw the conclusion that as far as these jet cases are concerned, when the particle Stokes number is larger than unity, the particle nozzle slip-velocity, $(U_f - U_p)$, plays an important role in the particle dispersion. In this case, the larger the nozzle slip-velocity is, the greater the particle dispersion is.

In order to determine how fast particles are moving in the flow field and also to determine how the mean of particle concentrations differs under different situations, time averaged particle velocity and particle concentration fields are presented in quantitative terms.

5.2. Statistical results. Mean properties. Consider Cases 1 and 3 where the forced jet is loaded with particles of different Stokes numbers. Figures 10 to 13 depict the particle axial velocity and the particle radial velocity at different axial positions. For particles with Stokes numbers of 0.03 and 1, the particle axial velocity decreases rather quickly at $r = 0.25D$, while for particles with Stokes number of 10, particle axial velocity begins to decrease only after $r = 0.5D$. The higher momentum of the larger particles is maintained until $r = 0.65D$. This is due to the larger inertia of those particles. It is interesting to note that the radial velocity at this axial station (Figure 11) is pointing towards the center for $r = 0.5D$. This is so in particular for $\gamma_\tau = 1$. However, as these particles get closer to the jet axis they gain axial velocity (from the fluid) and therefore tend to disperse with it. Altogether, these two counteracting mechanisms lead to an off-axial peak of particle number density (c.f. Figure 15) for the larger particles. The largest effect is noted for particles with

$\gamma_\tau = 1$. The smallest particles follow the fluid and disperse with it and therefore no such effects are observed. These effects have also been observed by Longmire and Eaton [1] experimentally. Their explanation was, however, that the particles gained negative radial velocity as they passed through the jet nozzle. However, in our current simulation, no radial velocities are specified for the particles at jet inlet. Combined with the phase averaged results shown in Figures 4 to 9, we may attribute this negative velocity to the particle-vortex interaction. When the vortex-rings developed and move downstream, they drag the particles with themselves. The motion of the individual particles depends upon the position of the particle relative to the core of the vortex.
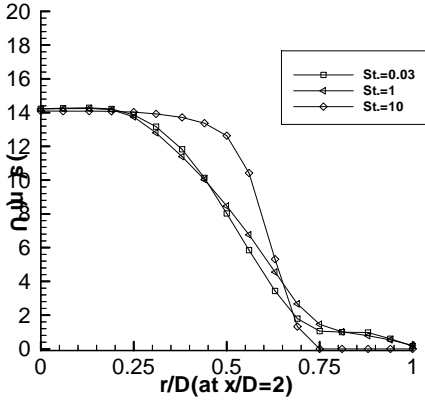

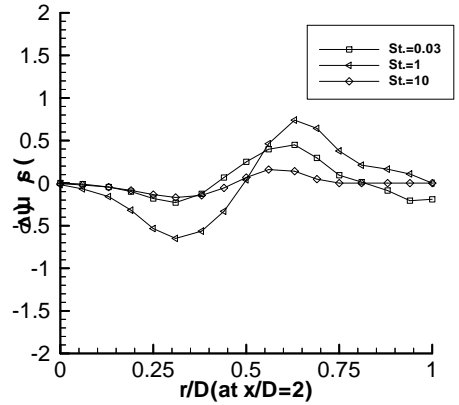Figure 10. Averaged particle axial velocity at $x/D = 2$

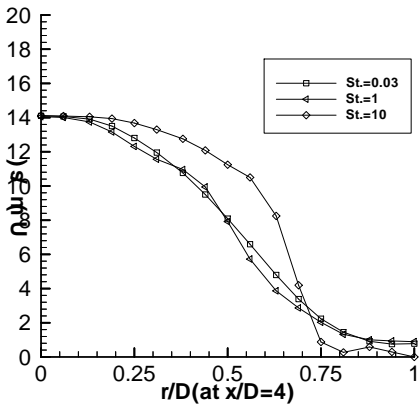Figure 11. Averaged particle axial velocity at $x/D = 4$

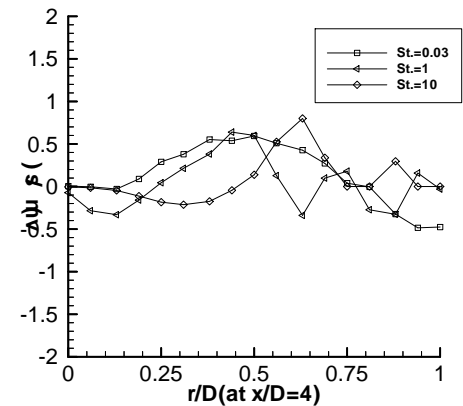Figure 12. Averaged particle radial velocity at $x/D = 2$

Figure 13. Averaged particle radial velocity at $x/D = 4$

Particles with Stokes number 1 gain the largest negative radial velocity in the main stream region and the largest positive velocity outside the main stream, this is most

clearly seen at $x = 2D$ (Figure 11). This is reasonable since particles with the medium Stokes number have moderate inertia to maintain their speed, while they are also light enough to be responsive to the local flow structure. It is interesting to note that the mean particle radial-velocity highly depends on the Stokes number. In Figures 11 and 13 we note that the radial velocity component changes sign. This implies that on average an even particle distribution at the inlet will lead to non-homogenous distribution later downstream. This is reflected also in the particle number densities. The fact that particles with Stokes number around unity disperse mostly is seen also in the radial velocity component. These particles may have positive and negative radial velocity directions. The smaller particles follow the fluid better and therefore have also a more monotonous particle number density distribution. The larger particles ($\gamma_\tau = 10$) are heavier and hence inertia dominates. Due to inertia, the particle motion of the individual particles will be rather complex. This observation supports the idea that non-linear effects (also in terms of the drag force) make simpler, linear type models for describing the interaction between the phases highly non-general.
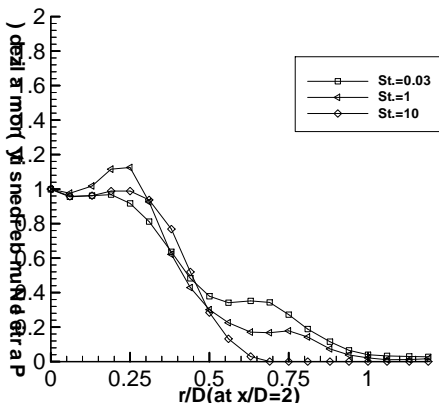

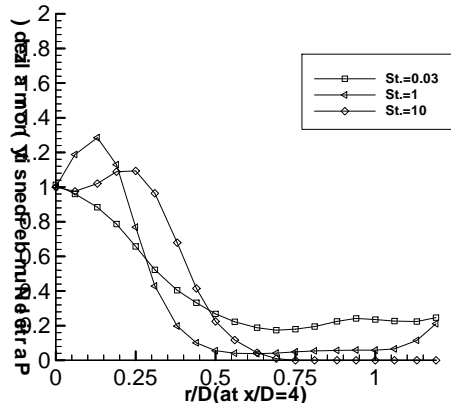Figure 14. Averaged particle number density at $x/D = 2$

Figure 15. Averaged particle number density at $x/D = 2$

To further understand the dispersion process, time averaged particle number density profiles are presented in Figures 14 and 15. The averaged particle number density is normalized by the particle number density at the centerline, for the given axial location. At both $x = 2D$ and $x = 4D$, a peak value which is greater than 1 is observed between centerline and jet edge ($r = 0.5D$) for particles with Stokes numbers greater than 1.

5.3. Statistical results. Second moments. The turbulent stresses of the fluid and particle phases together with fluid-particle correlations play an important role in understanding the interaction between the phases. We denote by $<>$ the (ensemble) averaging operator that is related to the particle phase.

Figures 16 and 17 depict the correlation between the fluid- and particle-fluctuations as well as the corresponding fluid Reynolds stresses at two different axial positions. For particles with Stokes number of 10 the absolute values of the fluid-particle cor-

relations are almost always smaller than the corresponding fluid turbulent Reynolds stresses, while for particles with Stokes number of 1, the absolute value of fluid-particle correlations may be higher than the corresponding fluid Reynolds stresses (Figure 17).
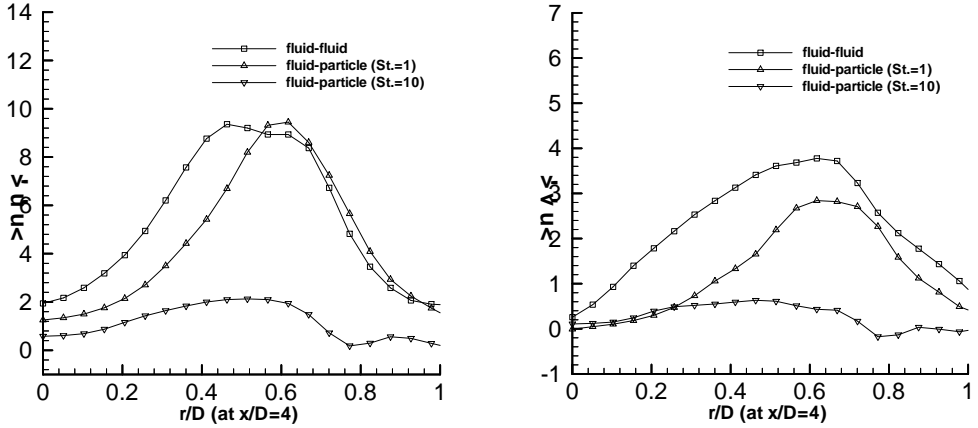

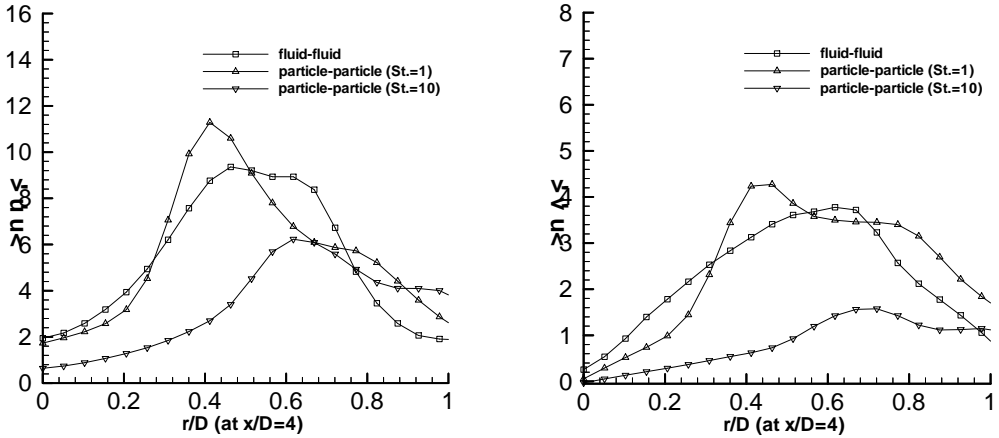Figure 16. Fluid-particle, axial-axial (left) and axial-radial (right), correlations

Figure 17. Particle phase Reynolds-stresses at $x/D = 4$

Figure 17 depicts the particle phase Reynolds-stresses at axial position of x/D=4. For both particles with Stokes numbers of 1 and 10, particle Reynolds-stresses may exceed the corresponding fluid turbulent Reynolds stress at certain radial positions. This means that particle turbulent properties are not only determined by their response to the fluid turbulent properties. We note that in this case the particles are not released at the fluid velocity at the jet nozzle. The inertia effect of the particles and

the particle initial conditions also play an important role in the turbulence properties of the particles. It is worth mentioning that Simonin [11] also found that the absolute value of particle Reynolds-stresses may be higher than the corresponding fluid turbulent Reynolds-stresses. Simonin [11] considered particle dispersion in turbulent shear flows. He attributed this to the existence of mean velocity gradients.

6. Concluding remarks

Unforced and forced jets loaded with heavy particles have been studied by Large Eddy Simulations. The combination with a Lagrangian Particle Tracking approach allows one to take into account the non-linear interactions between the phases. The numerical calculations have been compared with experimental data. Thus, the accuracy of the simulations in terms of mean and second moments has been established. The role of particle initial velocity for the dispersion process has been considered. For particles with Stokes numbers less than one, the initial velocity does not have much effect on the particle dispersion process. For particles with Stokes number of 10, different initial velocities may have a great effect on the dispersion process. We note that the larger the lag between the fluid velocity and particle velocity, the further downstream the dispersion may be observed. Quantitative analysis shows that particles are not only ejected away from the centerline of the jet, but also convected toward the jet axis. Due to this effect the particle number density distribution in the jet varies non-monotonously especially for particles with Stokes number around unity.

REFERENCES

1. LONGMIRE, E. K. and EATON, J. K.: *Structure of a particle-laden round jet*, J. Fluid Mech., **236**, (1992), 217-257.

2. KIGER, K.T. and LASHEARAS, J.C.: *The effect of vortex paring on particle dispersion and kinetic energy transfer in a two-phase turbulent shear layer*, J. Fluid Mech., **302**, (1995), 149–178.

3. SQUIRES, K.D. and EATON, J.K.: *Preferential concentration of particles by turbulence*, Phys. Fluids, **3**(5), (1991), 928-937.

4. CHUNG, J.N. and TROUTT, T.R.: *Simulation of particle dispersion in an axisymmetric jet*, J. Fluid Mech., **186**, (1988),199-222.

5. UIJTTEWAAL, W.S.J. and OLIEMANS, R.V.A.: *Handling complex boundaries on a Cartesian grid using surface singularities,* To appear in J. Num. Meth. in Fluids, 2000.

6. MARCU, B. and MEIBURG, E.: *The effect of streamwise braid vortices on the particle dispersion in a plane mixing layer. I. Equilibrium points and their stability*, Physics of Fluids, **8**, (1996), 715-753.

7. TANG, L., WEN, F., YANG, Y., CROWE, C. T., CHUNG, J. N. and TROUTT, T. R.: *Self-organizing particle dispersion mechanism in a plane wake*, Phys. Fluids A, 4,

(1992), 2244-2250.

 8. GULLBRAND, J. and FUCHS, L.: *A comparative study of sub-grid scale models for a co-annular swirling jet.* Submitted for publication, 2001.

 9. MAXEY, M. R. and RILEY, J. J.: *Equation of motion for a small rigid sphere in a nonuniform flow*, Phys. Fluids, **26**, (1983), 883-889.

10. GULLBRAND, J., BAI, X.S. and FUCHS, L.: *High order Cartesian grid method for calculation of turbulent flows.* To appear in Int. J. Num. Meth. in Fluids. 2000.

11. SIMONIN, O.: *Eulerian Formulation for Particle Dispersion in Turbulent Two-phase Flows, in 5th Workshop on Two-phase Flow Predictions*, Eds. M. Sommerfeld and D. Wennerberg, Forschungszentrum Julich GmbH, ISBN 3-89336-066-2, (1990), 156-166.

METHOD OF INCREASING STEAM TURBINE CONTROL STAGE EFFICIENCY

Krzysztof J. Jesionek
Turbomachinery Department, Institute of Heat Engineering and Fluid Mechanics,
Faculty of Mechanical and Power Engineering
Wrocław University of Technology, Poland
`jesionek@pwr.wroc.pl`

Abstract. In many cases when the turbine load diverges from the nominal value, the benefit which should result from nozzle governing may be all lost due to a sharp decrease in control stage efficiency. The magnitude of this decrease depends on the aerodynamic characteristics of the cascade profiles, on the conditions of inlet velocity fields forming in the nozzle chests and on the efficiency of the means which cause a decrease in the negative influence of partiality. Different blade profiles and their loss coefficients are presented.

Keywords: Aeroderivative turboengine, coal boiler, combined cycle, cogeneration.

1. Introduction

When analysing the development of large steam turbines we can notice that a long time passes before proposals of new solutions are applied in the industry. For example, methods of raising efficiency proposed $20-30$ years ago are only now being applied. This paper discusses the potential of a design which if adopted would bring about a considerable increase in the relative internal efficiency of steam turbines. According to our experience in the modernisation of steam turbines, it is possible to raise turbine effectiveness to theoretical limits under real conditions and at a relatively low investment input.

In recent years, practically all large factories producing steam turbines have been searching intensively for ways of increasing the efficiency of large steam turbines. It is worth looking not only at new solutions but also at the so far unrealised methods of reducing energy losses in blade systems. An overview of known solutions, for example, for blade cascades of a small relative height can be found in [2], [10] and [11].

Many authors, e.g. [4] and [9], give an assessment of efficiency increase possibilities for steam turbines, covering all elements along the entire steam flow path. The asymptotic character of the energy loss reduction process should be taken into account: it is impossible to reduce the losses in cases when they are very low. In other words, attempts at improving efficiency should be made in cases of turbine elements in which

energy losses are relatively high.

2. Nozzle governing

Partial steam admission is used in the first stage of turbines with nozzle-group steam flow control, where steam enters the turbine through one or several nozzle groups, Figure 1, depending on the turbine load. Such a stage is termed a control stage. In order to increase the available energy and obtain the proper steam conditions in the
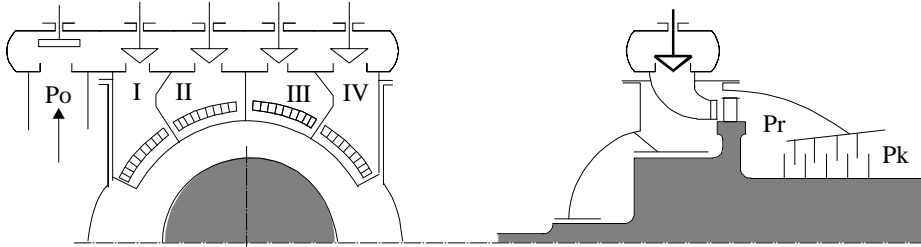

Figure 1. Scheme of nozzle governing

space after the control stage, the latter is usually of the impulse type, even when the other stages are of the reaction type. The control stage usually has an increased diameter and it is sometimes made (for older turbines of relatively moderate output) as velocity stages.

3. Control stage

The control stage is a necessary part of a steam turbine with nozzle governing. The operating conditions of this stage differ significantly from those of the other stages: when the turbine load diverges from the nominal value, two steam jets with different initial pressures appear in the control stage, [7] and [8].

The process for the control stage and its control valves is shown in Figure 2. Two steam flows can be seen there. The first steam flow through the fully open valves enters the segments of the control-stage nozzle row without additional losses. In the second flow, steam is throttled in the partially open valve to a certain intermediate pressure. Both steam flows expand in the control stage to steam pressure p_r.

This means that one part of the stage, where the non-throttled steam jet flows, works at an increased drop of enthalpy while the other part operates at a decreased drop of enthalpy (in comparison with the computational enthalpy drop). Thus in one stage two different operating regimes are realized - with a decreased value and an increased value of basic stage parameter

$$u/c_0 \, ,$$

where u is the blade (circumferential) velocity on the pitch diameter of the bucket wheel and c_0 is the velocity that corresponds to the disposable drop of enthalpy:

$$c_0 = (2H_{01})^{0.5}$$

The total blade efficiency η_{0B} drops significantly when the turbine load decreases.

Internal efficiency η_{0i} drops even more because when the consecutive control valves are being closed, the partiality of the stage decreases very sharply. Our experiments showed that when the partiality of the stage decreases from $\varepsilon = 0.82$ to $\varepsilon = 0.2$ (one control valve open), the relative stage efficiency η_{0i} decreases by 60%. Since the
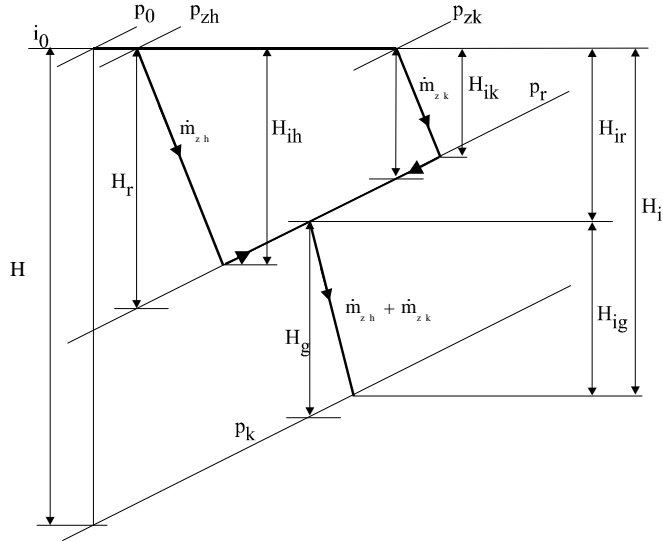

Figure 2. Steam expansion process on h-s axes for steam admission part of turbine with nozzle-group governing

efficiency decreases as a result of a change in the value of u/c_0 during the closing of the consecutive control valves, the stage begins operating in the regime of steam throttling. In other words, the benefit which should stem from nozzle governing may be all lost due to the sharp decrease in the control stage efficiency. The magnitude of this decrease depends on the aerodynamic characteristics of the cascade profiles, on the conditions of inlet velocity fields forming in the nozzle chests and on the efficiency of the means which contribute to a decrease in the negative influence of partiality.

4. Control stage under variable steam flow

A basic operating characteristic of the control stage blade apparatus is a wide range of velocities: from low subsonic velocities up to high supersonic ones, Figure 3. Therefore profiles cascades of the control stage should be multiregime and they

should ensure high reliability as regards sharp changes in static and dynamic loads. The first requirement connected with the low reaction of the control stage applies to the turbine nozzle cascade, the second one applies to the bucket cascade where a complex of forces occurs.
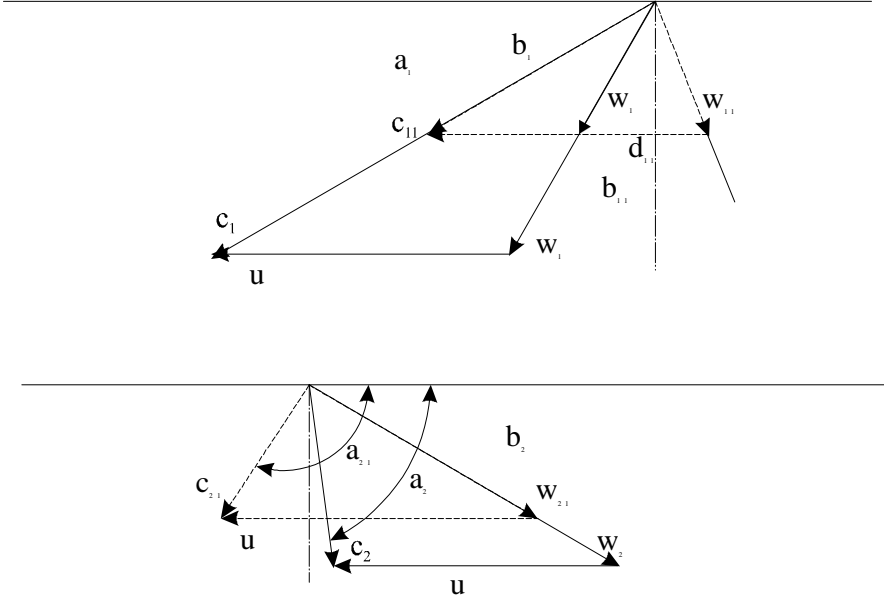

Figure 3. Velocity diagrams for control turbine stage: dashed lines - throttled steam stream, solid lines - non-throttled steam stream

The aerodynamic problems which arise in the cascades are illustrated by a relationship between profile loss coefficient ζ_{pr} and nondimensional velocity at outlet M_{1t} for a converging (line 1 in Figure 4) and diverging (line 2) turbine nozzle cascade. Accelerating cascades ensure a low level of losses $M_{1t} < 0.8 - 0.9$. The use of divergent cascades is justifiable for $M_{1t} > 1.3 - 1.4$.

When the turbine load decreases, the most characteristic velocity range for non-throttling stream seems to be in a range of $0.8 < M_{1t} < 1.4$ (then a massive increase in energy loss occurs in cascades of both types). That is why new profile cascade designs are needed for the control stage to ensure low losses for both subsonic and supersonic flows and a smooth transition from the former to the latter.

5. Multiregime blade profile

The above condition is fulfilled by profiles with inverse surface curvature of the nozzle blade-suction side at the nozzle exit zone (designed in the 1960s). One of such profiles is shown in Figure 5 and its characteristic is shown in Figure 4 (line 3). It is easy
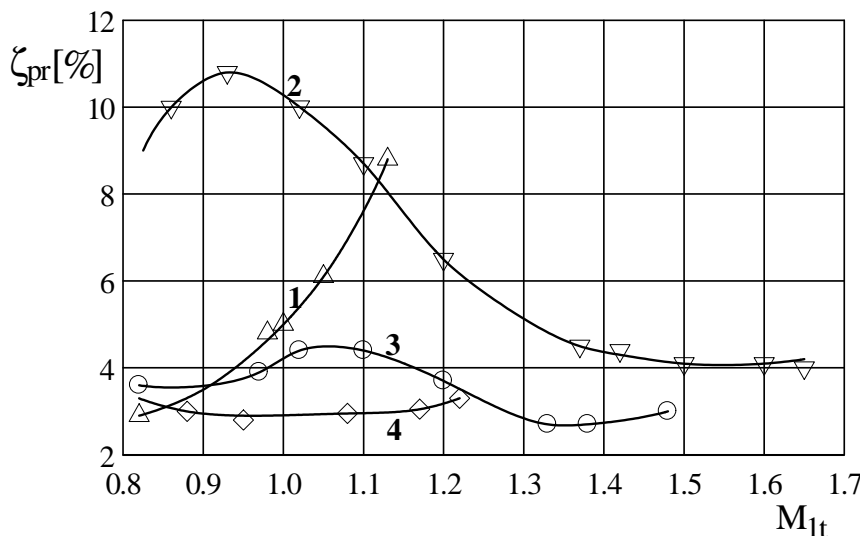
Figure 4. Dependence of profile loss coefficient ζ on Mach number M_{1t} in different airfoil nozzle cascades: 1 - converging blade cascade, 2 - diverging cascade, 3 - cascade with inverse surface curvature of nozzle blade suction-side at nozzle exit zone, 4 - nozzle cascade with longitudinal grooves on convex blade surface
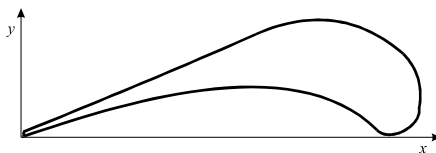
Figure 5. Multiregime blade profile

to see that a nozzle cascade made from such profiles has sufficiently low profile losses in the subsonic, transonic and supersonic ranges. The transition through the nozzle exit zone from the convex to concave surface allows us to avoid stream re-divergence in this section and at the same time to decrease the longitudinal positive pressure gradient in the range of subsonic velocities and to suppress the shock waves in the supersonic range.

6. Multiregime Cascades with Longitudinal Grooves

Cascades built from profiles with longitudinal grooves (rectangular in cross-section) in the nozzle exit zones are even more effective, [3], [5], [6], [12], [14] and [15]. In this design an increase in losses in the transonic area is avoided and sufficiently low level of profile losses can be maintained for the whole tested range of velocities (line 4 in

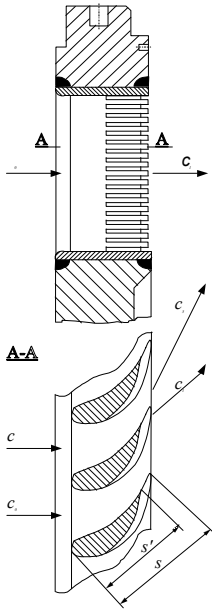Figure 4). Similar changes can be made in the shape of bucket cascades designed for the control stage.

Taking into account the above characteristics of the new cascade designs, it would be advantageous to use moving blade profiles with thin leading edges and decreased surface curvature in the nozzle exit zone. Such cascades were designed in the 60s (type $R - \beta_1\beta_2 B$ [1]) and their characteristics are compatible with modern requirements.

The presented relationships $\zeta_{pr} = f(M_{1t})$ for the control-stage blade system should be substantially corrected because the control stage receives the jet from the control valves after which the velocity field is characterised by high non-uniformity and a vortex flow occurs for several turbine loads.

The control stage always operates in conditions of a complex inlet velocity field, [16]. As our experiments showed, the losses in the nozzle cascade installed after the standard control valve when the latter is fully open increase by $1.5 - 2.0\%$ (in comparison with a uniform velocity field) and by $3.0 - 3.5\%$ when the valve is half open. If new valve designs

Figure 6. Turbine cascade are used, the nozzle cascade losses caused by inlet with longitudinal grooves non-uniformity will not exceed $0.8 - 1.2\%$, [13].

7. Summary

This analysis of the operation of control stages shows that because of several negative factors, they operate with relatively low efficiency and may (when the turbine load decreases considerably) operate in the steam throttling regime.

If multiregime profiles are used for control-stage cascades, it is possible to increase the efficiency of the control stage.

REFERENCES

1. DEJČ, M.E., FILIPPOV, G.A. and LAZAREV, I.JA.: *Profile Catalogue for Axial Turbines*, Mašinostroenie, Moskva 1965. (in Russian)

2. DEJČ, M.E., ZARJANKIN, A.E., FILIPPOV, G.A. and ZACEPIN, M.F.: *Methods for increasing the efficiency of turbine stages with short blades,* Teploenergetika, No 2, (1960), 18-24. (in Russian)

3. JESIONEK, K.J.: *Analysis of an incompressible diffuser flow and the arising losses*, Wrocław University of Technology, Scientific Papers of the Institute of Heat Engineering and Fluid Mechanics No 43, Series: Monographs No 21, Wrocław 1992. (in Polish)

4. JESIONEK, K.J.: *Efficiency improvement possibilities of steam turbine flow passages*, Scientific Papers of the Warsaw University of Technology, Series: Conferences No. 6,

Vol. I, Warsaw, 1995, 219-228. (in Polish)

5. JESIONEK, K.J.: *Prediction of flow separation and possibilities for its reduction in fluid-flow machinery*, Wroclaw University of Technology, Scientific Papers of the Institute of Heat Engineering and Fluid Mechanics, No 51, Series: Monographs No. 28, Wroclaw, 1998. (in Polish)

6. JESIONEK, K.J. and ZARJANKIN, A.E.: *Properties of fluid motion in diffusing passages and a method of raising the load of such channels*, Pumpentagung - Pump Congress, Preprints T.II, B6-06, 1-12, Karlsruhe, 1992.

7. LEYZEROVICH, A.: *Large Power Steam Turbines,* PenWell Books, Penwell Publishing Company, Tulsa, Oklahoma 1997.

8. MILLER, A. and LEWANDOWSKI J.: *Off-Design Performance of Steam Turbines*, Publishing House of the Warsaw University of Technology, Warsaw, 1992.

9. TROJANOVSKI, B.M.: *Methods for improving the efficiency of steam turbines*, Teploenergetika, No 5, (1993) 39-46, and No 7, (1993), 34-40.

10. TANUMA, T., NAGANO, S., SAKAMOTO, T. and KAWASAKI, S.: *Aerodynamic development of advanced steam turbine blades - PWR*, Proc. Joint Power Generation Conference, ASME, 1995, 57-63.

11. ZARJANKIN, A.E. and GARDZILEWICZ A.: *Loss reduction possibilities for turbine stages with short blades*, Turbomachinery Fluid Dynamics and Thermodynamics, 2nd European Conference, Proceedings, Antwerpen, March 1997, 225-231.

12. ZARJANKIN, A.E., GRIBIN, V.G. and PARAMONOV, A.N.: *Application of grooved surfaces in blade cascades*, Teploenergetika, No 1, (1989), 27-30. (in Russian)

13. ZARJANKIN, A.E. and JESIONEK, K.J.: *Steam flow modelling in the control valves of the steam turbines*, Scientific Papers of the Silesian University of Technology No 1266, Series: Mechanics No. 121, Gliwice, 1995, 345-353. (in Polish)

14. ZARJANKIN, A.E. and JESIONEK, K.J.: *Phenomenon of flow separation from a smooth surface and its occurrence prevention methods,* VDI Berichte. No 118, Turbomachinery - Fluid Dynamics and Thermodynamics Aspects, Experimental Fluid Dynamics/Spe-cial Problems of Turbomachinery, VDI Verlag, Düsseldorf 1995, 37-46.

15. ZARJANKIN, A.E., PARAMONOV, A.N., CZUSOV, S.I. and JESIONEK, K.J.: *A method to decrease energy losses in the nozzle block of a large meridian divergence of the flow part*, VDI Berichte. No 1280, Lines of Development of Energy and Power Station Technology - Entwicklungslinien der Energie- und Kraftwerkstechnik, VDI Verlag, Düsseldorf 1996, 157-180.

16. ZARJANKIN, A.E., ŽYLINSKIJ, V.P. and GARDZILEWICZ, A.: *The effect of the inlet stream nonuniformity on the turbine stage efficiency*, Vestnik MEI (MPEI Bulletin), No. 3, 1994, 23-27. (in Russian)

IMPROVED UNDERSTANDING OF TWO PHASE FLOW PHENOMENA BASED ON UNSTEADY BLADE PRESSURE MEASUREMENTS

Günter Kosyna, Priyatna Suryawijaya, Jens Friedrichs
Pfleiderer Institut für Stömungsmaschinen, TU Braunschweig
Langer Kamp 6, 38106 Braunschweig, Germany
`g.kosyna@tu-bs.de`

Abstract. Impeller blade and side wall pressure measurements deliver additional information of the energy transfer in a centrifugal pump under two phase flow conditions. This information is used to improve the phenomenological understanding as well as to calibrate numerical two phase flow CFD codes. This paper gives an introduction into the measuring technique based on subminiature pressure transmitters with telemetric data transmission and gives a choice of results, obtained by using this method.

Keywords: Two phase flow, unsteady pressure measurement, cavitation, blade pressure distribution.

1. Introduction

Two phase flow phenomena in centrifugal pumps are an important research subject even today. The present paper is concerned with two phase flows of two different types:

– with phase transition: cavitation,
– without phase transition, i.e. water plus undissolved air.

The reason to combine both fairly different types in one paper is the fact that basically the same test technique and the same test pump has been used for the investigation of two phase flow with and without condensation.

Throughout this paper the following notations and notational conventions are applied:

Nomenclature		Subscripts	
d	diameter	bld	blade
f	frequency	d	pressure side
H	pump head	opt	best efficiency point
M^*_{bld}	local blade pressure momentum $(p_{bld} - p_s) \cdot \Delta A \cdot r$	s	suction side
n	rotational speed	v	vapor
n_s	specific speed	0	in front of inlet
NPSH	net positive suction head	1	impeller inlet
p	pressure	2	impeller outlet

Nomenclature

Q	flow rate
r	radius
t	time
z	number of blades
β	blade angle
η	efficiency

Cavitation causes noise, deterioration of efficiency and what is most important, damage by erosion to the impeller and other components of the pump. CFD codes normally do not have problems to predict the inception of cavitation, but it is much more difficult to predict the $NPSH$ for a head drop of 3%, which is the most common cavitation criterion for pumps in industrial applications. At a head drop of 3%, cavities are extended, unsteady cloud cavitation may occur. Pump engineers know very well that the change in pump head is not a reliable indicator for the actual type of cavitation and for the pump wear.
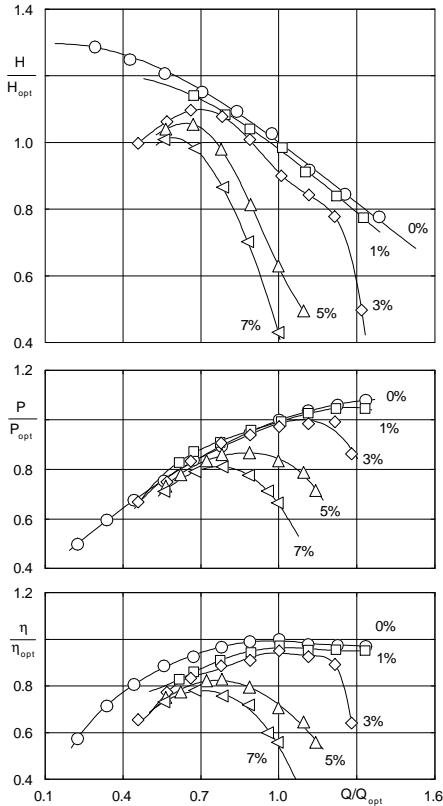

Cavities for example may produce an extra lift, that means an increase of the pump head as long as the cavities are attached [1], other phenomena like fluctuations or rotating cavitation may cause an extra head drop.

For a better understanding it is necessary to get a correlation between the type of cavitation on the one hand and on the change of pump head and on erosive attack on the other hand.

Though the flow with extended and unsteady cavities is very complex, the development of numerical codes showed large progress in the last few years - but of course there is a strong demand for detailed experimental results for validation.

In a wide range of pump applications, i.e. in the chemical industry or in the offshore oil production the liquid to be pumped contains certain contents of undissolved gas. It is well known that the performance of standard centrifugal pumps decreases rapidly in liquid/gas two phase flow - the deterioration starts from a gas void fraction of 2-3% - the total breakdown of pumping can be expected at gas contents of 8-15% (Figure 1).

For two phase flow applications of centrifugal pumps the influence of the gas void fraction on the pump performance must be predictable - best of all with a suitable nu-

Figure 1. Influence of the gas content on the performance of the centrifugal pump

merical code. The main problem is a proper modelling of the complicated impeller flow structures at higher void fractions with typical separation and demixing area. All attempts to develop a numerical two phase code must be backed up by detailed experiments.

2. Two phase flow test pumps

This situation is the background for several present experimental and numerical research projects on two phase flow at German Universities with and without phase transition.

The experimental methods used in the projects are:
– optical observations (CCD, High Speed Photography, laser optical methods)
– measurements of the erosive attack
– pressure measurements in the rotating impeller

In these projects three test pumps of same geometry but different scale are operated in Braunschweig (see Figure 2.), Darmstadt and Magdeburg - main components of the Magdeburg pump have been built in Miskolc.
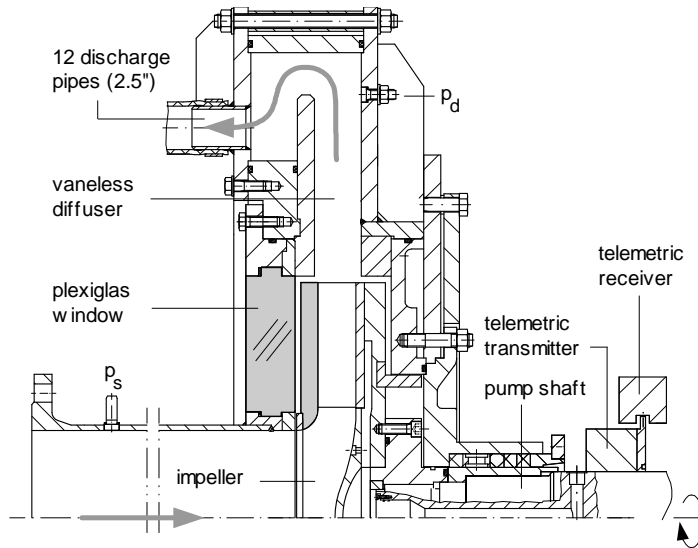
Figure 2. Two phase flow test pump

The background for the choice of this particular pump design was to have a simple geometry for easy grid generation, for precise machining and good access for optical methods. The first impeller has a one circular arc design of the bladings, the second impeller blading consists of two circular arcs (see Figure 3) in order to obtain a more steady deceleration of the impeller relative flow. Approximately the impeller flow

Figure 3. Design parameters of test impellers
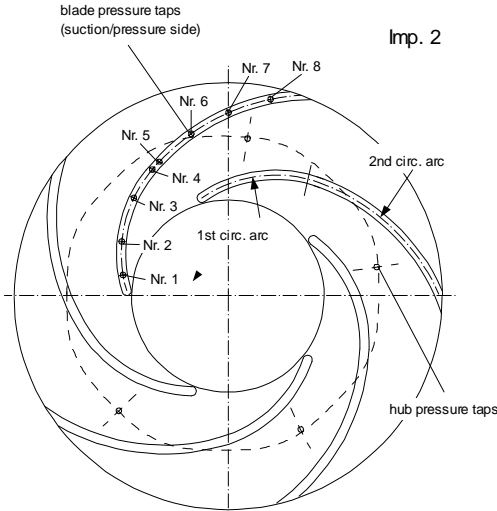
Impeller		No. 1 (17205)	No. 2 (19235)
Blade shape		1-cir.-arc	2-cir.-arc
Inlet Diameter	d_1	260 mm	260 mm
Outlet Diameter	d_2	648 mm	556 mm
Blade inlet angle	β_1	17 $^{\circ}$	19 $^{\circ}$
Blade outlet angle	β_2	20 $^{\circ}$	23 $^{\circ}$
Passage width	b	46 mm	46 mm
Number of blades	z	5	5
Specific speed	n_s	27	27.5
Rotational speed	n	6-12 Hz	6-12 Hz

may be regarded as a 2D-flow. The test pump either can be connected to a closed variable pressure circuit for cavitation tests or to an open circuit with components to mix and separate air for the liquid-gas-two phase flow tests.

3. Blade pressure measurements in the rotating impeller

The special task of the Pfleiderer-Institute of the Technical University of Braun-schweig in the above mentioned projects is the measurement of the impeller blading
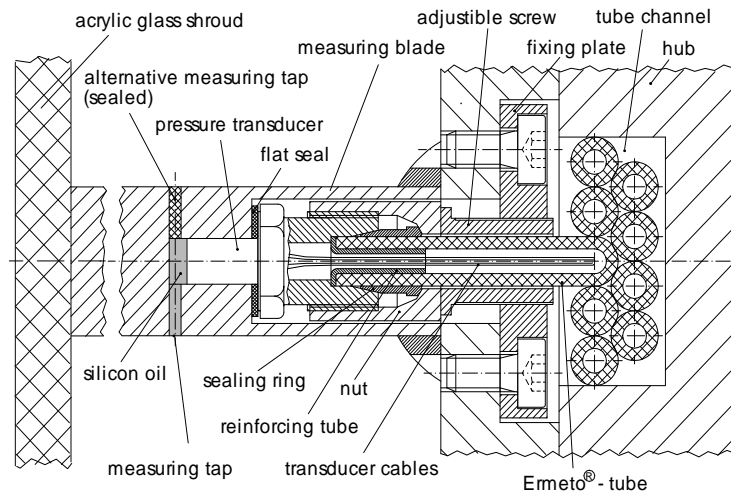
Figure 4. Installation of subminiature pressure transducer

and side wall pressure, using subminiature pressure transducers rotating with the impeller. The objectives are:

a. Cavitation. Investigate the type of cavitation, identify unsteady states of cavitation like fluctuations or rotating cavitation and find correlations between change of pump head and type of cavitation.

b. Liquid-gas flow. Improve the understanding of performance drop, deliver calibration data for the development of numerical codes.

Figure 5. Telemetric pressure data transmission
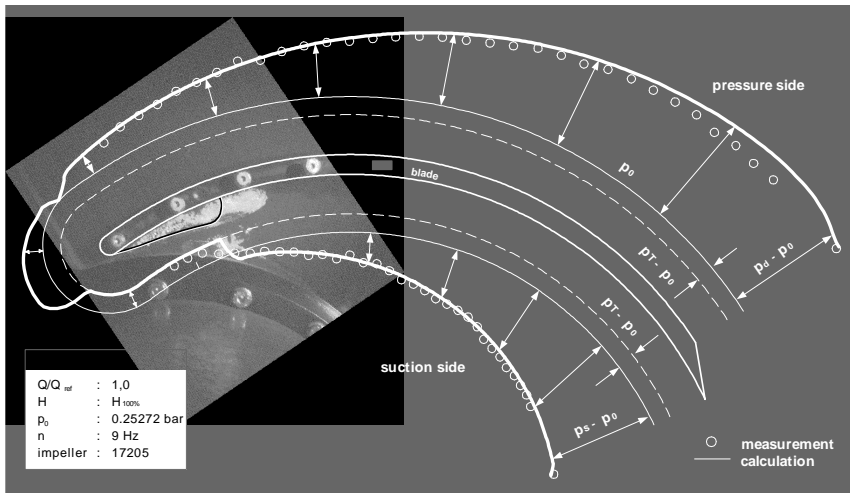
Figure 6. Impeller blade pressure and extension of the cavity

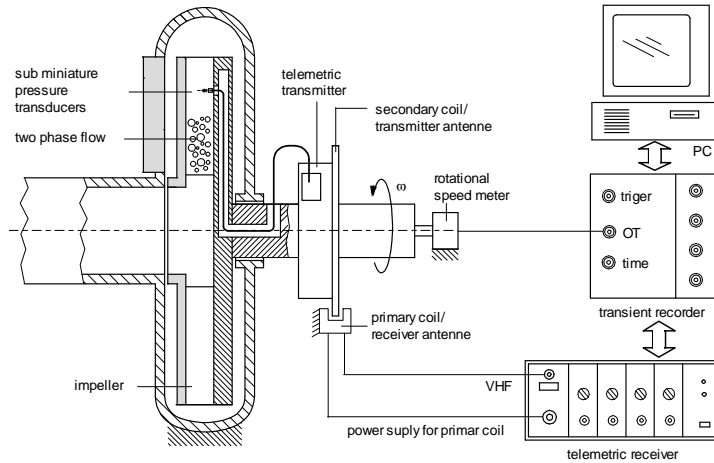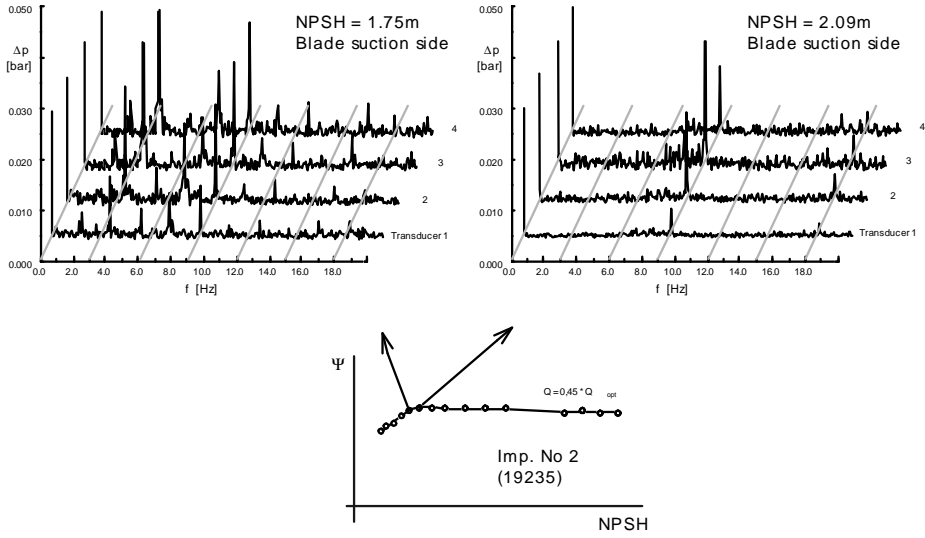Figure 7.   Frequency analysis of blade pressure signals under different cavitation modes
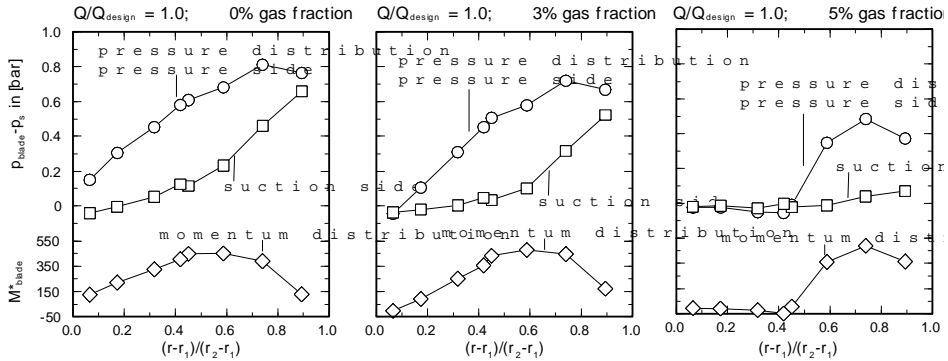
Figure 8. Influence of the gas fraction on blade pressure distribution

As the pressure measurement is scheduled for areas with high mechanical impact by cavitation, a robust design has to be developed in order to shelter the sensitive transducers – Figure 4.

The transducers are installed inside the blade contour, the membrane protected by silicon oil against direct attack of cavitation. This design needs a sufficient blade thickness - this is the reason why the pump used in Braunschweig has double scale compared with the Darmstadt and Magdeburg pumps.

Eight pressure transducers are installed inside an impeller blade, four transducers in the impeller hub, the locations of the transducers are shown in Figure 3.

Figure 9. Pressure fluctuations at transducer Nr. 8 at different gas void fractions

The signals of 8 transducers can be transmitted simultaneously by using a telemetric system (Figure 5.), type dt 204/301/612 from Datatel Telemetrie Elektronik. This system allows to transmit frequencies up to 2,5 kHz, which is sufficient, as it is intended only to detect macroscopic flow phenomena but not high frequency cavitational noise.

4. Results

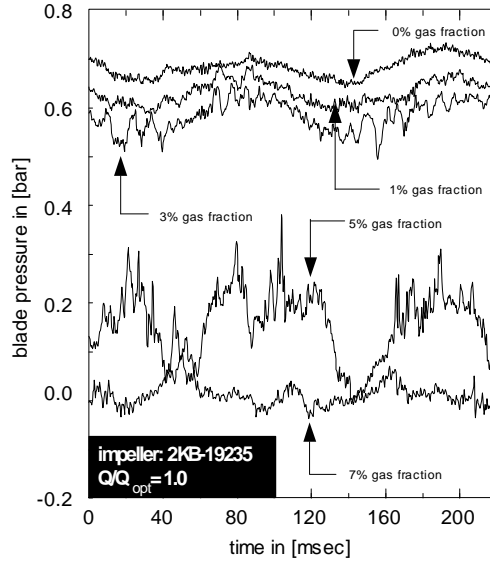*a. Cavitation.* In the following a choice of results is presented to demonstrate the potential of unsteady pressure measurement inside the rotating impeller. The first investigation using this technique was completed by Dreiß in 1997 [1] [2]. Two subsequent projects are under way now by the authors of this paper.

Figure 6 shows the result of time averaged impeller blade measurements under cavitation assembled with a stroboscopic CCD-snapshot of the cavity. The test results are compared with a numerical calculation by V. Schütte [3].

Figure 7 shows a result from the subsequent project on cavitation. It shows the FFT of the pressure signals transducer, in impeller 2 under 45% part load.

The frequency analysis shows the impeller rotating frequency as dominating in the right diagram for NPSH=2.09m (s=1.05). At a slightly lower $NPSH$ (1.75m; s=0.94) value other strong peaks at different frequencies appear - the head drop curve starts its "creeping" descend. This result indicates that the pressure drop is related to the onset of periodic or rotating cavitation phenomena - this first finding of course needs further investigation for confirmation.

b. Liquid-gas flow. The drop of the pump head with increasing gas void fraction is a result of the change of the impeller blade pressure. Figure 8 shows the drop of the blade pressure rise with increasing gas void fraction, i.e. at 5% gas no pressure rise can be observed at the first 40% of the impeller blade length, which is a result of a demixing of the two phase flow. Consequently there is no blade momentum transferred in the first 40% of blade length either.

The character of impeller flow changes with increasing gas void fraction (Figure 9). The pressure fluctuations increase with rising gas percentage, having a maximum at five percent, then decreasing with further increased gas void fraction.

5. Conclusions

This paper gives a short introduction to the unsteady impeller pressure measurement technique and presents a choice of typical results obtained with this method. Impeller measurements improve the general understanding of two phase pump flow phenomena and deliver detailed experimental data for further development of numerical two phase codes. Investigations will soon be extended to other impeller geometries with higher specific speeds.

REFERENCES

1. DREISS, A.: *Untersuchung der Laufradkavitation einer radialen Kreiselpumpe durch instationäre Druckmessungen im rotierenden System*, Dissertation TU Braunschweig. 1997.

2. DREISS, A. and KOSYNA, G.: *Experimental investigations of the cavitation states in a radial pump impeller*, Proceedings of the JSME Centennial Grand Congress, International Conference on Fluid Engineering, Tokio, Japan, 1997, Vol. 1., 231-238.

3. SCHÜTTE, V.: *Bubble and leading edge cavities in centrifugal pumps*, 2nd European Fluid Mechanics Conference, Warsaw, Poland, 1994.

NUMERICAL COMPUTATION OF THE TRANSIENT CHANGE OF FLOW IN A PIPE FROM PARTIAL TO FULL DEPTH

László Kullmann

Department of Hydraulic Machines, Budapest University of Technology and Economics
Po. Box. 51., 1521 Budapest - Hungary
`kullmann@vizgep.bme.hu`

Abstract. Three difference schemes are compared in the computation of open channel flow in circular pipes. During operation parts of the pipe may work with full and other parts with partial depth. Time steps are restricted in characteristics method and explicit finite difference schemes but they describe the flow properly, while implicit finite volume methods work with much larger time steps having the shortage of unrealistic minor oscillations.

Keywords: Pressure/surface waves, open-channel flow

1. Introduction

In the last decade, water consumption has drastically been reduced. Pipes originally dimensioned for higher flow rates often operate as open channels with partial depth. However, during transient operation they may transfer water at full cross section. In the latter case the driving force is pressure difference and gravity, while at partial depth gravity alone. Simulation of transient pipe flow is mainly based on the method of characteristics. This method defines the time step to a given mesh size through the celerity of pressure or surface waves. In a completely filled pipe the pressure wave velocity is about a hundred times as high as that in a water stream with open surface in the same pipe. For a mesh fixed along the pipe the time step gets extremely small when the water stream completely fills the cross section of the pipe. Explicit difference schemes such as the Lax-Wendroff scheme have the same disadvantage. Implicit schemes are much faster but produce minor surface waves without any physical background. In this paper the above listed three schemes are compared.

Nomenclature

B	width of water surface
D	inner diameter of pipe
E_p	elasticity of pipe material
E_l	bulk modulus of liquid
F	wetted area
g	gravitational acceleration
J_R	specific frictional resistance given as friction slope

J_S	pipe bottom slope
t	average liquid velocity
u	elasticity of pipe material
x	longitudinal coordinate
y	water depth above local pipe floor
δ	pipe wall thickness
ρ	liquid density

2. Basic equations for open channel flow

The basic equations of liquid motion through a pipe of constant (circular) cross section are the continuity equation, momentum equation and a relation between the wetted area of the pipe and the water depth:
Continuity:

$$\frac{\partial F}{\partial t} + \frac{\partial (Fu)}{\partial x} = 0 \tag{2.1}$$

Momentum equation:

$$\frac{\partial (Fu)}{\partial t} + \frac{\partial}{\partial x}\left[F\left(u^2 + gy\right)\right] = gF\left(J_S - J_R\right) + gy\frac{\partial F}{\partial x} \tag{2.2}$$

Equation of the cross section:

$$\frac{\partial F}{\partial y} = B \tag{2.3}$$

Using this last equation, derivatives of F may be rewritten, e.g.

$$\frac{\partial F}{\partial t} = \frac{\partial F}{\partial y}\frac{\partial y}{\partial t} = B\frac{\partial y}{\partial t} \tag{2.4}$$

The area of the wetted cross section depends only on water depth. The pipe being prismatic, its cross section does not depend explicitly on the location of the section. The above equations are given in conservation form. This form has the advantage that - if being discretized for a longitudinal pipe section of the computational grid - the flow rates at the section borders are properly described.

3. Equations for flow in a completely filled pipe

If the pipe is completely filled, the pressure difference between different sections is added to the gravitational driving force. In this case the absolute pressure or gage pressure is normally used together with the average velocity as unknown quantities. In the present case, as we suppose that parts of the pipe operate with full section, other parts with partial depth, the piezometric head rather than the pressure is the appropriate unknown quantity. For a pipe with free liquid surface the water depth is equal to the piezometric head. For completely filled pipes the piezometric head is the height of an imaginary water column above pipe floor which could be observed if a vertical transparent tube would be attached to the pipe.

By this notation the first two equations will not change. However, if the pipe is completely filled B will have a different meaning.

For a positive gage pressure the wetted area of the pipe section does not change as a result of water level rise or fall. It changes because the liquid is compressed and the pipe wall is expanding under gage pressure in the pipe. As it is well known, applying Hook's law for pipe wall expansion and liquid compression and supposing constant stress over the total thickness of the thin pipe wall, we get (see e.g. [1], [2])

$$\frac{\partial F}{\partial y} = \rho g F \left(\frac{D}{\delta E_p} + \frac{1}{E_1} \right) = B_s \ . \tag{3.1}$$

In this formula F means the total pipe cross section, the other parameters are also constant, so the right hand side of the formula can be calculated and this value has been denoted by B_s. B_s is the width of an imaginary longitudinal slot being cut at the top of the tube allowing the pipe cross section to vary under pressure rise even if the pipe section is completely filled with liquid.

Substituting the continuity equation (2.1) into the momentum equation (2.2) the latter gets a simpler form. Cross differencing the two equations with respect to time and space, respectively, and subtracting results in a linear partial differential equation of second order for liquid velocity u or for liquid level y. These equations are hyperbolic.

The two sets of real characteristic lines $\xi = $ const and $\eta = $ const are easily obtained and the equations can be transformed containing the new independent variables ξ and η. The slope of the characteristic lines in the natural coordinates x and t is $\mathrm{d}x/\mathrm{d}t = u + a$ and $\mathrm{d}x/\mathrm{d}t = u - a$, respectively. Here a denotes the celerity of pressure or surface waves

$$a = \sqrt{\frac{gF}{B}} \ . \tag{3.2}$$

If the pipe is completely filled, the above defined B_s has to be substituted for B.

It is important to understand that information on flow rate or water-level changes cannot travel faster relative to the liquid than at this speed.

4. Method of characteristics

The method is described in several books, see e.g. Wylie and Streeter [2]. In the present paper the computational grid is fixed by an equidistant mesh for the pipe. In every time step the time needed to pass the fixed mesh size Δx according to the locally varying slope $\mathrm{d}x/\mathrm{d}t$ of the characteristics ξ and η has been calculated. The result is a locally varying pair of time increments. The new overall time level $t + \Delta t$ is defined by the minimum of these local time increments. The locations of the base points (on the old time level t) of the two characteristics ending at the same fixed grid point on the new time level $t + \Delta t$ have been calculated. The physical parameters (y, u, etc.) on the old time level in the base points have been interpolated. Finally the two transformed equations for the two characteristics have been integrated over the actual time step.

When the pipe is completely filled with liquid, the slope of the characteristics drops by two orders of magnitude: The simulation is thus extremely slowed down although a large portion of the pipe operates with open water surface. Here there are only minor changes both in water level and flow rate, while pressure waves run along the filled pipe section.

5. Lax-Wendroff method

The two step Lax-Wendroff scheme described e.g. by Hirsch [3] has been applied for the conservative form of the equations. Points $i-1$, i, $i+1$ are used for the old time level t. As a first step, values of F, y and u are computed at the mid time level $t + \Delta t/2$. The points L (left) and R (right) are put to the locations $x_i - \Delta x/2$ and $x_i + \Delta x/2$. $\Delta x = x_i - x_{i-1} = x_{i+1} - x_i$ is the equidistant mesh size. F_L and F_R are computed from continuity (2.1), e.g.:

$$F_L = \frac{F_{i-1}}{2} - \frac{\Delta t}{2} \frac{u_i F_i - u_{i-1} F_{i-1}}{\Delta x} \ . \tag{5.1}$$

Liquid surface levels y_L and y_R are computed from continuity (2.1) combined with the equation of cross section (2.3) considering the actual liquid surface width

$$y_L = \frac{y_{i-1} + y_i}{2} - \frac{\Delta t}{2} \frac{u_i F_i - u_{i-1} F_{i-1}}{\Delta x} \frac{2}{B_{i-1} + B_i} \ . \tag{5.2}$$

Average fluid velocities u_L and u_R are computed using the momentum equation (2.2) discretized as for other quantities. Values of F, y and u at the new time level are computed in a similar way as before but using values at mid time level

$$F_i\left(t + \Delta t\right) = F_i\left(t\right) - \Delta t \frac{u_R F_R - u_L F_L}{\Delta x} \tag{5.3}$$

and

$$y_i\left(t + \Delta t\right) = y_i\left(t\right) - \Delta t \frac{u_R F_R - u_L F_L}{\Delta x} \frac{4}{B_{i-1} + 2B_i + B_{i+1}} \ . \tag{5.4}$$

For computing $u_i(t + \Delta t)$ the momentum equation (2.2) is used again. However at the upstream end and downstream end of the pipe the above formulae can not be used as either point $i - 1$ or $i + 1$ is missing. Integration along the characteristics $\mathrm{d}x/\mathrm{d}t = u - a$ for the upstream end and $\mathrm{d}x/\mathrm{d}t = u + a$ for the downstream end is performed.

6. Implicit scheme

The conservation form of the basic equations has been used. They were integrated for a pipe segment (1D finite volume) of length Δx between mesh points i and $i + 1$. Time levels are t and $t + \Delta t$.

Integrating the continuity equation (2.1) for the pipe segment $x_i \leq x \leq x_{i+1}$ between time levels t and $t + \Delta t$ and using mean values between the ends of the pipe segment gives:

$$0 = \int_{x_i}^{x_{i+1}} \int_t^{t+\Delta t} \left[\frac{\partial F}{\partial t} + \frac{\partial (uF)}{\partial x} \right] \mathrm{dt dx} = \int_{x_i}^{x_{i+1}} \left(\int_t^{t+\Delta t} \frac{\partial F}{\partial t} \mathrm{dt} \right) \mathrm{dx}$$

$$+ \int_t^{t+\Delta t} \left(\int_{x_i}^{x_{i+1}} \frac{\partial (uF)}{\partial x} \mathrm{dx} \right) \mathrm{dt} = \int_{x_i}^{x_{i+1}} (F(t+\Delta t) - F(t)) \, \mathrm{dx} + \int_t^{t+\Delta t} ((uF)_{i+1} - (uF)_i) \, \mathrm{dt} \ .$$

$$(6.1)$$

In the first integral applying the equation of the pipe cross section (2.3) we get

$$F(t + \Delta t) - F(t) = B(y(t + \Delta t) - y(t)) = \overline{B \Delta y}$$

at some inner point of the pipe segment. The overbar denotes a space-averaged value. Substituting this into the first integral it may be written as

$$\Delta x \left(\frac{B_i \Delta y_i + B_{i+1} \Delta y_{i+1}}{2} \right) \ .$$

In the second integral a mean value for the time increment Δt has to be substituted:

$$\overline{u_i F_i} \cong \frac{u_i F_i + (u_i F_i + \Delta u_i F_i + u_i \Delta F_i)}{2} \ .$$

Here again Δu_i, ΔF_i are increments during the time step Δt. A similar formula can be written for the time-averaged value in mesh point $i + 1$. Finally we have

$$\frac{B_i}{2} (\Delta x - u_i \Delta t) \Delta y_i + \frac{B_{i+1}}{2} (\Delta x - u_{i+1} \Delta t) \Delta y_{i+1} - \frac{F_i \Delta t}{2} \Delta u_i + \frac{F_{i+1} \Delta t}{2} \Delta u_{i+1}$$

$$= (u_i F_i - u_{i+1} F_{i+1}) \Delta t \ .$$

This equation contains four increments, these are the water depth-changes and liquid velocity variations at both ends of the pipe segment. The discretization of the momentum equation (2.2) takes place in a similar manner coupling the same four increments. For n pipe segments $2(n + 1)$ unknowns must be computed. One has $2n$ equations of the above type and two additional equations at the boundaries. The above system of pairs of equations has a pentadiagonal matrix. Such matrices may easily be factorized into the product of a lower and an upper triangular matrix resulting in an efficient solution procedure.

7. Initial and boundary conditions

Initial condition: For all schemes discussed the initial state is the steady flow at normal depth (constant velocity and water depth along the pipe) or the steady flow in the

case of a mild pipe bottom slope (constant flow rate as the product of a decreasing velocity and increasing depth).

Boundary conditions: Simple boundary conditions have been used such as prescribed water surface levels both in the upstream and downstream reservoirs connected to the pipe. Transient operation occurs if one of the reservoir levels changes over some time interval.

Two cases have been considered:
1. Linear downstream surface level rise followed by the level being kept constant
2. Flood wave having the form of a half sine wave starting from the upstream reservoir.

In case 1 if the water reaches the upper tangent of the pipe circular cross section the width B drops suddenly causing an abrupt rise of the wave velocity a. The time step reduces, the computation is slowed down extremely but no other problem occurs either when using the method of characteristics, or if applying the Lax-Wendroff method. The implicit scheme shows no change in the running time at all. Further increasing the downstream reservoir water surface level the piezometric head will increase as if the water surface would rise in the imaginary slot of width B_s above the pipe. All three schemes operate well and arrive at a new steady state solution if the reservoir water level comes to rest.

In case 2 the flood wave travels along the pipe and in the meantime changes its form by the damping effect of friction and by wavefront dispersion because of wave velocity dependence on water depth. Both in the method of characteristics and in the Lax-Wendroff scheme, the first rise of the water surface takes place when the wavefront reaches this downstream point moving with the surface wave velocity.
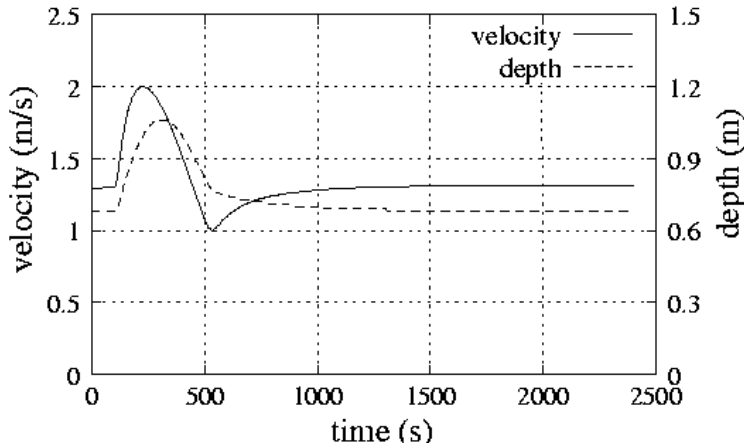

Figure 1. Results of a flood wave computation by the method of characteristics

Figure 1 shows results computed by the method of characteristics. The graph received by the Lax-Wendroff method would completely cover these curves.

In the implicit scheme all mesh points are coupled. Because of this coupling the
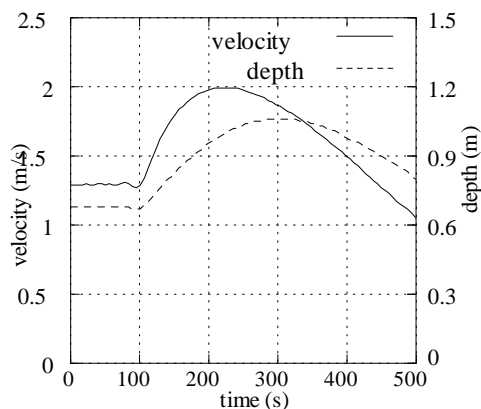
Figure 2. Results of the implicite scheme

water surface rise travels faster than the actual flood wavefront in the form of a small-amplitude high-frequency wave. Figure 2 shows the velocity and depth over the time at a fixed cross section of the pipe. The superposed small amplitude wave can be seen on the velocity graph. This superposed wave has no physical meaning. However, its amplitude is so small that the results are practically satisfactory and again the computation time resulting from the large time steps is shorter than when using the other two schemes.

8. Conclusions

All three investigated methods operate well if the water surface is lower than the top of the pipe. For full depth calculations the implicit scheme may be suggested because of the much shorter running time, especially if a complete set of pipes connected to each other through manholes or junction chambers has to be simulated.

REFERENCES

1. Zielke, W.: *Elektronische Berechnung von Gerinneströmungen*, Erich Schmidt Verlag, Berlin, 1974.
2. Wylie, E. B. and Streeter, V.L.: *Fluid Transients*, McGraw-Hill, New-York, 1979.
3. Hirsch, C.: *Numerical Computation of Internal and External Flows*, Volume 2, John Wiley & Sons, Chichester - New-York, 1995.

A MODEL FOR SIMULATION OF PARTICLE COLLECTION IN FILTER MATS

Tamás Lajos

Department of Fluid Mechanics, Budapest University of Technology and Economics
1111 Budapest XI. ker. Bertalan L. u. 4-6. , Hungary
`lajos@simba.ara.bme.hu`

Abstract. The most important parameters of fibrous filters: the separation efficiency and pressure drop change during the operation. Theoretical and experimental investigations have been carried out to develop an adequate model for numerical simulation of the clogging process. The model and some results of numerical simulations are presented in this paper. Also basic considerations on the combination of the particle deposition, on fibres inside the filter, and the formation of dust cake are suggested.

Keywords: Filtration, dust, clogging, numerical simulation, flow field

1. Introduction

Fibrous filter mats play a significant role in the separation of solid particles and drops suspended in gas. Their wide application in air pollution control and in different technologies is justified by their reliability of service and relatively low overall cost. The porous layers are produced either as woven fabrics or as felts. The most significant disadvantage of filters is the time dependence of their operation parameters. The temporal change is the consequence of the way of separation of particles in filters: the particles deposit on the fibres, increasing both the filtration efficiency and the pressure drop (at constant flow rate). This characteristic makes the design and in some cases also the operation of filters difficult. The objective of the research presented here is the investigation on the mechanism of particle deposition with special regard to the effect of the previously separated particles and the inhomogeneity of filter structure as well as the development of a model for simulation of the clogging process in fibrous filters.

2. Dust separation by filter mats

Industrial gases of usual concentrations, cleaned by fibrous filters, are very thin mixtures of gas and solid particles. Even in case of relatively high concentration, $c = 10 \frac{g}{m^3}$, the average distance between particles is about 50 particle diameters which is in most cases in the range $10^{-1} < d_p[\mu m] < 10$. Fibrous filters consist of cylindrical fibres of $d_f = 5 - 30\mu m$ diameter, the average distance between fibres is about $2 - 10$ fibre diameters. Since the distance between fibres is in general much bigger than the

particle diameter, the particles should be displaced relative to the gas in order to put them in contact with the fibres. This transport is caused by inertia of particles, by gravity and at smaller particles by diffusion. In case of charged particles and/or fibres the electrostatic attraction plays a role. Particles can contact the fibres also without displacement if they move along streamlines approaching the surface of the fibres at most at one particle radius distance (interception). The displacement of particles is hindered by viscous forces arising when particles move relative to the gas.

The influence of the deposited particle on the separation of further particles and on pressure drop was investigated and described by [1] - [3], but because of the neglect of significant influencing factors the results obtained are only qualitatively correct. Deposited particles form dendrites under certain condition , which act as thin fibres influencing both the filtration efficiency and the pressure drop [3] - [5]. The description of the very complicated processes of particle deposition has been simplified by using the isolated fibre approach. In [3], [5], [6] the effect of dust load on filter has been considered by modification of single fibre efficiency. Most of the authors suggested a linear relation between the concentration of deposited particles and the increase of single fibre efficiency:

$$\eta_\mathrm{l}/\eta_\mathrm{f} = 1 + \lambda c_\mathrm{d}, \qquad (2.1)$$

where η_l and η_f is the single fibre efficiency of loaded and clean fibres, respectively, $c_\mathrm{d}[\frac{\mathrm{kg}}{\mathrm{m}^3}]$ is the concentration of deposited particles, γ is a factor depending mainly on the characteristics of fibres. The value of single fibre efficiency expresses the ratio of the number of particles deposited on a given fibre and that of approaching the fibre in a layer of thickness equal to the fibre diameter d_f.

As a result of the first phase of research reported here, the author suggested a method for calculating 3D flow field in inhomogeneous filter mats [7], and a simplified 1D model for describing the clogging process in filters [8]. A 3D model for calculation of dust deposition in real filter mats was published [9] but it doesn't take the particle deposition into consideration. In the second phase of research, 3D calculation of flow in filter mats and the extended dust deposition model have been combined [10], [11]. At high filter load at first continuous layer of dust particles, later a dust cake arises at the inlet of the filter mat. A model and numerical simulation have been developed [12] to predict the process of cake formation. Recently measurement results have been published [14] on the size of dendrites of deposited particles. On the basis of these results development of a comprehensive model combining the dust deposition inside the filter mat and the formation of a dust cake in the final period of the lifecycle of the filter seems to be realistic.

3. Model for dust deposition inside filter mats

3.1. Simulation of particle deposition in filter mat. Because of the complexity of flow in real filter mats due to complex fibre structure and because of the large number of dust particles (in case of $d_\mathrm{p} = 3$mm particle size and $10\frac{\mathrm{g}}{\mathrm{m}^3}$ concentration the number of particles in 1cm^3 is $3.5 \cdot 10^5$) the direct simulation of dust separation process still seems to be impossible. That is why a simplified model has to be de-

veloped relying on basic laws of fluid mechanics as well as on assumptions based on experimental investigations. So since the dominant position of the fibres is parallel to the surface of the mat and the dominant direction of filtration velocity is perpendicular to it, the fibres are supposed to be perpendicular to filtration velocity. From the point of view of the flow field the individual fibres are disregarded: the filter mat is considered as a porous layer of spatially and temporally changing permeability. The model for calculation of the clogging process can be divided into two interconnected parts: simulation of particle deposition and calculation of flow field in filter mat. The model described here is elaborated for monodisperse (d_p = const.) dust particles.

As a result of considerable efforts made in this field a number of expressions have been published for the calculation of the collection efficiency of clean single fibres. The expressions proposed in [9] have been used by the author to calculate the single fibre efficiency in case of no dust deposition.

The suggested model takes the effect of collected particles in the following way into consideration. The deposited particles take part in the collection of subsequent particles by increasing the collecting surface of the filter mat. Not the whole surface area of the deposited particles should be regarded as additional collecting area, because the particles and fibres "shadow" each other (see Figure 1). This effect is considered by the shadowing factor $k = 0.5$, i.e. on the basis of simple geometrical considerations about half of the surface area of deposited particles (which are regarded as spheres) increases the collecting area of the filter mat.

On the basis of experimental observations three different models of particle deposition have been suggested. In case of low filter loading, at the beginning of the filtration process, the majority of the deposited particles cover the surface of the fibres, which can be taken into consideration as increase of fibre diameter: thickening model, see Figure 2.

At higher filter load the ratio of particles collected by the deposited particles is increasing, so more and more

Figure 1. Shadowing effect

model. During the filtration process the combination of these two models occurs, called combined model (Figure 2).

Since the particles deposited according to the thickening model and the dendrite model influence the separation and pressure drop differently, the share factor b is suggested expressing the ratio of amount of particles forming dendrites to the amount of all deposited particles. On the basis of the published evaluation of experimental results and our own measurements, linear correlation has been found between the share factor and the concentration of particles collected previously
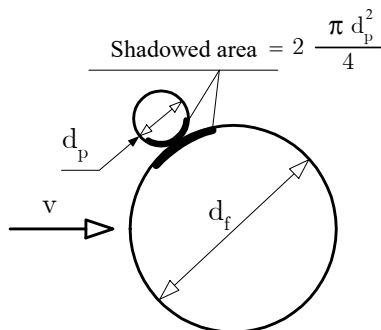
$$b = 0.024c_d \ . \tag{3.1}$$

The efficiency (E) of filter mat of Δx width can be expressed:

$$E = 1 - \frac{c_0}{c_i} = 1 - exp\left(-\frac{a_f \eta_l}{\pi} \Delta x\right), \qquad (3.2)$$

where c_0 and c_i $[\frac{kg}{m^3}]$ is dust concentration at the inlet and outlet of filter layer, respectively, and a_f $[\frac{m^2}{m^3}]$ is the specific area of fibres.

In equation (3.2) the single fibre efficiency of loaded filter ηl includes the effect of collected particles. According to the suggested model it can be expressed in the following way [11]:

$$\eta_l = \eta_f + \frac{\eta_f c_d}{\rho_p d_p a_f}\left[3(1-b) + \right.$$
$$\left. +4b\left(\frac{\eta_{dend}}{\eta_f} - k\right)\right], \quad (3.3)$$

where ρ_p $[\frac{kg}{m^3}]$ is the density of dust particle and η_{dend} is the single fibre efficiency of the dendrites. The comparison of equation (3.3) and equation (2.1) with experimental results shows that equation (3.3) based on model considerations describes much more accurately the influence of deposited particles on particle collection than equation (2.1) suggested previously [10].

a. Thickening model
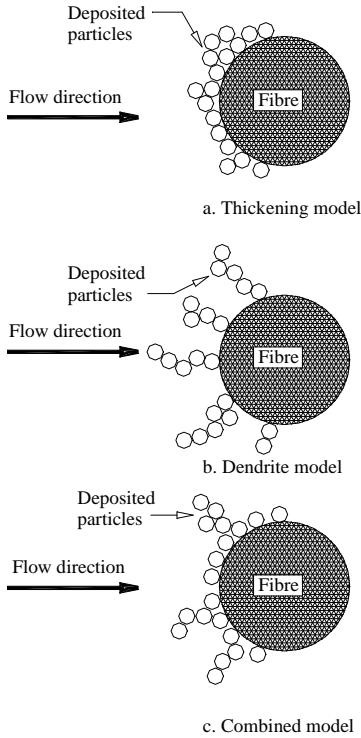
b. Dendrite model

c. Combined model

Figure 2. Deposition models

3.2. Calculation of 3D flow field in filter mats. Because of the small size of particles and fibres and the relatively low filtration velocity the particle or fibre Reynolds number is small, so the flow in porous filter mats is laminar. The pressure drop Δp [Pa] across the filter mat, needed to reach a given filtration velocity v_f $[\frac{m}{s}]$ through the filter mat can be determined as the aerodynamic force acting on fibres in filter mat of $1m^2$ area:

$$\Delta p = \frac{4\pi}{Ku}\mu L v_f, \qquad (3.4)$$

where μ $[\frac{kg}{ms}]$ is the dynamic viscosity, Ku is the Kuwabara coefficient [13]:

$$Ku = -0.5\ln\alpha - 0.75 + \alpha - 0.25\alpha^2, \qquad (3.5)$$

depending on the packing density $\alpha = \frac{V_f}{Vm}$ of the filter mat (V_f and V_m is the volume of fibres and filter mat, respectively), and L [m] the overall length of fibres in filter mat of $1m^2$ area and h [m] thickness:

$$L = 4\alpha s/d_f^2 \pi . \qquad (3.6)$$

Inserting equation (3.6) in equation (3.5) and substituting the thickness of the layer h [m] by Δx (x co-ordinate is perpendicular to the surface of the filter mat

and pointing in the direction of the flow) and considering that the gas is flowing in the direction of pressure decrease, the x component of the filtration velocity can be expressed:

$$v_{\mathrm{fx}} = -\frac{Ku{d_{\mathrm{f}}}^2}{16\mu\alpha}\frac{\Delta p}{\Delta x} \; . \tag{3.7}$$

Equation (3.7) shows that by neglecting the inertia of fluid and particles in comparison with viscous forces and effect of pressure gradient, the generalised form of Darcy equation can be formulated:

$$\mathbf{v} = -C\nabla p \tag{3.8}$$

where C $[\frac{\mathrm{m}^3\mathrm{s}}{\mathrm{kg}}]$ is the permeability coefficient which can be expressed in case of loaded filters as

$$C = \frac{Ku}{16\mu}\frac{1}{\dfrac{\alpha}{d_{\mathrm{f}}^2} + \dfrac{bc_{\mathrm{d}}}{\rho_{\mathrm{p}}d_{\mathrm{p}}^2}} \; . \tag{3.9}$$

Equation (3.9) takes both the thickened fibres and the dendrites into consideration.
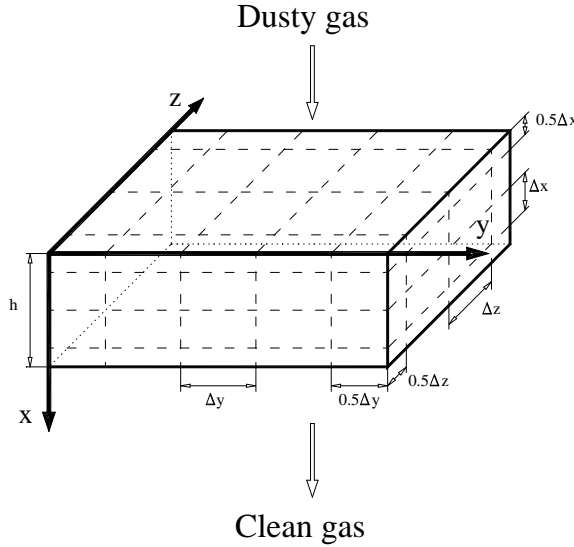

Figure 3. Co-ordinate system and division of filter mat

By neglecting the volume of fibres and particles and the compressibility of gas the continuity equation ($\nabla \cdot \mathbf{v} = 0$) can be transformed by using equation (3.8):

$$\nabla \cdot (C\nabla p) = 0 \; . \tag{3.10}$$

Knowing the actual 3D permeability distribution in filter mat and the boundary conditions: $x = 0$ $p = p_{\mathrm{in}}$, $x = h$ $p = p_{\mathrm{in}} - \Delta p_{\mathrm{f}}$, on the periphery (see Figure 3), the flow field can be calculated.

3.3. Simulation of particle collection process. The filter mat is divided into a number of elements (Figure 3) and the initial characteristics of the clean filter elements (packing density and fibre diameter) are given. Also particle diameter, inlet dust concentration, pressure drop across the mat (or filtration velocity), gas viscosity and particle density should be known. After calculating the permeability coefficient distribution by using equation (3.9), the pressure distribution can be determined by solving equation (3.10). The inlet and outlet velocities at all faces of volume elements can be determined from p distribution. Also the single fibre efficiency for clean fibres can be calculated for all filter elements as well as that of loaded fibres by using equation (3.3). Using these variables and the dust concentration at the inlet of the filter mat, a mass balance equation can be formulated for all filter elements: the difference of particle mass entering and leaving the filter element in a given time interval Δt [s] is equal to the increase of the quantity of collected particles. Summarising the mass of collected particles the filtration efficiency of the filter mat (E) can be calculated. At the end of the time interval the collected mass of dust and by using equation (3.9) a new distribution of permeability coefficient can be determined, so the next cycle of calculation for the next time interval can be started.

4. Considerations on the formation of dust cake

The lifecycle of a filter mat can be divided into two parts: in the first period of filtration the dust particles are collected by the fibres and already deposited particles
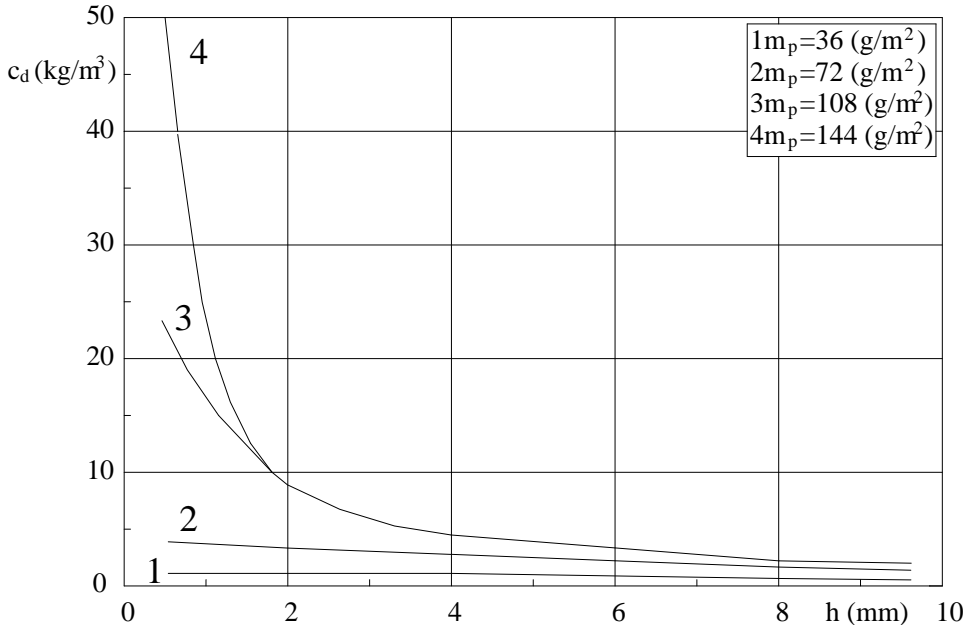

Figure 4. Variation of concentration of deposited particles across filter mats
$(d_\mathrm{p} = 1\mu\mathrm{m}, d_\mathrm{f} = 20\mu\mathrm{m}, h = 10\mathrm{mm}, v_\mathrm{m} = 0.1\frac{\mathrm{m}}{\mathrm{s}})$

are situated in the depth of filter mat (depth filtration). Since the particle concentration is the highest at the inlet of the filter mat, and the deposition of particles increases the subsequent collection, the concentration of the deposited particles increases very rapidly in the vicinity of inlet surface of the mat. Figure 4 shows the result of a 1D calculation of distribution of deposited particle concentration (c_d) across the filter mats at four different dust loads. If the dendrites created by the deposited particles near the inlet of the filter mat bridge the distance between fibres, the second period of the lifecycle of filter mat starts. A continuous and gradually thickening dust layer (dust cake) arises, assuming the task of collection of subsequent particles (surface filtration). While the regular removal of individual dust particles from the surface of the fibres situated inside of the mat is practically impossible because of the very strong attraction forces, the dust cake on the inlet surface of filter mat can be removed relatively easily by shaking the filter bags or by using reverse flow. Therefore those filter mats where the surface filtration dominates can be regenerated periodically, consequently they are widely used for cleaning gas of relatively high dust concentration.
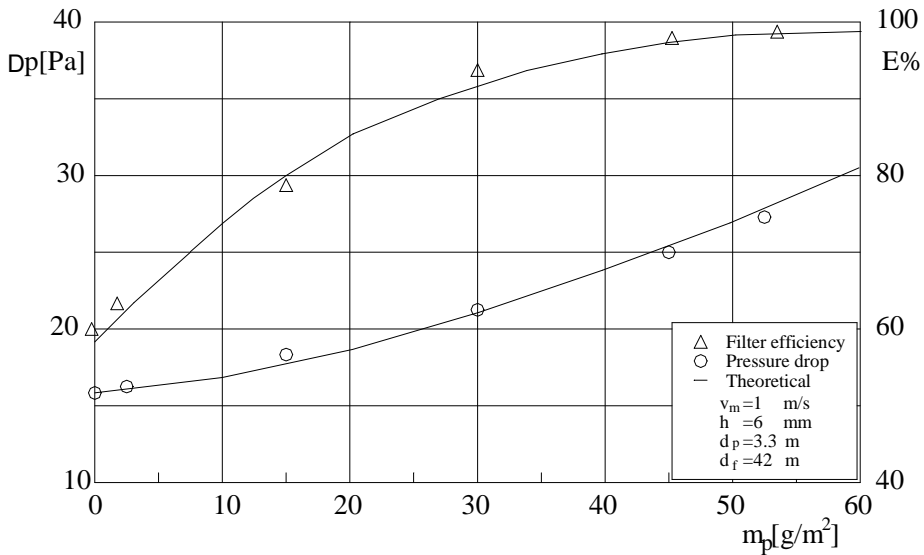

Figure 5. Change of filtration characteristics as function of dust load

The final objective of the research presented here is the combination of the simulation of filtration process in both periods of the lifecycle of the filter mat. The simulation of the first filtration period is outlined in this paper, and methods for calculation of the development of dust cake is also available [12]. The combination of the two simulation methods necessitates the correct description of the formation of continuous dust layer on the inlet surface of the filter mat, which is the starting point of the formation of a dust cake. Recent experimental investigations on the lateral size
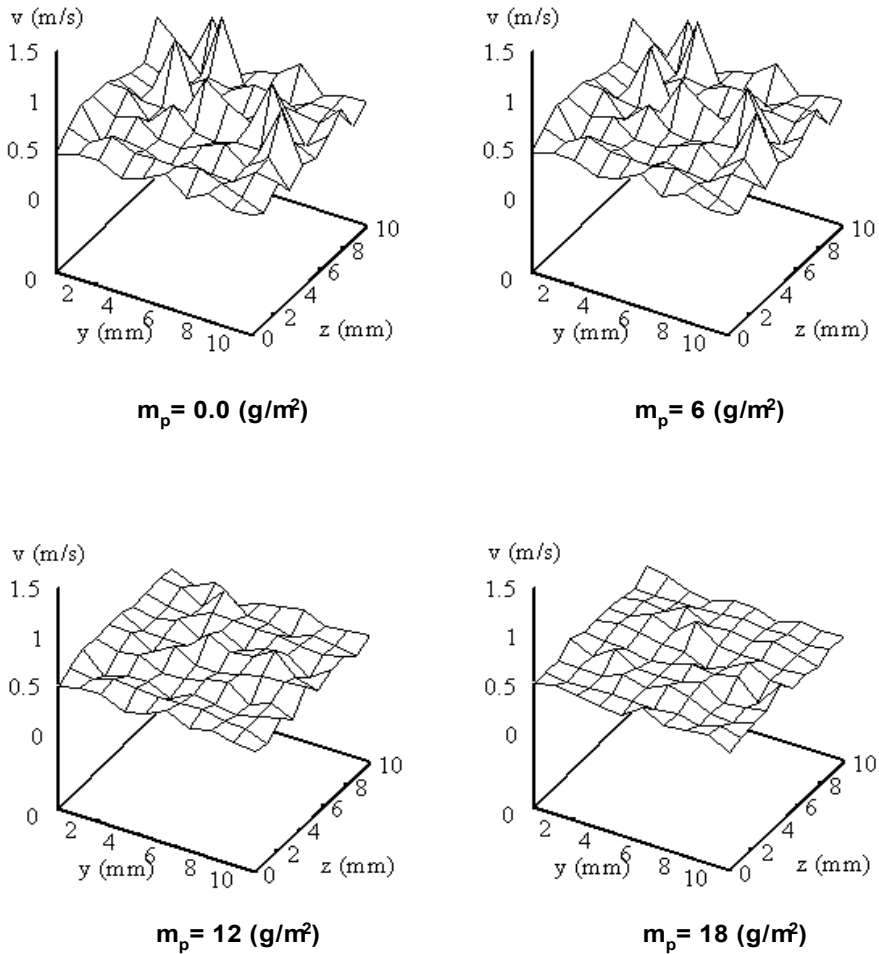
$m_p = 0.0$ (g/m²)

$m_p = 6$ (g/m²)

$m_p = 12$ (g/m²)

$m_p = 18$ (g/m²)

Figure 6. Computed velocity at filter inlet at different values of m_{p}

statements: the lateral size of the dendrite is much smaller than the average distance between the fibres. Consequently if the fibres are homogeneously distributed the formation of a continuous dust layer can arise only at a very high concentration of deposited mass.

The author suggests explaining the formation of a dust cake at a relatively low dust load by the inhomogeneity of fibre distribution. In this case first the relatively small distances between the fibres will be bridged and so "fibres" of much higher diameter
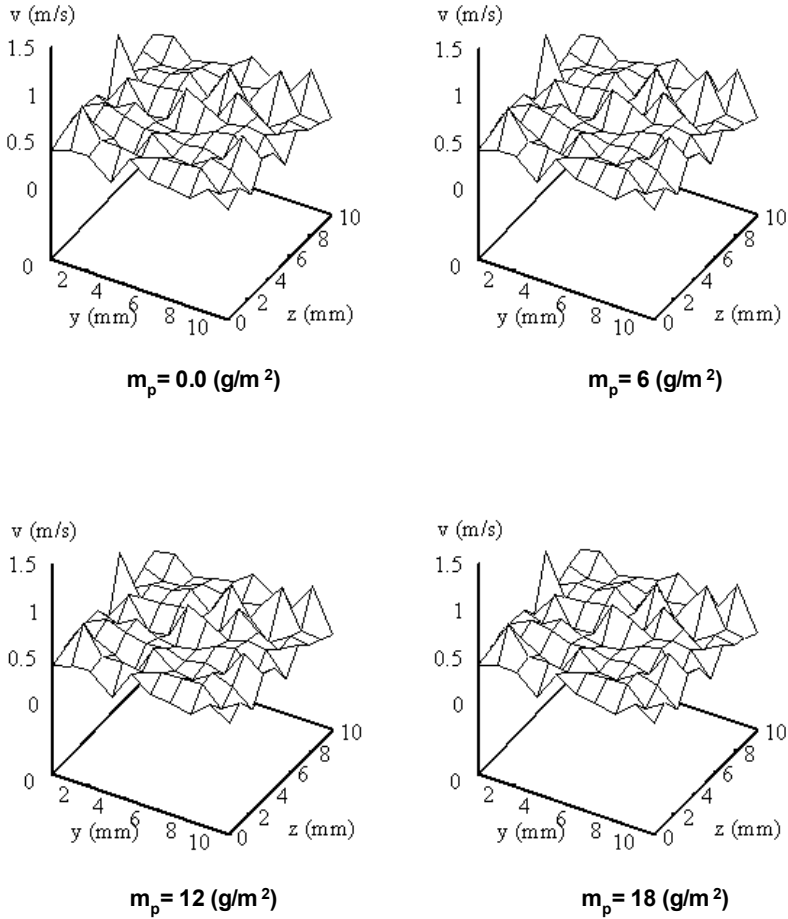
Figure 7. Computed velocity at filter outlet at different values of m_p

occur. The dendrites developing on these thicker formations can bridge much larger distances. The simulation of this phenomenon is in progress.

5. Simulation results

3D numerical simulation of flow field has been performed for filter mats of different inhomogeneity of fibre packing density. The model filters have been put together from

filter elements selected randomly from a set of filter elements, the permeability coefficient of which corresponded to the Gaussian normal distribution of given standard deviation. The calculated increase of the overall permeability of the filter mat with increasing the inhomogeneity has shown good agreement with experimental result [7].

The results of numerical simulation of the clogging process show acceptable agreement with results published in the literature. Figure 5 shows the calculated and measured change of pressure drop and filtration efficiency of filter mat as the function of a specific dust load (which is proportional to the filtration time).

The dust deposition decreases the inhomogeneity of overall packing density in y and z directions and increases in x direction (Figure 3). The decrease of inhomogeneity in $y - z$ planes depends also on the amount of collected particles: it is considerable close to the inlet plane and much less at the outlet. This is clearly demonstrated by the calculated velocity distributions at inlet and outlet of clean and loaded filter mats shown in Figures 6 and 7.

6. Conclusions

A model of dust particle collection relying on experimental investigations has been developed. It regards a part of surface of the deposited particles as additional collecting surface. The shadowing effect and the share factor have been suggested to simulate the real processes more accurately. A numerical method has been developed for calculation of 3D flow field in filter mat based on the generalized form of Darcy equation and continuity equation. The results of simulation of the filtration process show acceptable agreement with experiments. The numerical simulation of combination of the two phases of lifecycle of a filter mat needs further investigations concerning the formation of continuous dust layer on the surface of the filter mat. A significant influence of inhomogeneity of fibre structure on the formation of the dust cake is suggested.

REFERENCES

1. STENHOUSE, J.I.T. and TROTTIER,R.: *The loading of fibrous filters with submicron particles*, J. Aerosol Sci., **22**, (1991), S777- S780.

2. YOSHIOKA, N. ET AL.: *Filtration of Aerosols through Fibrous Packed Bed with Dust Loading*, Chem. Eng. Japan, **33**, (1969), 1013-1019.

3. KANAOKA C., ET AL.: *Simulation of the growing process of particle dendrite and evaluation of a single fibre collection efficiency with dust load*, J. Aerosol Sci., **11**, (1980), 377-389.

4. BERGMAN, W. ET AL.: *Enhanced Filtration*, Lawrence Livermore Laboratory, 1976.

5. LASTOW, O.: *Simulation of dendrite formations of aerosol particles on a single fibre*, J. Aerosol Sci., **25**, (1994), S199-S200.

6. MYOJO, T. ET AL.: *Experimental observation of collection efficiency of a dust-loaded fibre*, J. Aerosol Sci., **15**, (1984), 483-489.

7. LAJOS T.: *The effect of inhomogeneity on the flow in fibrous filters*, Staub Reinhaltung der Luft. Band 45, (1985), 19-22.

8. LAJOS T.: *A model for calculation of clogging process in filter mats*, 1. World Congress Particle Technology, Nürnberg, (1986), 175-188.

9. SCHWEERS, E. and LÖFFLER F.: *Realistic modeling of the behaviour of fibrous filters through consideration of filter structure*, Powder Technology, 80 (1994), 191-206.

10. ABD EL-HAMIED, A.A. and LAJOS, T.: *Investigation of loaded fibrous filter*, Periodica Polytechnica Ser. Mech. Eng., **41**(1), (1997), 3-20.

11. ABD EL-HAMIED, A.A.: *Investigation of the dust separation process in fibrous filters*, Thesis, Technical University of Budapest, 1997.

12. SCHMIDT, E. and LÖFFLER, F.: *Verification of dust cake compression by means of structure analysis and the effect of filtration performance*, 6th World Filtration Congress, Nagoya, Japan (1993), 54-59.

13. KUWABARA, S.: *The forces experienced by randomly distributed parallel circular cylinders or spheres in viscous flow at small reynolds numbers*, J. Phys. Soc., Japan, **4**, (1959), 527-532.

14. REMBOR, H. J. and KASPER, G.: *Transient filtration behaviour of fibrous filters: Deposited particulate structures studied with a confocal laser scanning microscope*, Proc. of the 1999 Fall Topical Conf. Minneapolis (1999), 39-46.

DEVELOPMENT OF VORTEX DYNAMICS FOR SIMULATION OF TURBOMACHINE CASCADES AND BLADE ROWS

R. Ivan Lewis
Bruce Building, University of Newcastle upon Tyne
NE1 7RU, United Kingdom
`R.I.Lewis@ncl.ac.uk`

Abstract. Vortex dynamics, as an extension of surface vorticity modelling, provides a powerful method for simulating flow through turbomachinery blade rows. Examples here include compressor rotating stall, flow through a turbine stage and new extensions of methodology to simulate radial turbomachines.

Keywords: Vortex dynamics, turbomachine, turbomachinery cascade, computational fluid dynamics.

1. Introduction

The main aim of this paper is to present solutions for the simulation of turbomachinery blade row flows derived recently by vortex dynamics modelling. It was felt appropriate to precede this by a brief review of vortex methods as a reminder of the depth of fundamental research that was required to give birth to these valuable numerical Computational Fluid Dynamics (CFD) tools, which today are almost taken for granted.

Vortex methods for modelling aerofoil and turbomachinery blade flows were among the very first forms of CFD which originated in the 1950s, stemming initially from thin aerofoil theory [1,2,3,4]. A number of exact solutions for cascade flows were already available at that time by classical mathematical methods, notably conformal transformation, such as those by Merchant and Collar [5] which were re-examined and programmed for early electronic computers by Gostelow [6] and Pollard & Wordsworth [7]. Indeed, although the main emphasis was on the *Direct* or *Analysis* method, there was already considerable interest developing also in the *Inverse* or *Design* method, using potential flow theory to automatically design blade shapes to deliver a prescribed surface velocity or pressure distribution. The theories of Ackeret [2] and Railly [8] are typical of these, both based on linearised thin aerofoil theory. Subsequently Pollard [9] extended the method for simulation of mixed-flow or radial turbomachinery blade rows including the effect of change in meridional streamline thickness (or the so-called AVR or axial-velocity-ratio effects).

In all of the above references to singularity methods however, the restrictions of

thin aerofoil theory were applied, namely that the singularities were concentrated onto the blade or aerofoil chord line, vortex singularities to represent lifting properties and source singularities to generate profile thickness. In parallel with this Scholz [10] introduced the concept of the carrier curve for the source/vortex singularities, enabling them to be more strategically placed on the blade camber line, to be later improved and applied by Czibere [11,12,13] and Baranyi [14], as later extended and reviewed by Rohatynski [15]. As early as 1959, however, it was realised by Martensen [16], in a key paper, that the complete potential flow could be represented instead by an appropriate distribution of surface vorticity around the profile perimeter. However, in parallel with this an alternative model was conceived by Smith and Hess [17] involving instead a surface distribution of source singularities for modelling the three-dimensional potential flow past arbitrary shaped bodies, although it was then clearly necessary to introduce appropriate bound vorticity into the body to generate lift forces. Although the latter so-called Douglas-Neumann method has been widely used with great success for fully three-dimensional flow simulation, Martensen's surface vorticity method has proved crucial to development of turbomachinery cascade and meridional (axisymmetric throughflow) inviscid flow models well geared to engineering design needs. Initial adaptations for numerical computation were developed by Jacob & Reigels [18] and Wilkinson [19,20] with extensions to mixed-flow radial cascades. This was extensively investigated by Fisher [21,22] including the derivation of datum exact solutions for mixed-flow rotors. Several of these works now also included AVR, namely the influence of variation in meridional stream-surface thickness [9,13,21].

Extension of the surface vorticity method to deal with viscous flows including flows with separation such as bluff body flows, was a natural step [23,24]. The literature and methodology of both surface vorticity and vortex dynamics have been fully reviewed elsewhere by the present author [25] followed by adaptation of suitable surface vorticity models and codes to general performance analysis for designers and students [26]. The remainder of this paper will focus on applications of vortex dynamics to turbomachine cascades and blade rows. Governing equations are presented in section 2.0 including a simulation of compressor rotating stall, followed in section 3.0 by application to turbine and fan stages including wake interaction between stator and rotor. In section 4.0 relevant analysis and numerical modelling are presented for extension of vortex dynamics to radial cascades and turbomachines, including sample calculations for radial pumps or fans.

2. Basic equations for surface vorticity and vortex dynamics modelling of blade rows

The basis for surface vorticity modelling of plane two-dimensional flow past a single body is illustrated in Figure 1 and Martensen's governing integral equation, which states the Dirichlet surface boundary condition of zero velocity parallel to the body surface at point m due a surface vorticity distribution $\gamma(s_n)$, is given by

$$\frac{1}{2}\gamma(s_m) + \oint k(s_m, s_n)\gamma(s_n)\mathrm{d}s_n + W_\infty(\cos\alpha_\infty \cos\beta_m + \sin\alpha_\infty \sin\beta_m) = 0 \quad (2.1)$$
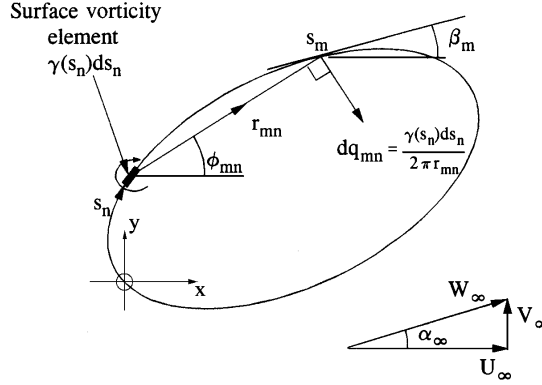
Figure 1. The surface vorticity model

where the coupling coefficient $k(s_m, s_n)$ linking the vortex element $\gamma(s_n)\mathrm{d}s_n$ at point n to point m is given by

$$k\left(s_m, s_n\right) \ = \ \frac{1}{2\pi} \left\{ \frac{(y_m - y_n)\cos\beta_m - (x_m - x_n)\sin\beta_m}{(x_m - x_n)^2 + (y_m - y_n)^2} \right\} \ . \tag{2.2}$$

The body here has been immersed into a uniform stream W_∞ with angle of attack α_∞ relative to the x axis and the local body profile slope is given by β_m.
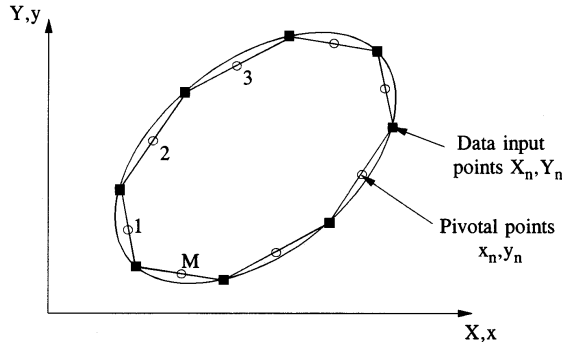

Figure 2. Numerical discretisation of the body surface

As shown fully elsewhere [16,25], for an infinite array of identical bodies spaced t apart in the y direction between $-\infty \leq y \leq +\infty$, (e.g. a cascade of aerofoils), the same governing equation (2.1) is valid provided the coupling coefficient is rewritten as follows:

$$k\left(s_m, s_n\right) = \frac{1}{2t} \left\{ \frac{\sin\frac{2\pi}{t}(y_m - y_n)\cos\beta_m - \sinh\frac{2\pi}{t}(x_m - x_n)\sin\beta_m}{\cosh\frac{2\pi}{t}(x_m - x_n) - \cos\frac{2\pi}{t}(y_m - y_n)} \right\} \ . \tag{2.3}$$

Numerical discretisation of the governing equation is achieved if the body surface is represented by a finite number M of small elements Δs_n as illustrated in Figure 2,
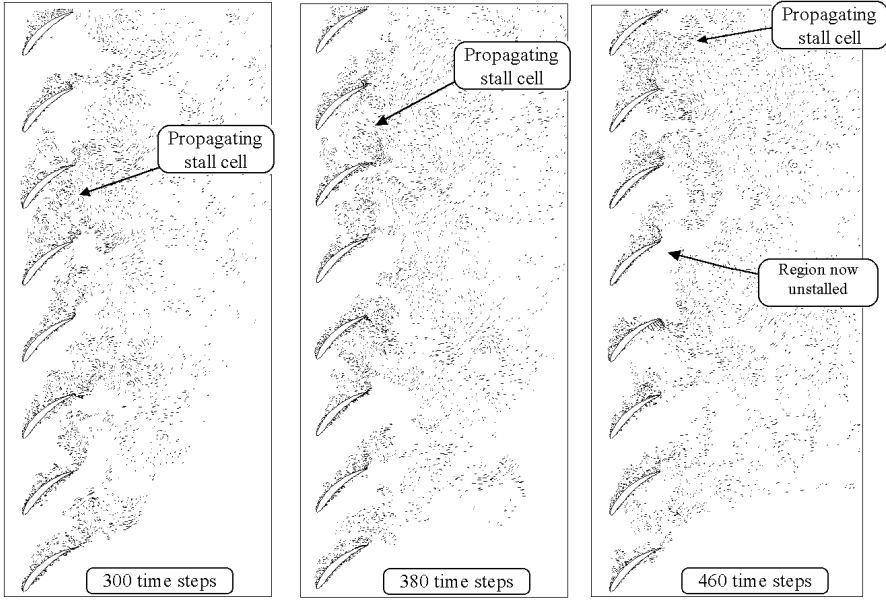
Figure 3. Simulation of rotating stall in an axial compressor cascade

whereupon the coupling coefficient for the infinite cascade becomes

$$K\left(s_m, s_n\right) = \, k\left(s_m, s_n\right) \Delta s_n \,. \tag{2.4}$$

The following system of linear equations is then obtained

$$\sum_{n=1}^{M} K\left(s_m, s_n\right) \gamma(s_n) = -U_\infty \cos\beta_m - V_\infty \sin\beta_m \tag{2.5}$$

where all the external influences, namely the component uniform streams U_∞ and V_∞, have been transferred to the right hand side. These equations may be easily set up and solved by matrix inversion after a number of essential numerical treatments (a) to correct the self-inducing coupling coefficient $K(s_m, s_m)$ for surface curvature and (b) the profile opposite coupling coefficients $K(s_m, s_{M-m+1})$ for possible errors due to close proximity. Details are given in full in ref. [25] including details of how to impose a trailing edge Kutta-Joukowski condition for the case of aerofoil or turbomachine cascade flows.

The above equations are of course only applicable as defined for inviscid/potential flows. For the extended case of vortex dynamics, the numerical equation for body point m may be easily modified as follows

$$\sum_{n=1}^{M} K\left(s_m, s_n\right) \gamma\left(s_n\right) = -U_\infty \cos\beta_m - V_\infty \sin\beta_m - \sum_{j=1}^{Z} \Delta\Gamma_j \left(U_{mj} \cos\beta_m + V_{mj} \sin\beta_m\right)$$

$$\tag{2.6}$$

where a cloud of Z discrete vortices of strength $\Delta\Gamma_j$ are spread throughout the domain, with unit induced velocities U_{mj} and V_{mj} given by

$$\left. \begin{array}{l} U_{mn} = \dfrac{1}{2t} \dfrac{\sin \frac{2\pi}{t} (y_m - y_n)}{\cosh \frac{2\pi}{t} (x_m - x_n) - \cos \frac{2\pi}{t} (y_m - y_n)} \\[4mm] V_{mn} = -\dfrac{1}{2t} \dfrac{\sinh \frac{2\pi}{t} (x_m - x_n)}{\cosh \frac{2\pi}{t} (x_m - x_n) - \cos \frac{2\pi}{t} (y_m - y_n)} \end{array} \right\} . \qquad (2.7)$$

As stated the above equations apply to both identical bodies and flow patterns repeated periodically with pitch t in the y-direction. This restriction may be partially lifted if the single body or aerofoil is broken down into say N independent (possible identical) aerofoils of y-pitch t/N. For a cascade, the greater the value of N the more representative will be the prediction of flow variations from blade to blade. The ultimate limit will be set by computational requirements. Thus the matrix size will now be increased in size to $NM \times NM$ requiring increased memory requirements of N^2 and similarly execution times.

At this stage it may be helpful, without giving more analytical development, to illustrate the final outcome of this procedure for simulation of the flow through a fairly heavily loaded axial compressor cascade as illustrated in Figure 3 where $N=8$. Thus the predicted flow pattern will repeat itself identically every eight blade pitches.

Table 1. Compressor cascade geometrical specification

Inlet angle $\beta_1 = 54.59°$	Stagger angle $= 41.11°$
Outlet angle $\beta_2 = 30.59°$	Camber angle $= 44.49°$
Inlet velocity $W_1 = 1.0$	(Circular arc camber)
Diffusion factor $= 0.6$	Pitch/chord $t/l = 1.162$
Flow coeff. $\phi = 0.5$	C4 Base profile
Work coeff. $\psi = 0.40662$	

The cascade design data for this case are given in Table 1 and are applicable to a typical axial compressor but with rather heavy duty coefficients ($\phi = 0.5$, $\psi \approx 0.4$). As may be expected the cascade experiences predicted rotating stall. As shown by Lewis [26] (pages 42 & 93), the diffusion factor must not exceed 0.6 for major stall and the value here of $DF = 0.6$, as given by equation (2.8) below, is thus in the range for incipient stall

$$DF = 1 - \sqrt{\frac{4\phi^2 + (1 - \psi)^2}{4\phi^2 + (1 + \psi)^2}} + \frac{t}{\ell} \frac{\psi}{\sqrt{4\phi^2 + (1 + \psi)^2}} . \qquad (2.8)$$

The remaining examples in this paper will be for the value $N = 1$, i.e. blades and flow patterns which repeat for each blade pitch t. However, the additional variations will be introduced of (a) two blade rows in relative motion, section 3, and (b) application of the method to radial turbomachines for which the relative eddy and Coriolis accelerations induce enormously significant effects, section 4. Before proceeding, however, it is important to draw attention to matters. First, the success of the vortex dynamics

technique for predicting such a complex flow as rotating stall. Second, the importance of relating CFD methods to the overall framework of turbomachinery performance analysis, which is the burden of Ref. [26]. Thus the stage duty (ϕ, ψ) combined with pitch/chord ratio t/l entirely and explicitly determine the diffusion factor DF imposed by the designer and hence the aerodynamic stability. Let us not despise such historical parameters as diffusion factor but use CFD in a research manner to confirm our wealth of experimental experience over many years of practical turbomachinery and much empirical ingenuity of earlier researchers.

To conclude this section mention should be made of the additional numerical features of full vortex dynamics modelling, the aim of which is to solve the Navier-Stokes equations. A full explanation and review has been given elsewhere [25]. Suffice it to say here that the following actions are required in a time-stepping sequence of numerical analysis:

1. Shedding of discrete vortices $\Delta\Gamma_j = \gamma(s_j)\Delta s_j$ from each surface element at each time step thus creating a cloud of vortex elements. This follows a potential flow analysis using equation (2.6) to calculate the slip flow and the newly created surface vorticity $\gamma(s_j)$.

2. Using a random walk procedure [24,25] for each discrete vortex $\Delta\Gamma_j$ to simulate viscous diffusion at each time step.

3. Performing a thermodynamically reversible process for the mutual convective influence of all members of the vortex cloud at each time step.

4. Recombining any vortices which become excessively close after the random walk. This has the beneficial side effect of reducing the total volume of the vortex cloud. Alternatively the cloud may be redistributed onto a fixed grid filling the regime.

5. Deleting any discrete vortices which stray inside the body profile during diffusion and imposing the circulation theorem to ensure that the equivalent loss is restored during the potential flow analysis in order to ensure overall conservation of vorticity.

3. Simulation of turbomachine stages

Figure 4 shows the solution of the above equations for flow through a typical 50% reaction axial turbine stage comprising stator and rotor for the following design conditions close to the ideal stage duty [26]: Table 2. Design data for sample turbine stage

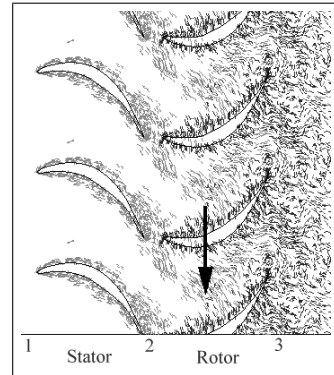|	
Flow coefficient ϕ	0.6
Work coefficient ψ	1.1
Stage reaction R	50%
Pitch/chord ratio t/l	0.8
Relative inlet angle $\alpha_1 = \beta_2$	4.764°
Relative outlet angle $\alpha_2 = \beta_3$	60.255°
Fluid deflection $\varepsilon_S = \varepsilon_R$	65.019°
Lift coefficient $C_{L\infty}$	2.8167

Figure 4. Simulation of a 50% reaction turbine stage

The selected duty (ϕ, ψ) duty is typical for a multi-stage gas or steam turbine for power generation and both stator and rotor show a basically stable flow. The simulation brings out the interaction of the stator wake with the downstream rotor flow as it traverses the rotor blade passage.

A second simulation example for flow through a turbomachine stage is given in Figure 5 for the case of an axial fan or compressor, again with 50% reaction and for design data as given in Table 3 below. Table 3. Design data for sample fan stage

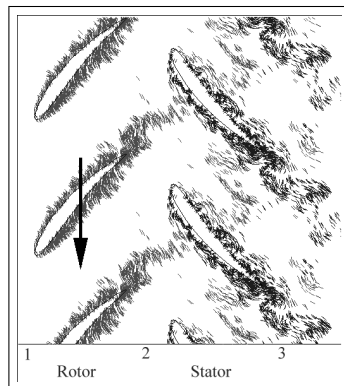|	
Flow coefficient ϕ	0.4
Work coefficient ψ	0.26
Stage reaction R	50%
Pitch/chord ratio t/l	1.0
Relative inlet angle $\alpha_1 = \beta_2$	57.59°
Relative outlet angle $\alpha_2 = \beta_3$	42.77°
Fluid deflection $\varepsilon_S = \varepsilon_R$	14.83°
Lift coefficient $C_{L\infty}$	0.8121

Figure 5. Simulation of the flow through a 50% reaction fan stage

In this case of course the rotor lies upstream of the stator which it then sweeps with its shed blade wakes. The progress of the rotor wake through the downstream stator is much more distinct in this example and there is some evidence here of rotor wake interference causing a small disruption of the flow on the pressure (convex) surface of the stator blade where the surface velocity is low. There is also evidence here of the previous wake impinging on the suction (convex) surface close to the trailing edge region and causing flow separation. This is a transient phenomenon which can be observed more easily if the simulation is shown as a movie in real time, one further advantage of vortex dynamics modeling.

Comparing Tables 2 and 3 it is worth pointing out that the design fluid deflection and consequent lift coefficient of the turbine blades are enormously greater than those imposed on the fan blades since the former involve accelerating cascade flows and the latter diffusing flows. The flow simulations of these two extreme turbomachine specifications confirm the general stability of both and are most encouraging confirmation of the scope of vortex dynamics modelling as a check upon design decisions which can be made at an early stage of the turbomachinery design process.

4. Simulation of radial turbomachines

To conclude this paper a brief outline will be given of the application of vortex dynamics to radial or mixed-flow turbomachines such as the radial fan rotor illustrated in Figure 6.

As illustrated in Figure 6, the most convenient approach to both surface vorticity and vortex dynamics modelling of a radial turbomachine is to transform it conformally
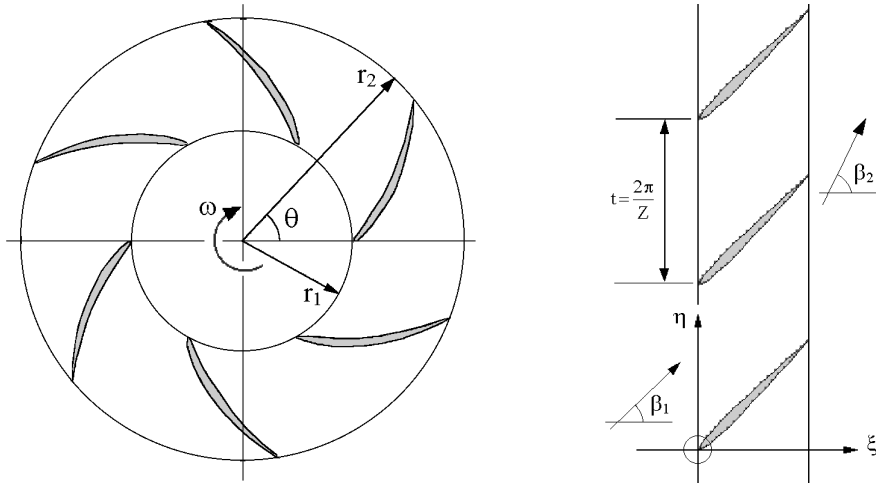
(a) Radial fan rotor in the $z(r, \theta)$ plane.   (b) Equivalent cascade in the $\zeta(\xi, \eta)$ plane.

Figure 6. Transformation of backward swept radial fan rotor into an equivalent infinite straight cascade

into an equivalent infinite straight cascade defined by Cartesian coordinates ξ, η in the ζ plane. For a purely radial meridional flow this is accomplished by the well known transformation,

$$\zeta = \ln z \tag{4.1}$$

which may be expressed in terms of the coordinate relationships as follows

$$\zeta = \ln r, \qquad \eta = \theta \tag{4.2a}$$

or in differential form

$$\mathrm{d}\xi = \mathrm{d}r/r, \qquad \mathrm{d}\eta = \mathrm{d}\theta . \tag{4.2b}$$

The velocity transformation between the two planes is then given by

$$q_\zeta = q_z r . \tag{4.3}$$

If the blade row is a rotor, however, the transformed cascade in the ζ plane will move vertically with a different velocity at each point on the blade surface according to equation (4.3). The main point of the transformation is to be able to apply the foregoing cascade vortex dynamics routines directly in the ζ plane and then to invert the transformation for visualisation of the actual flow in the z plane. The best approach here is to consider the flow relative to the rotor and thus transform all the vorticity across to the ζ plane including the relative eddy. Now with a rotor angular velocity of Ω, the field viewed relative to the rotor in the z plane will have a distributed vorticity 2Ω throughout. Conformal transformation remains valid provided any concentrated vortex or source singularities are transformed across unchanged in value.

Transformation of the vortex cloud elements thus presents no problem. However, the relative eddy 2Ω must also be first transformed piecewise across to provide the initially undisturbed flow field into which the rigid walled transformed cascade may then be immersed. As shown elsewhere in detail [25], with uniform stream components U_∞, V_∞ , the transformed vertical velocity becomes

$$v = V_\infty + \Omega \left\{ r^2 - \frac{1}{2} \left(r_1^2 + r_2^2 \right) \right\} \tag{4.4}$$

and the Martensen governing equation, by extension of equation (2.6) becomes

$$\sum_{n=1}^{M} K\left(s_m, s_n\right) \gamma\left(s_n\right) = -U_\infty \cos\beta_m - \left[V_\infty + \Omega \left\{ r^2 - \frac{1}{2} \left(r_1^2 + r_2^2 \right) \right\} \right] \sin\beta_m$$
$$- \sum_{j=1}^{Z} \Delta\Gamma_j \left(U_{mj} \cos\beta_m + V_{mj} \sin\beta_m \right) . \tag{4.5}$$

Figure 7 below shows the predicted flow patterns in the two planes for this 8 bladed rotor. As can be inferred from Figures 6 and 7, the blade profile here is based on a backward swept logarithmic spiral with angle 45°, which of course transforms into an uncambered blade profile in the ζ plane. In fact the author's software MIXFLO actually designs the blade profile in the ζ plane using standard cascade notation and in this case made use of a NACA0006 profile thickness superimposed on the camber line with zero camber. The general strategy for CFD design/analysis adopted here is to use a quasi-three-dimensional inviscid code combining axisymmetric meridional

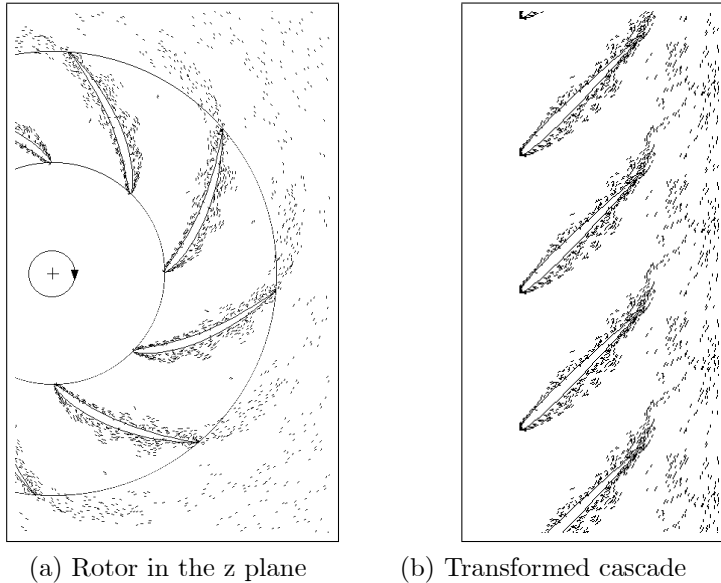(a) Rotor in the z plane   (b) Transformed cascade

Figure 7. Prediction of the flow through a radial backward swept fan rotor by vortex dynamics modelling

flow with superimposed blade-to-blade flows in order to create suitable blade geometry. This is then followed with vortex dynamics analysis to check on viscous blade-to-blade effects. As expected in this example stable flow was obtained for this fan with the design duty $\phi = 0.25$, $\psi = 0.5666$, which is a reasonable loading for this type of machine. There was zero prewhirl at entry to the rotor.

A second example is illustrated in Figure 8 for the much more demanding case of a heavily loaded radially bladed centrifugal machine.
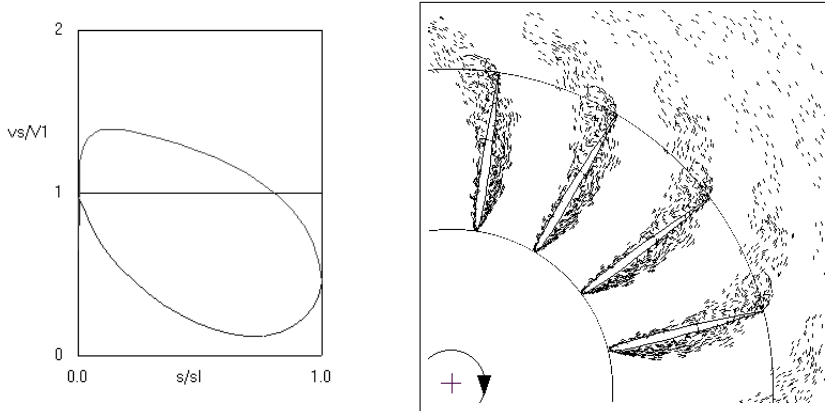

Figure 8. Flow through a radially blade centrifugal rotor

In this case some prewhirl was provided to avoid excessive relative angle of attack at the inlet edge. Also shown in Figure 8 is a prediction of the frictionless surface velocity distribution from the program MIXFLO, revealing at the design stage that we would expect very low velocities on the driving surface of the blades and high diffusion rates on the trailing (suction) surface. These phenomena result in the thickening up of the boundary layer on the driving surface and the tendency towards separation on the trailing surface toward the trailing edge due to the excessive diffusions. As explained elsewhere, the remarkable ability of such centrifugal machines to pump with high duty loadings is largely due to the presence of enormous Coriolis accelerations which are automatically included into the present fluid dynamic modelling techniques.

To conclude, it would be of interest to check the flow prediction for this radially bladed rotor for a reduced flow rate chosen deliberately to attempt to obtain a standing eddy on the driving surface. It is well known that even in inviscid flow the presence of the relative eddy or slip flow may become so strong that it will induce such a standing eddy at part load, and the power of vortex dynamics to predict this is illustrated in Figure 9 below.

First of all an inviscid "potential flow" computation has been undertaken to predict the expected surface velocity distribution v_s for ideal flow using the author's design/analysis software MIXFLO and expressing the blade surface velocity as a fraction of the relative inlet velocity V_1 at the leading edge, Figure 9a. As can be seen, in ideal frictionless flow we would expect to observe a standing eddy ($v_s < 0$) over a substantial section of the driving surface. In view also of the heavy diffusion over

(a) Inviscid ideal fluid flow analysis
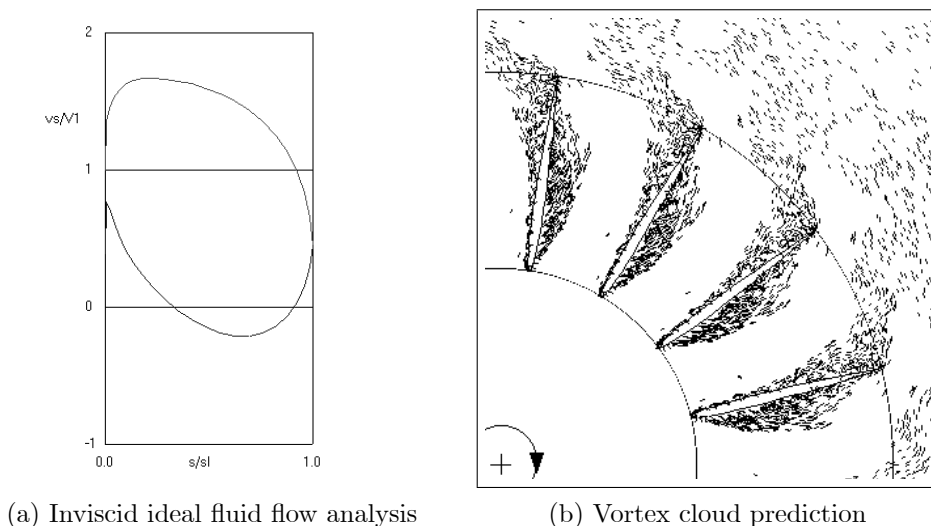

(b) Vortex cloud prediction

Figure 9. Prediction of the presence of a standing eddy in the radially bladed centrifugal compressor at 60% of design flow rate

most of the blade trailing surface, we would also expect there to be stability problems. Both of these phenomena have been very convincingly simulated here by the vortex dynamics technique.

5. Conclusions

The surface vorticity method for simulation of the potential flow past bodies or cascades of arbitrary shape emerged from classical methods as the most natural and powerful numerical model representing, in effect, the infinite Reynolds number flow for which the outer flow is bounded at the body surface by an infinitely thin vorticity sheet. As we have seen, extension of this to the simulation of fully viscous flows is equally natural if the surface vorticity sheet is discretised and shed from the surface as a vortex cloud over a series of discrete time steps, viscous diffusion being modelled by random walks. Application of this to turbomachinery blade rows here has resulted in:

1. Predictions of rotation stall in compressor blade rows.
2. Simulation of blade wake interactions in both turbine and fan or compressor stages.
3. Simulation of the flow through radial fan or compressor rotors including the effects of Coriolis accelerations and "relative eddy".

For practical design purposes the full vortex cloud method may be used in parallel with the simpler surface vorticity potential flow analysis and should always be used in context with more general performance analysis methods such as those which link stage duty (ϕ, ψ) to other well known experimental correlations such as diffusion

factors. It is considered essential for CFD tools to be used wisely in such a broader context, including the theoretical validation and extension of correlations for losses and general performance analysis. As may be seen from the results presented here, the vortex cloud method has proved to be a most valuable simulation technique as part of the designers tool kit.

REFERENCES

1. GLAUERT, H.: *The Elements of Aerofoil and Airscrew Theory*, Cambridge Univ. Press, 1948, 232 p.

2. ACKERET, J.: *Zum Entwurf Dichtstehendes Schaufelgitter*, Schweiz, Bauzeitung, **120**, No. 9, (1942), 103-108.

3. SCHLICHTING, H.: *Calculation of the Frictionless Incompressible Flow for a Given Two-dimensional Cascade (Direct Problem)*. NACA/TIL Misc. **128**, 1–88. Translation from VDI - Forschungsheft **447**, Edition B, Vol. 21, (1955).

4. LEWIS, R.I. and PENNINGTON, G.A.: *Theoretical Investigation of Some Basic Assumptions of Schlichting's Singularity Method of Cascade Analysis.* ARC C.P.813, Min. of Aviation, (1965).

5. MERCHANT, W. and COLLAR, A.R.: *Flow of an ideal fluid past a cascade of blades*, ARC R&M 1893, (1941).

6. GOSTELOW, J.P.: *Potential flow through cascades. Extension to an exact theory.* ARC C.P. 808, (1964).

7. POLLARD, D. and WORDSWORTH, J.: *A comparison of two methods for predicting the potential flow around arbitrary aerofoils in cascade.* ARC C.P. 618, (1963).

8. RAILLY, J.W.: *Ackeret method for the design of tandem cascades. Engineer,* London, **224** (5827), (1965), 405-416.

9. POLLARD, D.: *The extension of Schlichting's analysis to mixed-flow cascades.* Proc. Inst. Mech. Engrs., Vol. 180, (1966), 86-95.

10. SCHOLZ, N.: *Ein Berechnungsverfahren zum Entwurf von Schaufelgitterprofilen.* VDI-Forschungsheft **442**, (1954), 25-48.

11. CZIBERE, T.: *Berechnungsverfahren zum Entwurf gerader Flügelgitter mit stark gewölbten Profilschaufeln.* Acta Technica Acad. Sci. Hung. **28**, (1960), 43-71 & 241-280.

12. CZIBERE, T.: *Über die Berechnung der Schaufelprofile und der Strömung um die Schaufel von Strömungsmaschinen,* Ing. Archiv. 33, (1964), p. 215.

13. CZIBERE, T.: *Über die Berechnung der Schaufelprofile von Strömungsmaschinen mit Halbaxialer Durchströmung.* Acta Techn. Acad. Sci. Hung. **44**, (1963), 149-193.

14. BARANYI, L.: *Determination of the potential plane flow around bodies by means of two solutions belonging to different incidence angles*, Publ. Techn. Univ. for Heavy Industry, Miskolc, Series C., Machinery, **37**(1-2), (1982), 53-63.

15. ROHATYNSKI, R.: *Some general relations between velocities on the singularity carrier curve and velocities along the blade contour*, Publ. Techn. Univ. for Heavy Industry, Miskolc, Series C., Mechanical Engineering, Vol. 42. Fasc. 2-4, (1988), 95-104.

16. MARTENSEN, E.: *Berechnung der Druckverteilung an Gitterprofilen in ebener Potentialströmung mit einer Fredholmschen Integralgleichung,* Arch. Rat. Mech., Anal., **3**,

(1959), 235-270.

17. Smith, A.M.O. and Hess, J.L.: *Calculation of Potential Flow about Arbitrary Bodies*, Prog. Aero. Sci., **8**, Pergamon Press, (1966), 1-138.

18. Jacob, K. and Riegels, F.W.: *The calculation of the pressure distributions over aerofoil sections of finite thickness with and without flaps and slats*, Z.Flugwiss, **11**(9), (1963), 357-367.

19. Wilkinson, D.H.: *A numerical solution of the analysis and design problems for the flow past one or more aerofoils or cascades*, ARC R & M, No. 3545, (1967).

20. Wilkinson, D.H.: *The Analysis and Design of Blade Shape for Radial, Mixed and Axial Turbomachines with Incompressible Flow*, English Electric Co., Whetstone, MEL Rep. No. W/M(3F), (1969).

21. Fisher, E.H.: *Performance of Mixed-Flow Pumps and Fans*, Ph.D. thesis, Newcastle upon Tyne University, (1975).

22. Fisher, E.H. and Lewis, R.I.: *Exact solutions for conical flow rotors*, NEL Rep. No. 498, (1972).

23. Lewis, R.I.: *Surface vorticity modelling of separated flows from two-dimensional bluff bodies of arbitrary shape*, I. Mech. E., Jn. Mech. Eng. Sci., Vol. 23, No. 1, (1981), 1-12.

24. Porthouse, D.T.C. and Lewis, R.I.: *Simulation of viscous diffusion for extension of the surface vorticity method to boundary layer and separated flows*, I. Mech. E., Jn. Mech. Sci., Vol. 23, No. 3, (1981), 157-167.

25. Lewis, R.I.: *Vortex Element Methods for Fluid Dynamic Analysis of Engineering Systems*, Cambridge University Press, 1991, 566 p.

26. Lewis, R.I.: *Turbomachinery Performance Analysis*, Arnold co-published with John Wiley & Sons Inc., 1996, 328 p.

COMPUTATION OF HYDRAULIC FORCES ON A BWR VESSEL AT FEEDWATER PIPE BREAK USING RELAP 5 CODE

Ferenc Müller
ES-konsult Energi och Säkerhet AB
Box 12 049, SE-102 22 Stockholm
`ferenc@eskonsult.se`

Abstract. Pipe breaks are a major consideration when designing electrical power generation plants, especially for nuclear power plants. The most important pipes in nuclear power plants are those which are connected to the reactor vessel. The reactor vessel, its internal parts, and the connected pipes themselves all have to withstand forces generated due to pipe break. In this paper we give some results of the calculated forces on a BWR vessel at feedwater pipe break. The thermohydraulic calculations have been done by using the RELAP 5 code. This code has proven to be appropriate for calculation of hydraulic forces in such a situation.

Keywords: Hydraulic loads, break flow, RELAP 5

1. Introduction

The assumption of a pipe break is a general design basis of electrical power generation plants, especially of nuclear power plants. Forces generated due to pipe break must be withstood by the reactor vessel including its internal parts and the pipes themselves. Pipes connected to the reactor vessel are the most important ones in nuclear power plants. Usually the most severe pipe breaks are the break of those large pipes that are connected to the water filled part of the reactor vessel. These large diameter pipes include the recirculation lines for reactors with external recirculation systems and the feedwater lines for reactors with internal recirculation systems. Figure 1 shows a principal sketch of a boiling water reactor (BWR) and the main pipes connected to the water filled part of the reactor vessel.

In this paper we give some results for forces calculated for a BWR vessel and its internal vessel (called the moderator vessel) at feedwater pipe break.

2. Simulation using RELAP 5 of a pipe break

The RELAP 5 code (<u>R</u>eactor <u>Ex</u>-cursion and <u>L</u>eak <u>A</u>nalysis <u>P</u>rogram) [1] has been continuously developed since the 1970s. Idaho National Engineering Laboratory (INEL) was the first principal code developer contracted by the Nuclear Regulatory Commission (NRC). The latest code development is an international effort called CAMP [2]

and the principal code developer is Information Systems Laboratories (ISL), a San Diego based employee-owned research and development company [3]. ISL acquired the code development contract from SCIENTECH Inc.

The RELAP5/MOD3 computer code uses the two-fluid model, consisting of steam and water, with the possibility of the vapor phase containing a noncondensable component and the liquid phase containing a nonvolatile solute. The two-fluid model means that the code solves the continuity equation, the momentum equation and the energy equations for both the fluid phase and the gas phase. An Eulerian boron-tracking model is used in RELAP 5 that simulates the transport of a dissolved component in the liquid phase. There is a field equation for the conservation of the boron solute. The numerical solution scheme uses results in a system representation using control volumes connected by junctions. A physical system consisting of flow paths, volumes, areas, etc., is simulated by constructing a network of control volumes connected by junctions. Such a representation of a BWR vessel can be seen in Figure 1b.
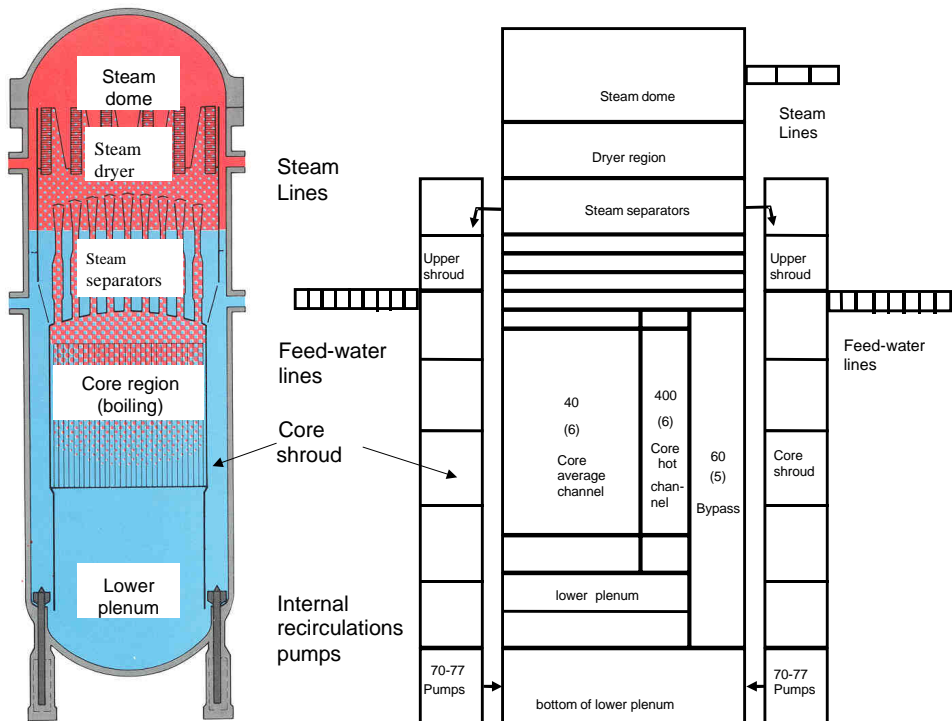

Figure 1. (a) Principle sketch of a BRW with internal recirculation system. (b) nodalization of a BRW vessel for simulations with the RELAP 5 code

The Swedish Nuclear Power Inspectorate for auditing calculations developed the model in Figure 1b. The main purpose for the model was to compute the maximum cladding temperature in the core hot channel with different assumptions on vessel break sizes. Basically this is the model that has been used in our computations. The model has been adapted with some updates to the force calculations.

3. Flow induced forces on pipes and structures

Many investigators [4, 5] have reported the theoretical solutions of unbalanced force on pipes and structures due to blowdown. The basic principles are summarized here. The resultant force acting on a container by the fluid it contains results from two sources (a) the pressure acting on the wetted surfaces of the container, and (b) the friction forces between the fluid and the container acting on the wetted surfaces of the container, i.e.

$$\mathbf{R} = \int_{w.s.} p\mathbf{n}\mathrm{d}s + \int_{w.s.} \boldsymbol{\tau}\mathrm{d}s \tag{3.1}$$

where

$\mathbf{R}$	resultant force acting upon container by fluid,
p	local pressure of fluid,
$\mathbf{n}$	unit vector normal to surfaces, positive outward,
$\mathrm{d}s$	differential surface area,
$\boldsymbol{\tau}$	local shear stress due to friction,
$w.s.$	wetted surface of container.

These forces can be computed by using the well-known momentum equation of fluid mechanics:

$$\mathbf{R} = \int_{w.s.} p\mathbf{n}\mathrm{d}s + \int_{w.s.} \boldsymbol{\tau}\mathrm{d}s = -\int_{c.v.} \frac{\partial}{\partial t}(\mathbf{v}\rho)\,\mathrm{d}V - \int_{inlet,\ outlet} [p\mathbf{n} + \rho\mathbf{v}(\mathbf{vn})]\,\mathrm{d}s - \int_{c.v.} \mathbf{g}\rho\mathrm{d}V$$
$$\tag{3.2}$$

where

$\mathbf{g}$	acceleration vector due to gravity,
$\mathbf{v}$	velocity of the center of mass of the fluid,
ρ	density,
$\mathrm{d}V$	differential volume element,
$c.v.$	control volume,
$inlet$	inflow surface,
$outlet$	outflow surface.

By proper choice of control boundaries, the integrations in equation (3.2) over the inflow and outflow areas can be greatly simplified. Figure 2 shows the situation at feedwater pipe break.

By using the equation for the total mass flow rate

$$\dot{m} = \rho v A \tag{3.3}$$

we can apply equation (3.2) to the situation shown in Figure 2 for computing the resultant force acting on the reactor vessel. Fortunately, for a simple geometry such as that of a pipe with constant cross sectional area like that in Figure 2, the integrations in equation (3.2) can be simplified as

$$R_x = -\left[L\frac{d\overline{\dot{m}}}{dt} + (p_2 - p_a)A + \dot{m}_2 v_2\right] \tag{3.4}$$

where

$\overline{\dot{m}}$ average mass flow rate in the pipe. This can be computed as the sum of the mass flow rates in the feedwater pipe control volumes divided by the number of control volumes

$\frac{d\overline{\dot{m}}}{dt}$ can be computed numerically by RELAP 5 internal control components.

The first term in (3.4) is called wave force, and the second and third terms together are called the blowdown force.
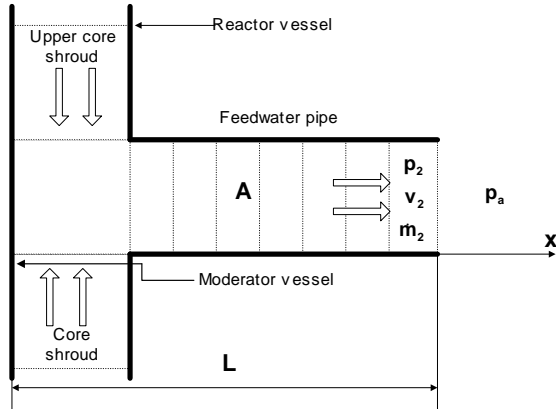

Figure 2. Detailed nodalization at feedwater inlet

The computed reaction force R_x can be correlated to the initial thrust, which is simply the break plane area multiplied by the initial pressure within the pipe. The thrust coefficient C_T is defined by

$$C_T = \frac{R_x}{p_0 A} \qquad (3.5)$$

where A is the break plane area and p_0 is the initial pressure within the pipe. The theoretical maximum value is $C_T = 2.0$ which occurs at steady state frictionless flow of subcooled water.

4. Computational results

According to [7] it is a conservative assumption to assume that the pipe break happens in 1 ms, and the break flow area reaches its maximum at 10 ms. RELAP 5 uses Henry-Fauske's model [6] for two-phase critical flow calculations. The pipe break is modeled by opening a break-valve connected to the pipe. The break-valve area is assumed to increase linearly from zero to the full pipe flow area in 10 ms. The computed flow rate in Figure 3 starts at a negative value, which is the normal feedwater mass flux into the reactor vessel, and reaches its maximum slightly above 8 kg/cm^{2}s at 22 ms.

The initial pressure in the vessel is 7 MPa and the feedwater temperatures are assumed to vary between $453 - 473$ K. The initial pressure in the pipe sinks very
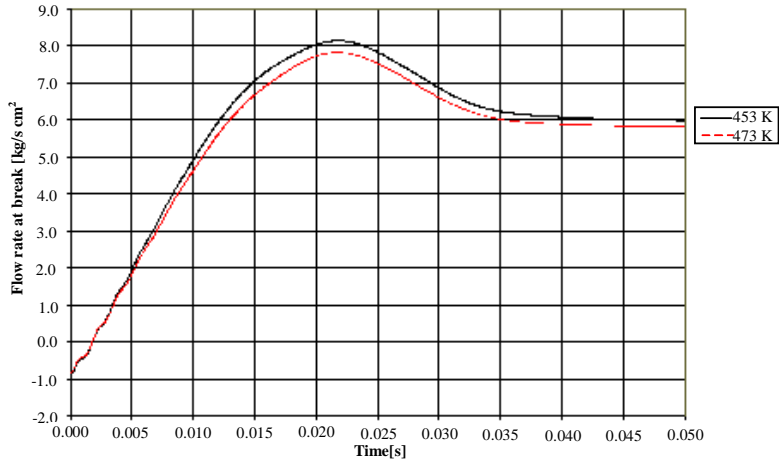
Figure 3. Break location flowrate at different water temperatures in the feedwater pipe
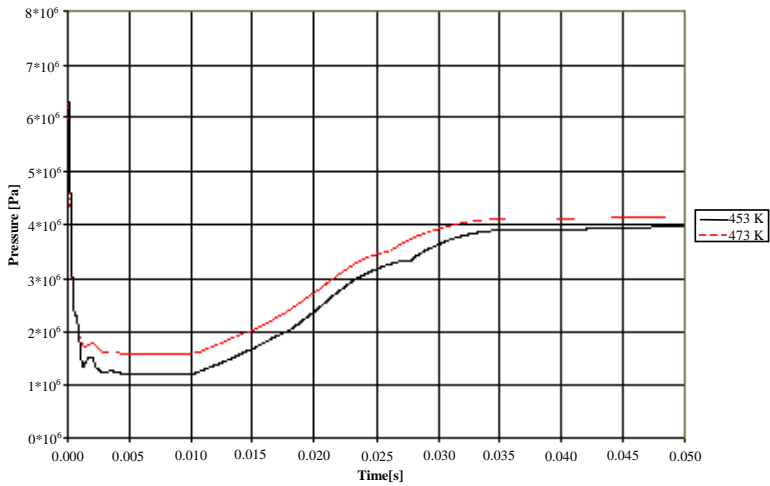

Figure 4. Pressure in the pipe at the break location, as function of time and water temperature

rapidly starting from the break location, as it is shown in Figure 4.

The computed forces (Figure 5) have an initial frequency, which is determined by the length of the remaining pipe attached to the vessel. These oscillations
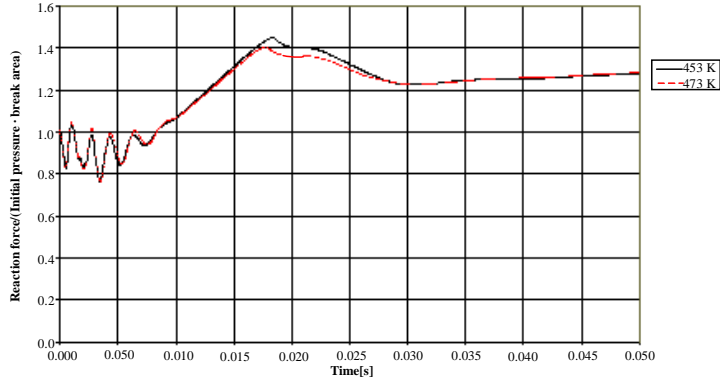
Figure 5. Computed thrust coefficient, C_T, as function of feedwater temperature and time
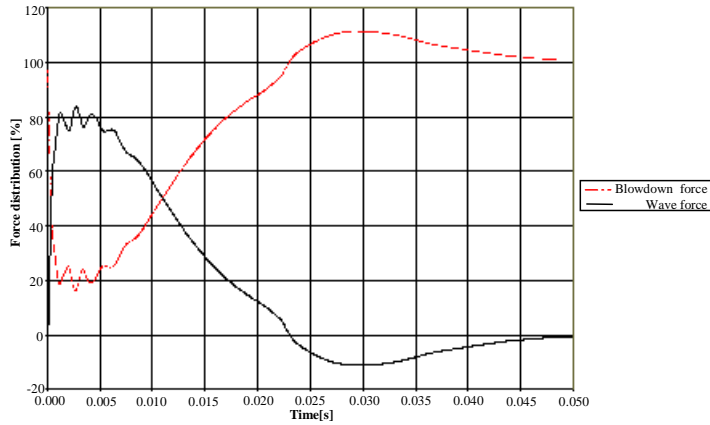

Figure 6. Distribution of the total force between "blowdown-" and "wave" forces as function of time

are attenuated very rapidly with the increasing void and decreasing speed of sound in the two-phase mixture. Finally Figure 6 shows the variations of the computed blowdown- and wave forces equation – see equation (3.4).

5. Conclusions

The paper demonstrates an application of the RELAP 5 code for computing global hydraulic loads due to a feed water pipe break at a nuclear boiling water reactor system. These computed hydraulic loads should be used for design of the reactor vessel and piping support structures. The computed loads have been evaluated against the theoretical maximum of such loads and are found to be within the theoretical limits.

This code has proven to be appropriate for calculation of hydraulic forces in such a situation.

REFERENCES

1. RELAP 5, Reactor Ex-cursion and Leak Analysis Program, `www.nrc.gov/RES/RELAP5/`

2. CAMP, Code Applications and Maintenance Program, `www.nrc.gov/RES/camp/`

3. Information Systems Laboratories (ISL), `www.islinc.com/`

4. MOODY F.J.: *Time-dependent pipe forces caused by blow-down and flow stoppage*, Journal of Fluids Engineering. Trans. ASME., **95**(3), (1973), 422-428.

5. LEE, M.Z., CHOU, L.Y. and YANG, S.H.: *PWR Safety/relief valve blowdown analysis experience,* Nuclear Engineering and Design, **72**, (1982), 421-427.

6. HENRY, R.E. and FAUSKE, H.K.: *The two-phase critical flow of one-component mixtures in nozzles, orifices and short tubes*, Journal of Heat Transfer, **93**, (1971), 179-187.

7. American National Standard. *Design basis for protection of light water nuclear power plants against the effects of postulated pipe rupture*, ANSI/ANS-58.2-1988.

VELOCITY DISTRIBUTIONS IN SMALL HYDRAULIC TURBINES

Miroslava Nagyová

Department of Power Engineering, Technical University of Košice
041 87 Košice, Letná 9, Slovakia
nagyovam@tuke.sk

Abstract. The paper presents some results of turbine investigations which can be utilized at small hydroelectric power plants. The influence of turbine runner and blade shapes on the velocity distributions in turbine channels based on calculations of various types of turbines is considered here. The analysis of individual solutions gives a description of their advantages and disadvantages for other utilization.

Keywords: Water turbine, turbine runner, velocity field

1. Introduction

The Department of Power Engineering has been concerned with the development of hydraulic turbines for small and micro hydroelectric power plants since its establishment [1], [2]. The aim of this research is the design and production of turbines which are simple from constructional points of view. This requirement is preferred because of lower investment costs of building these hydroelectric power plants.
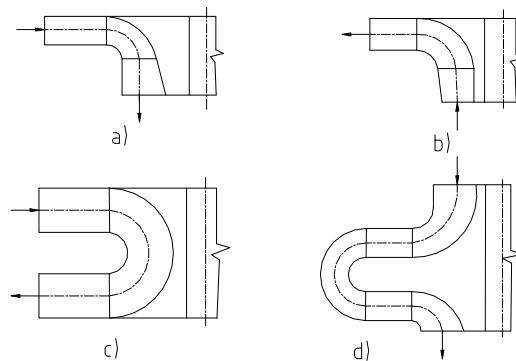

Figure 1. Types of turbines according to flow directions at inlet and outlet a) radial-axial b) axial-radial c) radial-radial d) axial-radial

The basic idea of simple turbine design is to divide complicated three-dimensional blades into two parts with a bladeless channel between them. It was assumed that the above mentioned simplification enables us to solve the problem of flow in these types

of turbines using mathematical formulas available for two-dimensional flows. Basic types of new hydraulic turbines according to flow directions at inlet and outlet are illustrated in Fig. 1.

2. Description of investigation of turbine types

The basic research is concentrated on the investigation of radial-axial hydraulic turbine with parallel channel walls in both stages – see Figure 2. Laboratory measurements were carried out on turbine models with diameter D_1=0.4 m and D_1=0.153 m. A turbine model with diameter of turbine runner D_1=0.4 m is illustrated in Figure 3.
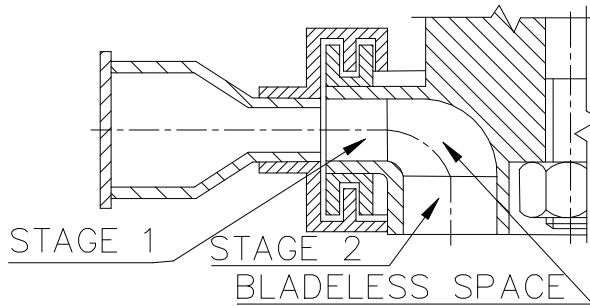

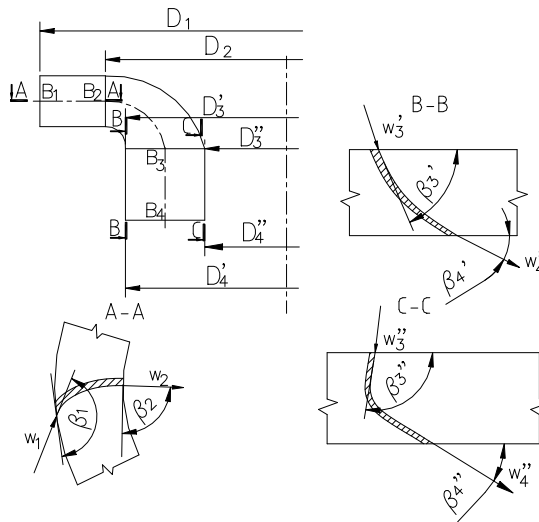Figure 2. Arrangement of the basic turbine type

Figure 3. Turbine model

The model parameters are as follows:

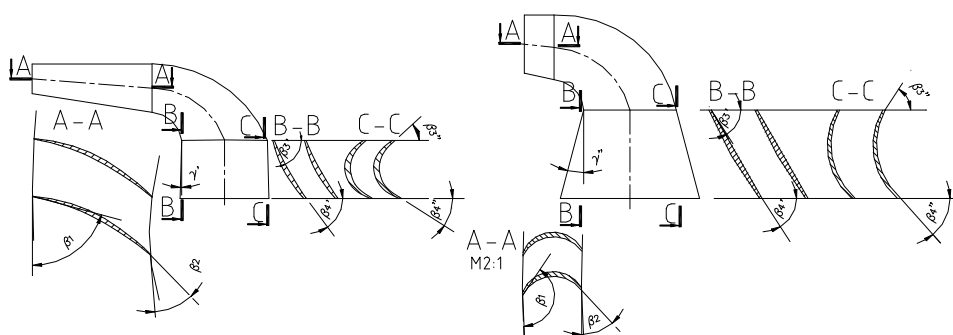|			
D_1=0.4 m	β_1=120°	D_2=1.8 m	β_2=74°
D_3'=D_4'=0.34 m	β_3'=82°	D_3''=D_4''=0.28 m	β_4'=31°
B_1=B_2=0.02 m	β_3''=118°	B_3=B_4=0.03 m	β_4''=35°

Figure 4. Scheme of turbines with extremely long and highly curved blades

The theoretical investigation of other types of turbines has been done in addition to the above mentioned basic type. The turbine runners with extremely long and highly curved blades on radial stage are presented in Fig. 4.

The calculations of velocity and pressure distributions ([3], [4]) were performed for these types of turbines. The results of calculations are utilized for the qualification of other turbines.

3. Results

Measured and calculated values of efficiency for turbine model with diameter D_1=0.153 m as well as calculated values of efficiency for turbine model with parallel channel walls in both stages with diameter D_1=0.4 m are illustrated in Fig. 5.
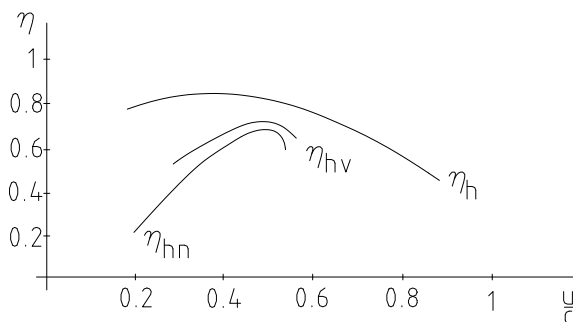

Figure 5. Curves of efficiency on turbine models

Notations:

η_{hv} calculated efficiency for a model with diameter D_1=0.153 m
η_{hn} measured efficiency for a model with diameter D_1=0.153 m
η_h calculated efficiency for a model with diameter D_1=0.4 m

The "MESH" method" was used for the calculations of the velocity field for the basic turbine type. A detailed description of the calculation process is given in [4].

This method is of sufficient accuracy for choosing the turbine type when appropriate choice of mesh nodal points and correct implementation of boundary conditions is ensured. More precise results can be obtained by using the Finite Element Method (for example by the program COSMOS/M). First of all it is necessary to evaluate preliminary results and to select the appropriate turbine type. Only after doing that can we continue with the simulation of turbine runner and also with the investigation of flow processes. The results of velocity calculations on the suction and pressure sides of the blades and also in the middle of the channel between the blades achieved by the method of Lakatos [5] in various sections according to Figure 6, are presented in Figure 7.
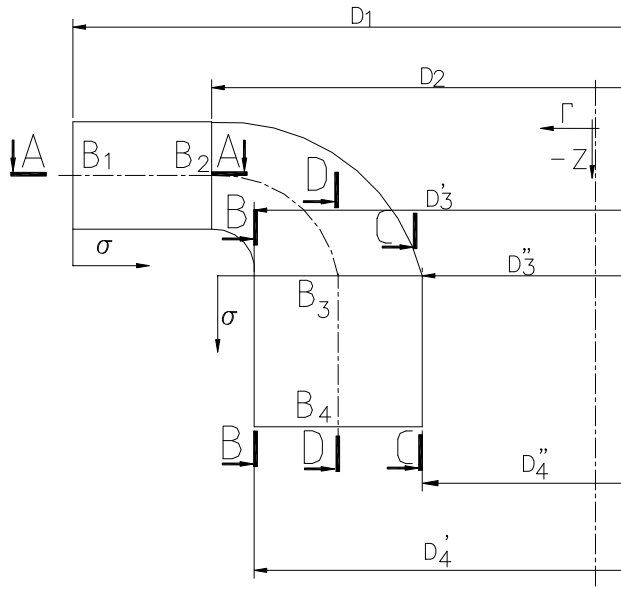

Figure 6. Sections on turbine runner

Notations:

A-A	$\Psi^* = 0.50$ - Stage 1
B-B	$\Psi^* = 0.05$ - Stage 2
C-C	$\Psi^* = 0.95$ - Stage 2
D-D	$\Psi^* = 0.50$ - Stage 2
	where Ψ^* is the non-dimensional Stokes stream function
r, z	cylindrical coordinates
σ	curvilinear coordinate in streamline direction
B_1, B_2, B_3, B_4	channel widths

Velocity curves for turbine with extremely long blades on radial stage (Figure 4a) are illustrated in Figure 8, particular sections are shown in Figure 6. Velocity curves for highly curved blades in the same sections are illustrated in Figure 9.
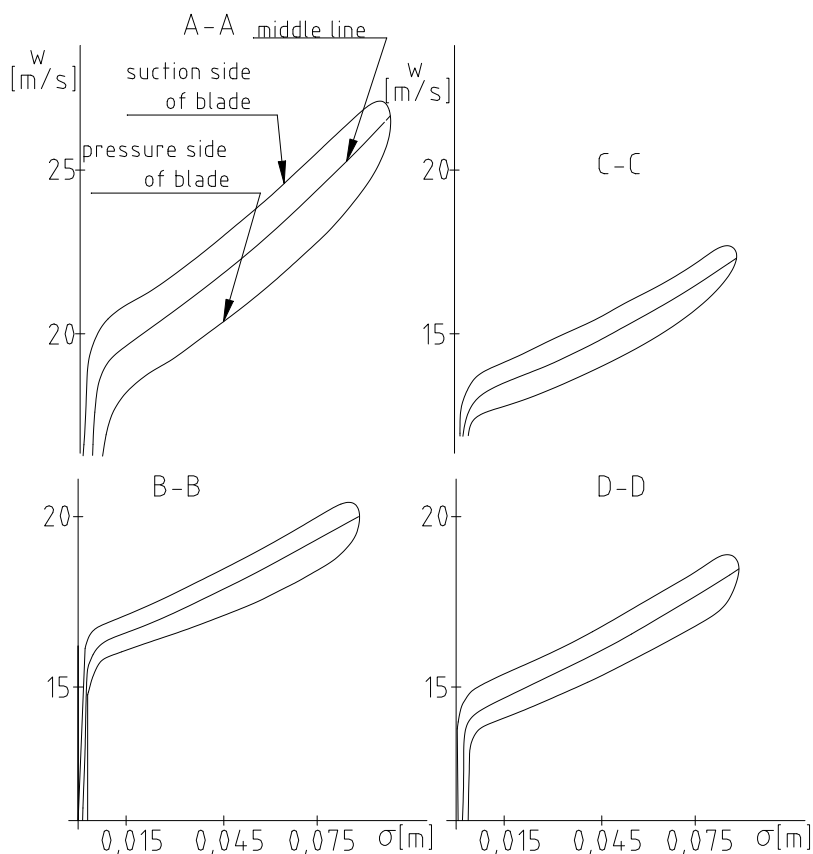
Figure 7. Velocity distributions

4. Evaluation of results

The analysis of results achieved up to the present time shows the following:

- for laboratory research of individual turbine types the model with the turbine runner diameter $D_1=0.4$ m is more suitable than the one with diameter $D_1=0.153$ m because of the better agreement between the measured and calculated results;
- the channel with non-parallel walls and with extremely long blades on radial stage is not appropriate because one part of the turbine runner blades works as a pump and the losses are increased;
- the extremely curved blades on radial stage enable the appropriate distribution of energy in both stages but their manufacture is complicated;
- the basic type of turbine with parallel channel walls in both stages is more appropriate from a productional point of view than the latter one, but the energy utilization is not the best.
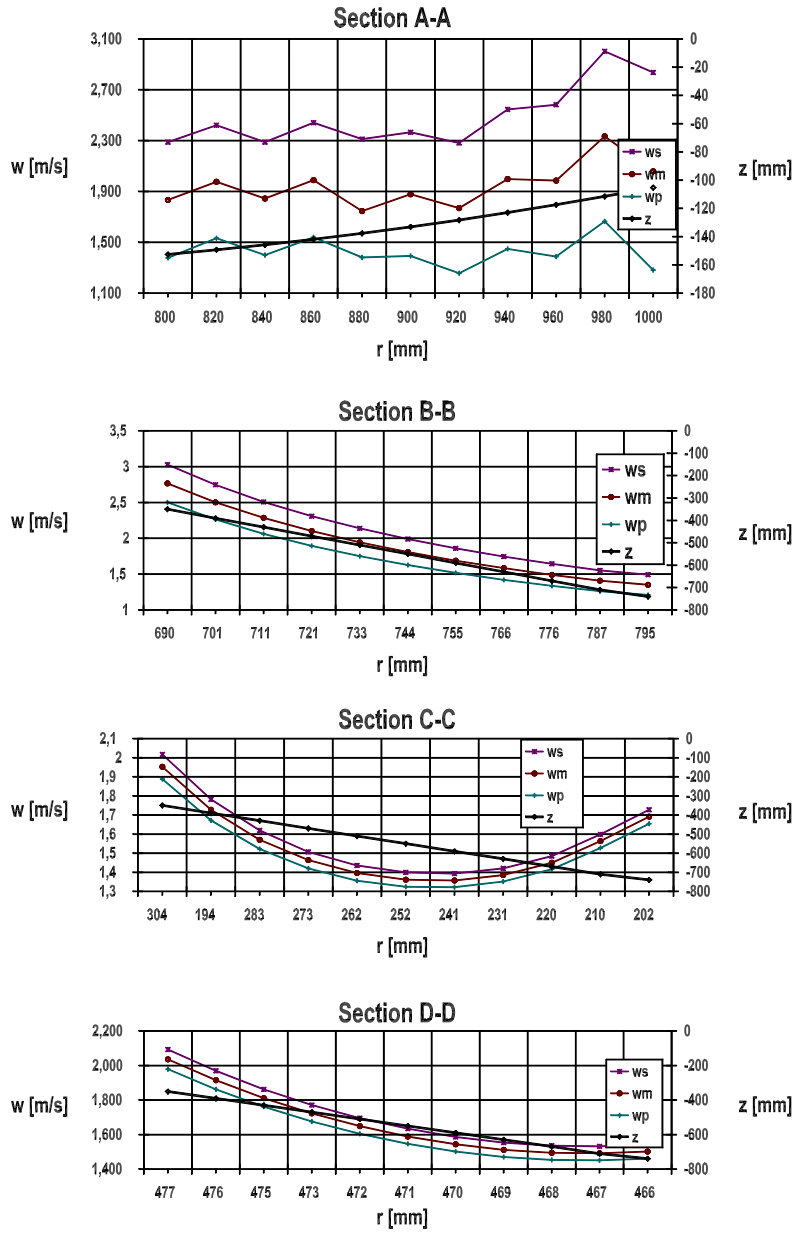
Figure 8. Velocity curves for extremely long blades

Notations:

w_m middle line between blades
w_p pressure side
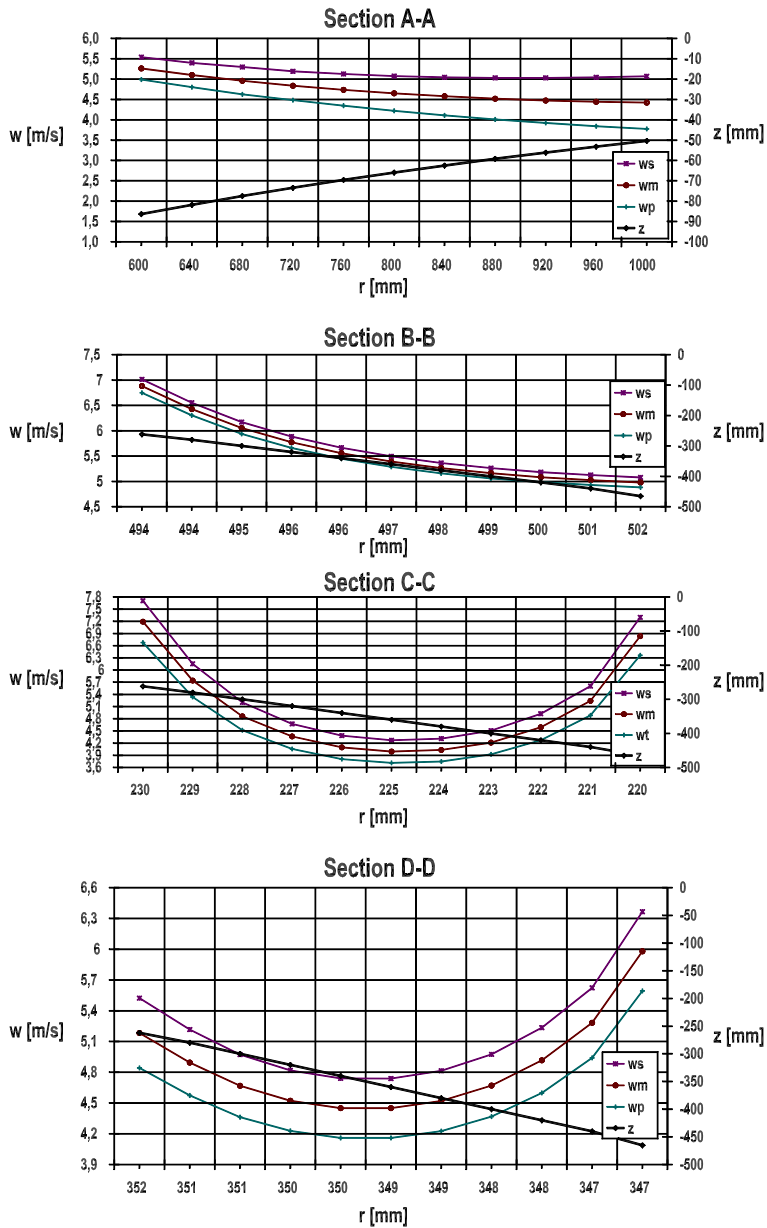w_s suction side
z coordinate

Figure 9. Velocity curves for highly curved blades

Notations:

w_m	middle line between blades
w_p	pressure side
w_s	suction side
z	coordinate

5. Conclusions

On the basis of the achieved results we can see, that the more appropriate type of turbine is the one shown in Figure 4b. Simplification in production process can be attained by changing the blade length in the radial stage because the curvature of the blades will be small. The distribution of energy gain between the stages can be controlled by changing the channel wall bevel angle and that of the blade length. A turbine efficiency of about 75 % can be achieved by optimization of the above mentioned parameters.

The production costs of these turbine types are very low in comparison with traditional turbines such as Francis and Girard turbines (about 30 %). This saving ensures refunding of investment for a small hydroelectric power plant in a relatively short time assuming relatively high efficiency.

The aim of the research by members of Department of Power Engineering is to design several new turbine types for small and micro-hydroelectric power plants. These types made the simple selection of appropriate turbine type for varied conditions according to the water flow and head, possible. The results of this project will be used in a future investigations.

REFERENCES

1. HOSSZÚRÉTY, Z.: *Principle and functional properties of radial-axial two-stage turbine*, Mechanical Engineering Journal of SAV a ČSAV, **38**(3), (1987), 73-77. (in Slovakian)

2. MOLNÁR, V. AT AL.: *Research of Two-Stage Hydraulic Turbines*, Research report, STU Bratislava 1993. (in Slovakian)

3. NAGYOVÁ, M.: *Calculation of speed field in two-stage hydraulic turbines by method of Lakatos*, IV. International Conference on „Energy transformations in industry", 224-227, September 11-13, 1994, Herľany. (in Slovakian)

4. NAGYOVÁ, M. and NAGY, E.: *Calculation of speed field in radial-axial turbine for extremely long blades by MESH method*, International Conference on „Mechanical Engineering '97", 342-346, October 24, 1997, Bratislava. (in Slovakian)

5. LAKATOS, K.: *The calculus regarding the small turbine runner with double blades*, Symposium Ecological Small Hydro Power Social and Economic Impact, 88-95, October 5-7, 1993, Timisoara, Romania.

6. NAGYOVÁ, M.: *Exploitation of radial-axial hydraulic turbine in small hydroelectric power plant*, International Conference on „Effective Production, Transmission and Consumption of Energy", 119-123, November 9-10, 1999, Herľany. (in Slovakian)

7. NAGYOVÁ, M. and NAGY, E.: *Innovation of constructional solution of hydraulic turbine*, XLI. International Conference of Departments of Machine Elements and Mechanisms, 230-233, September 6-8, 2000, Herľany. (in Slovakian)

VORTEX-INDUCED VIBRATION OF THE UPSTREAM CYLINDER OF A TWO-CYLINDER SYSTEM IN CRUCIFORM ARRANGEMENT

Masataka Shirakashi[1], Tsutomu Takahashi[1], Isao Kumagai[1] and Tsuyoshi Matsumoto[2]

[1]Nagaoka University of Technology, Department of Mechanical Engineering, [2]Mitsubishi Heavy Industry Co. Ltd

1603-1 Kamitomiokamachi, Nagaoka, 940-2188 Japan

`kumapu@stn.nagaokaut.ac.jp`

Abstract. Comprehensive wind tunnel experiments are carried out on the longitudinal vortex excitation of the upstream cylinder in a cruciform two-cylinder system. The vortex structure around the crossing is dominated by the ratio of gap s to the downstream cylinder diameter d_2, i.e., the trailing vortices shed when $s/d_2 < 0.25$ and the necklace vortices shed when $0.25 < s/d_2 < 0.7$. Based on measurements under variable damping factor, criteria for occurrence of the longitudinal vortex excitations are presented and substantial alternating lift coefficients are proposed for them to estimate the excitation force. These results are of practical importance to predict and to avoid these newly found vortex excitations.

Keywords: Vortex excitation, cruciform arrangement cylinders, longitudinal vortex, scruton number, alternating lift coefficient.

1. Introduction

It is well known that nearly two dimensional vortices shed alternately from both sides of a cylindrical body set in a uniform flow, which form two arrays of vortices in a staggered arrangement in the wake, i.e., Kármán's vortex street [1]-[4]. Since the periodic shedding of Kármán vortex can induce large cross-flow oscillation and/or sound emission which are usually undesirable from the practical point of view, numerous works have been carried out to control the Kármán vortex shedding and in turn the sound and oscillation. Inspired by Tomita et al.'s work [5] on sound depression effect of another cylinder set downstream in a cruciform arrangement as shown in Figure 1, the present authors investigated the oscillation suppressing effect of the downstream cylinder in the same arrangement [6]-[9]. Although the Kármán vortex excitation was eliminated when the cylinder diameters were equal and the gap between the cylinders was less than half the cylinder diameter, a new oscillation was found to occur over a certain velocity range around three times higher than the Kármán vortex excitation [6]. Recent investigations showed that the newly found oscillation is caused by one of two types of vortices which shed periodically around the crossing of the two cylinders, as seen in Figure 2 [7],[10],[11]. They are classified into longitudinal vortices since they have axes parallel to the free flow. Each of them is referred to as the *Trailing vortex* (Figure 2(a)) and the *Necklace vortex* (Figure 2(b)) according to their geometry.

Since very few works have been carried out on these longitudinal vortices and little is known about their nature concerning the vortex excitation yet, it is a problem of practical importance to clarify the characteristics of these longitudinal vortices and to know the conditions under which the longitudinal vortex shedding occurs, and to establish a way to predict the oscillation amplitude for given conditions.

Therefore, the objectives of this work are to obtain understanding of the global nature of the longitudinal vortices, to find a criterion for the occurrence of the vortex excitation and to estimate the exciting force due to the longitudinal vortices, based on comprehensive wind tunnel experiments.
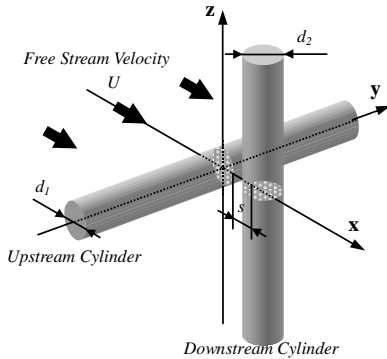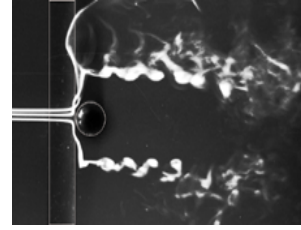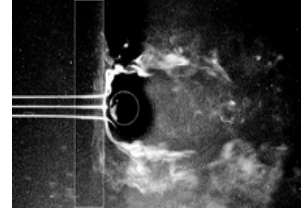

(a) Trailing vortex (*U*=12.8cm/s, *s/d*=0.08, *Re*=860)

(b) Necklace vortex (*U*=12.5cm/s, *s/d*=0.28, *Re*=900)

Figure 1. Arrangement of two cylinders and coordinate system.

Figure 2. Photographs of longitudinal vortices shedding from two cylinders in cruciform arrangement. (in water tunnel, $d = d_1 = d_2 = 10$mm)

2. Nomenclature

A	oscillation amplitude of the upstream cylinder $= \sqrt{2} \cdot Z_{rms}$
$(C_L)_{rms}$	fluctuating lift coefficient, equation (4.1)
$(C_L)'_{rms}$	substantial fluctuating lift coefficient, equation (4.2)
$(C_{LR})_{rms}$	alternating lift coefficient, equation (4.4)
$(C_{LR})'_{rms}$	substantial alternating lift coefficient, Equation (4.5a, 4.5b)
d	cylinder diameter in case of identical cylinder system, i.e. $d = d_1 = d_2 = 26mm$
f	frequency
f_c	oscillation frequency of the upstream cylinder
f_n	natural frequency of the elastically supported upstream cylinder

f_v	vortex shedding frequency
f_{v0}	vortex shedding frequency from a fixed system
l	effective length of cylinder
Re	Reynold's number defined by $Re = U \cdot d_1 / \nu$, where ν is the kinematic viscosity of air
s	gap between cylinders
Sc	Scruton number defined by equation (4.3)
St	Strouhal number for the vortex shedding frequency defined by $St = f_v \cdot d_1 / U$
St_0	Strouhal number for the fixed system defined by $St_0 = f_{v0} \cdot d_1 / U$
St_2	Strouhal number referred to d_2
S_L, Su	spectrum of lift force and velocity, respectively
Su_{AB}	cross spectrum of velocities detected at two positions A and B
$(Su_{AB})_{peak}$	maximum peak value of Su_{AB}
U	free flow velocity
U_0	the free flow velocity at which $f_{v0} = f_n$
Z_{rms}	root-mean-square value of z-displacement of the upstream cylinder
δ	logarithmic damping factor

3. Experimental apparatus and procedures

The arrangement of the two cylinders, the coordinate system and symbols used in this paper are shown in Figure 1. The wind tunnel is a blow down type. The maximum attainable velocity is 40 m/s and the turbulence intensity is less than 0.4% at 10 m/s. The measuring section is 320 mm∗320 mm in cross-section and 1000 mm in length. The upstream cylinder is set horizontally and perpendicularly to the free flow at the center of the measuring section. It passes through the slots on the sidewalls of the measuring section. End plates are fixed on the cylinder near both ends to avoid flow through the slots. The downstream cylinder is fixed vertically on a traverse device so as to make the gap s adjustable within an error of 0.01 mm. On the details of the apparatus, see [6].

The diameter of the downstream cylinder d_2 is varied from 18 mm to 32 mm, while the upstream cylinder diameter d_1 is fixed at 26 mm. The effective length l of the cylinder, i.e. the distance between the two end plates, is also fixed at 318 mm. Experiments are conducted first for a system with two identical cylinders, i.e. $d_1 = d_2$, and then influence of the diameter ratio d_2/d_1 is investigated. Hence, the diameters of both cylinders are simply denoted as d when the two cylinders are identical. In the following sections the diameters of both cylinders are equal at 26 mm whenever d is used as the cylinder diameter.

The upstream cylinder is fixed rigidly, or supported elastically by plate springs outside the measuring section. In the latter case, the motion of the elastically supported cylinder is almost purely translational in vertical ($z-$) direction. An eddy-current damper is applied to the elastically supported system to adjust the logarithmic damping factor δ from 0.008 to 0.2. The natural frequency f_n of the elastic system and the damping factor are determined from a free damping oscillation experiment in other-

wise quiescent air. A mechanical oscillator is used to oscillate the upstream cylinder sinusoidally in vertical direction with an arbitrary amplitude and frequency.

The free flow velocity U is measured by a ring type Kármán vortex velocimeter developed in the present authors' laboratory [12].

Hot wire anemometry is applied to detect u, the x-component of velocity fluctuation. Two hot wire probes, probe A and B, are set at opposite sides of the upstream cylinder near the crossing to detect the velocity fluctuation caused by the periodic vortex shedding. The positions of probes are determined by moving them to find places where the fluctuation component due to the longitudinal vortex shedding is most clearly discerned. The probe positions thus determined depend on the conditions such as the gap-to-diameter ratio and the downstream cylinder diameter, as indicated in the captions of figures. The vortex shedding frequency f_v is determined from the cross spectrum Su_{AB} of two velocity signals u_A and u_B. The relative peak height of Su_{AB} at f_v is considered to be a measure of the strength or regularity of the vortex, although that value of the height itself has no significance. By using the cross spectrum and its peak value, phenomena concerning the longitudinal vortices are discerned more definitely than only to depend on one velocity signal as applied so far.

The displacements at both ends of the upstream cylinder are measured by a non-contacting laser beam displacement detector within an error of 0.1 mm over a range of 0-13 mm.

The lift force acting on the fixed upstream cylinder is measured using a strain-gauge type load-cell.

4. Results and discussion

4.1. Characteristics of longitudinal vortices shedding from fixed system

4.1.1. *Influences of gap-to-diameter ratio and Reynolds number for identical-cylinder system.* In this section, results obtained for a system with an equal diameter two cylinders, i.e. $d_1 = d_2 = 26$ mm $(=d)$, are presented. Figure 3 shows the cross spectra of velocities detected at two positions around the crossing of the cylinders for various values of the gap-to-diameter ratio s/d under a fixed velocity. The two probe positions A and B are symmetrical with each other about the $x-y$ plane. Note that these probe positions are selected because they are most suitable to detect the periodic shedding of the respective longitudinal vortices. It is clearly seen that the shape of cross spectrum Su_{AB} and the peak frequency are definitely different between two regions of s/d, noted as the region T $(s/d = 0-0.25)$ and the region N $(s/d = 0.25-0.64)$. Strouhal numbers of these peak frequencies correlate well with those confirmed for the longitudinal vortex shedding frequencies based on various measurements, including counting the vortex shedding in the visualized flow, as shown in Figure 2.

The vortex shedding frequency f_{v0} is determined as the highest-peak frequency of Su_{AB}. In Figure 4 the Strouhal number St_0 for the vortex shedding frequency f_{v0} is plotted against s/d for various Reynolds numbers. The abrupt change at $s/d = 0.25$

observed in the earlier works is confirmed more clearly in this figure. The $St_0 - s/d$ curve of the trailing vortex ($s/d < 0.25$) has an irregular shape and depends largely on the Reynolds number in a somewhat incoherent way, while that of the necklace vortex ($s/d > 0.25$) collapses on a single curve. The maximum value of s/d for the necklace vortex shedding is shown to be 0.7, which is considerably larger than in the earlier works.

The peak value of Su_{AB} at f_{v0} is plotted against s/d in Figure 5 for various values of free flow velocity U. It is confirmed again in this figure that $s/d = 0.25$ is the boundary value separating the trailing vortex region and the necklace vortex region. In the earlier works by the authors, $s/d = 0.08$ and $s/d = 0.28$ were used as the representative values for the trailing vortex and the necklace vortex since the shedding of the two vortices were observed to shed most regularly at these values of s/d [8]. Since $(Su_{AB})_{peak}$ in Figure 5 has the local maximum value for these values of s/d in the respective regions, these s/d values are selected also in this work as the representatives for the two longitudinal vortices.
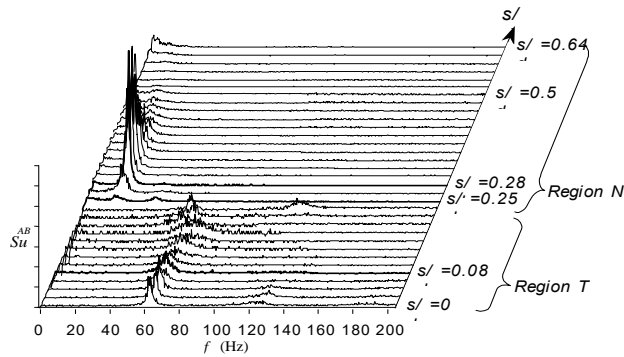

Figure 3. Cross-spectra of velocities at two locations around the crossing for various values of s/d. ($U = 8.0\ m/s, Re = 14,000$) Probe position: Region T ($x/d = 0.5,\ y/d = -1.25,\ z/d = 0.5\ or -0.5$) Region N ($x/d = 0.5,\ y/d = -0.75,\ z/d = 0.5 or -0.5$)

Strouhal numbers for the two longitudinal vortices at the above representative s/d values are plotted against Reynolds number in Figure 6, where the ranges of the results reported so far are compared. The Strouhal number for the necklace vortex increases continuously with Re when $500 < Re < 5,000$ and attains at a value around 0.04, then decreases very gradually up to $Re = 40,000$. Meanwhile, the Strouhal number for the trailing vortex increases with Re over the whole Re range of measurement, and has a discontinuous jump at Re around 5,000.

The results in this section as shown in Figures 3, 4 and 6 show the different natures of the two longitudinal vortices. The structure of flow near the crossing is definitely decided by the gap-to-diameter ratio, i.e., the trailing vortices shed when $s/d < 0.25$

and the necklace vortices when $0.25 < s/d < 0.7$ over a wide range of Reynolds number Re. The necklace vortex has a regular and definite nature in that the Strouhal number St_0 is nearly constant over the Reynolds number range 5,000 to 40,000 and that $St_0 - s/d$ data for various Re collapse on a single curve which decreases gradually with s/d. In contrast, St_0 for the trailing vortex increases from 0.02 to 0.09 in the same Re range, and the $St_0 - Re$ curve has a discontinuous jump at around $Re = 5,000$. The change of St_0 with s/d is quite large and irregular, and the influence of Re on the $St_0 - s/d$ relationship is not coherent. Besides, the peak value of the cross spectrum for the trailing vortex is usually lower than that for the necklace vortex as seen in Figure 3, showing that the periodicity of the trailing vortex shedding is less than that of the necklace vortex.
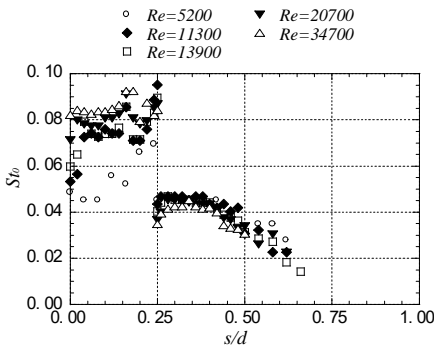

Figure 4. Relationship between Strouhal number and gap-to-diameter ratio for various Reynolds numbers for longitudinal vortices. (fixed system, $d = d_1 = d_2 = 26\ mm$)
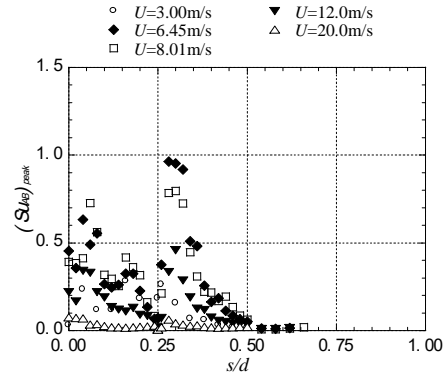
Figure 5. Peak values of cross-spectrum vs. gap-to-diameter ratio. (fixed system, $d = d_1 = d_2 = 26$ mm)

4.1.2. *Influence of diameter ratio.* Figure 7 shows the vortex shedding frequency f_{v0} plotted against the downstream cylinder diameter d_2 in a system where the two cylinders are not identical. While f_{v0} of the necklace vortex at a fixed free flow velocity decreases with d_2 for all the values of the gap, there was found no systematic tendency in the influence of d_2 on f_{v0} on the trailing vortex. Taking this behavior of the necklace vortex into consideration, the downstream cylinder diameter is taken as the reference length to define the Strouhal number, i.e. $St_2 = f_{v0} \cdot d_2/U$. In Figure 8, St_2 is plotted against the gap s divided by d_2 for several diameter ratios. In this figure it is clearly seen that St_2 changes abruptly at $s/d_2 = 0.25$, and the $St_2 - s/d_2$ relation is clearly different between the two regions bounded by this value of s/d_2, like in Figure 4 for the identical cylinder system. This result suggests that the downstream cylinder diameter has the decisive effect on the vortex structure around the crossing. However, St_2 plotted against s/d_2 scatters largely for the trailing vortex ($s/d_2 < 0.25$) and does not collapse well on a single curve for the necklace vortex ($0.25 < s/d_2 < 0.5$).
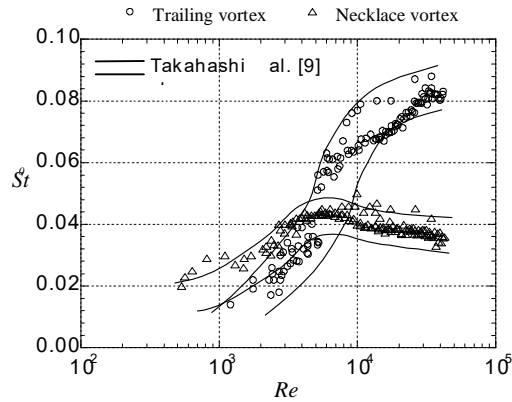
Figure 6. Relationship between Strouhal number and Reynolds number for the longitudinal vortices. (fixed system, $d = d_1 = d_2 = 26$ mm) Trailing vortex : $s/d = 0.08$, Necklace vortex : $s/d = 0.28$
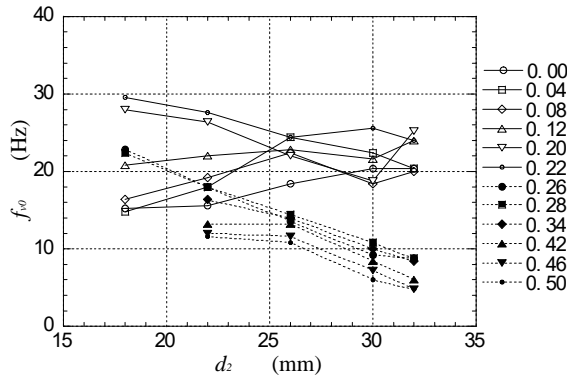

Figure 7. Relationship between the vortex shedding frequency and the downstream cylinder diameter. (fixed system, $U = 8.0\ m/s,\ Re = 14,000$)

To see the span-wise size of the longitudinal vortices, a hot wire probe is moved parallel to the upstream cylinder axis. Figure 9 shows the spectrum Su of the velocity detected by the probe for the identical cylinder system at various values of y/d. The gap is set at the representative values for (a) the trailing vortex and (b) the necklace vortex. In Figure (a), near the downstream cylinder, say $y/d < 2.4$, Su has the highest peak corresponding to the trailing vortex, and the maximum value of y/d at which the trailing vortex peak is observed is $y/d = 3.2$. At larger values of y/d, the Kármán vortex peak becomes dominant in a spectrum. From this figure, the span-wise extent of the trailing vortex is estimated around $y/d = 3.2$, as indicated in the figure as R_T. The span-wise extent R_N of the necklace vortex is also determined in

the same manner from Figure 9(b). R_T and R_N thus obtained are regarded as the measures of the span-wise size of the trailing and the necklace vortices, respectively. It is confirmed that R_T is considerably larger than R_N as observed in the photographs
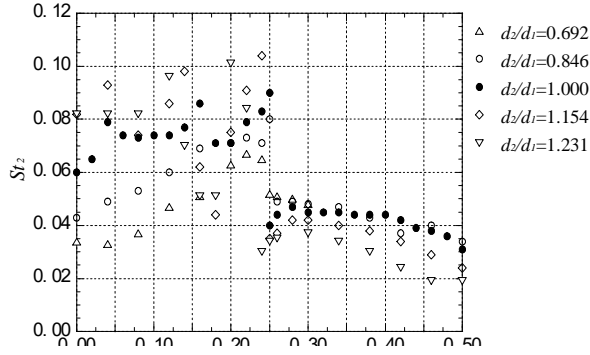

Figure 8. Relationship between Strouhal number and gap-to-diameter ratio referred to the downstream cylinder diameter. (fixed system, $U = 8.0$ m/s, $Re = 14,000$)
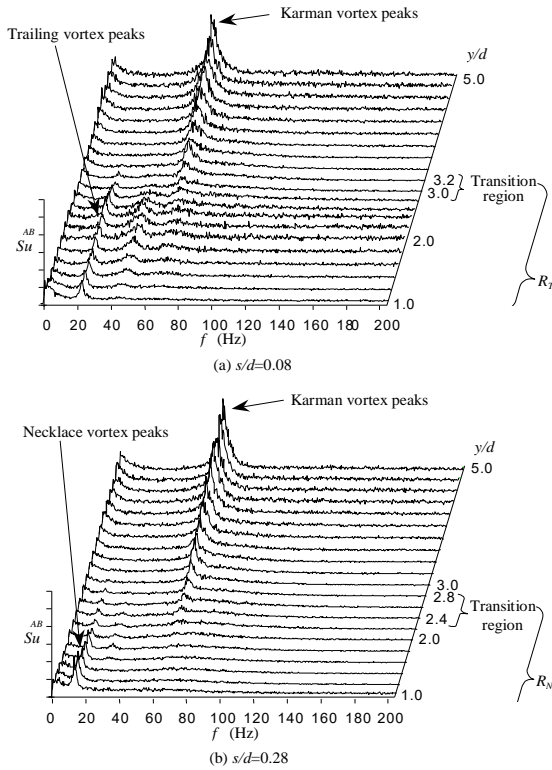

Figure 9. Variation of linear spectrum of velocity along the span wise direction of upstream cylinder. (fixed system, $d = d_1 = d_2 = 26$ mm, $U = 8.0$ m/s, $Re = 14,000$)

of the visualized vortices in Figure 2. Measurements on systems with various d_2/d_1 show that the span wise size of the two longitudinal vortices are roughly proportional to the downstream cylinder diameter.

4.1.3. *Fluctuating lift force acting on the upstream cylinder.* Oscillograms of the fluctuating lift force acting on the upstream cylinder in the identical cylinder system and its spectrum S_L are shown for $s/d = 0.08$, 0.25 and 0.28 in Figure 10. Velocities at the two reference positions, u_A and u_B, were measured simultaneously. At $s/d = 0.08$ and 0.28, a dominant frequency component is observed and the frequency of this dominant component is shown to coincide with the vortex shedding frequency f_{v0} determined from the velocity cross spectrum Su_{AB} for the respective values of s/d. At $s/d = 0.25$, two peaks appear in S_L corresponding to the trailing and the necklace vortices. The oscillogram shows that the two vortices shed not simultaneously but alternately at $s/d = 0.25$.

The lower peak in S_L at $f = 75$ Hz which appears for the three values of s/d is due to the Kármán vortex shedding.
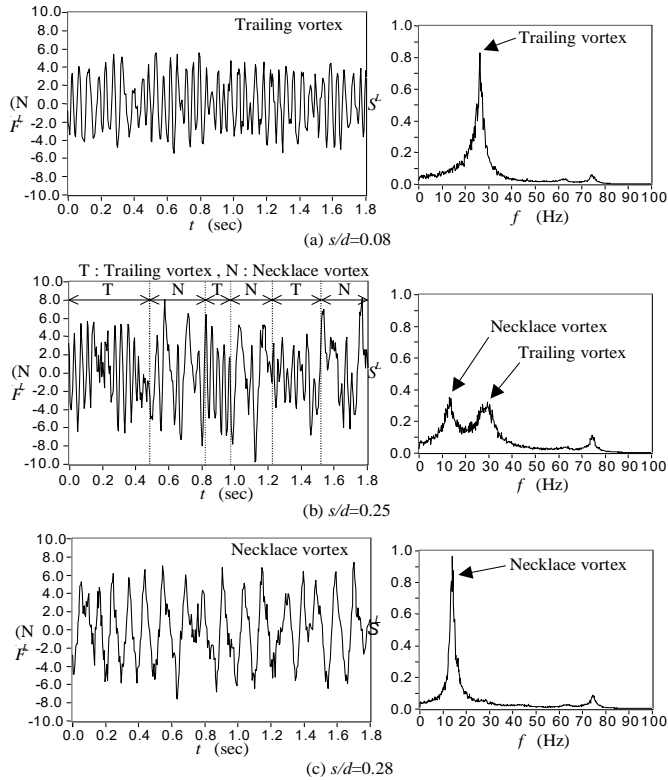

Figure 10. Oscillograms and spectra of fluctuating lift force on the upstream cylinder (fixed system, $d = d_1 = d_2 = 26$ *mm*, $U = 8.0$ *m/s*, $Re = 14,000$)

The root-mean-square value of the fluctuating lift coefficient $(C_L)_{rms}$ is calculated from the measured root-mean-square value of lift, $(F_L)_{rms}$, using equation (4.1) and plotted against Re in Figure 11.

$$(C_L)_{rms} = \left[(F_L)_{rms} / \frac{1}{2} \rho U^2 l d \right] \; . \tag{4.1}$$

$(C_L)_{rms}$ of the Necklace vortex is nearly constant over the Reynolds number range from 5,000 to 30,000, while that of the trailing vortex decreases by the factor of two over the same Re range.
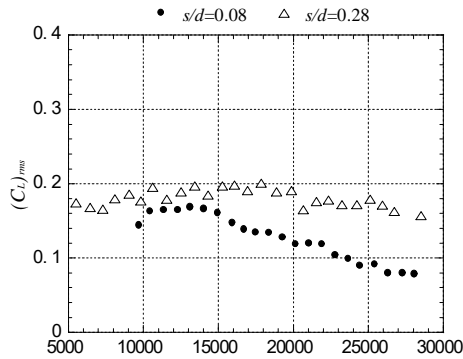
Figure 11. Fluctuating lift coefficient due to the longitudinal vortices (fixed system, $d = d_1 = d_2 = 26 \; mm$)
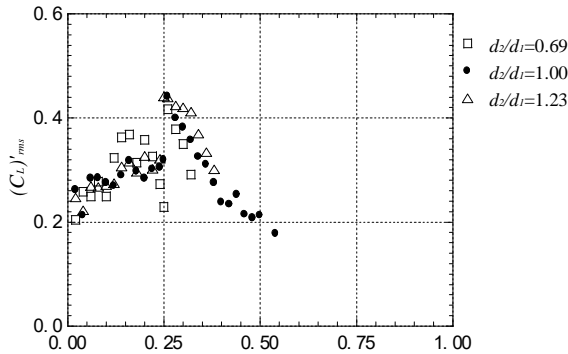
Figure 12. Substantial fluctuating lift coefficient vs. gap-to-diameter ratio (fixed system, $U = 8.0$ m/s, $Re = 14,000$, $d_1 = 26 \; mm$)

The alternating lift force is the resultant of the fluctuating pressure acting on the upstream cylinder surface caused by the periodical shedding of longitudinal vortices. The measurement of span-wise size of the longitudinal vortices as presented in Figure 9 shows that the fluctuating pressure due to the longitudinal vortices is exerted on

a limited part of the effective length of the upstream cylinder. $(C_L)_{rms}$ defined by equation (4.1) is based on the assumption that the lift force distributes uniformly over the whole span of the upstream cylinder. A practical improvement to define the lift coefficient is to use the real span wise length of the longitudinal vortices as given by R_T and R_N in Figure 9. Therefore, the substantial fluctuating lift coefficient is defined by the following equation

$$(C_L)'_{rms} = \left[(F_L)_{rms} / \frac{1}{2}\rho U^2 d \times 2R_T \,(or\ R_N) \right] \ . \tag{4.2}$$

$(C_L)'_{rms}$ thus obtained are plotted against s/d_2 in Figure 12 for three values of d_2/d_1. Figure 12 shows that the alternating lift force due to the longitudinal vortices is nearly proportional to their span wise extent along the upstream cylinder, and hence proportional to d_2 in turn.

Results in Figures 9 and 12 give a guide to estimate the fluctuating lift force exerted on the upstream cylinder when dimensions of a cruciform cylinder system, d_1, d_2 and s, and flow velocity are given.

4.2. Oscillation behavior of the upstream cylinder

The cross flow oscillation behavior of the upstream cylinder is observed when the free flow velocity is stepwisely increased and then decreased. In Figure 13, the rms value of the z-displacement of the upstream cylinder and the vortex shedding frequency f_v are plotted against the free flow velocity U. The vortex shedding frequency from the fixed equivalent, f_{v0}, and the natural frequency of the elastically supported upstream cylinder, f_n, are presented for comparison. Similarly to the well known Kármán vortex excitation, very large oscillations are caused by the two longitudinal vortices over a certain velocity range, always accompanied by the synchronization phenomenon of the vortex shedding with the cylinder oscillation. "Over range" means that the oscillation amplitude is beyond the range of measurement. The spectrum S_Z of the displacement shows that the frequency of these large excitations and hence the vortex shedding frequency f_v, coincide with the natural frequency f_n of the cylinder.

Outside the excitation region, the vortex shedding frequency f_v is nearly equal to f_{v0}, and S_Z has a maximum peak at $f = f_n$ irrespective of U, showing that the cylinder always oscillates at its natural frequency f_n. When U is a little higher than the vortex excitation range, an additional peak appears in S_Z at f_v. In this case, a beat motion is observed in the oscillogram of the cylinder displacement.

The vortex excitation regions expand around the velocity U_0, the velocity at which the vortex shedding frequency f_{v0} from the fixed equivalent is equal to the natural frequency f_n of the elastically supported system. A hysteresis behavior is also observed clearly in the necklace vortex excitation and less clearly but definitely for the trailing vortex excitation as seen in Figures 13(a) and (b), respectively. The different features between the two longitudinal vortex excitations are clearly observed as follows.

In Figure 13(a), the velocity range of the trailing vortex excitation expands to a value as low as one half of U_0, and it is narrower for U higher than U_0. Accordingly, the jump of f_v caused by the synchronization at the lower edge of the excitation range is very large. This may be associated with the jump of f_{v0} in the $f_{v0} - U$ curve which
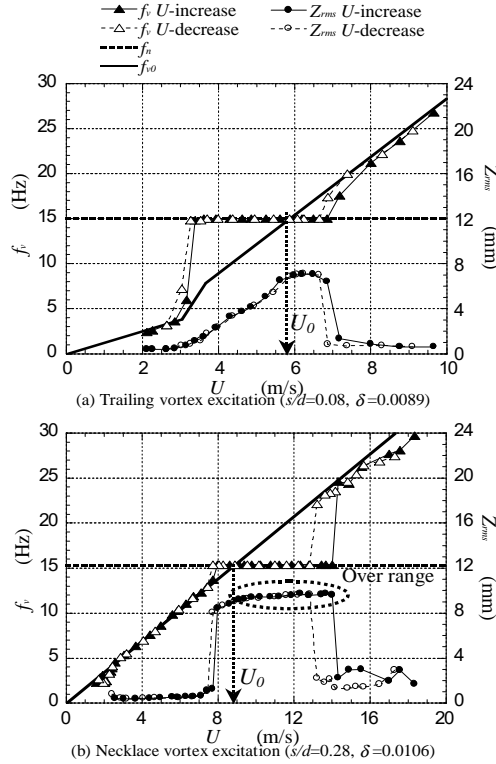
Figure 13.   Relationship between oscillation amplitude and flow velocity.   ($f_n = 15\ Hz,\ d = d_1 = d_2 = 26\ mm$)

results in the discontinuity in the $St_0 - Re$ relationship in Figure 6. In spite of this large jump of f_v at the lower edge of vortex excitation range, the change of oscillation amplitude there is continuous and the amplitude increases rather gradually with U in the excitation range up to $U = U_0$. In contrast, the necklace vortex excitation region starts at a velocity slightly lower than U_0 and the excitation region expands to a velocity much higher than U_0, as seen in Figure 13(b). In spite of the slight jump in f_v at the lower edge of the excitation region, the oscillation amplitude abruptly increases with a large step there.

In Figure 14, the relationship between the oscillation amplitude and the gap-to-diameter ratio under a fixed flow velocity is presented for various diameter ratios. The two values of flow velocity U in the figure are selected as the representatives of the trailing vortex excitation ($U = 7.0$ m/s) and the necklace vortex excitation ($U = 12.0$ m/s) in Figure 13. When $U = 7.0$ m/s, the oscillation is large in the region $s/d_2 < 0.25$ and almost disappears for s/d_2 larger than the boundary value of s/d_2, except the case of $d_2/d_1 = 0.692$. Since the cylinder oscillates at its natural frequency

f_n and f_{v0} of the trailing vortex at this velocity is close to f_n, the vortex shedding is "locked in" the cylinder oscillation and the oscillation amplitude becomes large due to the resonance, i.e. the trailing vortex excitation. In contrast, large excitations occur in the region $0.25 < s/d_2 < 0.75$ when $U = 12.0$ m/s. Since the natural shedding frequency f_{v0} of the necklace vortex at this velocity is close to the natural frequency f_n of the cylinder, this oscillation is attributed to the necklace vortex excitation.

The abrupt change of oscillation amplitude at around $s/d_2 = 0.25$ means that a very slight change of the gap can induce a large oscillation. Generally speaking, the maximum cylinder oscillation amplitude is larger when the downstream cylinder diameter d_2 is larger.
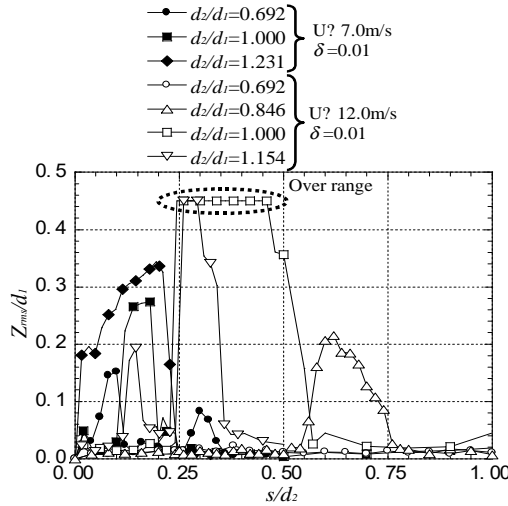
Figure 14. Oscillation amplitude vs. non-dimensional gap for various diameter ratio ($\delta = 0.01$, $d_1 = 26$ mm, $f_n = 14.8$ Hz)

In some cases large oscillations appear in the two regions of s/d_2, as the case of $d_2/d_1 = 0.692$ at $U = 7.0$ m/s and $d_2/d_1 = 1.154$ at $U = 12.0$ m/s. This behavior is explained by the result shown in Figure 8. For example, St_2 for $d_2/d_1 = 0.692$ in Figure 8 has an equal value in the both regions of the trailing vortex ($s/d_2 < 0.25$) and the necklace vortex ($s/d_2 > 0.25$). Hence, the natural vortex shedding frequency f_{v0} is equal to f_n in the two regions of s/d_2. Therefore, the vortex shedding synchronizes with the cylinder oscillation and the vortex excitation occurs in the two regions of s/d_2, i.e. two maximum peaks appear in the $Z_{rms}/d_1 - s/d_2$ curve for $d_2/d_1 = 0.692$ as seen in Figure 14.

Results shown in Figures 13 and 14 are well coherent with the results on the fixed systems, confirming that a large oscillation is induced by either of the two longitudinal vortices in the respective regions of s/d_2.

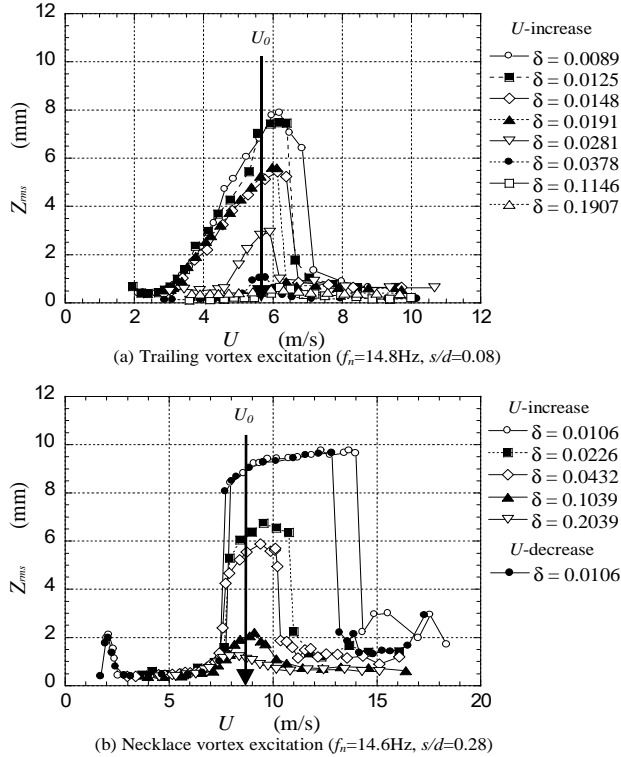(a) Trailing vortex excitation (f_n=14.8Hz, s/d=0.08)

(b) Necklace vortex excitation (f_n=14.6Hz, s/d=0.28)

Figure 15. Effect of damping factor on oscillation-velocity curve. ($d = d_1 = d_2 = 26\ mm$)

Figure 15 shows the effect of the damping factor on the longitudinal vortex excitations. When δ is increased, the oscillation amplitude decreases for both of the two longitudinal vortex excitations. The width of the velocity range of vortex excitation shrinks towards U_0, the velocity at which $f_{v0} = f_n$. For all the measured values of the damping factor, the maximum amplitude of trailing vortex excitation occurs at U_0, while that for the necklace vortex appears at U considerably higher than U_0.

The hysteresis behavior is not discernible for damping factors larger than those in Figure 13.

4.3. Lock-in phenomenon of the longitudinal vortex

Although the synchronization of the vortex shedding with the upstream cylinder oscillation (lock-in) occurs with the vortex excitation, it is not essential for the lock-in whether the oscillation is induced by the fluid force or not. The lock-in is a phenomenon in the flow caused by the cylinder oscillation irrespective of the mechanism of the cylinder motion. When the vortex shedding is said to "lock-in" the cylinder oscillation,

it is controlled by the cylinder oscillation so that the vortex shedding frequency f_v coincides with the cylinder oscillation frequency f_c and the velocity fluctuation caused by the vortex shedding is in phase with the cylinder displacement, consequently its periodicity becomes more regular. When the cylinder oscillation amplitude is smaller than a certain value, it cannot control the vortex shedding. The threshold value of amplitude for the lock-in is investigated using a mechanical oscillator [13]. The results are presented by the broken lines in Figure 16 where the abscissa expresses the ratio of the cylinder oscillation frequency to the natural vortex shedding frequency and the coordinate the relative amplitude of the cylinder oscillation. The lock-in threshold has a finite value even when $f_c/f_{v0} = 1$. It means that the vortex shedding is not controlled by a cylinder oscillation with an amplitude smaller than this threshold value even when the cylinder oscillation frequency is equal to the natural vortex shedding frequency.

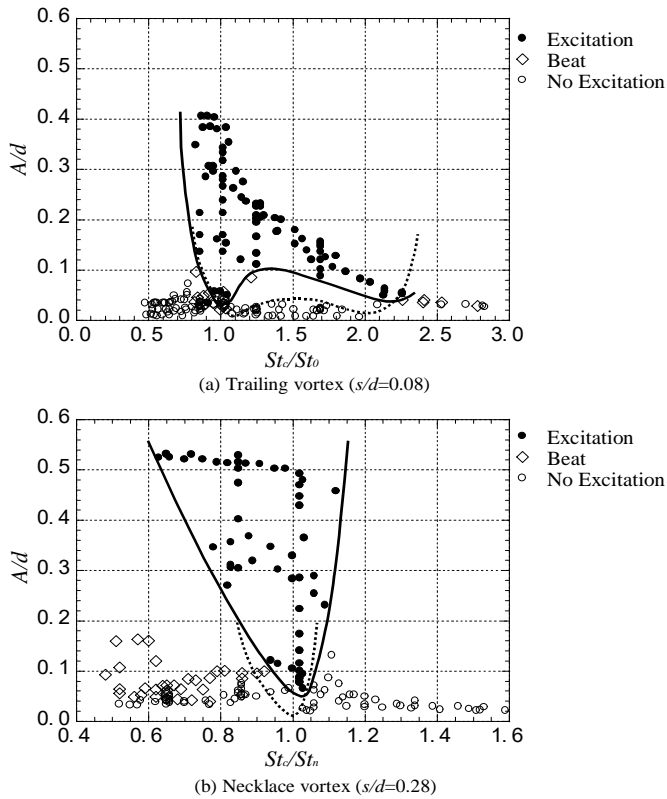(a) Trailing vortex (*s/d*=0.08)

(b) Necklace vortex (*s/d*=0.28)

Figure 16. Synchronization region and excitation region for the longitudinal vortices. ($d = d_1 = d_2 = 26\ mm$) Solid curve: Contour of excitation region. Broken curve: Contour of lock-in region measured by mechanical oscillator

The regions of the vortex excitation for the two longitudinal vortices are also presented in Figure 16. The solid lines express the contour of the region where the vortex excitations are observed. The vortex excitation regions observed for the elastically supported system seem to be included in the above lock-in regions for the respective vortices. The symbol "Beat" means that the cylinder oscillation contains both f_n and f_v components but the amplitude is very small, as mentioned in Section 4.2.

The lock-in region for the necklace vortex (Figure 16(b)) is understandable from the phenomenological point of view in that the lock-in threshold is minimum at $f_c = f_{v0}$ and it increases rapidly when f_c differs from f_{v0} in both sides of f_{v0}. However, for the trailing vortex (Figure 16(a)) the lock-in region expands to very large values of $f_c/f_{v0} > 1$ and the threshold amplitude does not increase monotonuously but has a second minimum value at around $f_c/f_{v0} = 2$. This peculiar behavior of the trailing vortex is not understood at present, but may be associated with the lock-in region widely expanding to a velocity lower than U_0 and the discontinuity in $f_{v0} - U$ curve in Figure 13.

Since the lock-in phenomenon is the feedback of flow to the cylinder oscillation which plays an essential role in the vortex excitation, it is acutely desired to clarify the conditions for the lock-in by appropriate non-dimensional parameters as shown in Figure 16. It is also desired to clarify the influences of other parameters, i.e. Reynolds number, gap-to-diameter ratio and diameter ratio of the two cylinders, on the contour lines in Figure 16.

4.4. Criterion for the longitudinal vortex excitation and estimation of the alternating lift force

From an engineering point of view, the most practical way to avoid the vortex excitation is to make the natural frequency of the system far enough from the vortex shedding frequency f_{v0} and/or to adopt a damping factor large enough to suppress the oscillation. Hence, in order to predict occurrence of vortex excitations of a system, it is a convenient way to present the vortex excitation range of f_{v0} at an arbitrary damping factor. To generalize the expression, these parameters are non-dimensionalized into the relative deviation of f_{v0} from f_n, i.e. $(f_{v0} - f_n)/f_n$, and the Scruton number as defined by the following equation [14].

$$Sc = 2m\delta/\rho d^2 l\,. \tag{4.3}$$

Occurrence of the longitudinal vortex excitations is expressed on the $Sc - (f_{v0} - f_n)/f_n$ plane in Figure 17 , where the criterion for the Kármán vortex excitation is added for comparison. Solid curves in the figure show the contour line of the longitudinal vortex excitation region. Although the definition of Sc by equation (4.3) is based on the two dimensionality of the flows, Figure 17 gives a useful and clear comparison of the features of longitudinal vortex excitations with the Kármán vortex excitation as seen in the figure.

The difference in nature between the two longitudinal vortex excitations is also clearly seen in Figure 17. While the trailing vortex excitation is suppressed with a damping factor measured by $Sc = 28$, which is around one half of the maximum value for the Kármán vortex excitation [14], the necklace vortex excitation is observed at

$Sc = 150$, which corresponds to the maximum damping attained by the eddy current damper used in this experiment. The width of necklace vortex excitation range of $(f_{v0} - f_n)/f_n$ gradually decreases with Sc. When Sc is small it is much wider in the positive side than in the negative side. The lower limit of the range is almost constant at around -0.1 over the whole Sc range.

In contrast, the $(f_{v0} - f_n)/f_n$ region for the trailing vortex excitation expands wider in the negative side and the total width decreases rapidly in the range of $Sc = 20-25$.

(a) Trailing vortex excitation (*s/d*=0.08)

(b) Necklace vortex excitation (*s/d*=0.28)
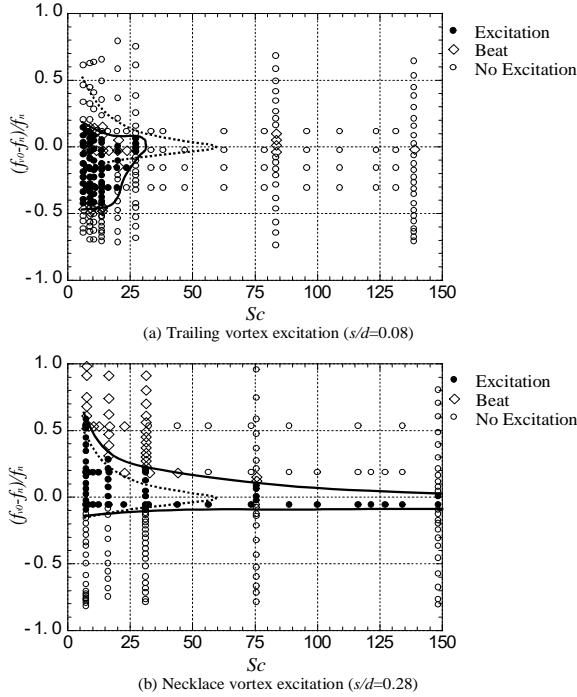
Figure 17. Criterion for longitudinal vortex excitation. ($d = d_1 = d_2 = 26$ mm) Solid curve: Contour of longitudinal vortex excitation region. Broken curve: Contour of Kármán vortex excitation region.

Since the oscillation frequency of the upstream cylinder is fixed at its natural frequency over the whole longitudinal vortex excitation region, the oscillation is regarded as the resonance of a linear elastic system with small damping. Hence, the amplitude of excitation force is calculated by the following equation.

$$(C_{LR})_{rms} = \frac{8\pi St_n^2 m\delta}{\rho d^2 l} \cdot \sqrt{2} \left(\frac{Z_{rms}}{d} \right) . \tag{4.4}$$

Taking into account the fact that span-wise region where the fluctuating pressure caused by the longitudinal vortices is exerted is limited to R_T and R_N as shown in

Figure 9, the substantial alternating lift coefficients of the longitudinal vortices are proposed as defined by the following equations.

$$\text{Trailing vortex} \quad : \quad (C_{LR})'_{rms} = \frac{8\pi St_n^2 m\delta}{\rho d^2 \cdot 2R_T} \cdot \sqrt{2}\left(\frac{Z_{rms}}{d}\right) \qquad (4.5a)$$

$$\text{Necklace vortex} \quad : \quad (C_{LR})'_{rms} = \frac{8\pi St_n^2 m\delta}{\rho d^2 \cdot 2R_N} \cdot \sqrt{2}\left(\frac{Z_{rms}}{d}\right) \qquad (4.5b)$$

In addition to the measurements of oscillation amplitude with varying U at a fixed damping factor as shown in Figure 13, measurements were carried out with varying damping factor δ at a fixed velocity. The oscillation amplitude at the vortex excitation

(a) Trailing vortex excitation (s/d=0.08)

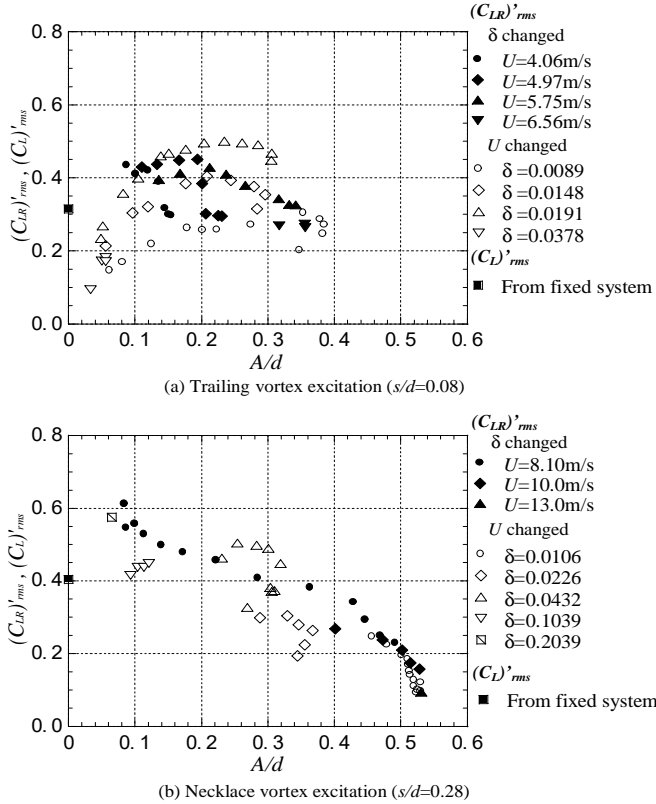(b) Necklace vortex excitation (s/d=0.28)

Figure 18. Substantial alternating lift coefficient due to longitudinal vortices ($d = d_1 = d_2 = 26$ mm)

is converted into the substantial alternating lift coefficient $(C_{LR})'_{rms}$ and plotted against the non-dimensional amplitude as shown in Figure 18, where results obtained for the fixed system presented in Figure 12 are also added. Note that the Reynolds

number varies for the fixed-δ measurements while it is constant for the fixed-U measurements.

$(C_{LR})'_{rms}$ for the necklace vortex seems to collapse on a single curve and decreases with the oscillation amplitude A/d. The maximum value appears at the smallest vortex excitation amplitude and has a value around 0.6, which is considerably larger than the value for the fixed system.

In contrast, $(C_{LR})'_{rms}$ for the trailing vortex scatters largely, and at the incidence of the vortex excitation $(C_{LR})'_{rms}$ is much smaller than that of the fixed system. It seems to increase with the oscillation amplitude till the maximum value 0.5 appears at around $A/d = 0.2$.

5. Conclusions

Comprehensive experiments are carried out to clarify the behavior of the longitudinal vortex excitations of the upstream cylinder in a cruciform two circular cylinder system in a uniform flow. Influences of the gap-to-diameter ratio, the diameter ratio of the two cylinders and the damping factor on the vortex shedding and the oscillation are investigated. Cross spectra of the velocities at properly selected two points near the crossing and measurements of the fluctuating lift force definitely reconfirmed and expanded the results so far reported by the present authors. The conclusions newly found in this work are summarized as follows.

1. The downstream cylinder diameter d_2 has a dominating influence on the longitudinal vortex structure formed near the crossing. That is, the trailing vortices shed when $0 < s/d_2 < 0.25$ and the necklace vortices shed when $0.25 < s/d_2 < 0.7$. The maximum value of s/d_2 for the necklace vortex shedding found in this work is considerably larger than reported so far.

2. Compared with the necklace vortex, the trailing vortex has a very irregular nature as follows. Its $St_0 - Re$ curve does not attain a constant value up to $Re = 40,000$, unlike the Kármán vortex or the necklace vortex, and has a large discontinuous jump at $Re = 5,000$. Under a fixed velocity f_{v0} changes irregularly with the gap s and there was found no coherent tendency in $f_{v0} - d_2$ relation.

3. The shedding area of the longitudinal vortex on the upstream cylinder surface is nearly proportional to the downstream cylinder diameter, and in turn, the alternating lift force caused by the longitudinal vortices is also proportional to the downstream cylinder diameter. Based on this result, the substantial lift coefficient of the longitudinal vortices is proposed to estimate the exciting force of the longitudinal vortices.

4. The criteria for the two longitudinal vortex excitations are presented as a curve on $Sc - (f_{v0} - fv)/f_n$ plane. The former parameter expresses the relative deviation of the natural vortex shedding frequency from the natural frequency of the upstream cylinder, and the latter is the Scruton number conventionally applied to two-dimensional flows. Compared with the Kármán vortex excitation of the same aspect ratio cylinder, the minimum value of Sc to suppress the trailing vortex excitation is smaller than that for the Kármán vortex. In contrast, the

necklace vortex excitation can occur even when Sc is three times as large as that to suppress the Kármán vortex excitation.

The criteria for the longitudinal vortex excitation in Figure 17 give the guideline for the occurrence of the excitation, and the substantial alternating lift coefficient given in Figure 18 can be applied to predict the vortex excitation amplitude for a system with an arbitrary aspect ratio. These results obtained in this work will be a guideline to predict and to avoid or suppress hazardous vibrations caused by longitudinal vortices.

REFERENCES

1. BISHOP, R.E.D. and HASSAN,A.Y.: *The lift and drag forces on a circular cylinder oscillating in a flowing fluid*, Proc. Royal Soc., London A-277, (1964), 51-57.

2. KOOPMAN, G.H.: *The vortex wakes of vibrating cylinders at low Reynolds numbers*, J. Fluid Mech., **28**, (1967), 501-518.

3. SARPKAYA, T.: *Vortex-induced oscillations*, Journal of Applied Mechanics, **46**, (1979), 241-258.

4. BEARMAN, P.W.: *Vortex shedding from oscillating bluff body*, Annual Review of Fluid Mechanics, **16**, (1984), 195-222.

5. TOMITA, Y., INAGAKI, S., SUZUKI, S. and MURAMATSU, H.: *Acoustic Characteristic of Two Circular Cylinders Forming a Cross in Uniform Flow (Effect on Noise Reduction and Flow Around Both Cylinders)*, JSME International Journal, 30-265, (1987), 1069-1079.

6. SHIRAKASHI, M., MIZUGUCHI, K. and BAE, H.M.: *Flow-induced excitation of an elastically-supported cylinder caused by another located downstream in cruciform arrangement*, J. of Fluids and Structures, **3**, (1989), 595-607.

7. SHIRAKASHI, M., BAE, H.M., SANO, M. and TAKAHASHI, T.: *Characteristics of periodic vortex shedding from two cylinders in cruciform arrangement*, J. of Fluids and Structures, **8**, (1994), 239-256.

8. SHIRAKASHI, M., SANO, M. and HIGASHI, K.: *Structure of vortices shedding periodically from two cylinders in cruciform arrangement*, ASME Separated and Complex Flows, **217**, (1995), 137-142.

9. TAKAHASHI, T., BARANYI, L. and SHIRAKASHI, M.: *Configuration and Frequency of Longitudinal Vortices Shedding from Two Circular Cylinders in Cruciform Arrangement*, Journal of the Visualization Society of Japan, 19-75, (1999), 328-336.

10. FOX, T.A.: *Flow Around Two Circular Cylinders Arranged Perpendicular to Each Other*, The Univ. of Queensland, Dep. of Civil Eng. Research Report, CE126, (1990).

11. HOSAKA, F.: *Proc. Visualization Society of Japan*, **16**(2), (1996), 159-162. (in Japanese)

12. SHIRAKASHI, M.: *An instructional fluids engineering experiment: Measurement of the Kármán vortex using HWA*, FED-Vol. 220, ASME, (1995), 13-17.

13. KUMAGAI, I.: *Influence of oscillation of upstream circular cylinder on flow around criss-cross circular cylinder*, Proc. JSME Annual meeting 1, 99-1, (1999-7), 471-472. (in Japanese)

14. SCRUTON, C.: *On the wind-excited oscillations of stacks, towers and masts*, Proc. Int. Conf. Wind Effects on Build. & Struc. (Teddington), Her Majesty's Stationary Office, Paper 16, (1963), 798-836.

ON UNSATURATED INFILTRATION IN SOILS

György Sitkei
Institut of Product Development and Technology
University of Sopron
H-9401 Sopron PoB. 132

Abstract. The infiltration of water into the soil was investigated by many researchers using both theoretical and experimental approaches. While the ponded infiltration more or less can also be treated with analytical methods, the unsaturated infiltration can generally be solved only by numerical procedures. Unfortunately, the latter method provides no generally valid relatonships.
Based on the analysis of the wetting front and on experimental results, some general relatonships were established to calculate the equilibrium moisture content corresponding to a given water flux.

Keywords: Unsaturated infiltration, ponded infiltration, soil.

1. Introduction

Infiltration from rainfall or sprinkler irrigation is of great importance for the practice. An excess of rainfall over infiltration may cause severe overland flow and soil erosion. In the case of saturated or ponded infiltration all of the pores are filled with water and the hydraulic conductivity of the soil equals the saturated conductivity. If the rate of supply of water is limited in comparison to the maximum rate, then the water content at the surface and in the transmission zone can not reach the fully saturated value W_s.

In the wetting front of an infiltration process the matric potential of the soil predominates and, therefore, the absorption of water takes place. Behind the advancing wetting front, in which the water content is nearly constant (transmission zone), the gravitational potential becomes dominant.

If the water content of the transmission zone for any infiltration rate were known, then the wetting front velocity (or pore water velocity) could simply be determined. From the continuity equation of flow it follows that the average depth of the wetting front is given by

$$y = \frac{v \cdot t}{W - W_1} = w \cdot t \tag{1.1}$$

where

v is the rain intensity, cm/h,
W_1, W are the initial and asymptotic volumetric water content,

t is the elapsed time,

w is the velocity of the wetting front.

Unfortunately, the asymptotic water content for different infiltration conditions is generally not known. Therefore we have analyzed the wetting front, especially the distribution of the matric potential and the gradient of water content in it. We used also experimental results obtained on packed plexiglass columns.

2. Theoretical Considerations

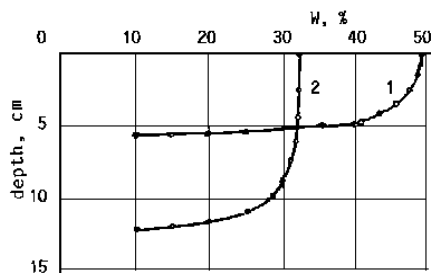In any infiltration process a wetting front starts as it is shown in Figure 1.

Figure 1. Wetting profiles for different water fluxes. $1 - v = K_s$, $2 - v = 0.001 \times K_s$

The profile of water content generally shows a very steep wetting front and, therefore, in many cases a simplified approach may be used. Measurements on different types of soils have shown that the steepness of the water profile decreases with increasing hydraulic conductivity. The driving potential is the sum of the matric potential of the dry soil and the gravitational potential. In the wetting front the absorption of water occurs by tension forces while behind the wetting front the gravitational effect becomes more dominant. The steady-state one-dimensional motion of water can be described by Darcy's law as

$$- v = K\left(W\right) \cdot \frac{\mathrm{d}\left(\Psi + y\right)}{\mathrm{d}y} = K\left(W\right) \cdot \frac{\mathrm{d}\Psi}{\mathrm{d}y} + 1 \tag{2.1}$$

where

$K\left(W\right)$ is the hydraulic conductivity of the soil,

Ψ is the matric potential.

In order to use equation (1.1), the asymptotic water content must be known. In the case of ponded infiltration $W = W_s$, that is the saturated water content. Under unsaturated conditions the water content at the surface should approach a value appropriate for K to equal v. Our main task is to find an appropriate relationship to describe the variation of the asymptotic water content in terms of soil physical properties such as the relative rain intensity K_s/v or the soil matric potential.

The soil water diffusivity and the hydraulic conductivity are interrelated by the soil matric potential as follows

$$K\left(W\right) = D \cdot \frac{\mathrm{d}W}{\mathrm{d}\Psi} \ . \tag{2.2}$$

The soil matric potential is approximated by the following expression [1]:

$$MR = \frac{1}{\left[1 + (\alpha \cdot \Psi)^n\right]^m} \text{ and } m = 1 - \frac{1}{n} \tag{2.3}$$

where the moisture ratio is defined as

$$MR = \frac{W - W_r}{W_s - W_r}.$$

In this equation W_r is a small moisture value and serves first of all to achieve a better fitting.

In order to use equation (2.2), the soil water diffusivity relationship is needed. Earlier experiments have shown that the diffusivity is influenced first of all by the degree of saturation [2]. Indeed, we have always found good correlation using the following expression

$$D = D_0 \cdot \exp\left[-A\left(1 - DS\right)\right] \tag{2.4}$$

where A is a constant (for soils in question its value is 9.75 and 7.39 respectively) and the degree of saturation is given by

$$DS = \frac{W - W_{\min}}{W_s - W_{\min}} \tag{2.5}$$

$W_{\min}$ means a minimum water content at which the liquid diffusion coefficient drastically decreases and it is corresponding to pF-values between 4.2 and 4.5 (wilting point). For water contents less than $W_{\min}$ Darcy's law becomes no longer valid and the water movement occurs more and more in vapor phase.

Examining equation.(2.1), it is easy to realize that the ratio of infiltration rate to saturated conductivity has a fundamental influence on the equilibrium moisture content in the transmission zone. In the following we analyze the structure of wetting front for different flux conditions. Using the term saturated and relative hydraulic conductivity and, keeping in mind that $\mathrm{d}\Psi/\mathrm{d}y = (\mathrm{d}\Psi/\mathrm{d}W) \cdot (\mathrm{d}W/\mathrm{d}y)$, the moisture gradient in the wetting front is given by

$$\frac{\mathrm{d}W}{\mathrm{d}y} = \frac{v}{K_s} \cdot \frac{1}{K_r\left(\dfrac{\mathrm{d}\Psi}{\mathrm{d}W}\right)} \ . \tag{2.6}$$

This relationship for soil 1 is demonstrated in Figure 2. The curves decline below 15% moisture content because of the deviation from Darcy's law.

Knowing the moisture gradient, the potential gradient can also be calculated, which for different relative flux values is plotted in Figure 3. From this Figure the equilibrium
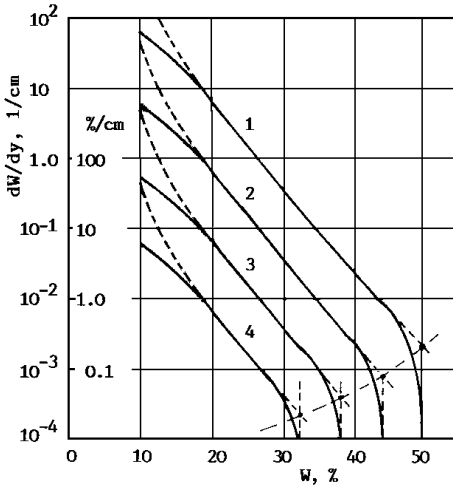
Figure 2. Moisture gradient in the wetting front as a function of moisture content. $1-$ $v = K_s$, $2-v = 0.1K_s$, $3-v = 0.01K_s$, $4-$ $v = 0.001K_s$.

moisture contents for any relative flux value can be read. Namely, in all cases the hydraulic potential gradient in the transmission zone is the unity given by the gravitational potential.

Figure 2 shows that the moisture gradient on the outer surface of the wetting front is the greatest and it rapidly decreases as the moisture content increases. A decreasing flux further decreases the moisture gradient at any moisture content and, therefore, the wetting profile changes from the steep shape to a gently sloping one. The measured wetting front profiles support this statement.

An integration of equation (2.6) gives the cumulative wetting front depth between two given moisture contents. We can write

$$\int \mathrm{d}y = \frac{K_s}{v} \int K_r\left(\Psi\right) \mathrm{d}\Psi . \qquad (2.7)$$

It is interesting to note that the integral on the right side is the so-called Kirchhoff-potential often used in analytical solutions. The solution of equation (2.7) for soil 1 is given in Figure 4. It can clearly be seen that the cumulative wetting front thickness with increasing moisture content and with decreasing water flux rapidly increases.

A dimensionless equation describing the wetting front propagation can be derived in the following way. The moisture variation by time is expressed as

$$\frac{\mathrm{d}W}{\mathrm{d}t} = \frac{\mathrm{d}W}{\mathrm{d}y}\frac{\mathrm{d}y}{\mathrm{d}t} = \frac{\mathrm{d}W}{\mathrm{d}y}w$$

where w means the effective pore velocity of water. Using equations (1.1) and (2.6) we can write

$$\frac{\mathrm{d}W}{\mathrm{d}t} = \frac{v^2}{W - W_1}\frac{1}{K_s K_r\left(\frac{\mathrm{d}\Psi}{\mathrm{d}W}\right)} \qquad (2.8)$$

Keeping in mind equation (2.2), a formal integration of equations (2.6) and (2.8) supplies the following relationship:

$$\frac{vy}{D} = \frac{v^2 t}{\left(W - W_1\right)D} \qquad (2.9)$$

which is equivalent to equation (1.1). In the above equation y means the average depth of the wetting front corresponding to the mean water content W. The left and right sides of equation (2.9) can be used as dimensionless coordinates to represent measurement data.
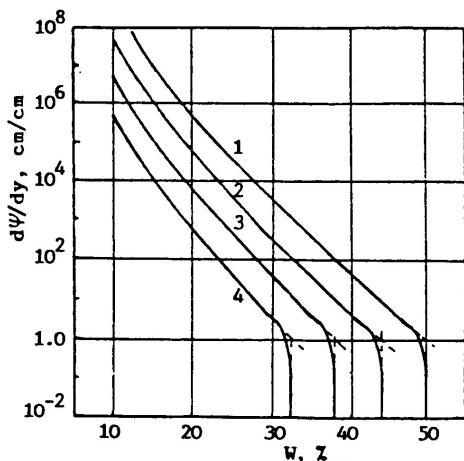
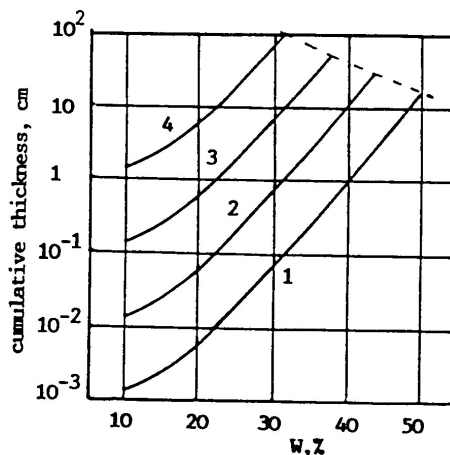Figure 3. Matric potential gradient in the wetting front. Different relative fluxes from those in Figure 2.

Figure 4. Cumulative wetting front thickness for different relative fluxes.

In all equations derived above the unknown water content W appears. In order to calculate this water content either the diffusion function $D(W)$ and the matric potential curve $\Psi(W)$ or the relative hydraulic conductivity $K_r(W)$ is needed. In the first case, the solution of the following equation (keeping in mind that $\mathrm{d}\Psi/\mathrm{d}y = 1$):

$$\frac{v}{K_s} = K_r = \frac{D(W)}{K_s}\frac{\mathrm{d}W}{\mathrm{d}\Psi}$$

supplies the equilibrium moisture content. In the second case, if the $K_r(W)$ function is available (see Figure 5), then the moisture content value can simple be read from the curve.

3. Results

From the above discussion it is obvious that a generally valid closed form relation for calculating the asymptotic moisture content cannot be obtained. Nevertheless, an appropriate approximation would facilitate a rapid estimation of the expected value.

In order to establish such a relationship both theoretically derived asymptotic values and experimentally obtained values were used. For measurements two different soils were used with several initial moisture contents. The hydraulic properties of soils are given in Figure 5 and in Table 1.

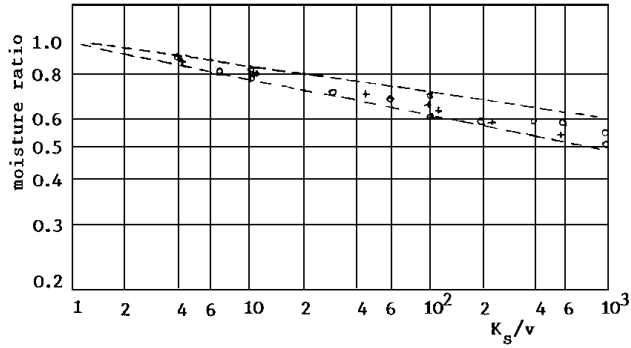| soil	porosity	D_0, $\frac{cm^2}{h}$	K_s, $\frac{cm}{h}$	$W_{\min}$	W_r	α, $\frac{1}{cm}$	n
silty loam	50%	2000	3.0	0.15	0.03	0.015	1.25
loam	40%	400	0.4	0.12	0.02	0.018	1.25

Figure 5. PF-curve and relative conductivity as a function of water content for soils.
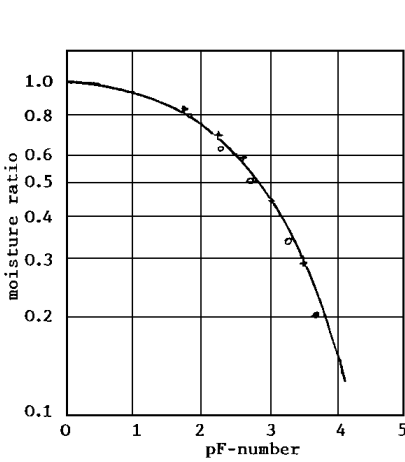1-silty loam, 2-loam

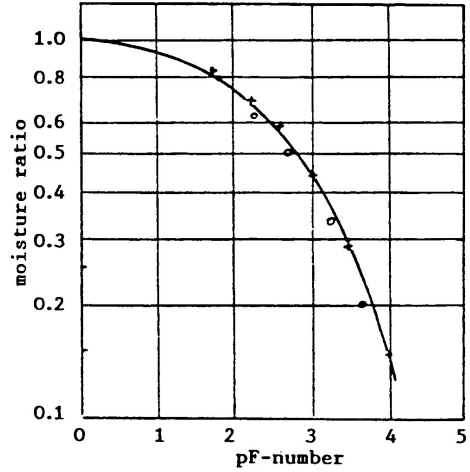Figure 6. Equilibrium moisture content as a function of the relative water flux.

Figure 7. Equilibrium moisture content as a function of pF-number.

Measurements were carried out on packed plexiglass columns with K_s/v ratios between 5 and 200 and with initial moisture contents of 10% and 20%.

The calculated and experimentally obtained results are plotted in Figure 6. using double logaritmic scale and dimensionless quantities. To describe the relationship the following simple equation is obtained:

$$\frac{W - W_1}{W_s - W_1} = \left(\frac{K_s}{v}\right)^{-n} \tag{3.1}$$

where the exponent n varies between 0.08 and 0.1.

Using equation (2.9), equation (3.1) can be rewritten as

$$\frac{vy}{D} = \frac{v^2 t}{D} \frac{\left(\frac{K_s}{v}\right)^n}{W_s - W_1} \ .$$

(3.2)

In some cases it is interesting to express the equilibrium moisture content as a function of matric potential or pF-number. Such relationship for the two soils in question is to be seen in Figure 7. This curve can be approximated by the following empirical equation:

$$\frac{W - W_1}{W_s - W_1} = 1 - ApF^m$$

where the constants have the following values: $A = 0.08$ and $m = 1.75$. The pF-number corresponds to the equilibrium moisture content for a given flux.

4. Conclusion

Based on theoretical and experimental investigations the following conclusions can be drawn:

— the steepness of the wetting front is determined by the local moisture content and the relative flux ratio v/K_s,

— the equilibrium moisture content in all cases can be approximated as the intersection of the matric potential gradient and the $d\Psi/dy = 1.0$ lines,

— a simple dimensionless equation is obtained for determining the equilibrium moisture content which is in good correlation with the experimental results,

— to represent wetting front propagations the dimensionless quantities vy/D and $v^2 t/[D(W - W_1)]$ can be used.

REFERENCES

1. VAN GENUCHTEN, M.: *A closed-form equation for predicting the hydraulic conductivity of unsaturated soils*, Soil Science Society of American Journal, **44**, (1980), 892-898.
2. SITKEI, GY.: *Applied Fluid Mechanics*, Mezõgazdasági Szaktudás Kiadó, Budapest, 1997. (in Hungarian)

INFLUENCE OF THE MATERIAL QUALITY OF PRIMARY GAS JETS ON THE FINAL VACUUM CREATED BY A SUPERSONIC GAS EJECTOR

Szilárd Szabó

Department of Fluid and Heat Engineering, University of Miskolc
3515 Miskolc-Egyetemváros, Hungary
`aram2xsz@gold.uni-miskolc.hu`

Abstract. The paper examines ejectors using supersonic gas jets in the wide range of ejectors. Previously [2] a method was developed to calculate the supersonic operational domains of ejectors when primary and secondary gas jets of different material quality are used. A methodology was also developed for designing ejectors creating a given operational domain. Now, in addition to the presentation of the fundamentals of the methodology developed, the analyses conducted by means of the methodology will be reported on. It is investigated what influence the material qualities of the two gas jets exert on the operation of an ejector with a given geometry. Furthermore, the paper presents how the geometry of the ejector creating a given final vacuum depends on the material quality of the gas operating it (primary gas).

Keywords: Supersonic gas ejector, polytropic model, primary and secondary gases.

1. Introduction

In the supersonic operation of gas ejectors four different operational domains can be distinguished [2]. The four different operational domains are easy to separate according to their locations on a surface in the spatial coordinate system of the primary pressure conditions $\pi' = p'_{or}/p_3$, the secondary pressure conditions $\pi'' = p''_{or}/p_3$ and the mass flow ratio $\mu = \dot{m}''/\dot{m}'$ developing on the pipe ends of the ejector. The diagram representing the relationship between these three quantities is called operational domain figure of the ejector [1]. In order to make plotting easier, the planar projections of the surface are used.

In Figure 1 the surface is shown in the $\pi''(\pi')$ coordinate system by means of the lines $\mu = const.$ as lines of levels. The figure shows the different operational domains and their boundary curves. (A point of operation means the comprehensive states of gas at the pipe ends of the ejector. Points of operation of the same kind belong into the same operational domain. The total of the different operational domains represents the operational domain figure.) The operational domain figure is the basis of any further investigation as it combines all the main features of the supersonic operation of the ejector. Therefore the main objective is to determine the operational domain figure, i.e., the total of values included in it.
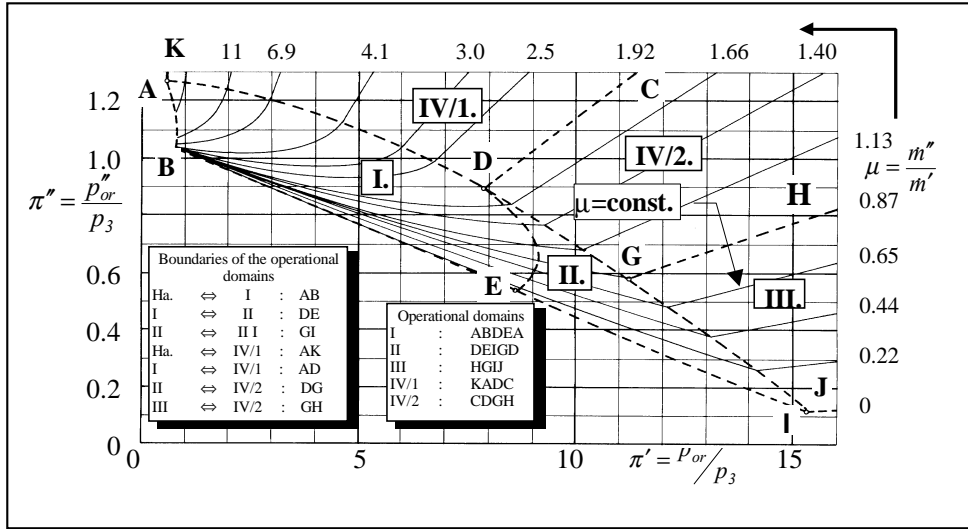
Figure 1. The operational domain figure of the ejector

The operation of ejectors using primary and secondary gas jets of different material qualities was investigated. The method describing the operation of the ejector was developed for operation in all the four operational domains [2]. Here only the basic relationships of the method will be presented. They project what a significant role the material quality of the operating and the working media plays in the operation of the ejector. Next analyses will be conducted regarding the injector operated by two different gases using the methodology developed.

Notations:

a	speed of sound	Re	Reynolds number
A	cross-sectional area	T	absolute temperature
c_p	specific heat at constant pressure	α	diffuser angle
		η	dynamic viscosity
c_v	specific heat at constant volume	η_{pol}	polytropic efficiency
		κ	ratio of specific heats
d	diameter	λ	pipe friction coefficient
F	force	v	velocity
g	acceleration due to gravity	ρ	density
		$f_1 = \left(A_1' + A_1''\right)/A_1'$	inlet cross-sectional area ratio
h	specific enthalpy		
ℓ	length	$M = v/a$	Mach number
$\dot{m}$	mass flow	$M_* = v_*/a_*$	critical Mach number
M_0	mole mass	$P' = \pi'/f_1$	primary reduced pressure ratio
n	polytropic exponent		
p	pressure	$P'' = \pi''\left(f_1 - 1\right)/f_1$	secondary reduced pressure ratio
Q	volume flow rate		
R	gas constant		

$\delta = \left(A_2 - A_1' - A_1''\right)/A_1'$ wall thickness parameter

$\varphi_1 = A_1'/A_t'$ cross-sectional area ratio of primary nozzle

$\mu = \dot{m}''/\dot{m}'$ mass flow ratio

$\pi' = p_{or}'/p_3$ primary pressure ratio

$\pi'' = p_{or}''/p_3$ secondary pressure ratio

$\pi_1 = p_1''/p_1'$ outlet pressure ratio

$\sigma = A_3/A_2$ diffuser cross-sectional area ratio

$\tau = T_0''/T_0'$ ejector temperature ratio

$\tau' = T_{03}/T_0'$ primary temperature ratio

$\tau'' = T_{03}/T_0''$ secondary temperature ratio

$\xi_K = \ell_K/d_2$ relative length of mixing tube

$N_A = 6.02283 \cdot 10^{26} \frac{1}{kmol}$ Avogadro's number

$k_B = 1.38048 \cdot 10^{-23} \frac{J}{kg}$ Boltzmann constant

Gas dynamic functions:

$$T\left(M_*\right) = 1 - \frac{\kappa-1}{\kappa-1}M_*^2 \qquad \rho_p\left(M_*\right) = T\left(M_*\right)^{\frac{1}{n-1}}$$

$$p_p\left(M_*\right) = T\left(M_*\right)^{\frac{n}{n-1}} \qquad \Gamma_p\left(M_*\right) = M_*\rho_p\left(M_*\right)\left[\frac{n+1}{2}\right]^{\frac{1}{n-1}}\left[\frac{\kappa-1}{\kappa-1}\frac{n+1}{n-1}\right]^{\frac{1}{2}}$$

Subscripts:

ax	axis		s	separation cross-sectional area of primary nozzle
cr	critical point			
D	diffuser		t	throat
ie	isentropic		$*$	critical state
k	critical		o	stagnation state
K	mixing tube		1	discharge cross-sectional area from a nozzle
L	Laval nozzle			
max	maximum		2	inlet cross-sectional area of diffuser
p	wall			
pol	polytropic		3	outlet cross-sectional area of diffuser
r	stagnation state ahead of ejector primary nozzle		$I.; II.; III.; IV.$	features of the individual operational domains

Superscripts:

$'$	primary flow		$''$	secondary flow

2. Description of ejector operation for primary and secondary gases

Figure 2 shows a schematic sectional drawing of the ejector under investigation. The figure presents the typical cross-sectional areas and the main gas parameters there. The process is presented for the most general operational domain, i.e., domain I., when the primary gas jet expands only as far as a cross section **s** of the primary gas jet, and there separates from the nozzle wall accompanied by a shock wave. The other three operational domains can be interpreted as a kind of boundary situation of this
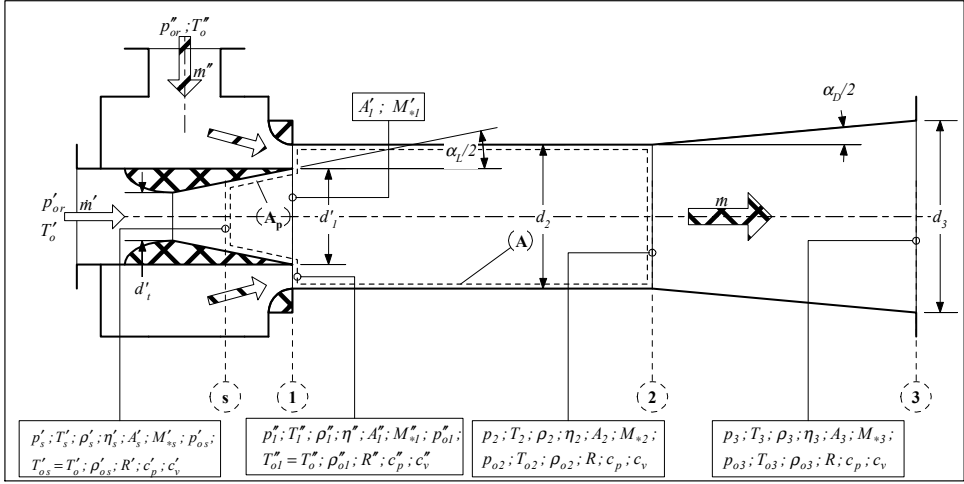
Figure 2. Control surface for the basic equations

state, therefore it will suffice to present this one here.

The energy transfer representing the operation principle of the ejector takes place in the mixing tube of the ejector. Let us therefore choose as a control surface the one shown in Figure 2, which surrounds the mixing tube and the section of the primary nozzle after separation. The general forms of the laws of mass conservation and energy conservation as well as the theorem of momentum concerning the control surface A are as follows:

$$\int_A \rho \left(\mathbf{v} \cdot \mathrm{d}\mathbf{A} \right) = 0, \tag{2.1}$$

$$\int_A \left(h + \frac{v^2}{2} \right) \rho \left(\mathbf{v} \cdot \mathrm{d}\mathbf{A} \right) = 0, \tag{2.2}$$

$$\int_A \rho \mathbf{v} \left(\mathbf{v} \cdot \mathrm{d}\mathbf{A} \right) = - \int_A p \cdot \mathrm{d}\mathbf{A} + \int_A \boldsymbol{\sigma} \cdot \mathrm{d}\mathbf{A}. \tag{2.3}$$

Flow in the primary and secondary nozzles of the ejector is considered to be adiabatic and frictionless. For the description of the flow in the nozzles therefore what is called the polytropic efficiency [2] was defined, which is interpreted as the ratio of elementary enthalpy changes due to elementary change in pressure dp in frictional or frictionless (isentropic) cases, respectively:

$$\eta_{pol} = \frac{\mathrm{d}h}{\mathrm{d}h_{ie}}. \tag{2.4}$$

Instead of the polytropic efficiency η_{pol}, the equality

$$\frac{1}{\eta_{pol}} \frac{\kappa}{\kappa - 1} = \frac{n}{n - 1} \tag{2.5}$$

can define the polytropic exponent n, which is $1 < n < \kappa$ in case of expansion, and $n > \kappa$ for compression. This yields relations whose forms resemble the equations of state valid for isentropic flow [1]. The resulting polytropic model will be used, but no details will be given here. It should be noted that in the course of developing the model, the modified gas dynamic functions were interpreted. They will play a major role in the relations later on. They are listed under Notations.

Continuity equation (2.1) with the mass flows now takes the form

$$\dot{m}' + \dot{m}'' = \dot{m}. \tag{2.6}$$

By using the relations between the ejector pipe ends and the inlet and outlet cross-sectional areas of the control surface, as well as dimensionless quantities, the gas dynamic constants α, β and γ, and by introducing the pressure ratios P', P'' equation (2.6) can be written in the following form:

$$\frac{P''}{P'} = (f_1 - 1)\frac{p''_{or}}{p'_{or}} = (f_1 - 1)\frac{p''_1}{p'_s}\frac{p_p\left(M'_{*s}\right)}{p_p\left(M''_{*1}\right)} = (f_1 - 1)\,\pi_s\,\frac{p_p\left(M'_{*s}\right)}{p_p\left(M''_{*1}\right)}. \tag{2.7}$$

This expression which includes the parameters valid at the ejector pipe ends is considered to be the continuity equation of operational domain I. Table 1 gives the interpretation of the gas dynamic constants α, β and γ.

Table 1. Interpretation of the gas dynamic constants α, β and γ

Primary jet	Secondary jet	Mixture
$\alpha'_0 = \left[\frac{\kappa'+1}{\kappa'-1}\right]^{\frac{1}{2}}$ $\alpha' = \left[\frac{n'+1}{n'-1}\right]^{\frac{1}{2}}$	$\alpha''_0 = \left[\frac{\kappa''+1}{\kappa''-1}\right]^{\frac{1}{2}}$ $\alpha'' = \left[\frac{n''+1}{n''-1}\right]^{\frac{1}{2}}$	$\alpha = \left[\frac{\kappa+1}{\kappa-1}\right]^{\frac{1}{2}}$
$\beta'_0 = \frac{\kappa'+1}{\kappa'-1}\left[\frac{\kappa'+1}{2}\right]^{\frac{1}{\kappa'-1}}$ $\beta' = \frac{n'+1}{n'-1}\left[\frac{n'+1}{2}\right]^{\frac{1}{n'-1}}$	$\beta''_0 = \frac{\kappa''+1}{\kappa''-1}\left[\frac{\kappa''+1}{2}\right]^{\frac{1}{\kappa''-1}}$ $\beta'' = \frac{n''+1}{n''-1}\left[\frac{n''+1}{2}\right]^{\frac{1}{n''-1}}$	$\beta = \frac{\kappa+1}{\kappa-1}\left[\frac{\kappa+1}{2}\right]^{\frac{1}{\kappa-1}}$
$\gamma' = \left[\frac{\kappa'}{R'}\left(\frac{2}{\kappa'+1}\right)^{\frac{\kappa'+1}{\kappa'-1}}\right]^{\frac{1}{2}}$	$\gamma'' = \left[\frac{\kappa''}{R''}\left(\frac{2}{\kappa''+1}\right)^{\frac{\kappa''+1}{\kappa''-1}}\right]^{\frac{1}{2}}$	$\gamma = \left[\frac{\kappa}{R}\left(\frac{2}{\kappa+1}\right)^{\frac{\kappa+1}{\kappa-1}}\right]^{\frac{1}{2}}$

Thus equation (2.7) contains the material quality of the gases mainly through the gas dynamic constants α, β and γ. Their significant role is easy to perceive.

Using the definition of stagnation enthalpy together with equality $T_{o2} = T_{o3}$ the **energy equation** (2.2) yields the following important relation for mass flow ratio μ:

$$\mu = \frac{\dot{m}''}{\dot{m}'} = \frac{c_p T_{03} - c'_p T'_0}{c''_p T''_0 - c_p T_{03}} = \frac{\frac{c_p}{c'_p}\tau' - 1}{\frac{c''_p}{c'_p}\tau - \frac{c_p}{c'_p}\tau'}. \tag{2.8}$$

Expression (2.8) demonstrates univocally the emphatic influence of the specific heats of the two gases as their material quality on the mass ratio.

Momentum theorem (2.3) is obtained by using the mean values valid at the inlet and outlet cross-sectional areas of the control surface:

$$- \rho'_s v'^2_s A'_s - \rho''_s v''^2_s A''_s + \rho_2 v_2^2 A_2 = p'_s A'_s + p''_1 A''_1 - p_2 A_2 - F_{sk} + F_p + F_v \qquad (2.9)$$

where the last three terms on the right-hand side are as follows: friction force on the wall of the mixing tube, the force transmitted on the wall behind the separation cross-sectional area of the primary nozzle, as well as the force transmitted on the nozzle wall with finite wall thickness at the outlet cross-sectional area of the primary nozzle, respectively.

Using appropriate relations for determining the forces, as well as extending expression (2.9) to cover the ejector pipe ends yields the form of the momentum theorem which is suitable for further computations:

$$P' \frac{1+M'^2_{*s}}{M'_{*s}} \frac{1}{\varphi_1} \frac{\alpha'_0 \alpha'}{\alpha^2 \beta'} + P'' p_p \left(M''_{*1} \right) \left\{ \frac{\alpha''^2_0}{\alpha^2} \frac{1+M''^2_{*1}}{\alpha''^2_0 - M''^2_{*1}} + \frac{1}{f_1 - 1} \left[\frac{f}{\alpha^2} \left(1 - \frac{1}{\varphi_1 \Gamma_p \left(M'_{*s} \right)} \right) + \frac{\delta}{\alpha^2} \right] \right\} =$$

$$= \frac{1}{M_{*2}} \left[1 + M^2_{*2} \left(1 + \lambda \xi_K \frac{\alpha^2 + 1}{2\alpha^2} \right) \right] \sigma \frac{\delta + f_1}{f_1} \frac{M_{*3}}{\alpha^2 - M^2_{*3}}. \qquad (2.10)$$

It is easy to see that material dependent constants play an important role in this expression as well.

By means of the three fundamental equations outlined here and by using a number of further relations and considerations, a computational method and the related computer code were compiled, which can be used to compute the corresponding states of the gases passing through the inlet sections of the primary and secondary gases and at the outlet section of the ejector. Among the supplementary relations those will be highlighted here which have been included in the computational method due to the differences in the primary and secondary gases, i.e. they play a decisive role. In the greater part of the mixing tube and in the diffuser the two gases are already mixed completely. It is the material parameters of this mixed medium that are included in the relations on this flow domain. The individual material parameters of the gas mixture can be determined by means of the mass ratio $\mu = \dot{m}'' / \dot{m}'$ using the following well-known expressions:

$$R = \frac{R' + \mu R''}{1 + \mu}, \qquad (2.11)$$

$$c_p = \frac{c'_p + \mu c''_p}{1 + \mu}, \qquad (2.12)$$

$$c_v = \frac{c'_v + \mu c''_v}{1 + \mu}, \qquad (2.13)$$

$$\kappa = \frac{c_p}{c_v}. \qquad (2.14)$$

It is somewhat more complicated to calculate the viscosity of the gas mixture. Further, the fact that viscosity is greatly temperature dependent is also to be taken into consideration. All those effects are treated in the following way. The resulting viscosity of the mixture of the primary and secondary gases is computed according to Branley and Wilke [4] by using the mole masses M_o with the following expression:

$$\eta = \frac{\eta^{'}}{1 + \mu \Phi_a} + \frac{\eta^{''}}{1 + \frac{1}{\mu} \Phi_b}, \tag{2.15}$$

where

$$\Phi_a = \frac{\left[1 + \left(\frac{\eta^{'}}{\eta^{''}} \right)^2 + \left(\frac{M_o^{''}}{M_o^{'}} \right)^{1/4} \right]^2}{2\sqrt{2}\sqrt{1 + \frac{M_o^{'}}{M_o^{''}}}}, \tag{2.16}$$

$$\Phi_b = \Phi_b \frac{\eta^{''}}{\eta^{'}} \frac{M_o^{'}}{M_o^{''}}. \tag{2.17}$$

In calculating the viscosities $\eta^{'}$, $\eta^{''}$ their temperature dependence is taken into consideration according to Linneken [5]:

$$\eta(T) = H_1 \eta_{id,cr} \left(\frac{T}{T_{kr}} \right)^{2/3} \left[\frac{\left(\frac{T}{T_{cr}} \right)^2}{1 + \left(\frac{T}{T_{cr}} \right)^2} \right]^{1/4}. \tag{2.18}$$

In expression (2.18) H_1 is a material dependent viscosity factor and $\eta_{id,cr}$ is the critical viscosity belonging to an ideal gas, which can be computed from constants independent of other material parameters and materials and is a constant typical of the material of the gas. The relevant relation for the computation is:

$$\eta_{id,cr} = \left[\frac{M_o}{N_A} \right]^{1/2} \frac{p_{cr}^{2/3}}{(k_B T_{cr})^{1/6}}, \tag{2.19}$$

where N_A is the Avogadro number, k_B is the Boltzmann constant, further p_{cr} and T_{cr} are pressure and temperature of the gas in the critical point, respectively. Expression (2.18) yields the best approximation for viscosity exactly in the range of low pressure used for ejectors.

On the basis of the fundamental equations outlined above and by using the supplementary relations described, the methodology for computing the operational domain figure of an ejector with a given geometry was developed. The design method determining the geometrical data of the ejector creating a given final vacuum was also developed. Now they will be used for analyses.

3. Dependence of ejector operation on the gases transported

3.1. Material quality of the gases transported. In order to characterize the material properties, let us examine four characteristically different gases. The gases and their relevant properties essential for our purposes are summarized in Table 2. The data in the Table belong to gas temperature $T = 293K$.

Table 2. Gases and their material properties

Gas	Propane (C_3H_8)	Carbon dioxide (CO_2)	Air	Argon (Ar)
Symbol	P	C	L	A
R [J/kgK]	188.8	188.9	287.2	208.2
c_p [J/kgK]	1549.5	814.8	1003.6	523.0
$\kappa = c_p/(c_p - R)$	1.14	1.30	1.40	1.66
M [kg/kmol]	44.097	44.009	28.964	39.948
T_{cr} [K]	370.8	304.2	132.5	150.7
p_{cr} [bar]	42.6	73.8	37.67	48.7
$10^6 \cdot \eta_{id,cr}$ [Ns/m²]	17.135	25.510	15.182	20.710
H_1	0.693	0.718	0.735	0.725

Further it is assumed that the degrees of changes in state are such that these values can be taken to be constant with a good approximation. In the following these material properties will be used, at the same time the other properties of the concrete materials will be neglected, i.e., it will be assumed that they do not undergo changes of phase and no chemical processes take place. The change of phase in both nozzles will be considered isentropic so that the influence of the material properties can be distinguished from the influence caused by friction. Therefore the approximation $n = \kappa$ will be used for both gas jets.

3.2. Dependence of the operational domain figure of an ejector with a given geometry on the material quality of the gases transported. The dependence of the operation of a supersonic gas ejector on the material quality of the gas transported can be followed by means of the changes in the operational domain figure. That analysis was carried out earlier [3].

The first case under examination is the combination when the two gas jets are of the same material quality. Then the cases P-P, C-C, L-L and A-A can take place. The second case is the analysis of the option when the operating primary gas jet is air, but the secondary gas jet differs from case to case (L-P, L-C, L-L, L-A). And finally the third case involves identical transported secondary gas jets, i.e., air, while the operating primary gas jet is different again from case to case (P-L, C-L, L-L, A-L). In all the three cases significant shifts were demonstrated in the operational domain figure together with dependence on the isentropic exponent κ . Now only the results obtained in the first case will be referred to as those findings project what is to be described in detail in the following. Figure 3 shows the operational domain figures for identical primary and secondary gases for each of the four gases. It can be seen
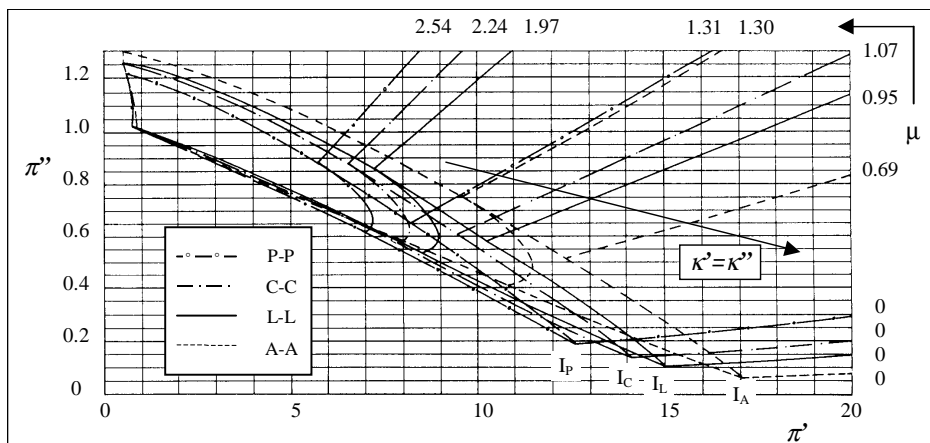
Figure 3. Operational domain figure of ejector for identical primary and secondary gases

that increasing the isentropic exponent κ pushes the boundaries of the operational domains towards higher π' and lower π'' pressure ratios. The curves belonging to mass ratio $\mu = 0$, showing the elimination of the secondary gas jet, deserve special attention. Point I in Figure 1, which is one of the final points of the operational domains boundary II-III, lies on this curve. It is at the same time the point belonging to the smallest secondary pressure ratio π'' in the operational domain figure. This operational domain will be called final vacuum value (points I_P, I_C, I_L, and I_A in Figure 3). This is what our investigation will focus on.

3.3. Dependence of the geometry of an ejector producing a given final vacuum on the material quality of the primary gas jet. One of the important uses of ejectors is to suck gas from a tank and to maintain a given vacuum value there. This often provides the basis of designing ejectors, i.e., design for final vacuum. Then the secondary flow has already ceased, i.e., the mass flow ratio is $\mu = 0$. Thus, due to the termination of secondary gas transportation, the curve $\mu = 0$ in the operational domain figure of the ejector is naturally independent of the material quality of the secondary gas flow [3]. Similarly, design for final vacuum is only concerned with the properties of the primary gas flow. For ejectors with a given geometry, the operational domain figure depended on the material quality of the primary gas and for ejectors ensuring a given final vacuum the geometry will differ according to the material quality of the primary gas. Using the methodology developed earlier [2], let us now examine the dependence of the main geometrical data of the ejector to be designed on the material qualities of the gas. Again the four different gases listed in Table 2 will be used. Any of the main material properties of the gases, the gas constant R, the specific heats c_p and c_v, as well as the exponent κ can be expressed by any other two, starting from the well known relations $\kappa = c_p/c_v$, $R = c_p - c_v$. Let us consider the other three properties as functions of κ for the four gases.

According to the relation shown in Figure 4 there is no monotonous relation between the properties, mostly due to the data on air. In spite of this, as it will be seen the geometrical data of the ejector to be designed based on exponent κ will keep

mostly continuously changing. This means that it is the ratio of specific heats that plays the most significant role regarding the final vacuum among the material properties.
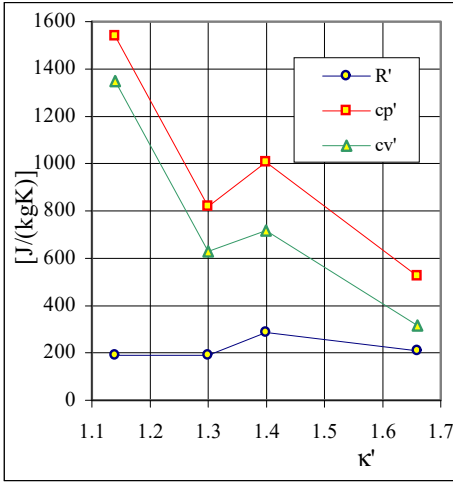

Figure 4. Dependence of material properties on exponent $\kappa^{'}$

In order to set up the relation sought, let us now consider a typical real-life example. The notations in Figure 2 will be used. The temperature and quantity of the operating primary gas jet are $T_0^{'} = 293\ K$, $Q_3 = 283\ m^3/h$, respectively, and the operating primary pressure ratio is $\pi^{'} = p_{or}^{'}/p_3 = 18.18$. The secondary pressure ratio to be obtained is $\pi^{''} = p_{or}^{''}/p_3 = 0.121$, which means producing a very strong vacuum. (In the concrete case examined the value of the final vacuum was only $p_{or}^{''} = 666 Pa = 5 Torr$!). The design method referred to is expedient to determine an ejector operating in point I in Figure 1. That operation point belongs namely to the absolute maximum value of vacuum to be obtained by the given ejector.

The relation shown in Figure 5 was found between the typical diameters shown in
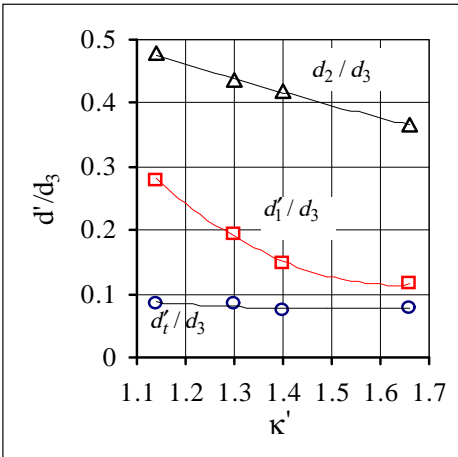
Figure 5. Dependence of ejector geometry on exponent $\kappa^{'}$ in designing for final vacuum
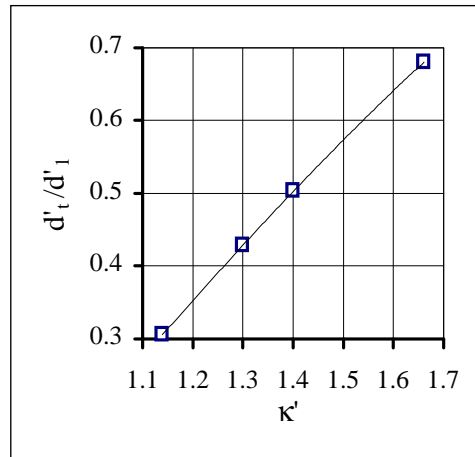
Figure 6. Dependence of the diameter ratio of a Laval nozzle on exponent $\kappa^{'}$ in designing for final vacuum

Figure 2 of the ejector designed by the method and the primary ratio of specific heats κ . Accordingly and considering the diameter ratio of the nozzle throats $d_t^{'}/d_3$, it

can be stated that the throat cross-sectional area of the primary nozzle d'_t is almost constant for a given ejector pipe end dimension d_3, i.e. it hardly depends on the material quality of the gas. The case is different for the outlet diameter ratio of the Laval nozzle d'_1/d_3. This, namely, decreases almost quadratically with an increase in the exponent κ'.

This means that the outlet cross-sectional area of the primary nozzle d'_1 will continue to decrease for a given ejector pipe end dimension d_3 if κ' increases. Thus considering a constant Laval nozzle diffuser angle α_L, the length of the nozzle will also considerably decrease. The quadratic decrease in the outlet diameter of the Laval nozzle is accompanied by an almost linear decrease in the diameter of the mixing tube. This is shown by curve d_2/d_3 in Figure 5. The Figure also shows the interesting fact that the size of the mixing tube carries outstanding significance even though there is only one gas jet in the relevant operational domain.

Figure 6 demonstrates an important relation. It shows that the ratio of the throat and outlet diameters of the Laval nozzle d'_t/d_1 increases almost linearly with exponent κ'.

3.3. Dependence of final vacuum obtained with an ejector of a given geometry on the material quality of the primary gas jet. Section 1.1 gave an analysis of how the operational domain figures shifted for ejectors of a given geometry depending on the material quality of the gases. Now particularly great emphasis will
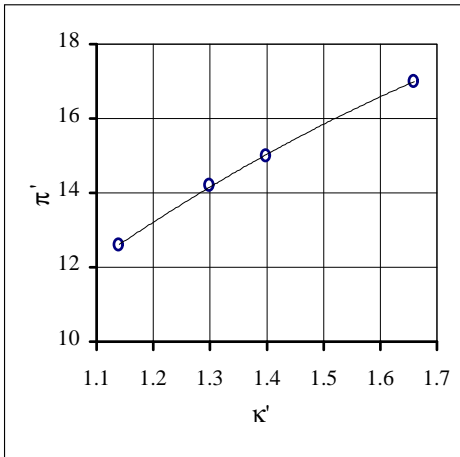

Figure 7. Dependence of primary pressure ratio π' on exponent κ' in designing for final vacuum.
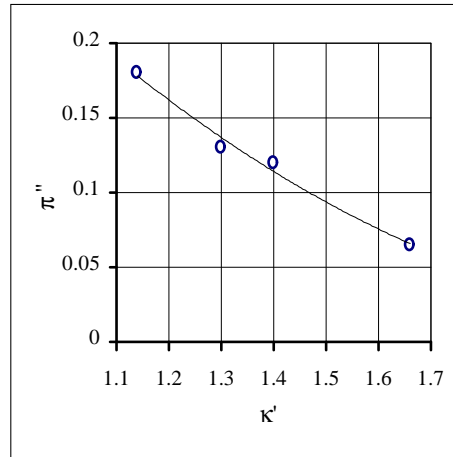
Figure 8. Dependence of secondary pressure ratio π'' on exponent κ' in designing for final vacuum.

be given to the analysis of the dependence of the maximum vacuum values to be obtained by a particular ejector on the material quality of the gases.

The particular emphasis is justified, as already mentioned, by the fact that supersonic gas ejectors are primarily used to increase the vacuum value, i.e. to produce the

largest possible pressure difference between the secondary $(p_{or}^{''})$ and outlet pipe end (p_3) of the ejector, i.e. to produce a small pressure ratio $\pi^{''} = p_{or}/p_3$. The operational domain to be investigated is the one denoted by I in Figure 1. According to Figure 3 this final vacuum value greatly depends on the material quality of the primary gas (See points I_P, I_C, I_L, I_A one by one.).
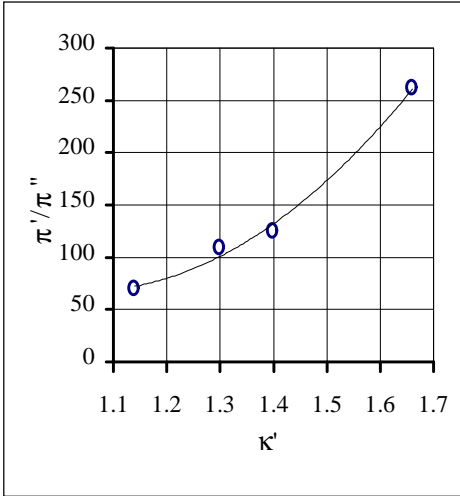

Figure 9. Dependence of pressure ratio $\pi^{'}/\pi^{''}$ on exponent $\kappa^{'}$ in designing for final vacuum.

Let us now analyze its sequence and degree by using the data of the four gases examined earlier. As secondary flow ceases when the final vacuum is obtained, i.e. the mass flow ratio is zero ($\mu = 0$), only primary gas plays a role in obtaining the final vacuum, and the final vacuum value is independent of the material quality of the secondary gas. In order to demonstrate the tendencies, let us consider an ejector with a concrete geometry, with the main data given by the notation in Figure 2:

$$d_t^{'} = 6.03 \text{ mm}, \ d_1^{'} = 12.4 \text{ mm},$$
$$d_2 = 27.9 \text{ mm}, \ d_3 = 65 \text{ mm},$$
$$\alpha_L = \alpha_D = 8°.$$

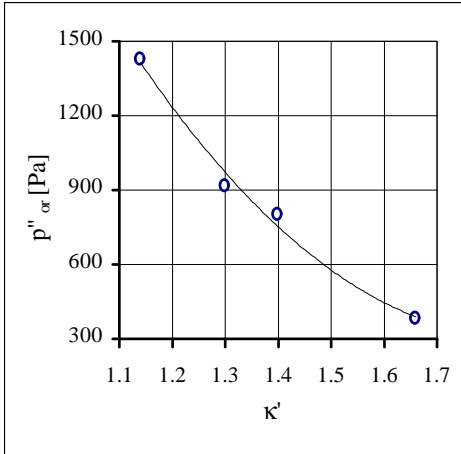When the coordinates of operational point I of the ejector with a given ge-

Figure 10. Dependence of secondary stagnation pressure $p_{or}^{''}$ on exponent $\kappa^{'}$ for final vacuum.
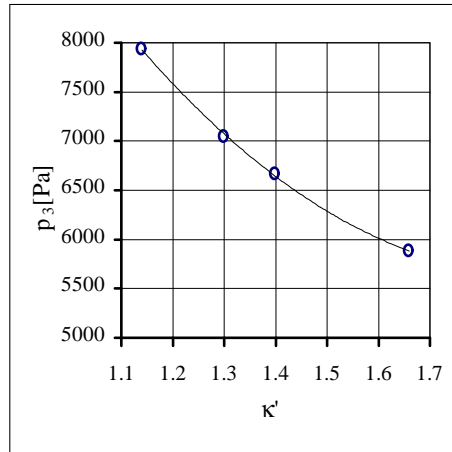

Figure 11. Dependence of outlet pressure p_3 on exponent $\kappa^{'}$ for final vacuum.

ometry are determined by the computation method and computer code mentioned above, the results shown in Figures 7 and 8 are obtained. Figure 8 shows that the secondary pressure ratio π'' decreases almost linearly when exponent κ' is increased, but to achieve that an (again almost linearly) increasing primary pressure ratio π' is required. The relation between the two is expressed by pressure ratio $\pi'/\pi'' = p'_{or}/p''_{or}$. A great change in that is shown by Figure 9. It demonstrates that in order to obtain a strong vacuum, i.e. to achieve a low secondary stagnation pressure p''_{or}, a primary stagnation pressure p'_{or}, which exceed this value to an ever increasing extent, is required. In order to perceive the concrete orders, let us consider the

example with a primary jet pressure $p'_{or} = 1 \ bar = 10^5 \ Pa$. Now the obtainable final vacuum values p''_{or} are shown in Figure 10, and the relevant outlet ejector pipe end pressure p_3 can be seen in Figure 11. Considering the two extreme cases, it can be stated that increasing the isentropic exponent κ' results in decreasing the pressure value p''_{or} belonging to the final vacuum to a quarter of its value.

4. Summary and conclusions

Previously a one-dimensional polytropic model was developed [2] which was suitable for describing frictional supersonic flow in nozzles with changing cross-sectional areas. That model served as a basis for developing a procedure to determine the supersonic operational domains of a supersonic ejector. The method can be used to give the relations between the gas flows at the inlet and outlet sections of the ejector and the gas states for every supersonic operational domain. It is a speciality of the methodology that not only may the primary and secondary gas jets be different from each other but they can be of different material qualities as well.

Special emphasis was given to the analysis of the influences arising from the different material qualities of the gases. Examining ejectors designed for given final vacuum it was shown that their geometry greatly depended on the material quality of the operating primary gas. That relation can be best described by the dependence on the ratio of specific heats κ'. It is to be stressed that increasing the exponent κ' will almost linearly increase the cross-sectional area ratio of the primary (Laval) nozzle (d'_t/d'_1), while the cross-sectional area ratio of the diffuser behind the mixing tube d_2/d_3 will linearly decrease.

Investigating the operation of an ejector with a given geometry at the final vacuum, it was found for gases with different material qualities that the pressure ratios developing showed a monotonous change mainly depending on the ratio of specific heats κ'. For the primary and secondary ratios π' and π'' best describing the pressure conditions of the ejector, it was shown that they underwent almost linear change with κ', i.e. π' increased while π'' decreased. As a major characteristic it can be stated that using a gas with a higher isentropic exponent π' will increase the final vacuum.

To sum it up, it can be stated that the material quality of gases exerts a significant influence on the ejector operation, and that influence can be described by means of a suitable model. Further investigations may aim to consider the changes in material

quality due to temperature and pressure changes in gases. Currently, that is significantly hindered by a lack of understanding of the relevant relations, particularly concerning gas mixtures.

REFERENCES

1. LEISTNER, G.: *Experimentelle und theoretische Untersuchungen an einem Hochtemperatur-Überschallejektor mit zylindrischer Mischkammer, (Dissertation) Darmstadt*, 1966, p. 125.

2. SZABÓ, SZ.: *A procedure for the Design of Supersonic Ejectors. Thesis for the Ph.D. degree, Miskolc*, 1994, p. 139. (in Hungarian)

3. SZABÓ, SZ.: *Numerical analysis of the operation of a supersonic ejector handling two gases of different kinds, 10th Conference on Fluid Machinery, Budapest*, 1995, 448-452.

4. BROMLEY, L. A. AND WILKE, C.R.: *Viscosity Behavior of Gases, Ind. Engng. Chem.* 43 (1951), 1641-1648.

5. LINNEKEN, H.: *Temperaturverhalten der Viskosität von Gasen bei mäßigem Druck, Forschung in Ingenieurwesen* 43 (1977), Nr.1, 19-25.

FLOW CONDITIONS DURING BLOW-OFF OF GAS PIPELINE

László Tihanyi, Elemér Bobok

Petroleum and Natural Gas Institute, University of Miskolc

3515 Miskolc-Egyetemváros, Hungary

`tihanyil@kfg2.kfgi.uni-miskolc.hu, boboke@kfg2.kfgi.uni-miskolc.hu`

Abstract. The authors worked out a computational process and software for calculating the working conditions of blow-off systems at technological stations of gas pipelines. One part of the investigated system is the closed gas pipeline section, the other is the blow-off pipe provided with a control valve. To create the model they analysed the blow-off process, on the basis of which the simplifying assumptions were determined. The calculation model gives unsteady values of pressure, temperature and the gas flow at chosen points of the system. In the second part of the article the authors demonstrate the application of the computational algorithm by solving an example.

Keywords: Pipeline depressurising, venting system, blow-off pipe, Fanno flow, energy equation, subsonic flow.

1. Introduction

The high-speed pipe flow with friction has been investigated first by Frössel [1]. Pressure distribution charts were obtained both for subsonic and supersonic flow. Prandtl [2] elaborated the first mechanical model in which the friction factor depends not only on the Reynolds number but also on the Mach number. Shapiro, Hawthorne and Edelman [3] gave a complex mechanical and thermodynamical analysis of the problem. Their results are provided in tabulated form for numerical solutions. Landau and Lifsic [4] investigated the high speed gas flow through an adiabatic pipe. Their sophisticated analysis has mainly academic interest from the point of view of theoretical physics. Tihanyi, Bobok and Bódi [5] provided an analytical solution oriented to applications in natural gas engineering.

2. Blow-off system

The blow-off system is a complementary part of disconnecting or technological stations, which serves for depressurising pipeline sections. During blow-off, the gas in the pipeline section which is closed at both ends is discharged through a special pipeline system, and throughout the process the own pressure energy of the gases is used. Because of environmental regulations, the discharged gas is generally burnt, therefore

the process is also called flaring of gas. Gas pipeline blow-off systems are infrequently in operation, while refinery and gasworks flares are continuously being burnt. That is why their sizes and arrangements are different.
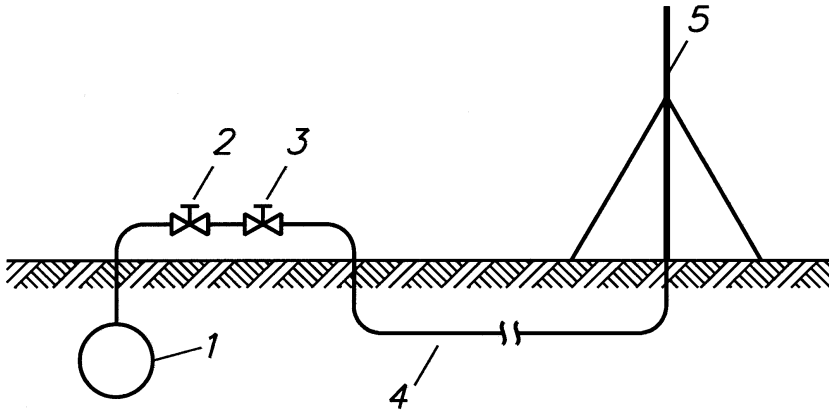

Figure 1. Arrengement of the blow-off system. 1 closed section of the main pipeline, 2 control valve, 3 gate valve, 4 blow-off pipe, 5 stack

For technological and safety reasons, gas outflow can be controlled by reducing the cross-section of the discharge area of the stack. Regulations in Hungary allow Mach number 0.2 under normal circumstances, while 0.6-0.8 is allowed in an emergency. The usual technological arrangement of blow-off systems at pipeline disconnecting stations can be seen in Figure 1.

At the entrance of the blow-off pipe, a control valve and a gate valve are built in. The volume of gas escaping from the closed pipeline section can be controlled manually by means of a control valve.

3. Pressure and temperature changes in the closed pipeline section

When calculating the blow-off process, the examined system can be clearly divided into two parts. One part is the closed pipeline section which has to be depressurised and can be regarded as a "reservoir". The other is the blow-off pipe, the cross-section of which is either fixed or adjustable. At the "reservoir" of the whole system, changes in pressure and temperature have to be controlled by assumptional blow-off gas flow. For the part including the blow-off pipe and the control valve, the gas flow rate must be calculated considering hydraulic assumptions for the initial and final points and the control mode. The calculation for the complete system can only be done using approximation methods.

The pressure change in the closed pipeline section can be calculated applying the perfect gas law:

$$\frac{p_1}{z_1} - \frac{p_2}{z_2} = \frac{RT}{M_g V_{pipe}} \Delta m \; . \tag{3.1}$$

The formula gives the pressure change when altering the amount of gas in volume V_{pipe} with a mass of Δm. Subscript 1 refers to the initial, while subscript 2 refers to the final conditions. Since the compressibility factor depends on pressure and temperature, the equation can only be solved by successive approximation.

As pressure and temperature in the closed pipeline section change simultaneously, different assumptions can be used as starting points

a) the expansion is isentropic, only gas temperature changes,

b) the expansion is polytropic, only gas temperature changes,

c) during expansion gas temperature and the temperature of the steel pipe change in the same measure, but no heat exchange occurs between the system and its environment,

d) during expansion gas temperature in the latter two cases, pipe wall temperature and also the heat content of the gas in the pipeline section are to be taken into consideration.

Supposing environmental heat exchange between the gas and its surrounding, we have to consider heat convection between the gas flow and the soil in area A of the pipe. Choosing heat transmission coefficient $k = 0$, the effect of the latter can be disregarded. The formula to calculate the temperature of the gas in the closed pipeline section regarded as a "reservoir" derived from the balance of heat is the following:

$$T_{i+1} = \frac{c_s m_s T_i + c_g m_g T_i + kA\Delta\tau T_t}{c_s m_s + c_g m_g + kA\Delta\tau T_t} \tag{3.2}$$

The specific heat of the gas can be calculated from the equation of state at the actual pressure and temperature; the specific heat of the steel can be determined by extrapolating chart values. The mass of gas is the actual value in the pipeline section at the examined time; the mass of steel is to be given as basic data. Similarly, the heat transmission coefficient is to be given as input data, the heat convection area is to be calculated from pipeline section parameters. Time step $\Delta\tau$ depends on the calculation algorithm. Temperature can be determined from formula (3.2) by successive approximation.

Comparing the results of calculations on the basis of assumptions a/ ... d/ with blow-off experiences, it seems reasonable to choose the boundary area not on the internal but on the external surface, at the passive insulating layer. It is because the mass and heat contents of the pipeline are multiples of the mass and heat contents of the gas inside it, that the balancing effect of the mass of the steel pipe cannot be neglected. For example, the specific mass of a pipeline with 600 mm nominal diameter is 164 kg/m, while the mass of the gas at a pressure of 50 bar in a 1 m pipeline section is only 10.7 kg. Since the gas is in direct contact with the inner wall of the pipeline, thermal equilibrium can take place in a short period of time. In the calculation model

of formula (3.2) the temperature of the pipeline and that of the gas inside it change in the same extent.

Another question in connection with the "pressure vessel or reservoir" is whether a significant gas flow develops in the pipeline section during the blow-off process, which would cause a non-negligible pressure difference. Considering that the blow-off process is not for its own sake but is the preparatory phase of maintenance, we have to aim at minimising the process time. If there is no excluding factor, the blow-off process is carried out at both ends of the pipeline at the same time. In this case pressure will change evenly along the pipeline section and no significant gas flow will develop. On this basis, at all the points along the closed pipeline section pressure should be taken as constant.

4. Gas flow in the blow-off system

In the blow-off system linked with the "reservoir", i.e. the pipeline section, a complicated form of flow develops. Pressure and temperature at the initial point of the blow-off system are derived from the "main line section model". The first element of the blow-off system is a short pipe section which links the main pipeline section with the control valve. In this pipe section pressure is still high and flow velocity is relatively low. The control valve is joined with the branch pipe, with the help of which pressure can be reduced, therefore the gas flow can be controlled. Throttling control can be regarded as an isoenthalpic change of state. The gas flow developing at the nozzle or at the throttle is determined by the back pressure at the outflow end of the nozzle. In the pipe section following the nozzle, i.e. the real blow-off pipe, the pressure of the gas further decreases but its velocity increases. Depending on the gas flow and the length of the blow-off pipe, a critical velocity can develop at the outflow end. During the blow-off process the flowing gas expands, its pressure and temperature decrease point by point.

The physical model and the calculation formulas describing high-velocity gas flows developing in blow-off systems are different from those describing flowing conditions in normal pipeline operation. The pressure loss is increased by friction and very fast expansion, which mostly depends on the Mach-number [6]. For the purpose of practical calculations, the most important flow parameters are given in charts according to the Mach-number [7]. In the case of high-velocity gas flows there is a significant difference between the stagnation pressure p_0 and the static (or free-stream) value p_s. Similarly the stagnation temperature T_0 is higher than static T_s, because the sensing element is brought to rest. Thus the kinetic energy of the gas is converted into enthalpy, which results in the higher temperature reading [8]. Therefore the stagnation pressure and temperature may be written as functions of the Mach-number:

$$p_s = \frac{p_0}{\left(1 + \frac{\kappa - 1}{2} M^2\right)^{\frac{\kappa}{\kappa - 1}}} \tag{4.1}$$

$$T_s = \frac{T_0}{\left(1 + \frac{\kappa - 1}{2} M^2\right)} . \tag{4.2}$$

Because of the extremely high velocity of the gas flow moving along the blow-off pipe, the environmental heat exchange is negligible. Thus, from the viewpoint of the gas the system behaves as if it was heat-insulated [9]. At the same time, the energy loss due to friction must be taken into consideration for actual pipelines. The gas flow developing under such conditions is called Fanno-flow. To describe the process, the differential form of the mechanical balance of energy for high-velocity, frictional gas flows developing in heat-insulated pipes can be applied:

$$v \mathrm{d}v + \frac{\mathrm{d}p}{\rho} + \frac{\mathrm{d}p'}{\rho} = 0 . \tag{4.3}$$

In the equation $\mathrm{d}p'$ is the frictional pressure loss for length element $\mathrm{d}l$. The Weissbach-equation can be applied to the length element:

$$\mathrm{d}p' = f_D \frac{\mathrm{d}l}{D} \rho \frac{v^2}{2} \tag{4.4}$$

where f_D is the friction factor, and D is the pipe diameter. As the gas expands the flow velocity and the friction factor change point by point. The pressure change for length element $\mathrm{d}l$ is:

$$\mathrm{d}p = -\rho v \mathrm{d}v - \frac{f_D \rho v^2}{2D} \mathrm{d}l . \tag{4.5}$$

From the continuity and state equations the following correlation can be derived for the pressure, velocity and temperature:

$$\frac{\mathrm{d}p}{p} = -\frac{\mathrm{d}v}{v} + \frac{\mathrm{d}T}{T} . \tag{4.6}$$

Term dT/T can be determined by differentiating the equation for sonic speed:

$$2\frac{\mathrm{d}a}{a} = \frac{\mathrm{d}T}{T} . \tag{4.7}$$

Combining equations (4.6) and (4.7) yields:

$$\frac{\mathrm{d}p}{p} = -\frac{\mathrm{d}v}{v} + 2\frac{\mathrm{d}a}{a} . \tag{4.8}$$

When transforming the equations, we have to consider that

$$\frac{\rho}{p} = \frac{\kappa}{a^2}$$

where κ is the specific heat ratio. Finally we get the following differential equation:

$$2\frac{\mathrm{d}a}{a} - \frac{\mathrm{d}v}{v} = -\frac{\kappa f_D}{2D} \left(\frac{v}{a}\right)^2 \mathrm{d}l - \kappa \frac{v \mathrm{d}v}{a^2} . \tag{4.9}$$

From this equation we can see that the frictional loss coefficient for the length element $f_D \mathrm{d}l/D$ depends only on flow velocity and sonic speed, and is independent of viscosity

and surface roughness. If we consider that the ratio of flow velocity and sonic speed is the Mach number equation (4.9) can be reshaped:

$$f_D \frac{\mathrm{d}l}{D} = \frac{2\left(1 - M^2\right)\mathrm{d}M}{\kappa M^3 \left(\frac{\kappa - 1}{2}M^2 + 1\right)} \; . \tag{4.10}$$

Integrating this equation between two given points of the pipeline we get a formula by means of which the change in the Mach number can be calculated between two points of the pipeline. The Mach number distribution along the pipeline can be determined by repeating the calculation steps [10]:

$$\frac{f_D L}{D} = \frac{1}{\kappa M_1^2} - \frac{1}{\kappa M_2^2} + \frac{\kappa + 1}{2\kappa} \ln \frac{M_1^2}{M_2^2} \left[\frac{2 + (\kappa - 1)M_2^2}{2 + (\kappa - 1)M_1^2}\right] \; . \tag{4.11}$$

If Mach numbers are known at chosen points of the pipeline, pressure and temperature can be calculated using the following formulas:

$$\frac{p_{s2}}{p_{s1}} = \frac{M_1}{M_2}\left[\frac{2 + (\kappa - 1)M_2^2}{2 + (\kappa - 1)M_1^2}\right] \tag{4.12}$$

$$\frac{T_{s2}}{T_{s1}} = \frac{1 + \frac{\kappa - 1}{2}M_1^2}{1 + \frac{\kappa - 1}{2}M_2^2} \; . \tag{4.13}$$

Applying equations (4.11), (4.12) and (4.13), the flow conditions can be determined in the actual flare system [11].
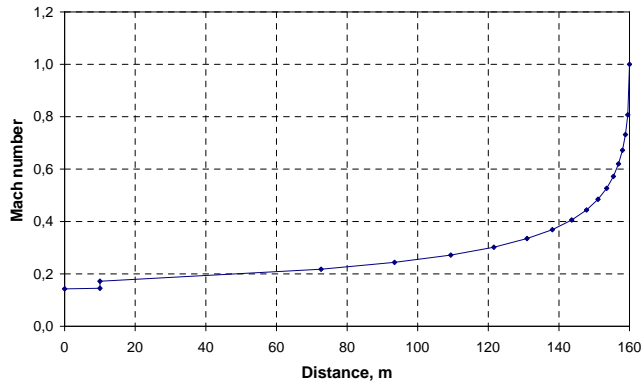

Figure 2. Changes in the Mach number according to distance

As an example let us see a blow-off system where the pipeline section to be venting and the control valve placed on the surface are connected by a 10 m long branch pipe, and the blow-off pipe. Following the control valve there is a 150 m long blow-off pipe, through which the gas flows into the environment. The blow-off pipe before and after the control valve is of 100 mm nominal diameter. In Figure 2 changes in the Mach

number can be seen in the complete system. In the short pipe between the main line and the control valve, the Mach number is 0.14 in accordance with the blow-off gas flow rate, which barely changes along the pipe. Because of pressure decrease between the two sides of the control valve, the Mach number at the output point is 0.17. Because of the expansion, flow velocity in the blow-off pipe grows continuously and reaches the Mach number 1, i.e. critical flow velocity, at the outflow end.
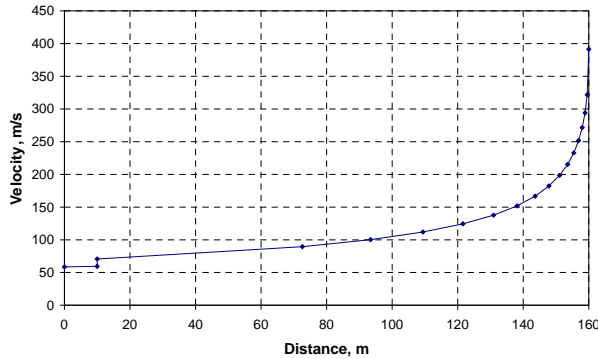

Figure 3. Changes in flow velocity according to distance

The changes in flow velocity are not linear along the blow-off pipe. In the section following the control valve, the velocity change is rather slow, the Mach number is only 0.5 at 10 metres before the outflow end. However, in the last 10 m section velocity changes extremely fast. The characteristic shape of the curve in Figure 2 has to be taken into consideration when dividing the blow-off pipe into sections, which means that the sections have to get shorter towards the outflow end. Figure 3 shows that the growth of flow velocity along the pipeline is similar to that of the Mach number. It is only moderate along nine tenths of the blow-off pipe but is powerful in the last one tenth.

Temperature of the gas flow changes as a result of adjustment and expansion. Figure 6 shows that temperature at the beginning point of the blow-off system is 2.4 ^{o}C, after adjustment it is 1.8 ^{o}C lower. There is significant cooling during the flare process at the outflow end where temperature reaches the lowest value -35 ^{o}C. Figure 5 illustrates changes in pressure along the blow-off pipe. In the short pipeline section before the control valve, pressure decrease is only 0.3 bar because of low flow velocity. At the output point of the control valve pressure is 17.2 bars because pressure decreases by 3 bars during the control process. The pressure loss of 15.3 bars in the blow-off pipe is mainly due to the large gas flow. Eventually, pressure at the outflow end is 2 bars higher than environmental pressure.

Figure 6 illustrates the correlation between limiting conditions at the outflow end of the blow-off pipe and the developing gas flow rate in the case of a 100 mm nominal diameter pipeline. While the Mach number is below 1, pressure at the outflow end of
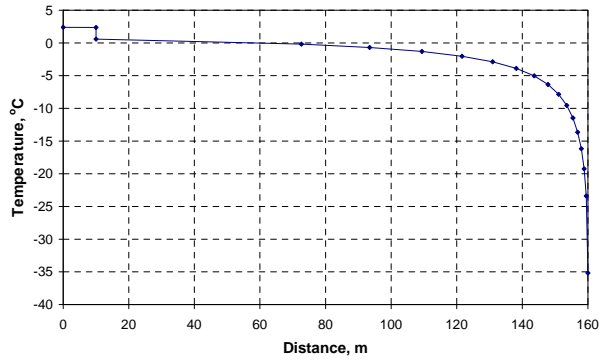
Figure 4. Changes in temperature according to distance
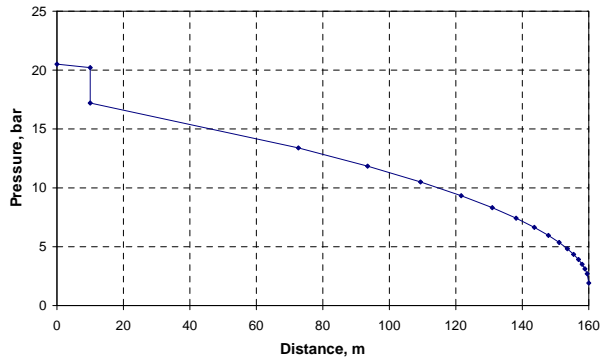

Figure 5. Changes in pressure according to distance

the blow-out pipe is equal to ambient pressure, i.e. there is no overpressure. Under this flow condition the outflow rate is proportional to the Mach number. If the critical outflow velocity is reached by increasing the flare gas flow, further increase can only be achieved by increasing density, and not velocity. Under this flow condition the pressure at the outflow end will exceed ambient pressure.

5. Practical application

The examined system is a 15 km long 600 mm nominal diameter pipeline section, in which the pressure at the beginning of the blow-off process is 25 bars, and (soil) temperature is 5 °C. The flare system consists of a 10 m long linking pipe, an adjusting valve and a 150 m long blow-off pipe with 100 mm nominal diameter.
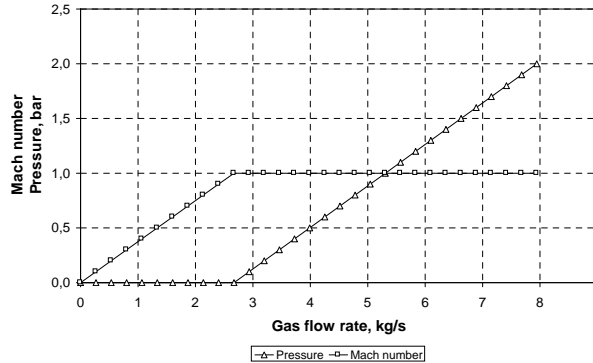
Figure 6. Outflow rate according to the Mach number and pressure

When processing computational results, subscript 1 always refers to the "reservoir", i.e. the closed pipeline section, subscript 3 to the output point of the control valve and subscript 4 to the outflow end.

During the blow-off process different control methods can be implemented, which result in different flow conditions. Each control method also influences the venting time through the gas flow rate.

Figure 7 shows volumes of three different gas flows under different technical conditions:

– pressure difference at the control valve is a constant of 3 bars,
– the volume of the controlled gas flow is a constant of 5.73 kg/s,
– the Mach number at the outflow end is a constant of 0.8.

If the control valve allows, adjusting at constant pressure difference is chosen. The blow-off process can be carried out within a short period of time initially with large, then fast decreasing gas flow. At constant gas flow first large, then gradually decreasing throttling must be ensured on the control valve, and the process is to be finished with the control valve completely open. If the critical velocity is not reached, i.e. the Mach number is below 1, the gas flow in the first phase will be constant, then it will gradually decrease.

Controlling the blow-out process by given pressure difference the constant pressure decrease at the adjusting valve is 3 bars. Figure 8 shows that the flare process can be divided into three parts. The first phase lasts 2 hours 47 minutes, and constant throttling of 3 bars can be sustained between the two sides of the control valve. In this period pressure loss can be neglected in the short branch pipe linking the main pipeline section with the throttling valve, therefore "stagnation pressure" p_1 and the output pressure of the control valve decrease simultaneously. In the second period throttling must be gradually decreased, and finally in the third period after 3 hours 41 minutes the control valve has to be opened completely, and there is no need for adjusting.
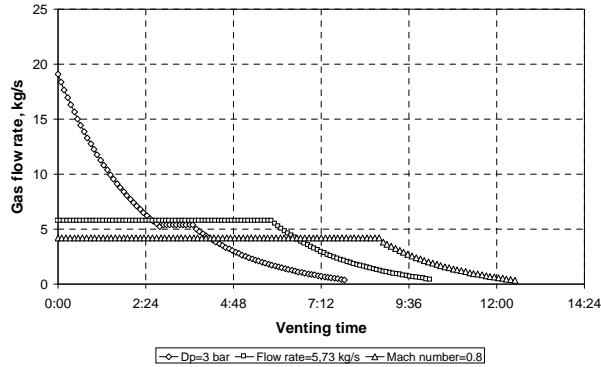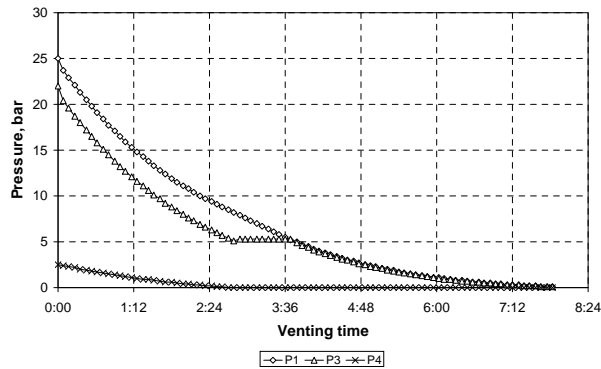
Figure 7. Comparing control methods

Figure 8. Pressure change versus time

In the first phase when pressures p_1 and p_3 decrease simultaneously, p_4 at the outflow cross-section is higher than the ambient pressure. After 2 hours 47 minutes, the Mach number 1 at the outflow end could only be kept by reducing throttling. In 3 hours 41 minutes throttling reaches zero, thus in the remaining venting time is carried out without throttling, with completely open control valve. The figure shows that stagnation pressure in the last phase decreases below 5 bars. The blow-off process is continued for 7 hours 50 minutes with gradually decreasing outflow. After 3 hours 41 minutes, i.e. in the last phase, pressure at the outflow cross section is equal to ambient pressure.

Figure 9 shows the temperature calculated throughout the process. Stagnation temperature T_1 in the first, intensive phase decreases from soil temperature of 5 ^{o}C to -0.8 ^{o}C, then in the next phase it increases due to surrounding heat convection. At the output point of the throttling valve temperature T_3 changes parallel with T_1 due to constant pressure difference. At the outflow point of the stack in the first phase, gas
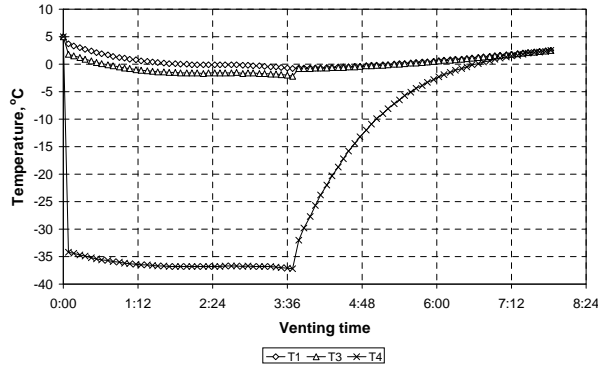
Figure 9. Change of temperature versus time

temperature T_4 becomes very low because there is a significant expansion when flow velocity reaches sonic speed. Later, as the outflow Mach number decreases, expansion becomes smaller along the pipe, thus outflow temperature gradually approaches temperature T_3 at the beginning point of the blow-off pipe.
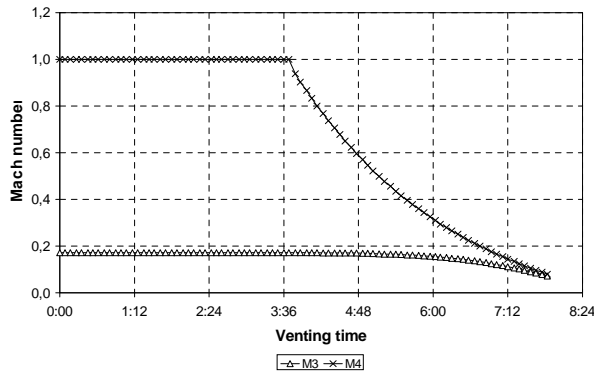

Figure 10. Changes in Mach number versus time

Figure 10 shows that gas velocity reaches sonic speed in the phase of throttling controlling when $\Delta p > 0$, i.e., Mach number M_4 at the outflow end is 1. In the last phase of blow-off without throttling M_4 decreases due to the gas flow decrease.

Mach number M_3 refers to the output point of the control valve. There are no breakpoints on the curve at the ends of the blow-off phases, which means that the transition between the different control methods is continuous. In the last phase of process, due to gradual gas flow decrease, the Mach number at the output point of the control valve decreases as well, and the two curves approach each other fast.

6. Conclusions

Blow-off systems are important complementary parts of gas transportation systems. Blow-off is generally needed when gas needs to be removed from a pipeline section. During the process a high-velocity gas flow develops, which shows a significant difference compared with change of state and form of flow under normal operation of gas transportation systems. It is reasonable to divide the system into two parts: the closed section of the main pipeline in which the gas volume continuously decreases; and a blow-off pipe provided with a control valve, through which the controlled gas flow is discharged into the environment.

Assumptions have to be examined for both parts of the system in order to get the best approach to the process taking place. The next step is to determine the mathematical model. Setting out from the calculation formulas, an algorithm can be created to be realized in software form.

With the help of the example presented in the article, the changes in the most characteristic parameters can be seen along the blow-off pipe and also their unsteady changes at chosen points of the system. So the reader can be convinced of not only the accuracy of the calculation process, but can also see the process under different adjusting conditions.

REFERENCES

1. FRÖSSEL, W.: *Strömungen in glatten geraden Rohren mit Über- und Unterschall - geschwindigkeit*, Forsch. Ing. Wes., **7**, (1936), 75-84.

2. PRANDTL, L.: *Führer durch die Strömungslehre*, Braunschweig, 1942.

3. SHAPIRO, A.H., HAWTHORNE, W.R. and EDELMAN, G.M.: *The Mechanics and Thermodynamics of Steady One-dimensional gas Flow with Tables for Numerical Solution*, Bureau Ordnance Meteorology Rept. **14**, Contract NOrd 9661, 1947.

4. LANDAU, L.D.-LIFSIC, E.M.: *Hydrodynamics*, Tankönyvkiadó, Budapest, 1980. (in Hungarian)

5. TIHANYI, L., BOBOK, E. and BÓDI, T.: *A New Method for Blow-off of a Gas Pipeline*, Intellectual Service for Oil & Gas Industry Proceedings UFA State Petroleum Technological University - University of Miskolc, Ufa Publ. USPTU, ISBN 5-7831-0311-X, 234-246, 2000.

6. OSWATITCH, K. and KUERTI, G.: *Gas Dynamics*, Academic Press, New York, 1957.

7. STREETER, V.L.: *Handbook of Fluid Dynamics,* McGraw Hill, New York.

8. CZIBERE, T.: *Fluid Mechanics, Physical Handbook for Engineers*, Műszaki Könyvkiadó, Budapest, 1980. (in Hungarian)

9. LIEPMAN, H.W. and ROSHKO, A.: *Elements of Gasdynamics,* John Wiley, New York, 1957.

10. COULTER, B.M.: *Compressible Flow Manual Handbook for the design of compressible flow piping systems*, Fluid Research and Publishing, Melbourne, 1984.

11. TIHANYI, L., BOBOK, E. and BÓDI, T.: *FLARE 1.0 User Manual*, Research Report, University of Miskolc, Miskolc, 1998. p.68.

AIR FLOW THROUGH AN EJECTOR WITH ANNULAR SUPERSONIC NOZZLE

Emília Wagnerová, Ivan Imriš

Department of Power Engineering,Technical University of Košice

041 87 Košice, Slovak Republic

hugo@tuke.sk, imris@tuke.sk

Abstract. During development of the continuous production of copper dried concentrate and fluxes were injected through the top-blowing lance into the molten bath. The properties of the equipment designed were determined by both classical measurements and modern flow visualization methods. The results of the classical measurements of the air flow parameters through an ejector with annular supersonic nozzle were confirmed by the Shleer and the shade methods of flow visualization.

Keywords: Ejector, annular nozzle, supersonic flow, copper.

1. Introduction

During development of the continuous production of copper dried concentrate and fluxes were injected through the top-blowing lance by preheated, compressed and
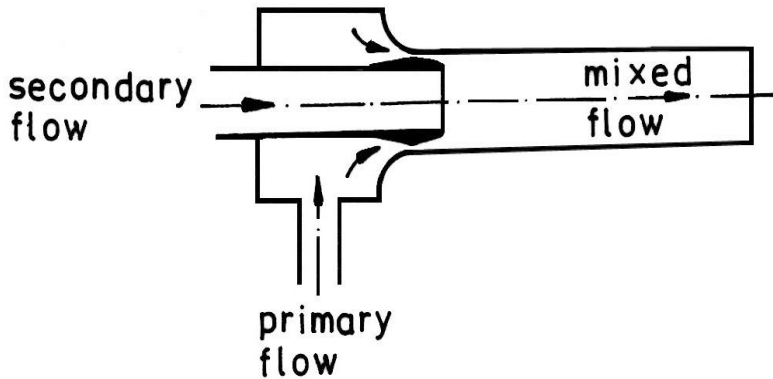

Figure 1. Schematically illustrated lance with annular supersonic nozzle ejector

oxygen enriched air into the molten bath in the copper production zone [1-3]. Using an ejector with an annular supersonic nozzle for the top-blowing lance, the experimental study of the air flow parameters was performed.
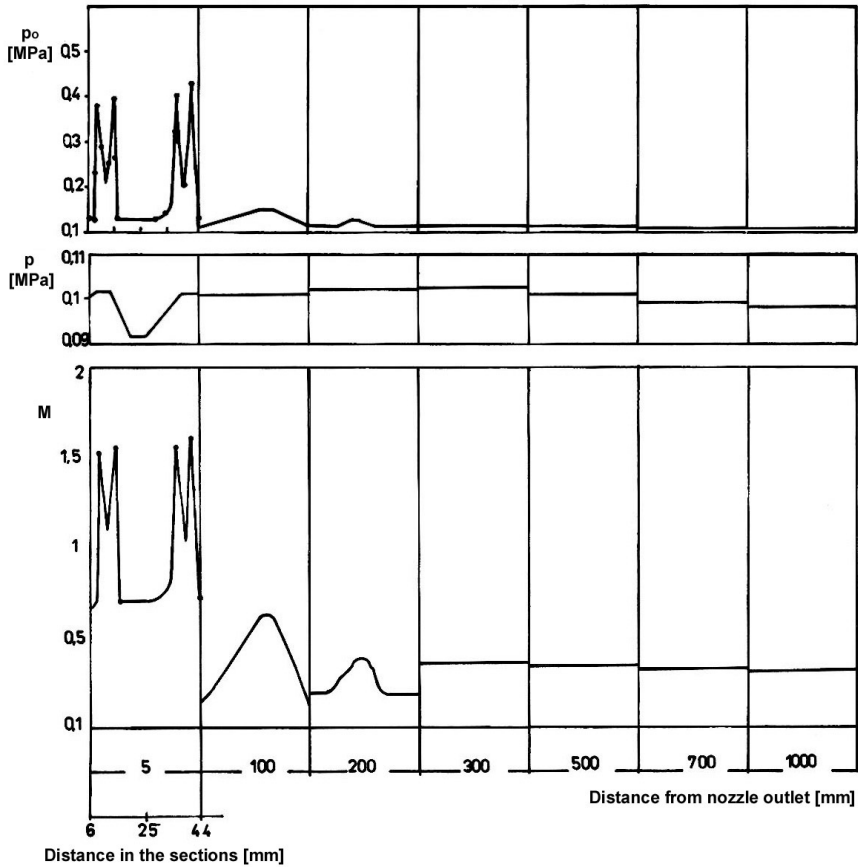
Figure 2. Graphical illustration of measured and calculated aerodynamic character-
istics for the lance with annular supersonic nozzle ejector.

Gas flow in the ejector with annular supersonic nozzle can be characterized as an
anisotropic discontinuous flow of viscous gas. The flow discontinuity is the result of
the energy losses due to the friction of air on the ejector walls and due to the shock
waves in supersonic flow [4-6].

2. Experiments

The experimental study of air flow through the ejector with annular supersonic nozzle
was realized on the lance schematically illustrated in Figure 1. The measurements of
the air flow parameters in the ejector mixing chamber with the simultaneous mea-

surements of the pressures of primary, secondary and mixed flow were carried out for the total air pressures of 0.4, 0.5, 0.595 and 0.69 MPa.

The results of the measurements for the primary flow with total pressure $p_o = 0.69$ MPa in the mixing chamber of the ejector are given in Figure 2.

It was difficult to carry out the measurements to determine the shock waves in the air flow, so the Shleer and shade methods were applied. These optical methods make the air flow visible. The visualized free flows under the total air pressure $p_o = 0.69$ MPa are shown in Figures 3 and 4.
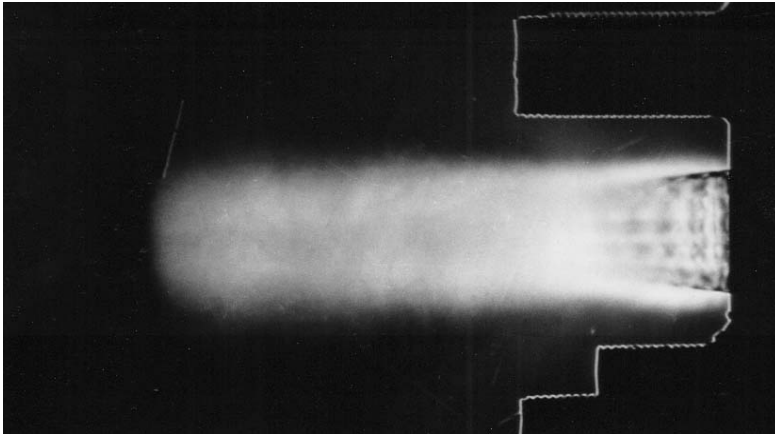

Figure 3. Photograph of the free flow of the air from the lance with annular supersonic nozzle ejector visualized by the Shleer method
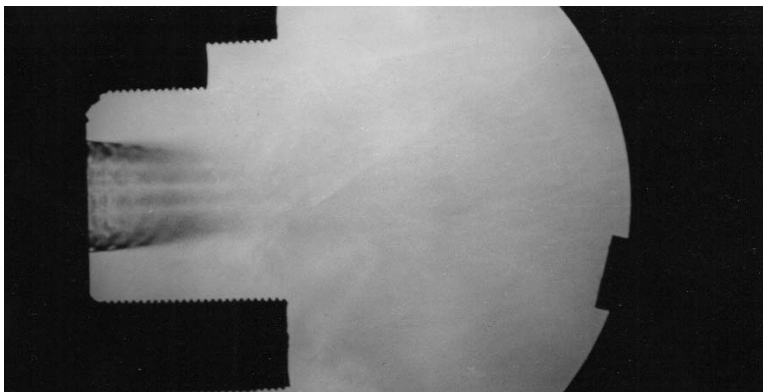

Figure 4. Photograph of the free flow of the air from the lance with annular supersonic nozzle ejector visualized by the shade method

3. Discussion

The visualization of the free flow from the ejector with annular supersonic nozzle showed shock waves of similar character to those in the flow originating from the Laval nozzle. The air flow from supersonic annular nozzle slows down in the boundary layer due to the contact of the flow with the surrounding air as well as due to the reciprocal effect of the shock waves in the annular section of the air flow. Further influencing factors are the energy losses and the flow deformation. Measurements confirm that an ejector with supersonic annular nozzle has lower efficiency than the Laval nozzle.

4. Conclusion

This investigation of the air flow in an ejector with a supersonic annular nozzle showed that the flow was similar in character to the flow from the Laval nozzle but the efficiency of the former device is lower.

The investigated basic aerodynamic data of the air flow in the ejector with supersonic annular nozzle have been used for the construction of a top-blowing lance for a continuous copper reactor.

REFERENCES

1. SEHNÁLEK, F., HOLECZY, J. and SCHMIEDL, J.: *A new process - continuous converting of copper mates*, Journal of Metals, **5**, (1964), 416-420.

2. SEHNÁLEK, F.: *General concept of continuous copper smelting in its starting period*, Metallurgical Review of MMIJ., **3**, (1986), 1-12.

3. IMRIŠ, I. and MACKEY, P.J.: *The continuous copper production*, Acta Metallurgica Slovaca, **3**, (1997), 511-522.

4. WAGNEROVÁ, E., SCHMIEDL, J., REPÈÁK, V. and TOMÁŠEK, K.: *Blowers development for continuous copper production*, Hutnícke listy, **6**, (1982), 415-419. (in Slovakian).

5. SZEKELY, J. and THEMELIS, N.J.: *Rate Phenomena in Process Metallurgy*, Wiley-Interscience, New York. 1971.

6. WAGNEROVÁ E.: *A study in the air flow through an ejector with annular supersonic nozzle*, Strojírenství, March (1988), 151-157. (in Slovakian).

THROUGH THE EYES OF A FELLOW WORKER

ANDRÁS NYIRI

Deptartment of Fluid and Heat Engineering, University of Miskolc

3515 Miskolc-Egyetemváros, Hungary

`aramnya@gold.uni-miskolc.hu`

Abstract. The paper aims to present the most important results of Tibor Czibere.

1. Years in the Works Ganz

I learned about the vivid professional public life of experienced colleagues as well as of promising young fellow workers at the Engineers' Club of the Ganz Locomotive and Wagon Manufacturers and Mechanical Engineers in the second half of the 1950s. *Ernő Trenka*, head of the Hydraulic Department - earlier the Design Division of Pumps and Turbine - attached me to the Pump Division, though my intention was to join the turbine designers. His aim was to introduce me into the pump design that had been taught in the school of professors *Pattantyús*[1] and *Gruber*[2]. The lectures in the Club by assistant professor *Fűzy* offered a very good opportunity to ask him a lot of questions concerning the problems I had trouble in what today is called numerical computational methods. But before he was able to respond another beginner gave surprisingly very competent and thoroughgoing answers to my questions. The name of the other young man was *Tibor Czibere*, who was working on the design of the blade rows of torque converters at another division of Ganz. Since the turbine blades of a converter were made of highly curved profiles, he necessarily had to deal with the cascades. In theis way he must have gone over the task of designing hydrofoils for pump blades having straight camber lines. A short time after that we worked at desks opposite each other in the newly established Research Division of the Department. *Czibere*'s task was the design of water turbine runners and mine involved pump impellers.

Czibere was able to exceed the old and still applied concept of solving engineering tasks on an empirical basis because he represented a different way of approach. *Kármán* had been a pioneer of the concept of using mathematics as the language of problem solving in engineering. Professor *Samu Borbély* founded a school in Miskolc which belonged to *Rothe*'s famous school of applied mathematics in Berlin.

---

[1] Géza Á. Pattantyús (1885-1956) Professor of Hydraulic Machines
[2] József Gruber (1915-1972) Professor of Fluid Mechanics

2. A nonlinear heat conduction problem

Before coming to the Ganz *Czibere* worked as an assistant of Professor *Borbély* for two years.

Metallurgy flourised in those years so the heat transfer problems arose related to the heating of blocks [1,2]. The non-linear partial differential equation (PDE) of heat conduction is as follows:

$$\nabla \cdot [k(\vartheta) \nabla (\vartheta)] = \rho(\vartheta) \, c(\vartheta) \, \frac{\partial \vartheta}{\partial t}$$

where the density ρ, the specific heat c, the heat conductivity k depend on the temperature ϑ and t is time. Without entering into details I refer only to the excellent technique of integral transformation by which the task of solving the PDE becomes a linear PDE of potential theory:

$$U(\mathbf{r}, t) = \int_0^{\vartheta(\mathbf{r},t)} k(\lambda) \, d\lambda$$

where $U(\mathbf{r}, t)$ depends on the radius vector $\mathbf{r}$ and the time t. Transforming the PDE we get the equation:

$$\Delta U = A(U) \frac{\partial U}{\partial t}, \qquad \text{where} \qquad A(U) = \frac{\rho \, c}{k}.$$

Applying *Green*'s formulas one arrives at an integro-differential equation. The solution of a complicated problem should contain the solutions valid for its special case. As is well known, the solution of the heat conduction problem for physical parameters independent of the temperature can be given in terms of *Bessel* functions. *Czibere*'s solution coincides with the solution valid for that special case.

3. Computational method for the design of a straight cascade of airfoils

The paper Computational method for the design of straight cascade of airfoils with highly curved profile blades by Czibere was published in the Acta Technica Academiae Scientiarum Hungaricae in 1960 [3]. In this profound article a method of computation to determine a straight cascade with a prescribed deflection angle of flow was presented. In another approach the deflection means the lift force arising on a profile, or putting it another way again, the change of the energy content of the flow passing through the blades. The treatise was based on the determination of the velocity field induced by vortices and sources on the plane of complex numbers. The vortex and source-sink distributions along a curve mean tangential and normal velocity jumps across it. These distributions are the so-called hydrodynamic singularities. The integral of the vortices along the curve gives the circulation around the profile, i.e., the deflection and the source-sink distribution determine the shape of the foil. Because the task is to find the very shape of the foil, i.e., the carrier curve of the hydrodynamic singularities, the solution can only be obtained by iterative computations.

In the middle of 1950s *Scholtz* and *Schlichting* published their work on straight cascade but the camber line was supposed to be a straight line and the thickness of the profile was also restricted size. *Czibere* extended the method in his paper on 69 pages including not only the theory but the detailed algorithm of computations as well. The sequence of calculations was supported with appropriate tables applicable by anyone. Furthermore several elaborated examples showing blade shapes, velocity and pressure distributions proved the practical use of the method. The value and importance of the algorithm and the pattern of computation can really be appreciated if we remember the tools of calculation available forty years ago. In the age of mechanical calculators the numerical evaluation of improper integrals with acceptable accuracy was really of a high value. I remember when after having returned from a conference held in London in 1963, I was given a possibility to acquire a computing machine from abroad but the western company refused to sell it to Hungary. I scarcely believe that one could find anybody willing to undertake a task like that having such rudimentary tools nowadays.

Achieving such a theoretical result could justly be praised any time. But it should not be forgotten that we worked for an industrial company where the goal is always to serve customers with products, therefore a pure theoretical method can satisfy just a few people but not the company. Research activities must be determined accordingly.

In the year of publication, in 1960 the 10th Congress of International Applied Mechanics was held at Stresa, Italy, where *Czibere* presented a paper entitled *Iterative method for the determination of straight and radial cascades* [4]. *Theodore von Kármán* also attended the congress and noticee the young lecturer for two reasons. First the name *Czibere* had to be a Hungarian one, and secondly, the idea of vortex had made *Kármán*'s name famous all over the world. The appreciation by *von Kármán* put *Czibere*'s name onto the list of the world-famous engineers of the Ganz Works. There was a common saying: an engineer either belonged or belongs or will belong to the Ganz. Unfortunately this a saying of the past now.

In 1963 the Hungarian Academy of Sciences awarded Czibere the Ph. D. degree for the thesis in which he worked out a method for the determination of highly cambered straight cascade of foils [5,6]. His method was worth mentioning in the book Vorlesungen über Theoretische Mechanik by Professor *István Szabó* of the Technische Universität Charlottenburg, West-Berlin. Professor *Szabó* invited Czibere as visiting professor to deliver lectures about his method.

4. Two main tasks concerning the cascade of airfolds

The design method of straight cascades can only be applied to runners and impellers of axial flow machines having a constant meridional width. The blade channels of mixed-flow machines with a variable channel width needed the extension of the method. The functions of complex variables can only be applied to plane flow. The conformal mapping provides a possibility to establish the relation between the flow around straight and radial cascades. A cascade cut off a mixed flow impeller is also a two dimensional one but it is on a surface of revolution. One can obtain an integral transformation

between a plane flow and the flow on a surface of revolution having the same properties like that of a conformal mapping by solving an ordinary differential equation. Let us denote the arc length of the meridional curve of the surface of revolution by σ, the distance from the axis of rotation by $r(\sigma)$, and the angle of a point by φ. The angle and ratio preserving the transformation between the points on the surface and the points (σ, φ) on the plane of Descartes coordinates (x, y) are as follows:

$$x = K \left[-\frac{1}{2} + \frac{1}{a} \int_0^\sigma \frac{\mathrm{d}\sigma}{r(\sigma)} \right], \; y = K \frac{\varphi}{a} \; ,$$

where K and a are constants. The connection between the velocity components on the plane and on the surface F is:

$$c_{x,y} = \frac{a}{K} r(\sigma) \; c_{F\sigma,\varphi}.$$

This transformation brought a decisive change in the determination of the velocity field in a part channel with variable width b and density of fluid ρ of a mixed-flow machine.

The PDE for the velocity potential function ϕ on the plane is of the form

$$\Delta\phi = -\frac{\partial\phi}{\partial x} \frac{1}{\rho b} \frac{\mathrm{d}(\rho b)}{\mathrm{d}x}.$$

One has to write another equation between the velocity and the density of the flow. The solution of these equations relates not only to the hydraulic machines but to the compressors and turbines working with compressible fluid as well.

I must make a remark concerning the applicability of the method. While the theoretical work was being made by *Czibere*, I designed the first double suction pump with a mixed-flow impeller of the type DST.

There are two main tasks concerning the cascade of airfoils: 1.) to design the geometry of the foils apt to deflect the flow as required, 2.) to determine the velocity field around the given cascade of foils. In the first case the boundary curve is sought for on which the distributions of hydrodynamic singularities are prescribed and in the domain around the PDE has to be satisfied. The second task could be solved utilizing the potential theory directly, i.e., the PDE can be reduced to an integral equation. By solving the integral equation a potential density is obtained. Substituting the latter into the *Green* formula, the solution of the PDE, i.e., the velocity potential function will be determined. However, we do not need the velocity potential but its derivatives only. The velocity jump across the boundary is either prescribed or sought for. On the right hand side (RHS) of the PDE the through flow velocity component and the varying flow density are included. Because the PDE is *Poisson* like, which includes the unknown velocity distribution on the RHS, the solution can only be obtained by iterative computations. Consequently, the canonical way is not advantageous, instead, the extension of the method worked out for the straight cascade with constant width and density - for which the same PDE stands with zero RHS - offers a more suitable computational procedure. Without showing the details, I must make a remark that

in the early 1960s we could not know that the applied method would later be called as the boundary element method.

For the thesis that contained the solutions of the two main tasks of the hydrodynamic cascade theory the Hungarian Academy of Sciencis awarded Czibere the degree Doctor of Technical Sciences in 1967, see [7,8] for details.

The application of the method in engineering practice proved to be fruitful in the hydraulic design of several Francis and Kaplan turbines. *Czibere* not only directed but also took part in the work.

I would also like to mention a detail from his career here. He was appointed Minister of Culture and Education in 1988. I think it was because of his scientific, industrial and academic activities and his successful work as the head of the University. Being a minister is first and foremost a political position, where – I think – the assertion of the professional's intention, his engineering expertise, integrity, scientific talents and personal excellence may have to yield priority to other issues.

5. Further investigations in incompressible and compressible flows

Czibere was chosen to be a corresponding member of the Hungarian Academy of Sciences (1976). His inaugural speech was *The determination of the boundary layer plane flow based on vortex discontinues* [9]. The basic idea is that a boundary layer around the surface of a solid body in the stream is simultaneously a vortex layer. The vortex density function is either discontinuous or has a pole on the surface. After having determined the vector potential of the vortex layer, an integral expression will serve to compute the velocity field around the body. The proper choice of the vector potential ensured that the computed theoretical results had good agreement with the experiments. This study proved the generally accepted concept that the flow can be dealt with as an ideal fluid apart from the immediate vicinity of the body first stated by *Prandtl.*

Czibere was promoted to be an ordinary member of the Hungarian Academy of Sciences in 1985. The theme of his inaugural lecture was quite different from the previous one and had the title *Shock waves in a supersonic gas ejector* [10]. The nature of the supersonic flow is quite different from the subsonic one. Shock waves always occur if the speed of the compressible fluid exceeds the speed of sound. This is the case when the gas is flowing around a bullet or an aeroplane and if the gas flows in a channel. The properties of the gas - like velocity, pressure, density, temperature, and entropy - passing over a shock wave suddenly change therefore the basic equations of motion are not applicable. These jumps take place in a narrow strip. Depending on the angle of crossing we speak about normal or oblique shock waves. Since entropy always increases, the shock wave can only be an expansion wave. Two fluids are mixed in a gas ejector flowing in the same direction but with a different speed: one below, the other above the speed of sound. The driving gas arrives from a *Laval* nozzle, which accelerates the gas over the speed of sound. First the possible flow patterns in the *Laval* nozzle are examined. Then mixing procedures are dealt with depending

on the pressure, density, mass ratios of the gases and the ratio of cross sections the gases flow through. This subject requires different mathematical tools as the tasks mentioned earlier. The process must be followed step by step. The practical goal of this study was to decrease the vacuum in order to avoid cavitation in the water ring vacuum pump coupled with the ejector. The comparison of the calculated and the measured pressure distributions proved the theoretical approach.

6. Research for the industry

The forces exerted on the rotor of a turbomachine are of hydrodynamic origin. Due to the variation of the eccentricity in circumferential direction between the staying and rotating sleeves of a multistage pump unsteady forces arise like in a slide bearing. The impellers are subjected to axial thrust because the area opposite the impeller eye is under less pressure than the pressure on its back shroud. The thrust can be balanced automatically by a rotating disk mounted onto the shaft. The axial gap between the rotating and staying disk also varies because of the flexible deformation of the shaft. This causes a non-symmetrical pressure distribution around the shaft which leads to a pulsing bending moment in the shaft. The study *Determination of the dynamic interacting between solid and fluid continua* suggests a more comprehensive method to compute the unsteady hydrodynamic forces and momenta. The special cases, e.g., the theory of lubrication of slide bearings can be deduced from the general method.

The next paper *Computation of the eigenfrequencies of multicomponent rotors loaded by hydrodynamic forces and momenta* employs the previous report. The conditions supposed in this paper are much less restrictive than in other investigations. The angle torsion of a cross section of the shaft revolving with constant angular velocity perpendicular to the axis of rotation is allowed. The rotating shaft will make precessional motion. After having determined the hydrodynamic and shearing forces and momenta, a fourth order PDE is set up for the neutral axis which will be deformed to a space curve. The function sought for is of a complex value with complex variables. The PDE can be reduced to an ordinary differential equation the eigenfunctions of which are complex functions depending on real variables. The method is for analyzing the bending vibration of a rotating shaft with finite length. The complex deformation and angular torsion of the center of gravity of a cross section and the bending moment as well as the shear forces can be computed. The rotor of a multistage machine can be divided to loaded and unloaded parts. All the cases which may occur to a shaft are treated: e.g. varying cross sections, rigid disk, clutch, fixed shaft end, flexibly supported bearing etc. Matrix equations describe these sections of the rod. These transfer matrices can be coupled in a rather simple way. The study ended by an example analyzing numerically the bending vibrations of a multistage boiler feed pump.

The computer simulation of the air and exhaust system including the boiler of the 200 MW block of the Mátra Power Plant was a new task. The operational parameters such as the temperature, pressure, etc. were to be determined for varying thermal loads of the boiler, different fuels and air inputs. The setting of the closing and

throttling valves and the unavoidable leaks and through flows were to be taken into consideration. The characteristics of the pulverizer fan, which is a special part of the system, had to be determined for different concentrations and grain sizes of the lignite. The balance equations and the continuity conditions at the nodal points resulted in a non-linear system of 45 equations. A great number of constant parameters of the block were also needed but their site measurements could not been carried out with acceptable accuracy or at all. The original design parameter values were not available. Had those been available, they would have been obsolete. After all the model of the system had to correspond with the measurable operational values. Finally the software developed had to be apt for the every day use by the staff running the block.

To determine the real characteristics of a turbomachine the viscous effects should be taken into account [11,12]. An extension of the cascade theory must involve frictions. A method was worked out for a cascade of foils bounded by two plane walls [13]. The effect of blading and friction on the flow were taken into consideration separately. The blade effect is represented hydrodynamically by a field of constraint forces which are determined by the change of the moment of momentum in the inviscid flow. The frictional effect on the fluid flowing through a cascade is taken into account based on the analogy between the channel flow and the flow in the bladed space. The results are the energy loss along the blades in the through flow direction and other quantities. Further steps aiming at the application to a mixed-flow channel made it possible to compute the real head-discharge characteristics of a pump for different flow rates and pre-whirl of the absolute flow. The calculated and measured characteristics showed a good agreement.

7. A heat transfer problem associated with phase change

One of the important courses of the Ph.D. programs at our University is thermodynamics for which Professor *Czibere* is responsible. Within this heat conduction is his favorite as he dealt with it in his younger age. The transport processes are treated in his book *Heat conduction* published in 1998 [14]. The global balance equations, the conservation laws, the main laws of thermodynamics and the similarity laws are dealt with in a much more comprehensive way than one could expect it upon the title of this book. The general PDE of heat conduction and its initial and boundary conditions are discussed including the heat transport in metals when phase change occurs. A great many steady and unsteady tasks in 1, 2, and 3 dimensions are solved on about 200 pages, several amongst them would be worth publishing as separate scientific papers. The mathematics applied in the book can be found in its appendix. Not only the Ph.D. students but researchers can use the book in their work as well.

8. A three dimensional stochastic turbulence model

The investigation of turbulence phenomena of flow has been the basic problem of fluid dynamics since the end of the 19th century, when the first concept was created by *Osborne Reynolds*. *Theodore von Kármán* stated n 1930 that the flow patterns at different points of the velocity field are mechanically similar in a fully developed

turbulent flow. His hypothesis was restricted only to two dimensional flow though the turbulence is always three dimensional. Recently *Czibere* extended the mechanical similarity to three dimensional flow. Details in connection with his investigations can be found in the first paper of the present issue. In spite of this I would like to present repeatedly the most important result of his paper in order to give a somewhat different interpretation to it and for the sake of completeness as well. According to *G. I. Taylor*'s at that time (1935) quite new concept, the turbulent velocity fluctuation **v**' is to be considered a random variable. **v**' is the difference of the instantaneous velocity and the mean velocity **v**. The assumptions were also made that the turbulence is homogenous and isotropic. These hypotheses cannot be maintained for a real turbulent flow today. The correlation tensors by which the phenomenon attempted to describe the turbulence led to more unknown variables than equations could be set up. Consequently, the determination of the *Reynolds* stress tensor $\mathbf{F}_R$ could not be attained. There are tremendous models for turbulence but they are valid only in special particular cases. Attempts to obtain the *Reynolds* tensor assumed some connection between it and the strain rate tensor. As *Czibere*'s theory proves it $\mathbf{F}_R$ cannot be coupled with the strain rate tensor [15].
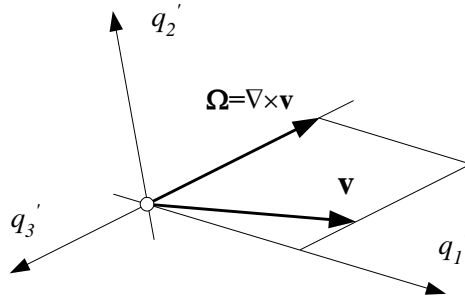

Figure 1.

Applying *Friedman*'s theorem for conservation of vector lines to flow of fluids of constant density ρ, *Czibere*'s theorem states, as analogy to *Helmholtz*'s vortex theorem, that

$$\frac{\partial \mathbf{\Omega}}{\partial t} + (\mathbf{v} \cdot \mathbf{\nabla})\, \mathbf{\Omega} - (\mathbf{\Omega} \cdot \mathbf{\nabla})\, \mathbf{v} = \nu \cdot \mathbf{\Delta}\mathbf{\Omega} + \mathbf{\nabla} \times \left(\overline{\mathbf{v'} \times \mathbf{\Omega'}} \right) \ ,$$

where $\mathbf{\Omega} = \mathbf{\nabla} \times \mathbf{v}$, $\mathbf{\Omega}' = \nabla \times \mathbf{v'}$, ν is the kinematic viscosity coefficient, t is time and the time average is denoted by an overbar. The conclusion is that the vortex line will not persist either in fully viscous or in fully turbulent flow. The vortex theorem for the turbulent velocity fluctuation is:

$$\frac{\partial \mathbf{\Omega}'}{\partial t} + (\mathbf{v'} \cdot \mathbf{\nabla})\, \mathbf{\Omega}' - \left(\mathbf{\Omega}' \cdot \mathbf{\nabla} \right) \mathbf{v'} = (\mathbf{\Omega} \cdot \mathbf{\nabla})\, \mathbf{v'} + \nu\, \mathbf{\Delta}\,\mathbf{\Omega}' \ .$$

It follows from this that the vortex diffusion occurs even in an inviscid fluid. One can conclude that the source of turbulence is the vorticity of the main flow $\mathbf{\Omega}$.

The velocity fluctuation vector can be expressed as the rotation of a vector potential function. After proper geometrical and physical similarity transformations, a PDE

for the dimensionless vector potential $\mathbf{f}$ can be obtained. Applying the solution, the *Reynolds* stress tensorwill have the following form:

$$\mathbf{F}_R = -\rho \left(\mathbf{v}\text{'} \circ \mathbf{v}\text{'}\right) = -\rho\,\ell^2\,|\Omega|\,\Omega\,\left(\overline{\nabla \times \mathbf{f} \circ \nabla \times \mathbf{f}}\right)\;,$$

where ℓ is the scale factor of turbulence.

The representation of the stochastic process of the intrinsic mechanism of turbulence in the natural orthogonal coordinate system $(q_1\text{'}, q_2\text{'}, q_3\text{'})$ with a coordinate plane spanned by the vectors $\mathbf{\Omega} = \nabla \times \mathbf{v}$ and $\mathbf{v}$, - the direction of $\mathbf{\Omega}$ being opposite to $q_3\text{'}$ - looks like

$$\Omega = \frac{1}{H_1\text{'} H_2\text{'}}\,\frac{\partial\,(v_1\,H_1\text{'})}{\partial\,q_2\text{'}}.$$

where $H_i\text{'}$ are the *Lamé* coefficients. The *Reynolds* stress tensor will have the form:

$$\mathbf{F}_R = \rho\,\kappa^2\,\ell^2\,\mathbf{H}_0\,\left|\frac{1}{H_1\text{'} H_2\text{'}}\,\frac{\partial\,(v_1\,H_1\text{'})}{\partial\,q_2\text{'}}\right|\,\frac{1}{H_1\text{'} H_2\text{'}}\,\frac{\partial\,(v_1\,H_1\text{'})}{\partial\,q_2\text{'}},$$

here κ is the *Kármán's* constant and the similarity tensor is:

$$\mathbf{H}_0 = \begin{pmatrix} \alpha & 1 & \mu \\ 1 & \beta & \vartheta \\ \mu & \vartheta & \gamma \end{pmatrix}.$$

The elements of $\mathbf{H}_0$ are constant numbers. A very important circumstance is that the number of equations and the unknown variables of the turbulent flow are equal.

The shortly outlined concept of turbulence applied to the flow in tubes of circular cross-section resulted in velocity distributions that are in good agreement with the measurements carried out by *Nikuradse* about 70 years ago. *Czibere* is currently working on more complicated applications of his concept.

I ought not forget to mention that the computer codes are worked out and numerical computations are carried out by himself.

I suppose that this unavoidably short summing up the activities of *Tibor Czibere* would make any evaluation superfluous. What I may only do is to express my pleasure that I could be a witness of the thoughts arising and from time to time I was a fellow worker to discuss the problems. I am also very proud of my friendship with him. At the same time the fact that Czibere's work has not yet been utilized as completely as it would be required and possible – like the achievements of many other Hungarian Scientists – fills me with sorrow. One can only hope that time will make up for the delay.

REFERENCES

1. CZIBERE, T.: *Investigation of the non-linear heat conduction problem of a block based on the first boundary condition*, MTA Műsz. Tud. Közleményei, **24**, (1959), 23-32. (in Hungarian)

2. CZIBERE, T.: *Investigation of the non-linear heat conduction based on the potential theory*, Publications of the University of Heavy Industry, **XIV**, (1967), 61-72. (in Hungarian),

3. CZIBERE, T.: *Berechnungsverfahren zum Entwurf gerader Flügelgitter mit stark gewölbten Profilschaufeln*, Acta Techn. Hung., **28**, (1960), 43-71.

4. CZIBERE, T.: *Iterationverfahren zur Profilbestimmung von geraden und radialen Schaufelngittern mit hilfe beliebiger Trägerkurven der hydrodynamischen Singularitäten,* 10th Congress of Applied Mechanics, Stresa (1960); Periodica Polytecnica, **M**(V/1), (1961), 65-77.

5. CZIBERE, T.: *Design method of highly cambered straight cascade of blades*, Thesis for the Ph.D. degree, 1962, pp. 1-71. (in Hungarian)

6. CZIBERE, T.: *Über die Berechnung der Schaufelprofile und der Strömung um die Schaufeln von Strömungsmaschinen*, Ingenieur Archive, **33**, (1964), 215-230.

7. CZIBERE, T.: *The solution of the two main tasks of cascade theory based on potential theory*, Thesis for the degree of Doctor of Sciences, (1965), pp. 1-154. (in Hungarian)

8. CZIBERE, T.: *Erfahrungen über die Anwendung zweidimensionaler Berechnungsmethoden bei der Auslegung von Radialer- und Halbaxialgittern im Pumpenbau*, Pumpen und Verdichter Int. Symp. Leipzig, (1967), 33-42.

9. CZIBERE, T.: *Determination of the plane boundary layer flow by discontinuous vortex layers*, Műszaki Tudomány, **53**, (1977), 347-374. (in Hungarian)

10. CZIBERE, T.: *Shock waves in a supersonic gas ejector*, Inaugural speach at the Hungarian Academy of Sciences, 1985, (Manuscript).

11. CZIBERE, T.: *Die Berechnung der turbulenten Strömung in den beschaufelten Räumen von Strömungsmaschinen,* Mitt. des Pfleiderer-Inst. TU Braunschweig Heft 1 (1994), pp. 97-104.

12. CZIBERE, T. and NYIRI, A.: *Computation of pump characteristics based on cascade theory*, Proc. of the Tenth Conf. on Fluid Machinery, Budapest, (1995), 280-289.

13. CZIBERE, T., NYIRI, A. and KALMÁR, L.: *Computation of the energy loss of flow through a straight cascade of aerofoils bounded by two plane walls*, ICIAM/GAMM The Third Cong. on Ind. and Appl. Math., Hamburg (1995), ZAMM Vol.76, Suppl. 5(1966), 109-110.

14. CZIBERE, T.: *Heat Conduction*, Miskolc University Press, 1998., pp. 1-274. (in Hungarian)

15. CZIBERE, T.: *Mechanische Ähnlichkeit der turbulenten Flüssigkeitsströmungen*, Publications of the University of Miskolc, Series C, **50**, (1999), 3-12.

Notes for Contributors
to the Journal of Computational and Applied Mechanics

Aims and scope. The aim of the journal is to publish research papers on theoretical and applied mechanics. Special emphasis is given to articles on computational mechanics, continuum mechanics (mechanics of solid bodies, fluid mechanics, heat and mass transfer) and dynamics. Review papers on a research field and materials effective for teaching can also be accepted and are published as review papers or classroom notes. Papers devoted to mathematical problems relevant to mechanics will also be considered.

Frequency of the journal. Two issues a year (approximately 80 pages per issue).

Submission of Manuscripts. Submission of a manuscript implies that the paper has not been published, nor is being considered for publication elsewhere. Papers should be written in standard grammatical English. Two copies of the manuscript should be submitted on pages of A4 size. The text is to be 130 mm wide and 190 mm long and the main text should be typeset in 10pt CMR fonts. Though the length of a paper is not prescribed, authors are encouraged to write concisely. However, short communications or discussions on papers published in the journal must not be longer than 2 pages. Each manuscript should be provided with an English Abstract of about 50–70 words, reporting concisely on the objective and results of the paper. The Abstract is followed by the Mathematical Subject Classification – in case the author (or authors) give the classification codes – then the keywords (no more than five). References should be grouped at the end of the paper in numerical order of appearance. Author's name(s) and initials, paper titles, journal name, volume, issue, year and page numbers should be given for all journals referenced.

The journal prefers the submission of manuscripts in LaTeX. Authors should prefer the standard LaTeX article style and are not recommended to define their own LaTeX commands. Visit our home page for further details concerning the issue how to edit your paper.

For the purpose of refereeing, two copies of the manuscripts should initially be submitted in hardcopy to an editor of the journal. The eventual supply of an accepted-for-publication paper in its final camera-ready form (together with the corresponding files on an MS–DOS diskette) will ensure more rapid publication. Format requirements are provided by the home page of the journal from which sample LaTeX files can be downloaded:

<center>http://www.uni-miskolc.hu/home/web/pumns/mechanics</center>

These sample files can also be obtained directly (via e-mail) from a member of the Editorial Board, Gy. Szeidl (mechszgy@gold.uni–miskolc.hu), upon request.

Twenty offprints of each paper will be provided free of charge and mailed to the correspondent author.

The Journal of Computational and Applied Mechanics is abstracted in Zentralblatt für Mathematik and in the Russian Referativnij Zhurnal.

A Short History of the Publications of the University of Miskolc

The University of Miskolc (Hungary) is an important center of research in Central Europe. Its parent university was founded by the Empress Maria Teresia in Selmecbánya (today Banska Štiavnica, Slovakia) in 1735. After the first World War the legal predecessor of the University of Miskolc moved to Sopron (Hungary) where, in 1929, it started the series of university publications with the title *Publications of the Mining and Metallurgical Division of the Hungarian Academy of Mining and Forestry Engineering* (Volumes I.-VI.). From 1934 to 1947 the Institution had the name Faculty of Mining, Metallurgical and Forestry Engineering of the József Nádor University of Technology and Economical Sciences at Sopron. Accordingly, the publications were given the title *Publications of the Mining and Metallurgical Engineering Division* (Volumes VII.-XVI.). For the last volume before 1950 – due to a further change in the name of the Institution – *Technical University, Faculties of Mining, Metallurgical and Forestry Engineering, Publications of the Mining and Metallurgical Divisions* was the title.

For some years after 1950 the Publications were temporarily suspended.

After the foundation of the Mechanical Engineering Faculty in Miskolc in 1949 and the movement of the Sopron Mining and Metallurgical Faculties to Miskolc, the Publications restarted with the general title *Publications of the Technical University of Heavy Industry* in 1955. Four new series - Series A (Mining), Series B (Metallurgy), Series C (Machinery) and Series D (Natural Sciences) - were founded in 1976. These came out both in foreign languages (English, German and Russian) and in Hungarian.

In 1990, right after the foundation of some new faculties, the university was renamed to University of Miskolc. At the same time the structure of the Publications was reorganized so that it could follow the faculty structure. Accordingly three new series were established: Series E (Legal Sciences), Series F (Economic Sciences) and Series G (Humanities and Social Sciences). The seven series are formed by some periodicals and such publications which come out with various frequencies.

Papers on computational and applied mechanics were published in the

Publications of the University of Miskolc, Series D, Natural Sciences.

This series was given the name Natural Sciences, Mathematics in 1995. The name change reflects the fact that most of the papers published in the journal are of mathematical nature though papers on mechanics also come out.

The series

Publications of the University of Miskolc, Series C, Fundamental Engineering Sciences

founded in 1995 also published papers on mechanical issues. The present journal, which is published with the support of the Faculty of Mechanical Engineering as a member of the Series C (Machinery), is the legal successor of the above journal.

Contents